The Jet Energy Scale Uncertainty Derived from γ-jet Events for Small and Large Radius Jets and the Calibration and Performance of Variable R Jets with the ATLAS Detector

Lucy A. Kogan

Hertford College, Oxford

Thesis submitted in partial fulfilment
of the requirements for the degree of
Doctor of Philosophy

Trinity Term, 2014

The Jet Energy Scale Uncertainty Derived from γ-jet Events for Small and Large Radius Jets and the Calibration and Performance of Variable R Jets with the ATLAS Detector

Lucy A. Kogan
Hertford College, Oxford

Thesis submitted in partial fulfilment of the requirements
for the degree of Doctor of Philosophy

September 2014

Abstract

In this thesis the jet energy scale uncertainty of small and large radius jets at the ATLAS detector is evaluated in-situ using γ-jet events. The well calibrated photon in the γ-jet events is used to probe the energy scale of the jets. The studies of the jet energy scale of small radius jets are performed using 4.7 fb^{-1} of data collected at $\sqrt{s} = 7$ TeV in 2011.

The γ-jet methods which were developed are then adapted and applied to large radius jets, using 20.3 fb^{-1} of data collected at $\sqrt{s} = 8$ TeV in 2012. The new jet energy scale uncertainties are found to be $\sim$1 % for $|\eta| < 0.8$, rising to 2-3 % for $|\eta| > 0.8$. These uncertainties are significantly lower than the 3-6 % precision which has previously been achieved at ATLAS using track jets as a reference object. Due to the increase in precision, uncertainties due to pile-up and the topology of the jet also had to be evaluated. The total energy scale uncertainties for large radius jets are reduced by $\sim$1-2 % (0.5-1 %) for $|\eta| < 0.8$ (> 0.8). This reduction will be beneficial to analyses using large radius jets and it is specifically shown to benefit the $t\bar{t}$ resonance search in the semi-leptonic channel. The $t\bar{t}$ search looks for events with two top quarks in the final state, where one decays leptonically and the other hadronically. The hadronically decaying top quark is reconstructed using a large radius jet, and the jet energy scale uncertainty is a dominant source of uncertainty in the analysis.

In addition to the studies of the jet energy scale of large radius jets, the first derivation of a calibration, and jet energy scale uncertainties derived with γ-jet events, are shown for Variable R jets. The Variable R jet algorithm is a new type of jet algorithm with a radius that is inversely proportional to the size of the jet, making it useful for the study of high momentum top quarks. It is shown that similar methods can be used to calibrate and assess the uncertainties of Variable R jets as are used for standard, fixed radius jets at the ATLAS detector, although some adaptations will be necessary. The studies provide a basis for the calibration of Variable R jets in the future.

Acknowledgements

There are many people who I would like to thank for their help and support over the last 4 years. First of all, I would like to thank the STFC for funding my PhD and the Oxford physics department and Hertford College for their help to attend conferences and summer schools. These events are really useful and the additional funding required to attend is greatly appreciated.

Next I would like to thank my supervisor, Cigdem Issever, for her support and guidance over the last few years. I would also like to thank her for her help and patience during the writing and preparation of this thesis over the last months.

Many thanks goes to all those on ATLAS and in the Oxford ATLAS group who I have worked with during my PhD. Thank you to the FSI team, including Andree Robichaud-Veronneau, Richard Nickerson, Elizabeth Gallas and Zhijun Liang, who helped to make my service work project on FSI interesting and enjoyable. Thanks to the people who started me off on the γ-jet analysis when I arrived at CERN (at which point I had only a very vague understanding of what the Jet Energy Scale was): Francesc Vives, Jiri Kvita, Andres Tanasijczuk and Tancredi Carli. Many thanks to everyone else in Jet EtMiss, which has been a fun and supportive group to work within. There are far too many people there to thank individually but none of you are forgotten! Also thanks to those in the $t\bar{t}$ resonance search who I have had support from, including Jiahang Zhong who has always been helpful when I have needed any top-related help. Thank you to Sarah Livermore for introducing me to Variable R jets and to Katharina Behr for joining the Variable R jet effort and really helping to push the project ahead.

Many thanks to those who have read all or parts of this thesis when they didn't have to: James Ferrando (I appreciated the additional joke per chapter which made the process easier), Caterina Doglioni (who knows everything about jets), and Dan Short (who will be mentioned again later). Next, thank you to my fellow students: Alex Dafinca, David Hall and Jacob Howard who have been there for coffee and lunch throughout. Thanks also to the students at Oxford who were there when I arrived (Sam, Caterina, Ellie, Rob, Alex, James, Dan, Gemma, Phil and Chris), who helped me settle in, and to those who have arrived since (including Mireia, Jim, Craig, Shaun, Kate and Katharina). Also thanks to everyone at CERN, including everyone else on LTA and Kat's wine class, who made my stay there fun. Many thanks also to the particle physics secretaries (Sue, Kim, Francesca, Daniella and Laura) for all of their help with forms, LTA etc over the last few years.

Thank you to friends and family outside of physics who provide welcome fun and support. To Bryony, Rosie, Grace and Dee who I have known for a very long time, who I have seen less of then I would have liked over the last few years, but who I know are always there when I surface from the work. Many thanks go to my Mum, who is always there and almost always knows what to say and how to keep me calm, not just for this PhD but for all the times before that as well. Thank you also to my sister, Sarah, who I know is always at the end of the phone and in person when our busy lives allow it, and always there when needed. Thank you to my grandparents and everyone else who I have not mentioned here.

Finally, thank you to Dan, who has been there throughout this process and has patiently put up with me while I've been writing up. Without him this would have been much more difficult, and less fun.

Preface

The large nature of the ATLAS collaboration means that analyses are performed using work and contributions from many people. As far as possible, this thesis focuses on studies which I have performed. However, for clarity, my contributions are detailed here:

- γ-jet **calibration for small-R jets (Chapter 6):** I produced the nominal response distributions for the direct balance γ-jet method, the photon energy scale systematic, the JER systematic and the studies of the impact of the pile-up uncertainties on the method. I also developed the $E_{\mathrm{T}}^{\gamma\ \mathrm{cluster}}/(\sum p_{\mathrm{T}}^{\mathrm{tracks}})$ requirement for converted photons, which is discussed in Section 6.2. These studies are published in Ref. [1] and internal ATLAS back-up documentation can be found in Ref. [2].
- γ-jet **uncertainties for large-R jets (Chapter 7):** I derived the γ-jet uncertainties presented in Sections 7.3, 7.4 and 7.5. The pile-up uncertainties presented in Section 7.7 are also my own work. The studies of the photon response distribution for different substructure variables (Figures 7.15 and 7.16), in the topology uncertainty section (Section 7.6) are my studies. The γ-jet uncertainties and pile-up uncertainties will be presented in a conference note, which is currently in preparation. The draft for this note can be found in Ref. [3] and back-up documentation with further details can be found in Ref. [4].
- **Variable R jet calibration and uncertainties (Chapters 8 and 9):** The studies presented in these two chapters are my own work. No public documentation is available but two internal notes are in preparation, including detailed plots of the pile-up subtraction and calibration, which can be found in Refs. [5] and [6].

Throughout the text I have given references where further details can be found about the studies shown here. As far as possible publicly accessible references are given. However, in many cases no public document is available, in which case internal ATLAS documentation is cited. Where figures were not produced by myself for this thesis, or where the figures are published in a conference note or paper, a reference is given in the caption.

In addition to the work presented here I also developed a visualisation tool for the Frequency Scanning Interferometry system (FSI), which was my service work project to gain ATLAS authorship.

This thesis will use natural units ($c = \hbar = 1$) throughout.

Contents

Chapter 1

Introduction

The Standard Model of Particle Physics has been one of the most successful theories to date, describing all observed particles and interactions (with the exception of the gravitational force) to a high precision [1]. Despite this success the Standard Model is not believed to be the final theory of particle physics, and it is expected that new theories and new particles will be needed at the TeV scale and above [7]. Over the last 5 years, experiments such as the ATLAS experiment [8] at the Large Hadron Collider (LHC) [9] have investigated and measured many aspects of the Standard Model of Particle Physics, as well as pushing searches for new physics into the TeV energy regime. The observation of the Higgs boson was one of the most important discoveries of recent years [10, 11]. The Higgs boson arises as a consequence of the Higgs field and mechanism [12–14] that generate the mass of the fundamental particles. Within experimental precision recent results show that the properties of the new boson are consistent with the Higgs boson that is predicted by the Standard Model of particle physics [15–19].

This discovery, and the many measurements and searches which are performed at the LHC, are made possible due the unprecedentedly high-energy proton-proton collisions which are delivered to the experiments. Centre-of-mass energies of $\sqrt{s} = 7$ TeV and $\sqrt{s} = 8$ TeV have meant that the ATLAS detector is operating in a challenging environment with high

---

[1] Additionally, the masses of the neutrinos are not naturally part of the model but must be added to it.

densities of particles in the detector. Some of the most common products of hard scattering processes in proton-proton collisions are quarks and gluons. These quarks and gluons are not directly observed in the detector but hadronise and decay into showers of particles which are reconstructed as *jets*. Jets dominate many of the final states that are seen in the ATLAS detector. The study and performance of these objects is a field of its own and an experimental understanding of jets is vital for any measurement or search which uses them at the LHC.

Additionally, in the high-energy regime in which the LHC operates, particles such as the W and Z bosons, the top quark, and the Higgs Boson, are produced with a momentum that can greatly exceed their mass. When these *boosted*, heavy particles decay the resulting products are highly collimated, making it difficult to resolve their individual decay products, due to the limited spatial resolution of the detector. This has resulted in the development of many new methods, jet algorithms and techniques, such as the use of jets with a large enough radius to encompass the decay products of these boosted particles. The way that the energy and mass are distributed within the jets is studied and it is known as *jet substructure* [20]. Studying jet substructure allows for discrimination between large radius jets which contain the decay products of, for example, a top quark as opposed to light quarks or gluons.

This thesis will present results relating to the performance of jet algorithms and the calibration of the jet energy at the ATLAS detector. A brief summary of relevant theory, including that of jet physics and boosted objects will be given in Chapter 2. The ATLAS detector will be introduced in Chapter 3 followed by an overview of the reconstruction of physics objects including photons and jets and their calibration in Chapters 4 and 5.

The in-situ calibration of small radius jets using γ-jet events (events with a photon and jet travelling in opposite directions in the final state) is presented in Chapter 6. These studies form the basis for the evaluation of the jet energy scale uncertainties for large radius jets using γ-jet events, which will be shown in Chapter 7. The development of these uncertainties was driven by the need for a more precise method to measure the jet energy scale of large radius jets, which is often one of the dominant systematic uncertainties for analyses making use of these jets. These studies are the first studies of the jet energy scale of large-R jets derived using γ-jet events at the ATLAS detector, and they were the first method used to probe the jet energy scale of large-R jets in the forward regions of the detector.

In the second part of this thesis (Chapters 8 and 9) the development of a new calibration and set of uncertainties for a new type of jet algorithm that has a variable jet radius will be presented. These jets have the property that their radius becomes smaller as the transverse momentum of the jet increases. Similarly, the area into which the decay products of a boosted particle fall decreases as the momentum of the parent particle increases since the decay products become increasingly highly collimated. This makes Variable R jets an ideal candidate for reconstructing boosted objects as they can be tuned to reflect the topology of the decay of boosted particles.

The first studies of these jets at the ATLAS detector [21] showed that their use could increase the efficiency of reconstructing the decay products of boosted top quarks, in comparison to fixed radius jets. The analyses presented here are the first studies of the calibration and uncertainty of Variable R jets at the ATLAS detector.

Chapter 2

Theory and Motivation

In this chapter, a brief overview of the Standard Model of particle physics is given. This is followed by an overview of the physics of jets, and of their use for the study of particles such as the W and Z bosons and top quark in the TeV regime. Finally, an introduction to γ-jet events (events containing a photon and a jet) is given.

2.1 The Standard Model of Particle Physics

The Standard Model of particle physics describes all the fundamental particles and forces that have so far been observed in nature, with the exception of the gravitational force [1]. It is a gauge theory based on a $SU(3) \otimes SU(2) \otimes U(1)$ symmetry which results in the particles and force carriers shown in Figure 2.1.

The model describes two families of matter particles: quarks and leptons, and three fundamental forces: the electromagnetic, the weak and the strong force. The quarks are spin 1/2 fermions which interact via the electromagnetic, the weak and the strong forces. The leptons are spin 1/2 fermions, of which the neutrinos only interact via the weak force and the electron, muon and tau interact via the electromagnetic and the weak forces. The spin 1 force carriers are the photon of the electromagnetic interaction, the W^{+-} and Z

---

[1] Additionally, the masses of the neutrinos are not naturally part of the model but must be added to it.

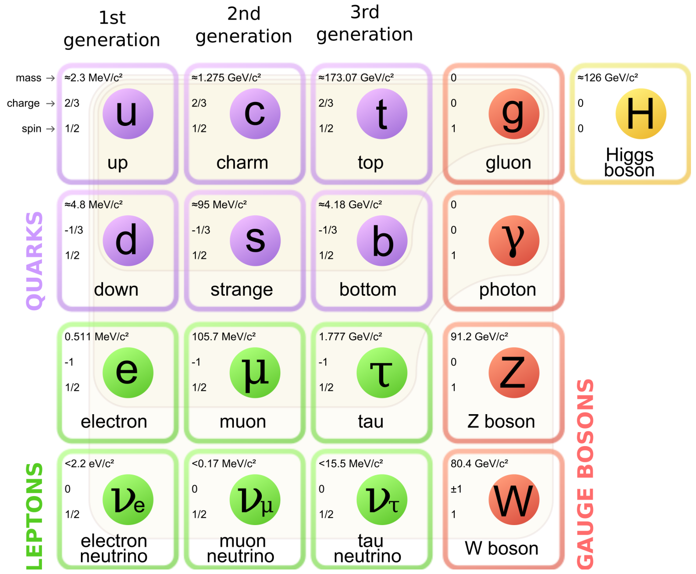

Figure 2.1: The fermions and bosons of the Standard Model of particle physics including their mass, charge and spin [22].

bosons of the weak interaction and the gluon of the strong interaction. The matter particles are grouped into three generations. Each generation has a set of particles with the same quantum numbers but different masses.

The following section briefly introduces the theory of Quantum Chromodynamics (QCD) which is the SU(3) theory that describes the behaviour of quarks and gluons. QCD is important for understanding the properties of the collimated showers of particles, reconstructed as jets, which are the observable signals of quarks and gluons. There are many more detailed overviews of the Standard Model of particle physics and QCD, one such introductory text can be found in Ref. [23].

2.1.1 QCD: SU(3)

The SU(3) symmetry of the Standard Model is the theory of Quantum Chromodynamics (QCD), a gauge theory that describes quarks and gluons and their interactions. The fundamental charge of QCD is colour, which can take three states: red, green or blue. Quarks carry colour and therefore interact via the strong interaction. The force carrier of QCD is the gluon, a massless boson which exists in 8 states, each of which is a superposition of colour and anti-colour states.

The strong coupling constant (α_s) dictates the strength of interactions between coloured particles. An important property of α_s is how its value changes at different energies. In the case of the electromagnetic coupling constant, which dictates the strength of electromagnetic interactions, the value of the coupling constant increases at higher energy scales. However, in the case of QCD the strong coupling constant decreases at higher energy scales. This *running* of the strong coupling constant has been verified by many experimental and theoretical results as can be seen in Figure 2.2

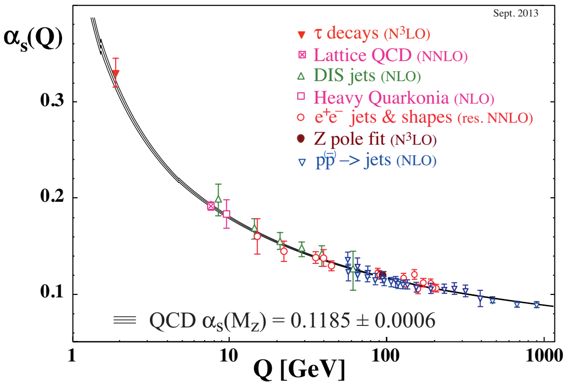

Figure 2.2: The strong coupling constant, α_s, measured at different experiments and using lattice QCD calculations, as a function of the momentum scale Q and the prediction of the running of the coupling constant using the world average value of α_s at M_Z as an input [24].

At lower energy scales and larger distances the strong coupling constant becomes stronger, resulting in the *confinement* of quarks and gluons. As quarks and gluons move apart from each other the binding energy between them increases and when the binding energy becomes too large, new quarks or gluons are created which bind together to form hadrons. The hadrons formed are always colour neutral. This process is known as *hadronisation*. Hadronisation is a non-perturbative process [25] (meaning it cannot be described using a perturbative series expansion). Therefore, it must be simulated using Monte Carlo generators, to give predictions for the final state hadrons which are observed at particle physics experiments.

At high momentum scales the running of the strong coupling constant means that quarks and gluons can be treated as free particles (this is known as asymptotic freedom) and QCD can be *factorised* [25]. This means that perturbative calculations of observables, such as the rate of production of quarks or gluons, can be performed separately to the evaluation of non-perturbative effects.

For proton-proton collisions, such as those at the LHC, a collision involves many different processes (some of which are depicted in Figure 2.3). A simulated collision roughly follows the following time-line (as described in [26]):

- The two protons collide. Each proton contains many quarks and gluons which carry the momentum of the proton. Quarks and gluons are known as *partons* in this context. The momentum fraction carried by the quarks and gluons is described by *Parton Density Functions* [25] (PDFs).
- One parton from one proton interacts with one parton from the other proton, this is known as the *hard interaction, scatter* or *process.* This interaction can be described by perturbative QCD calculations and sets the energy scale of the hard interaction.
- Short lived resonances such as the top quark, W^{+-} and Z bosons decay into either quarks (eg. $Z \to q\bar{q}, W \to q\bar{q}$, $t \to Wb \to q\bar{q}b$) or leptons and neutrinos (eg. $Z \to l\bar{l}$, $W^{+} \to \bar{l}\nu$, $t \to W^{+}b \to \bar{l}\nu b$).
- The incoming partons in the collision radiate gluons and photons via Bremsstrahlung radiation. This is known as *Initial State Radiation* (ISR).
- Radiation also occurs from the outgoing partons from the hard interaction, this is known as *Final State Radiation* (FSR).
- In addition to the hard interaction the other quarks and gluons in the protons can interact, these interactions are known as *Multiple Parton Interactions* (MPIs). MPIs also have associated ISR and FSR.
- The quarks and gluons involved in the hard interaction and MPIs take a fraction of the total energy of the initial protons. The remaining energy is carried by the remnants of the protons (the *beam remnants*) which have a momentum approximately along the direction of the incoming protons. Together the MPIs and beam remnants are known

as the *underlying event* (UE).

- As discussed above, the increasing strength of the strong coupling constant as the quarks and gluons move away from each other results in the hadronisation of the outgoing quarks and gluons into colourless hadrons. The resulting hadrons are often unstable and decay further into particles with a lifetime long enough to be detected.

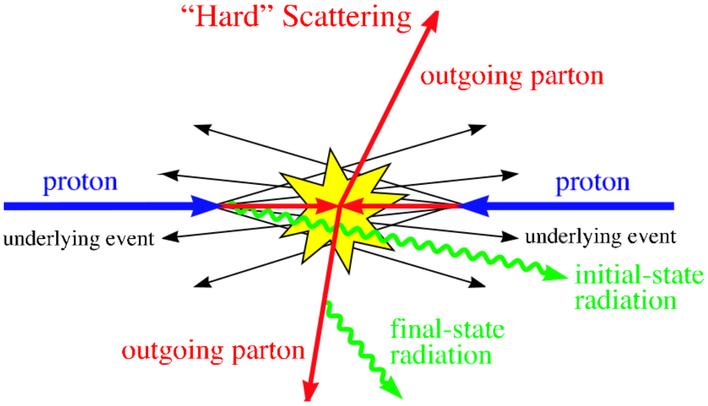

Figure 2.3: Diagram illustrating a proton-proton collision [27], copyright © IOP publishing. The decay of the outgoing partons and hadronisation is not shown.

The ability to model the non-perturbative effects that describe PDFs, ISR, FSR, the underlying event and hadronisation is crucial for making predictions that can be tested against experimental results. The models used to simulate ISR and FSR are known as *parton showers*. There are many different Monte Carlo generators which use different models for parton showers, hadronisation and the underlying event. The parameters in many of these models are tuned using data.

Two Monte Carlo generators are used to simulate events for this thesis: PYTHIA (versions 8 [28] and 6.425 [29]) and HERWIG (v6.510 [30] and HERWIG++ v2.5.2 [31]). The PYTHIA and HERWIG generators have different models for the parton shower and for hadronisation. The parton shower is modelled as a series of probabilities for a parton to split into two partons (these probabilities are the DGLAP splitting functions [32–34]). In the case of PYTHIA these probabilities are p_{T}-ordered, whereas in the case of HERWIG and HERWIG++ they are angular-ordered, according to the angle of emission.

For the hadronisation, PYTHIA uses the Lund string model [35], where the strong force between partons is modelled as a colour-flux tube. The potential energy in this 'string' increases as the partons move apart from each other. Eventually the string breaks and new partons are formed, which bind to form hadrons. In the case of HERWIG and HERWIG++ the cluster hadronisation model [36] is used. This model splits gluons into $q - \bar{q}$ pairs, and uses the colour-flow in the parton shower to form colour singlets (known as clusters), which then decay to form the hadrons.

The versions of these Monte Carlo generators that were used to simulate events for this thesis will be discussed further in Section 3.9.

2.2 Jets

The collimated showers of particles that are produced by the hadronisation of quarks and gluons, and the resulting energy deposits in the detector, are reconstructed as *jets*. In order to define a jet it is necessary to decide how to combine the particles produced during hadronisation and subsequent decays. The way in which this combination is performed is known as a *jet definition*.

Jets can be formed such that their properties (e.g. transverse momentum and direction) are similar to those of the particles produced by the hadronisation of a quark or gluon. Alternatively, they can be formed such that they contain the hadronic decay products of, for example, the W or Z bosons or the top quark. The definition of a jet is inherently ambiguous since the processes underlying hadronisation and fragmentation include many non-perturbative effects. Therefore the choice of jet definition must depend on many different experimental and theoretical factors, not only the physics that one wishes to observe.

The Snowmass accord, constructed by the experimental and theoretical community in 1990, states that a jet definition should aim to satisfy the following properties [37]:

- *Simple to implement in an experimental analysis.*
- *Simple to implement in the theoretical calculation.*

- *Defined at any order of perturbation theory.*
- *Yields finite cross sections at any order of perturbation theory.*
- *Yields a cross section that is relatively insensitive to hadronisation.*

A jet definition consists of a *jet algorithm*, which describes which particles to combine into jets and a *recombination scheme* that defines how to combine the 4-vectors of the particles. There are multiple types of jet algorithm and various recombination schemes, an overview of which can be found elsewhere [38]. The recombination scheme most widely used at current experiments and for all the jet definitions discussed here is the 4-vector recombination scheme. In this scheme 4-vectors are simply summed in order to combine particles.

An important property of any jet algorithm is that it is infrared (IR) and collinear safe. This means that the jets which are found by the algorithm are not affected by soft emissions (particles emitted with a small energy, ie. $E \to 0$) or collinear emissions (particles emitted with a small angle of emission, ie. $\Delta\theta \to 0$) as illustrated in in Figure 2.4. Therefore, the same set of jets, with the same properties, is found with and without soft and collinear emissions. Additionally, infinities that arise in the calculation of soft and collinear emissions cancel when the jets are IR and collinear safe, so that theoretical calculations can be made. IR and collinear safety are very important since they make jets (relatively) insensitive to the modelling of hadronisation. This in turn allows for measurements using jets to be compared to accurate theoretical predictions.

Jet algorithms can be split into two categories: *cone algorithms* and *sequential recombination algorithms*. As the name suggests, cone algorithms group together particles within a cone with a fixed radius in (y, ϕ) space. Here, ϕ is the azimuthal angle and y is the rapidity which is defined as:

$$y = \frac{1}{2} \ln \left(\frac{E + p_z}{E - p_z} \right), \tag{2.1}$$

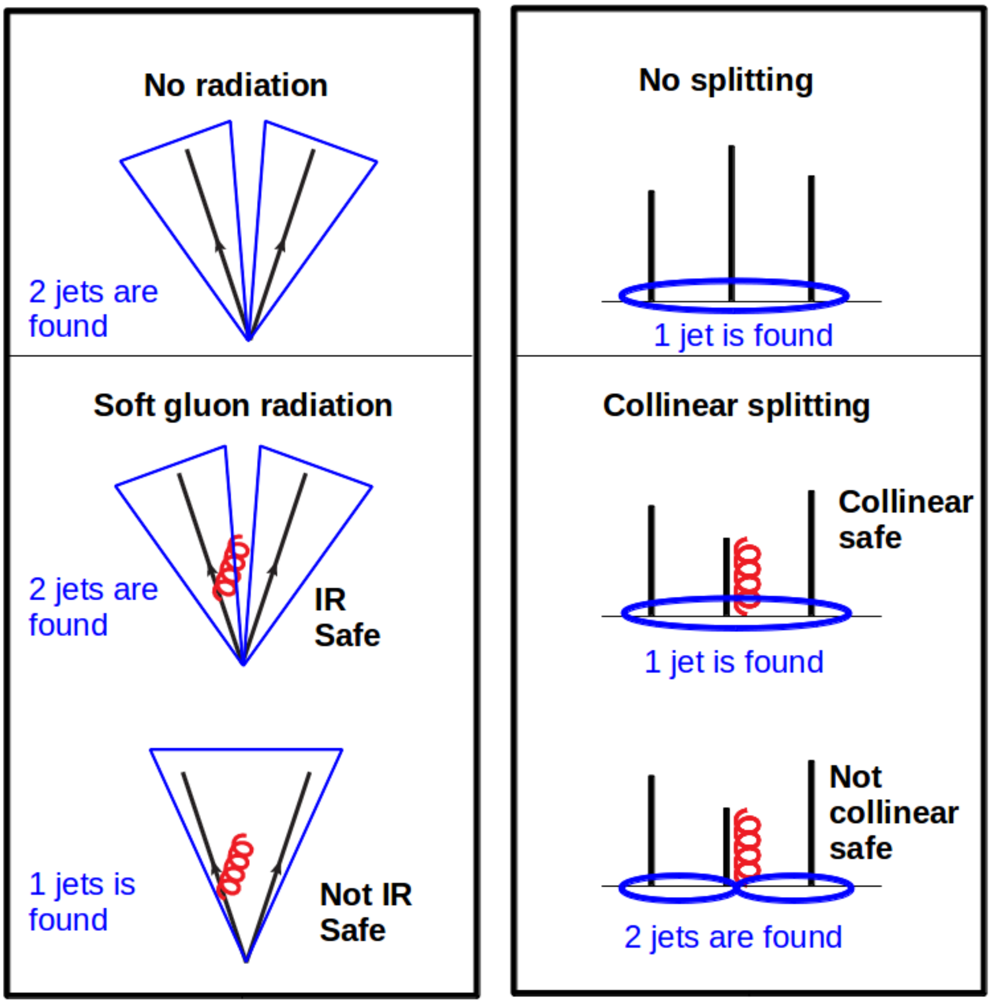

(a) (b)

Figure 2.4: a) An example of infrared (IR) safety. Without any radiation the two partons form two jets. In the case of the middle diagram the formation of jets is unaffected by soft gluon radiation (two jets are still formed) and therefore the jet algorithm is IR safe. However, in the case of the bottom diagram the soft gluon radiation results in the formation of only one jet where there were previously two and therefore the jet algorithm is IR unsafe. b) An example of collinear safety. With no collinear splitting one jet is formed. In the case of the middle diagram one of the partons splits collinearly into two. Only one jet is found as was the case without the collinear splitting and therefore the jet algorithm is collinear safe. However, in the case of the bottom diagram the collinear splitting of the parton results in two jets being found rather than one, in which case the jet algorithm is collinear unsafe.

where E is the energy and p_z is the momentum in the longitudinal direction. Differences in rapidity are invariant under Lorentz boosts along the z-axis.

Most variations of cone algorithms use *seed* particles to decide where the centre of the cones should be at the start of the algorithm. Unfortunately, this leads to IR unsafe algorithms. The only experimentally usable implementation of a cone algorithm is the SIScone algorithm [39]. However it is not used at ATLAS since many aspects of the performance were shown to be worse (the reconstruction time, the efficiency of reconstructing jets, the purity of jets and the trigger efficiency) or similar (noise suppression and sensitivity to the UE) when compared to the anti-k_t jet algorithm [40].

The jet definitions used at ATLAS are IR and collinear safe sequential recombination algorithms. At hadron colliders, such as the LHC, sequential recombination algorithms make use of two values: the cluster-cluster[2] distance d_{ij} and the cluster-beam distance d_{iB}, defined as:

$$d_{ij} = min(p_{Ti}^{2p}, p_{Tj}^{2p})\Delta R_{ij}^2, \tag{2.2}$$

$$d_{iB} = p_{Ti}^{2p} R_{\text{eff}}^2, \tag{2.3}$$

where $min(p_{Ti}^{2p}, p_{Tj}^{2p})$ is the minimum p_T of cluster i and j, $\Delta R_{ij}^2 = \Delta\phi^2 + \Delta y^2$ is the distance between cluster i and j and R_{eff} is the distance parameter of the jet algorithm. The value of R_{eff} defines the approximate radius of the jets which are formed.

Using d_{ij} and d_{iB} the following sequence is used to construct jets:

1. Calculate d_{ij} for all combinations of clusters in the event and d_{iB} for all clusters in the event.
2. Find the smallest d_{ij} and the smallest d_{iB} in the event.

---

[2] In this context a cluster is taken to be either a single particle or a group of particles which have already been combined by a previous step of the algorithm.

3. If $d_{ij}^{\text{min}} < d_{iB}^{\text{min}}$ then clusters i and j are combined.
4. If $d_{iB}^{\text{min}} < d_{ij}^{\text{min}}$ then cluster i is set aside as a jet.

Steps 1-4 are then repeated until there are no pairs of clusters remaining which satisfy $d_{ij} < d_{iB}$.

The value of p in Equations 2.2 and 2.3 affects the order in which the particles in an event are clustered together and hence the final shape of the jets.

- **The k_t algorithm, $p = 1$:** Soft particles cluster first. The sequence of the clustering is related to the probabilities for one parton to split into two partons in QCD [38].
- **The Cambridge-Aachen algorithm, $p = 0$:** Particles which are geometrically close cluster first. The sequence of clustering contains information about the angular structure of a jet.
- **The anti-k_t algorithm, $p = -1$:** Hard particles cluster first. The clustering sequence is not meaningful but the jets which are produced are approximately circular in shape.

An illustration of the different jets formed by these three algorithms, when applied to the same event, is shown in Figure 2.5.

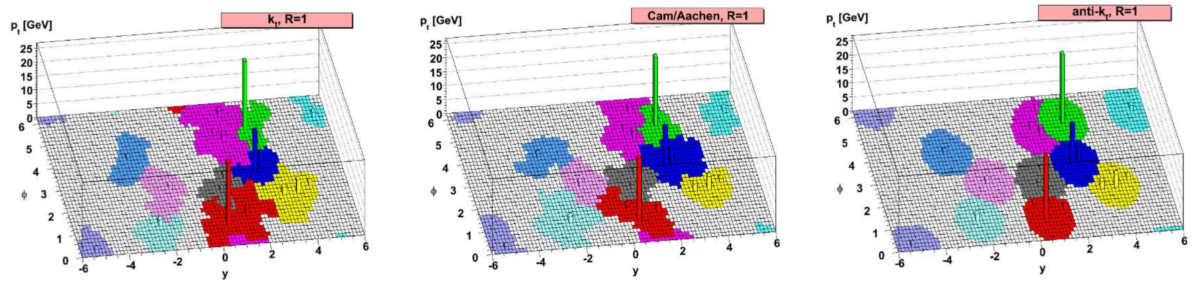

(a) (b) (c)

Figure 2.5: The diagrams show the jets formed by a) the k_t algorithm, b) the Cambridge-Aachen algorithm and c) the anti-k_t algorithm[41]. All the jets have a distance parameter of $R_{\text{eff}} = 1$. The bars represent the jet constituents that the jets were built from. The height of the bars is proportional to their p_{T} and their colour indicates which jet they belong to.

The Variable R (VR) jet algorithm [42] is a variant of the sequential recombination algorithms that uses a variable R_{eff} rather than a constant R_{eff}:

$$R_{\text{eff}}^{\text{VR}} = \frac{\rho_{\text{VR}}}{p_{Ti}}, \tag{2.4}$$

where ρ_{VR} is a parameter which is chosen by the user of the algorithm and p_{Ti} is the p_{T} of cluster i. The result of defining R_{eff} in this way is that the size of the jet is inversely proportional to the p_{T} of the jet. The type of jets which are formed with the VR jet algorithm can be seen in Figure 2.6, compared to those formed by the anti-k_t algorithm. It can be seen that some of the jets are smaller when reconstructed with the Variable R jet algorithm in comparison to the anti-k_t algorithm (e.g. the blue jet) and some jets are larger (e.g. the yellow jet) due to their respectively higher and lower values of p_{T}.

When using the standard sequential recombination algorithms jets are circular in (y, ϕ) space. Therefore, jets in the central rapidity region will have a larger size in (θ, ϕ) space in comparison to those in the forward rapidity region. Using the VR jet algorithm, the jets will have the same $E\Delta S$ for all rapidity, where $\Delta S = \sqrt{(\Delta\theta)^2 + (\sin\theta\Delta\phi)^2}$ and E is the energy of the jet. Therefore, jets with a given energy will have the same angular size for all rapidity. This is beneficial since it is expected that the angular size of jets produced from the decay of a resonance will be circular in (θ, ϕ) space. Therefore, the VR jet algorithm captures the natural shape of the jets more accurately than the fixed radius sequential recombination algorithms. This is the original reason for the development of the VR jet algorithm [42].

The VR jet algorithm can be run as a Cambridge-Aachen or anti-k_t algorithm. The studies in this thesis focus on the anti-k_t variant of the VR algorithm. A minimum jet size (R_{min}) is defined in order to prevent the jets becoming smaller than the granularity of the experimental apparatus and a maximum jet size (R_{max}) is defined to prevent the jet size from tending to very large values at low p_{T}.

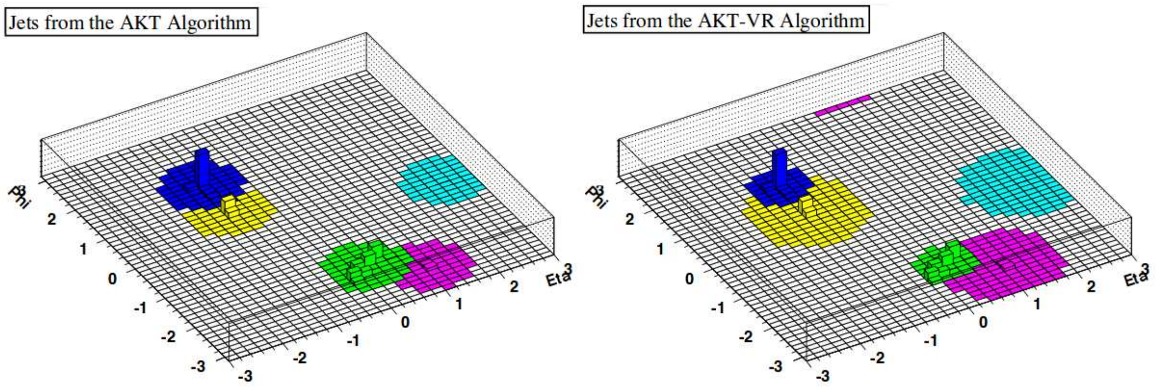

Figure 2.6: The diagrams show jets formed by a) the anti-k_t algorithm and b) the anti-k_t version of the VR algorithm [42]. The bars represent the jet constituents which the jets were built from. The height of the bars is proportional to their p_{T} and their colour indicates which jet they belong to.

2.3 Boosted Physics and Jet Substructure

The high centre-of-mass energies reached by the LHC result in the production of particles with a high transverse momentum. For W bosons, Z bosons, top quarks and the Higgs boson the transverse momentum that they carry can greatly exceed their mass ($p_T >> m$). When these particles decay hadronically (ie. $Z \to q\bar{q}, W \to q\bar{q}$, $t \to Wb \to q\bar{q}b$, $H \to b\bar{b}$), they are detected using jets .

When the heavy particle's transverse momentum is close to, or less than, their rest mass then the decay products are well separated and one jet can be used to represent one parton. At the ATLAS experiment jets with a radius of $R = 0.4$ and $R = 0.6$ are the standard choice for this situation [1, 43] whereas at the CMS experiment jets with a radius of $R = 0.5$ and $R = 0.7$ are used [44].

However, when $p_T >> m$ the decay products are highly collimated due to the Lorentz boost of the parent particle. This is illustrated in Figure 2.7 for top quark decays. The tops are produced in simulated $Z' \to t\bar{t}$ events. The Z' boson is a spin-1 boson, proposed by theories including the theory of topcolour-assisted technicolour [45]. Here the Z' has a mass of 1.6 TeV and it is used as a source of high p_{T} top quarks. In Figure 2.7 a) the separation of the W boson and the b quark resulting from top decays is shown. For $p_T^{\mathrm{top}} < 200$ GeV it can be seen that the W and b quark are well separated. However, for higher p_{T} the separation rapidly becomes small and for $p_T^{\mathrm{top}} \gtrsim 300 - 400$ GeV the separation enters the regime $\Delta R(\mathrm{W},\ \mathrm{b}) < 0.8$. Similarly, the separation between the quark and anti-quark from the hadronic decay of the W decreases rapidly with increasing top quark p_{T}, as can be seen in Figure 2.7 b), where for $p_T^{\mathrm{W}} \gtrsim 200$ GeV the separation enters the regime $\Delta R(q,\ \bar{q}) < 0.8$. When the partons from the top decay are within $\Delta R < 0.8$ of each other then the individual partons can not be resolved using jets with $R = 0.4$.

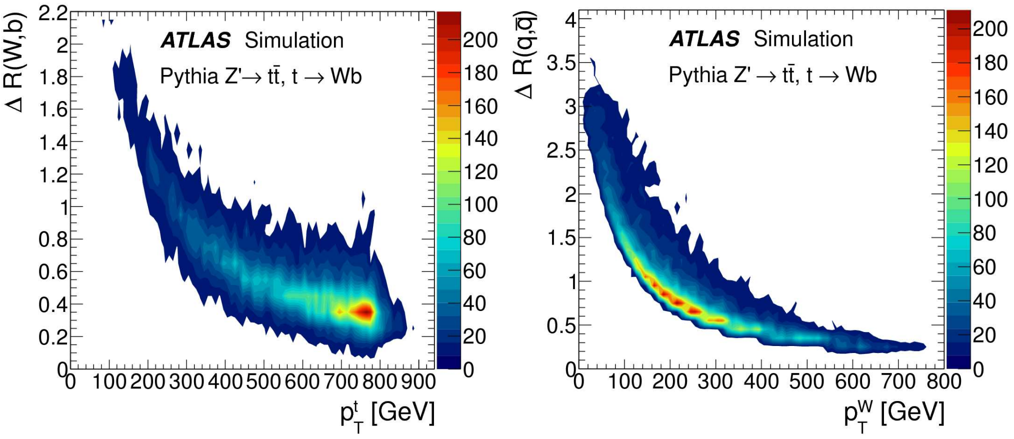

(a) (b)

Figure 2.7: a) ΔR between the W and b from a top decay as a function of the p_{T} of the top quark and b) ΔR between the quark and anti-quark from the hadronic decay of the W boson, as a function of the p_{T} of the W boson. The tops are the result of simulation of the decay of $Z' \to t\bar{t}$ using the PYTHIA v6.425 [29] Monte Carlo generator with a Z' mass of 1.6 TeV [46]. The distributions shown are at parton-level: meaning that they do not include effects due to ISR, FSR, the underlying event, or any detector effects.

For these high p_{T} regimes jets with a large distance parameter (known as large-R jets) can be used to encompass the decay products of the decaying particle (e.g. the quarks from a hadronically decaying top quark). Similarly searches looking for events with high jet multiplicities (e.g. $\gtrsim 6$ jets) where the jets can not be resolved individually can be studied using large-R jets. Jets with distance parameters of 1.0 and 1.2 are currently studied at the ATLAS experiment [46] whereas at the CMS experiment jets with distance parameters of 0.8 and 1.5 are studied [47, 48]. Both anti-k_t jets and Cambridge-Aachen jets are used. The former are relatively insensitive to soft energy deposits due to their circular shape. The clustering sequence of the latter contains useful information about the angular structure of a large-R jet.

To differentiate large-R jets containing the energy deposits due to the decay of a heavy particle from large-R jets containing only light quarks or gluons, the substructure of the jet is studied. Jet *grooming* (procedures that remove energy deposits from the jet) is used to pick out this hard substructure more easily, by removing energy deposits that are due to the underlying event and additional proton-proton interactions in the event. There are many types of jet grooming, an overview of those used at ATLAS and their performance can be found in Ref. [46]. For the studies presented in this thesis anti-k_t jets with $R = 1.0$ with a type of grooming known as *trimming* are used. Trimming is applied to each jet using the following procedure:

- The constituents of the large-R jet (the initial inputs to the jet finding algorithm which are contained within the jet) are re-clustered using the k_t algorithm with a distance parameter of $R = 0.3$ to form *subjets*.
- Any subjet with $p_T^{\mathrm{subjet}}/p_T^{\mathrm{jet}} < 0.05$ is discarded and the jet 4-vector is recalculated from the 4-vectors of the remaining subjets.

Following jet grooming it is easier to assess the substructure of a large-R jet. For example, a large-R jet containing the decay products of a hadronically decaying top quark is expected to have three clusters of energy deposits within the large-R jet; one due to the b-jet and one due to each of the quark and the anti-quark from the W boson decay. Various substructure variables have been developed to probe the substructure of large-R jets and they are used in various different combinations, depending on the specific analysis being performed. A few of the most commonly used substructure variables are listed below and more details of their performance at the ATLAS experiment can be found in Ref. [46].

- **Jet mass:** the mass of the jet (m^{jet}) is calculated from the 4-vectors of the constituents of the jet:

$$m^{\mathrm{jet}} = \sqrt{\left(\sum_i E_i\right)^2 - \left(\sum_i \mathbf{p}_i\right)^2}, \tag{2.5}$$

where E_i is the energy of the i^{th} jet constituent and $\sum_i \mathbf{p}_i$ is the vector sum of the three-momentum vectors of the jet constituents.

- k_t **splitting scales:** The jet is re-clustered using the k_t algorithm with a distance parameter of 1.5. At each step of the jet clustering the following splitting scale is defined:

  $$\sqrt{d_{ij}} = min(p_{Ti}, p_{Tj}) \times \Delta R_{ij}, \tag{2.6}$$

  where $min(p_{Ti}, p_{Tj})$ is the p_{T} of cluster i or cluster j, depending on which is the smallest, and $\Delta R_{ij} = \sqrt{\Delta y^2 + \Delta\phi^2}$ is the separation of clusters i and j in $(y,\ \phi)$ space. For the last step in the jet clustering $\sqrt{d_{ij}}$ is $\sqrt{d_{12}}$, for the second to last step $\sqrt{d_{23}}$ etc.

  For large-R jets with substructure (e.g. large-R jets containing a high p_{T} top quark) the energy deposits within the large-R jet will be less diffuse and they will be concentrated into more than one core. The k_T algorithm clusters soft energy deposits first and hard energy deposits last. Therefore, the scale of the final steps of the jet clustering will, in general, be larger for large-R jets with substructure than for large-R jets containing a light quark or gluon. This effect can be seen in Figure 2.8 which shows $\sqrt{d_{12}}$ and $\sqrt{d_{23}}$ for anti-k_t $R = 1.0$ jets with and without trimming. The distributions are shown for di-jet events (events containing two jets) where the large-R jets contain a light quark or gluon. They are also shown for $t\bar{t}$ events where the large-R jets contain the top quarks that are the decay products of a Z' boson with a mass of 1.6 TeV. It can be seen that, on average, $\sqrt{d_{12}}$ and $\sqrt{d_{23}}$ have much larger values for the large-R jets reconstructed in the Z' sample compared to the di-jet sample. It can also be observed that $\sqrt{d_{12}}$ has larger values than $\sqrt{d_{23}}$. This is expected due to the fact that the hardest energy deposits cluster last in the k_T algorithm.

- **N-subjettiness:** The n-subjettiness variables [52] (τ_N) give a measure of how much the energy deposits within a jet look like N or fewer subjets. The variables are constructed by re-clustering the jet constituents with the k_T algorithm and requiring that

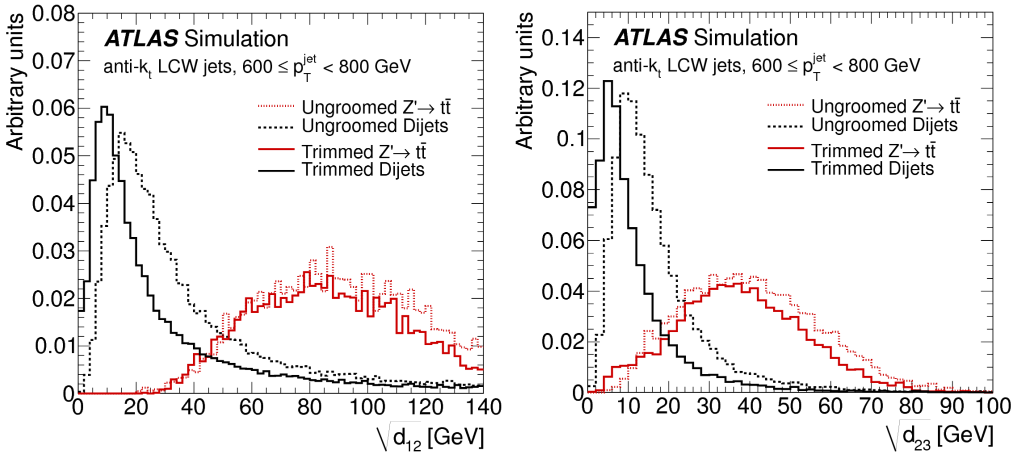

(a) (b)

Figure 2.8: Distributions of the k_T splitting scales a) $\sqrt{d_{12}}$ and b) $\sqrt{d_{23}}$ for anti-k_t $R = 1.0$ jets with $600 < p_T^{\text{jet}} < 800$ GeV [46]. The solid lines show the distributions for trimmed jets and the dotted lines show the distributions for ungroomed jets. The distributions are shown for large-R jets reconstructed in di-jet events (black) and for large-R jets reconstructed in $Z' \rightarrow t\bar{t}$ events where the Z' boson has a mass of 1.6 TeV (red). The di-jet events were simulated using POWHEG-BOX [49–51], interfaced with the PYTHIA v6.425 [29] Monte Carlo generator and the Z' events were simulated using the PYTHIA v6.425 generator.

N subjets are formed [3]. τ_N is defined as:

$$\tau_N = \frac{1}{d_0} \sum_k p_{Tk} \times min(\Delta R_{1k}, \Delta R_{2k}, ..., \Delta R_{Nk}), \quad d_0 \equiv \sum_k p_{Tk} \times R \tag{2.7}$$

where R is the jet distance parameter, p_{Tk} is the p_{T} of constituent k and ΔR_{ik} is the distance from subjet i to constituent k. In this way τ_N is a measure of how much the jet constituents are well aligned with the axes of the subjets. Therefore, τ_N will take lower values the more the jet looks like it has N or fewer subjets.

The ratio of n-subjettiness for different values of N provides a discriminant to distinguish jets containing multiple decay products from jets containing only one light quark or gluon. For example, if a jet contains two distinct clusters of energy deposits (e.g. from the decay of a Z boson) then $\tau_2 < \tau_1$ since the jet is more consistent with having two subjets or fewer (τ_2) than with having one subjet or fewer (τ_1). Therefore it would be expected that $\tau_2/\tau_1 < 1$.

---

[3] This is achieved using the *exclusive* version of the k_T algorithm, where the jet clustering is terminated when N jets have been found [52, 53].

Large-R jets and jet substructure are used in a variety of measurements and searches for new particles at the ATLAS and CMS experiments. They have been instrumental in pushing the exclusion limits for new physics searches into the TeV regime. Furthermore, as the LHC moves to increasingly high centre-of-mass energies these techniques will become increasingly important for measuring the properties of boosted objects. A large number of *top-tagging* techniques, which make extensive use of large-R jets and jet substructure, have been developed to identify boosted top quarks [4]. Techniques to identify Z bosons, W bosons, boosted Higgs bosons and large-R jets containing multiple light quarks or gluons have also been developed.

When making use of large-R jets it is of vital importance that the energy and the mass of these jets is well known, and that the way in which they and their substructure are sensitive to additional proton-proton interactions in the event is well understood. For many analyses using large-R jets, the jet energy scale is the dominant source of systematic uncertainty. Measuring the jet energy, mass and substructure of these jets as precisely as possible is therefore important so that the power of large-R jets and jet substructure can be fully exploited. A method of measuring the jet energy scale uncertainty for anti-k_t $R = 1.0$ trimmed jets to a high precision using γ-jet events will be presented in this thesis in Chapter 7. The impact of the JES uncertainty will be put into context using results from the semi-leptonic $t\bar{t}$ resonance search [55–58]. In this analysis new high mass resonances are searched for using the invariant mass distribution of the $t\bar{t}$ pair where one of the tops decays leptonically ($t \to Wb \to l\nu b$) and one of the tops decays hadronically ($t \to Wb \to q\bar{q}b$). The analysis uses anti-k_t $R = 1.0$ trimmed jets to reconstruct the hadronic top quark for the high mass regime where the top quarks are highly boosted. The large-R jets are required to have $m^{\text{jet}} > 300$ GeV and $\sqrt{d_{12}} > 40$ GeV in order to distinguish large-R jets which contain the decay products of the top quark from large-R jets containing quarks and gluons from background events.

---

[4] A comparison of top-tagging techniques used at the ATLAS experiment can be found in Ref. [54]

2.4 Variable R Jets for Boosted Top Reconstruction

The VR jet algorithm provides an interesting prospect for the reconstruction of boosted objects. The shrinking jet size with increasing jet p_{T} can be used to reflect the topology of boosted events. VR jets have been studied in the context of the semi-leptonic $t\bar{t}$ resonance search. Preliminary studies [21] showed an increase of ∼20 % in the acceptance of top quarks when using VR jets to resolve all the decay products of the hadronically decaying top quark separately, compared to fixed radius jets. This increase in signal acceptance has been confirmed in 8 TeV and 14 TeV Monte Carlo studies and an overview of more recent studies are given in [5] and in [6].

The semi-leptonic $t\bar{t}$ resonance search makes use of two different reconstruction strategies, known as the *resolved* and the *boosted* analyses, in order to be able to reconstruct $t\bar{t}$ events with invariant masses from ∼500 GeV up to ∼2-3 TeV. In the resolved analysis, depicted on the left of Figure 2.9, the event is required to contain at least four jets with $R = 0.4$: one of which is due to the b-quark from the leptonically decaying top quark, one of which is due to the b-quark from the hadronically decaying top quark and two of which are due to the quark and anti-quark from the hadronic decay of the W boson.

In the boosted analysis, depicted on the right of Figure 2.9, the event is required to contain at least two jets: one jet with $R = 0.4$ which is due to the b-quark from the leptonically decaying top quark and one jet with $R = 1.0$ containing the decay products of the hadronically decaying top quark. The jet with $R = 1.0$ is needed for the boosted regime due to the merging of the small-R jets from the top decay that was previously described in Section 2.3.

Ongoing studies are investigating the benefits of the VR jet algorithm in the resolved and the boosted regimes. They make use of the event selection criteria of the semi-leptonic $t\bar{t}$ resonance selection in order to select events containing a $t\bar{t}$ pair where one top decays leptonically and the other decays hadronically. Only the hadronically decaying top quark is studied here. Details of the semi-leptonic $t\bar{t}$ event selection and analysis can be found

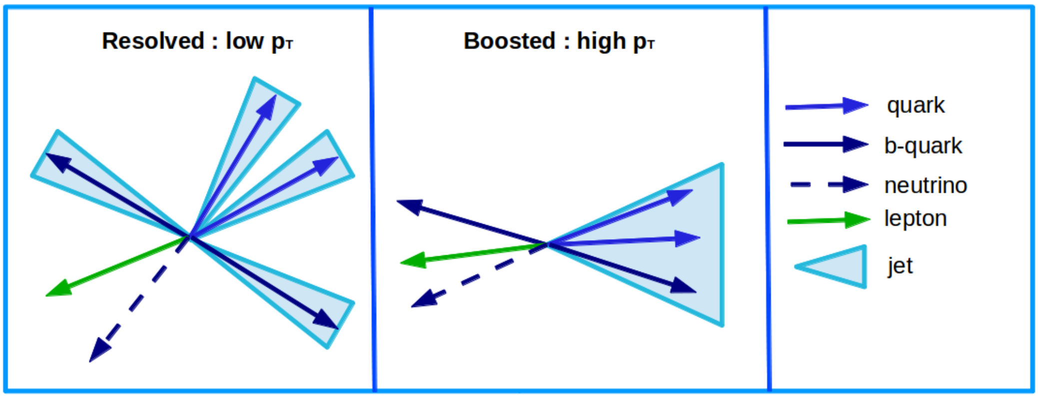

Figure 2.9: An illustration of the resolved and boosted analyses used to select $t\bar{t}$ pairs. On the left the resolved analysis is shown where each of the decay products of the top quark is reconstructed separately. On the right the boosted analysis is shown where the decay products of the hadronically decaying top quark are reconstructed using one large radius jet.

in Refs. [55, 56]. The studies shown here are performed using a signal sample where the $Z' \rightarrow t\bar{t}$ process is simulated for a Z' boson with a mass of 3 TeV using the PYTHIA 8 [28] Monte Carlo generator. The background samples are di-jet events, also simulated using the PYTHIA 8 Monte Carlo generator.

For the resolved regime small radius VR jets are used to resolve the individual decay products of the hadronically decaying top quark to a higher p_{T}. For the boosted regime large radius VR jets are used to capture the decay products of the hadronically decaying top quark. The choice of parameters and initial studies of small and large VR jets are discussed below.

If the VR jets which are discussed here are to be used for $t\bar{t}$ searches (or any other physics analysis) at ATLAS it is important that their performance and calibration is well understood. The second part of this thesis will deal with the first derivation of a Jet Energy Scale calibration and uncertainty for VR jets.

2.4.1 Small Variable R Jets

In the context of the resolved analysis VR jets with a small radius can be used to resolve the decay products of the top quark to higher values of $m_{t\bar{t}}$, when compared to using fixed radius anti-k_t jets. A maximum and minimum radius must be chosen for VR jets, as well as the value of ρ_{VR} [5]. In previous studies the maximum radius of the VR jets was chosen to be $R = 0.6$. For the studies presented here a maximum radius of $R = 0.4$ is chosen. This corresponds to the $R = 0.4$ fixed radius anti-k_t jets which are used in the resolved $t\bar{t}$ analysis. $R_{\text{min}} = 0.2$ is chosen in order to prevent the VR jets becoming smaller than the granularity of the calorimeters.

Figure 2.10 shows the fraction of events in which the partons from the hadronically decaying top quark are merged for fixed radius $R = 0.4$ anti-k_t jets and for VR jets with $\rho_{\text{VR}} = 60$ GeV (which have a variable size for $150 < p_T^{\text{jet}} < 300$ GeV). Partons are considered to be merged if $\Delta R(a,b) < 0.8$ for $R = 0.4$ fixed radius anti-k_t jets or if $\Delta R(a,b) < R^a_{\text{eff}} + R^b_{\text{eff}}$ for VR jets. $R^a_{\text{eff}} = \rho_{\text{VR}}/p^a_T$ and $R^b_{\text{eff}} = \rho_{\text{VR}}/p^b_T$ are the radii of the VR jets. Three categories are shown: *no merging* where none of the partons are merged; *partially merged* where two partons are merged; and *all merged* where all three of the partons are merged. In Figure 2.10 a) it can be seen that there are ∼6 % more events in the no merging category for VR jets in comparison to fixed radius jets and in Figure 2.10 b) it can be seen that there are ∼ 8 % more events in the partially merged category. Collectively this contributes to ∼ 14 % fewer events in which all of the partons are merged when comparing VR jets to FR jets, as can be seen in Figure 2.10 c). Further studies investigating the benefits of using small VR jets in the $t\bar{t}$ resonance search are ongoing [5].

The calibration and uncertainty studies presented in Chapters 8 and 9 of this thesis use small VR jets with $R_{\text{max}} = 0.4$, $R_{\text{min}} = 0.2$ and $\rho_{\text{VR}} = 60$ GeV.

2.4.2 Large Variable R Jets

In the boosted analysis, fixed radius anti-k_t $R = 1.0$ trimmed jets are used in order to capture the decay products of the hadronically decaying top quark. However, as the p_{T} of the top quark increases, the decay products of the top quark start to fall into an area much

---

[5] ρ_{VR} was defined in Equation 2.4 and it defines how the radius of the VR jets shrink as the jet p_{T} increases

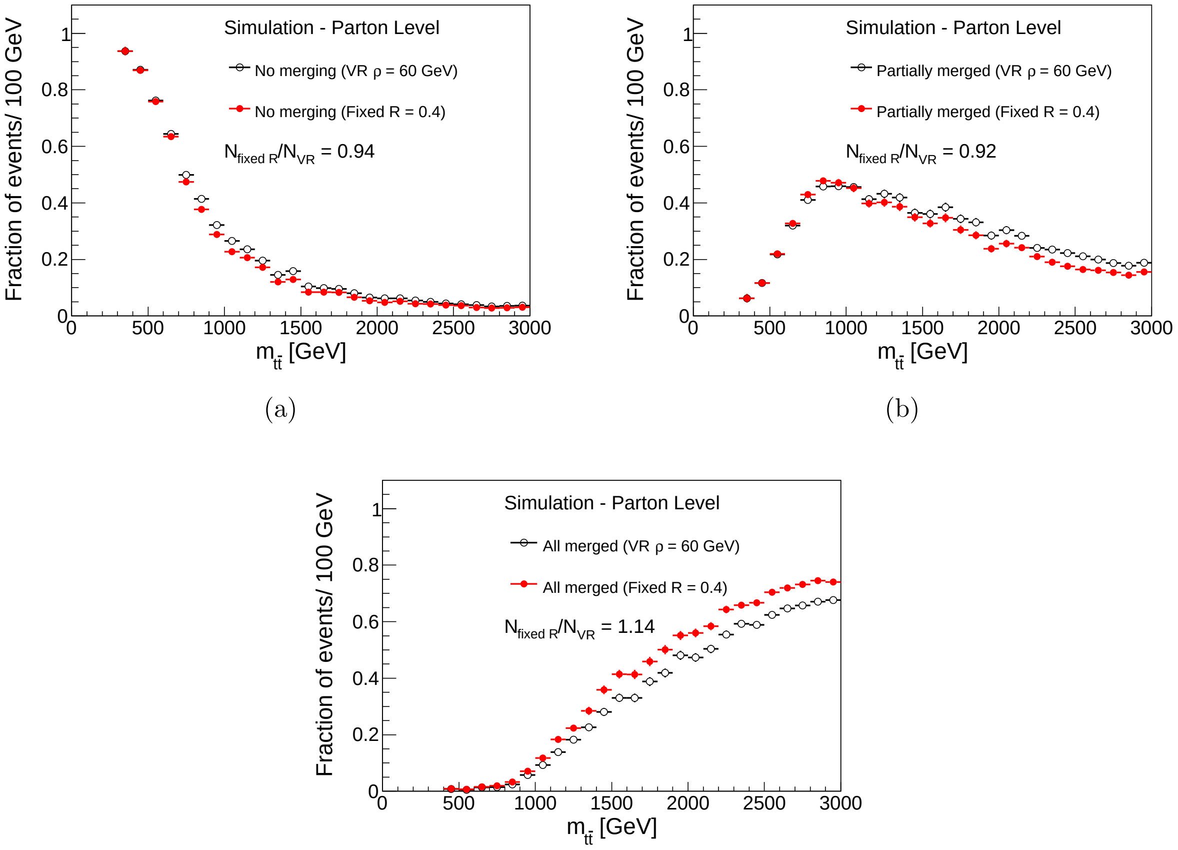

(a)

(b)

(c)

Figure 2.10: The fraction of events falling into the a) no merging, b) partially merged and c) all merged categories for VR jets with $R_{\text{max}} = 0.4$, $R_{\text{min}} = 0.2$ and $\rho_{\text{VR}} = 60$ GeV in black and for fixed radius $R = 0.4$ anti-k_t jets in red [5]. $Z' \to t\bar{t}$ events are used for these figures, with a Z' mass of 3 TeV, simulated using the PYTHIA 8 [28] Monte Carlo generator.

smaller than that captured by the $R = 1.0$ jets. This can be illustrated by looking at the distribution of transverse momentum inside anti-k_t $R = 1.0$ trimmed jets which have passed the semi-leptonic $t\bar{t}$ event selection. Figure 2.11 a) shows ΔR(jet constituent − jet axis) as a function of the p_{T} of trimmed anti-k_t $R = 1.0$ jets, where the entries are weighted by the p_{T} of the jet constituents. It can be seen that with increasing jet p_{T} the energy deposits in the jet are concentrated in a decreasing area around the jet axis.

Due to their decreasing size as the jet p_{T} increases, VR jets can be used to reflect this behaviour. The parameters of the VR jet algorithm need to be optimised in order to capture the decay products of the top quark, or in this case to capture the majority of the energy deposits of the anti-k_t $R = 1.0$ trimmed jets. The ΔR values required to contain 90 %, 92.5 % and 95 % of the p_{T} of trimmed anti-k_t $R = 1.0$ jets are shown in Figure 2.11 b) as a function of the p_{T} of the trimmed anti-k_t $R = 1.0$ jets. A fit is performed using the function $f(p_T^{\mathrm{jet}}) = p[0]/(p_T^{\mathrm{jet}} - p[1])$ in order to capture the shrinking behaviour of the decay products of the top quark. The value of $p[0]$ can be used as a guideline for the optimal value of ρ_{VR} which is required to contain the decay products of the top quark. To contain 90 % of the p_{T} of the anti-k_t $R = 1.0$ jets $p[0] \sim 500$ GeV, to contain 92.5 % $p[0] \sim 600$ GeV and to contain 95 % $p[0] \sim 700$ GeV. Each of these values of $p[0]$ was studied and it was found that using $\rho_{\mathrm{VR}} = p[0] = 600$ GeV gives the best performance [6].

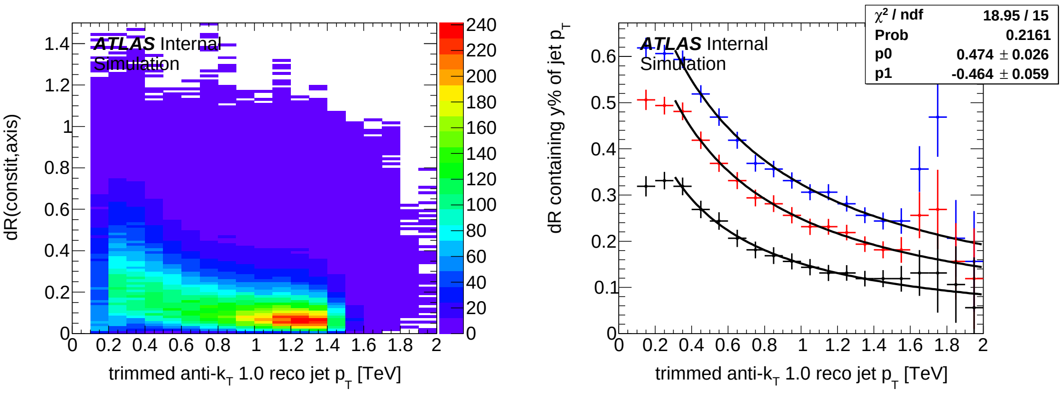

(a) (b)

Figure 2.11: a) $\Delta R(\text{jet constituent} - \text{jet axis})$ as a function of the p_{T} of trimmed anti-k_t $R = 1.0$ jets and b) the radius required to contain 90 % (black), 92.5 % (red) and 95 % (black) of the p_{T} of trimmed anti-k_t $R = 1.0$ jets [6]. $Z' \to t\bar{t}$ events are used for these figures, with a Z' mass of 3 TeV, simulated using the PYTHIA 8 [28] Monte Carlo generator.

The distribution of the jet mass for the signal and for the background can be seen in Figures 2.12 a) and b) for jets with a p_{T} of 500-1000 GeV and 1000-1500 GeV respectively. The distributions are shown for large VR jets with $R_{\mathrm{max}} = 1.0$, $R_{\mathrm{min}} = 0.2$ and $\rho_{\mathrm{VR}} = 600$ GeV, fixed radius $R = 1.0$ anti-k_t trimmed jets and fixed radius $R = 1.0$ anti-k_t jets with no grooming. It can be seen that for the signal sample the large VR jets have a similar mass distribution to that observed for fixed radius $R = 1.0$ anti-k_t trimmed jets. However, for $500 < p_T^{\mathrm{jet}} < 1000$ GeV the large VR jet mass distribution for the background is shifted to higher values in comparison to that for fixed radius $R = 1.0$ anti-k_t trimmed jets. This is due to the fact that large VR jets have no jet grooming applied and therefore a significant proportion of their energy is from additional proton-proton interactions in the event. As the jets shrink in size they capture less energy from additional proton-proton interactions. Therefore, this is less of a problem at higher p_{T} where the jet size is smaller.

From Figures 2.12 a) and b) it is clear that a cut on the jet mass can help to reject background events whilst retaining signal events. By varying the cut on the jet mass the background efficiency ($\epsilon_B = N_{\text{background selected}}/N_{\text{background total}}$) and the signal efficiency ($\epsilon_S = N_{\text{signal selected}}/N_{\text{signal total}}$) can be used to assess the performance of the different jet algorithms. In Figures 2.12 c) and d) the background rejection (defined as $1 - \epsilon_B$) is shown as a function of the signal efficiency for $500 < p_T^{\text{jet}} < 1000$ GeV and $1000 < p_T^{\text{jet}} < 1500$ GeV respectively.

For $500 < p_T < 1000$ GeV the large VR jets have a similar background rejection and signal efficiency as fixed radius $R = 1.0$ anti-k_t trimmed jets. However, for $1000 < p_T < 1500$ GeV it can be seen that large VR jets have a significantly higher background rejection rate for a given signal efficiency, in comparison to fixed radius $R = 1.0$ anti-k_t trimmed jets.

The calibration and uncertainty studies presented in Chapters 8 and 9 of this thesis use large VR jets with $R_{\text{max}} = 1.0$, $R_{\text{min}} = 0.2$ and $\rho_{\text{VR}} = 600$ GeV.

2.5 γ-jet Production

Many of the studies in this thesis make use of events containing a photon and a jet in the final state, known as γ-jet events. At the LHC this type of final state is either the result of $q\bar{q} \rightarrow \gamma g$ or $qg \rightarrow \gamma q$ as can be seen in Figure 2.13. The first of these is known as annihilation and the second as Compton scattering. The Compton scattering process dominates the cross-section for γ-jet events, resulting in the majority of jets from γ-jet events originating from a quark. This is of importance when using γ-jet events for jet calibration since jets originating from a quark (quark jets) have a narrower shower profile than those originating from gluons (gluon jets) [59].

The studies in this thesis require a sample of γ-jet events which is as pure as possible. Therefore the selection of events is designed in order to reject events containing two or

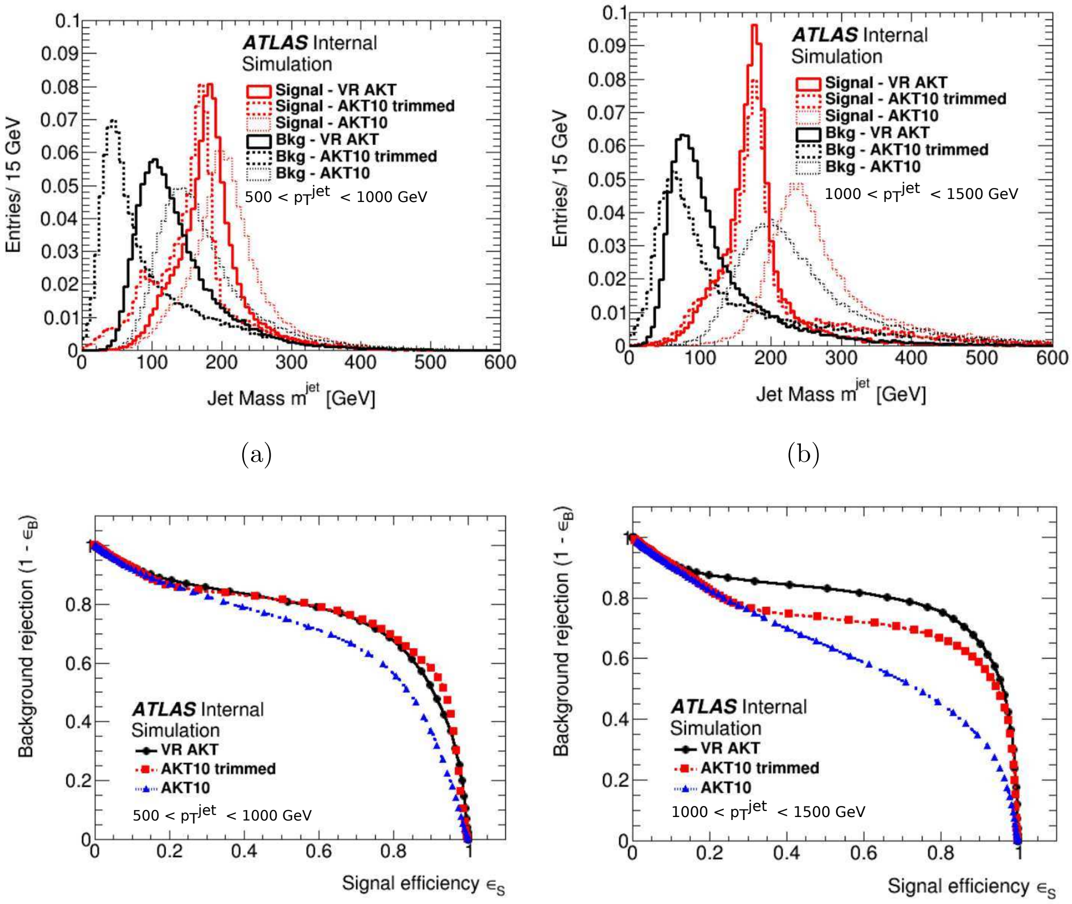

(a) (b)

(c) (d)

Figure 2.12: The jet mass distribution of the signal and background samples for anti-k_t $R = 1.0$ jets with and without trimming and large VR jets for a) $500 < p_T^{\text{jet}} < 1000$ GeV and b) $1000 < p_T^{\text{jet}} < 1500$ GeV. c) and d) show the background rejection as a function of the signal efficiency for $500 < p_T^{\text{jet}} < 1000$ GeV and $1000 < p_T^{\text{jet}} < 1500$ GeV respectively, calculated from the jet mass distributions [6]. The signal sample is the Z' sample with $m_{Z'} = 3$ TeV and the background sample is the di-jet Monte Carlo sample. $Z' \to t\bar{t}$ events are used for these figures, with a Z' mass of 3 TeV, simulated using the PYTHIA 8 [28] Monte Carlo generator.

more jets and a photon in the final state. Some examples of γ+2 jet events can be seen in Figure 2.14. This will be discussed in more detail in Chapters 6 and 7.

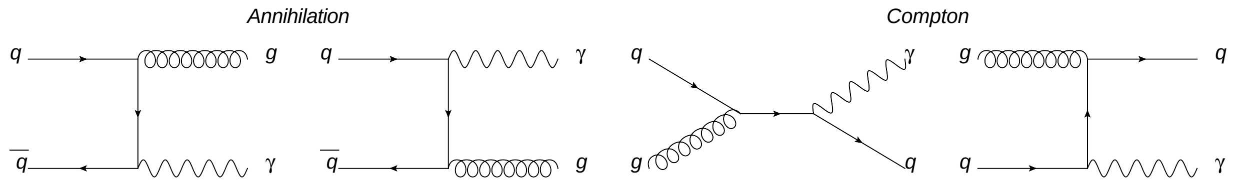

Figure 2.13: γ-jet production at the LHC at tree level.

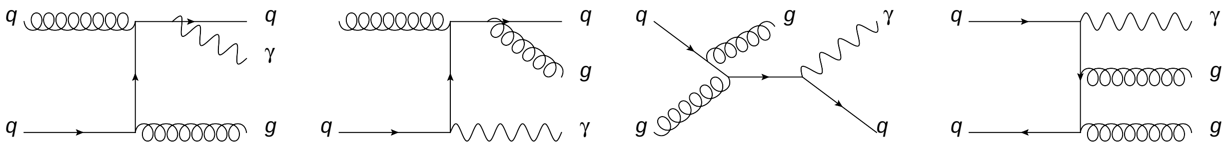

Figure 2.14: Example diagrams for $\gamma + 2$ jet production at the LHC.

Chapter 3

The ATLAS Detector at the LHC and Data Collection

This chapter briefly describes the Large Hadron Collider and the ATLAS detector. The data samples and Monte Carlo simulations that were analysed for this thesis are also discussed.

3.1 The Large Hadron Collider

The Large Hadron Collider (LHC) at CERN is the world's highest energy particle collider [9]. The studies presented in this thesis make use of data collected during proton-proton collisions, although the LHC can also collide lead ions. The LHC consists of a ring with a circumference of 26.7 km in which the protons are accelerated and steered using superconducting RF (radio-frequency) cavities and magnets. Before injection into the LHC the proton beams are accelerated up to energies of 450 GeV by a sequence of accelerators: Linac2, the Proton Synchrotron Booster (PSB), the Proton Synchrotron (PS) and the Super Proton Synchrotron (SPS). This accelerator complex can be seen in Figure 3.1.

The LHC has a design luminosity of $10^{34}\text{cm}^{-2}\text{s}^{-1}$ and a design centre-of-mass energy of 14 TeV. However, during Run 1 (2009 - 2013) the LHC operated at lower luminosities and centre-of-mass energies [60]. The LHC will restart collisions in 2015 at a centre-of-mass energy of 13 TeV and is expected to achieve design luminosity and energy during Run 2 (2015 - 2018).

The work presented in this thesis is based on data collected during two time periods: the 2011 run (from March to November 2011), which had a peak luminosity of 3.7×10^{33} cm^{-2}s^{-1} and a centre-of-mass energy of 7 TeV (3.5 TeV for each proton beam), and the 2012 run (from April to December 2012), which had a peak luminosity of 7.7×10^{33} cm^{-2}s^{-1} and a centre-of-mass energy of 8 TeV (4 TeV for each proton beam). The peak luminosity of the detector during these two operating periods can be seen in Figure 3.2 a) and the total integrated luminosity delivered to and recorded by the ATLAS detector can be seen in Figure 3.2 b). During 2011 and 2012 the LHC operated with a maximum number of bunches of 1380 and a bunch spacing of 50 ns (compared to the design bunch spacing of 25 ns).

Data taking is divided into *runs* during which the instantaneous luminosity decreases as the run progresses. Runs are further divided into *luminosity blocks* which cover time periods of approximately one minute, the shortest time period needed for the measurement of the instantaneous luminosity.

3.1.1 Pile-up

In each bunch crossing there can be multiple proton-proton interactions. The highest p_{T} proton-proton interaction in an event is known as the *hard scatter* and additional proton-proton interactions are known as *pile-up*. The average number of proton-proton interactions per bunch crossing (μ) is related to the instantaneous luminosity (L) and the number of colliding bunches (N_{bunch}):

$$\mu = \frac{L \times \sigma_{\mathrm{inelastic}}}{N_{\mathrm{bunch}} \times f_{\mathrm{LHC}}}, \tag{3.1}$$

where $\sigma_{\mathrm{inelastic}}$ is the total inelastic pp cross section and $f_{\mathrm{LHC}} = 11.25$ kHz is the LHC machine revolution frequency. The distribution of μ for the 2011 and 2012 datasets can be seen in Figure 3.2 c). In 2011 the value of μ ranged from approximately 3 up to 20. Whereas in 2012 it was significantly higher, ranging between approximately 6 and 40, due to the higher luminosity achieved in 2012.

Pile-up in the ATLAS detector can be categorised into *in-time* and *out-of-time* pile-up. In-time pile-up consists of the additional energy deposits in the detector that are due to additional proton-proton interactions in the current bunch crossing. In-time pile-up can be parametrised by measuring the number of *primary vertices.* Primary vertices are interaction points in the ATLAS detector resulting from the collision of the protons rather than the decay of the particles produced in the proton-proton collisions. The primary vertex which is due to the hard scatter is defined as the vertex with the highest value of $\sum p_T^{\mathrm{track}}$ where p_T^{track} is the transverse momentum of tracks originating from the vertex. All other primary vertices are assumed to be due to in-time pile-up.

The ATLAS calorimeters (which absorb and measure the energy of photons, electrons and hadrons) are also sensitive to energy deposited in previous bunch crossings, with respect to the current bunch crossing. These energy deposits are known as out-of-time pile-up. Out-of-time pile-up can be parametrised by μ for a fixed value of the number of primary vertices (NPV). This is due to the fact that μ is the *average* number of proton-proton interactions per bunch crossing where the average is taken over all bunch crossings in a given luminosity block. Therefore μ is a measure of the pile-up in previous bunch crossings. However, μ is also highly correlated with the in-time pile-up in the current bunch crossing. Therefore μ only provides a sole measure of the out-of-time pile-up when considering many events with the same value of NPV but different values of μ. Methods have been developed by ATLAS to account for the additional energy deposits in the detector due to pile-up, some of which will be discussed in this thesis.

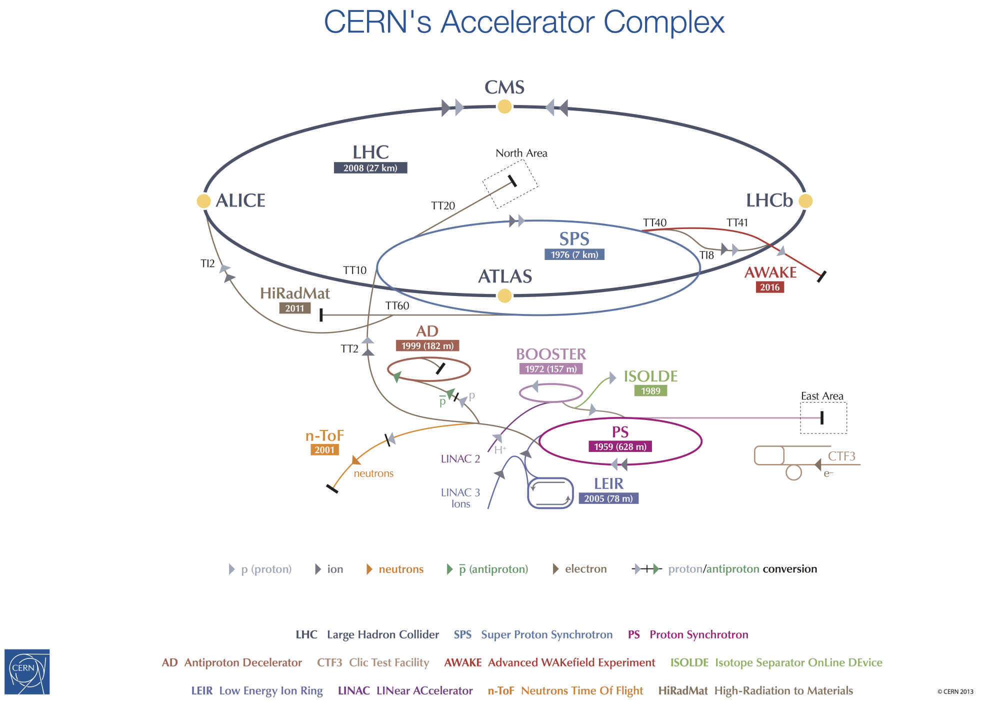

Figure 3.1: The LHC accelerator complex [61]. Protons are accelerated in the linear accelerator Linac2 up to 50 MeV, boosted to 1.4 GeV in the Booster (PSB), accelerated to 25 GeV in the PS and then to 450 GeV in the SPS before being injected into the LHC. Copyright © CERN.

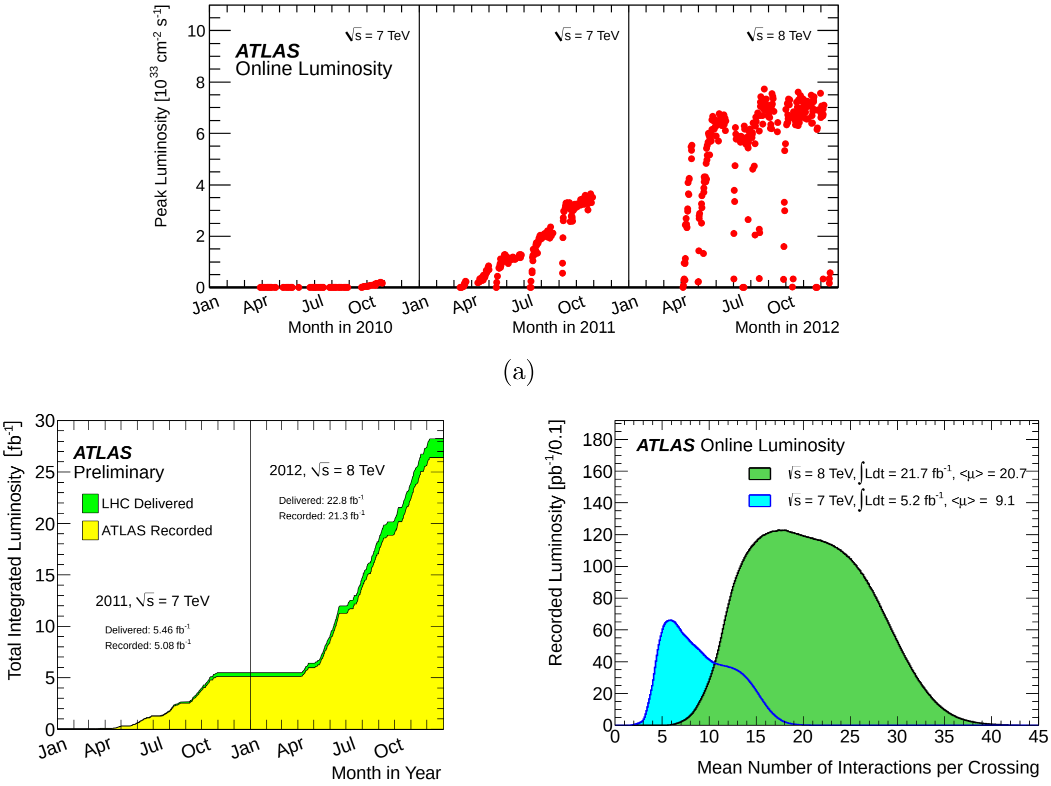

(a)

(b)

(c)

Figure 3.2: a) The peak instantaneous luminosity as a function of time, b) the luminosity delivered and recorded by to the ATLAS detector as a function of time, and c) the mean number of interactions per bunch crossing [62]. All plots show conditions during 2011 and 2012 data taking. a) also shows the instantaneous luminosity delivered to ATLAS in 2010 which was not used in the studies presented in this thesis.

3.2 Overview of the ATLAS Detector

The ATLAS detector is one of four main detectors at the LHC and one of two general purpose detectors that are designed for the detection and measurement of a wide range of high-energy particles and processes. The ATLAS detector is composed of several different sub-detectors, each of which is designed to measure different properties of the particles produced in proton-proton collisions. A diagram showing the main detector components can be seen in Figure 3.3. An overview of each of the components of the detector is given here and further details can be found in [8].

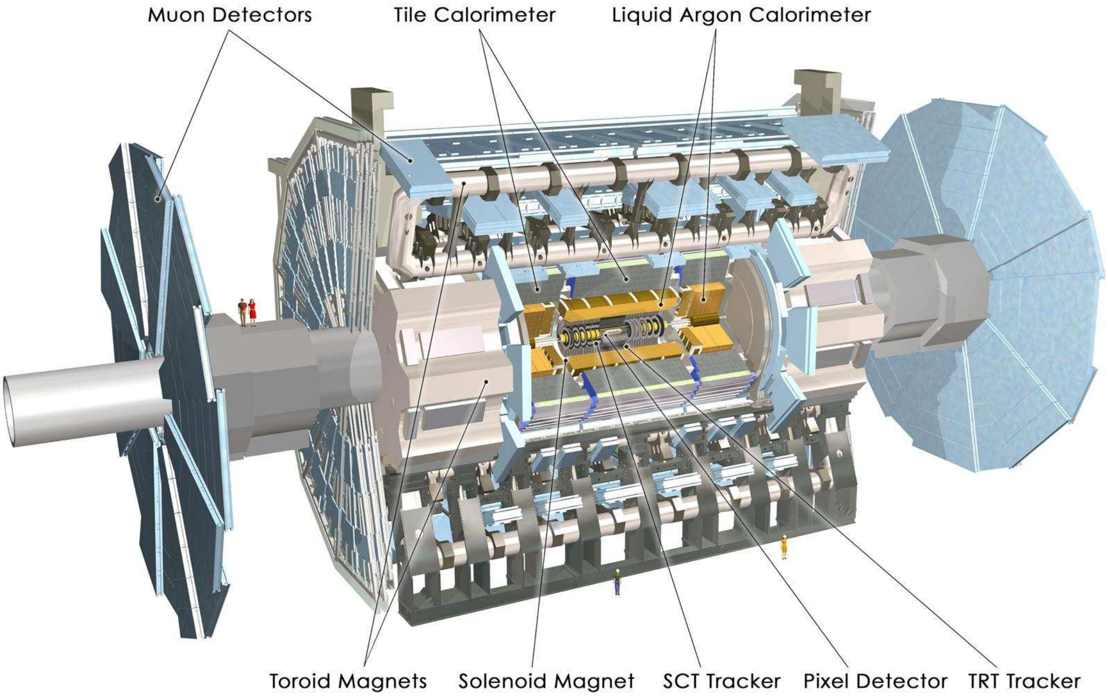

Figure 3.3: A diagram of the ATLAS detector [63]. ATLAS experiment copyright © 2014 CERN.

3.2.1 The Co-ordinate System of the ATLAS Detector

The co-ordinate system of the ATLAS detector is right-handed: it is defined such that the x-axis points to the centre of the LHC ring, the y-axis points upwards and the z-axis points along the direction of the beamline. The polar angle (θ) is measured from the z-axis. However, the pseudorapidity is the preferred variable to measure this angle since differences in pseudorapidity are Lorentz invariant for massless particles. Pseudorapidity is defined as:

$$\eta = -\ln\left(\tan\left(\frac{\theta}{2}\right)\right) \tag{3.2}$$

The pseudorapidity is zero when perpendicular to the beam-line and tends to infinity in the ±z-direction. For the case where a physics object has $p_T \gg m$ the pseudorapidity is approximately the same as the rapidity, which was defined in Equation 2.1.

The azimuthal angle, ϕ, is measured in the x-y plane, starting from the x-axis.

3.3 Inner Detector

The inner detector is a tracking system that is used to reconstruct the tracks of charged particles. The inner detector is surrounded by a 2T solenoid magnet, which causes the tracks of the charged particles to bend such that their momenta and charge can be measured. As well as measuring the momenta and charges of charged particles, the tracking detector is also used to find primary and secondary vertices in the detector. Secondary vertices are points in the detector where particles with a long lifetime (e.g. B hadrons) have decayed at some distance from the primary interaction point. Identification and measurement of the position of secondary vertices is therefore important in the identification of jets originating from the decay of a B hadron (b-jets).

The inner detector consists of three concentric sections. From the inside out they are: the pixel detector, the SemiConductor Tracker (SCT) and the Transition Radiation Tracker (TRT). Together they provide measurements of particle tracks up to $|\eta| = 2.5$.

The pixel detector uses silicon pixels to detect charged particles. It has three barrel layers which are parallel to the beam pipe and three endcap layers, placed either side of the barrel layers, which are perpendicular to the beam pipe. The innermost barrel layer is 50.5 mm from the beam pipe in the radial (R) direction. The pixel detector has an intrinsic resolution of 10 μm in the R$-\phi$ plane and 115 μm in the z direction. The pixel detector consists of 80.4×10^6 pixels in total. The fine granularity of the pixel detector allows for the reconstruction of tracks in the dense environment close to the beam line, as well as providing the ability to identify and measure the position of primary and secondary vertices.

Outside of the pixel detector is the SCT, a silicon strip detector with a strip pitch of 80 μm. It consists of four barrel layers and nine endcap layers. The strip detectors are arranged in stereo; meaning that for each module of the SCT there are two layers of silicon strips that are aligned such that the strips in the two layers cross at an angle of 40 mrad. This arrangement allows for measurement of the position of a hit along the z-axis, as well as in the R-ϕ plane. In the barrel the intrinsic resolution is 17 μm in R$-\phi$ and 580 μm in the z-direction. There are approximately 6.3 million readout channels in the SCT.

The outermost section of the inner detector is the Transition Radiation Tracker (TRT). The TRT consists of straw tubes with a diameter of 4 mm, which are arranged parallel to the beam axis in the barrel region and radially in the endcap regions. The TRT provides coverage up to $|\eta| = 2$, with an intrinsic resolution of 130 μm in the R$-\phi$ plane. Between the straw tubes there are layers of fibres and foils with different dielectric constants. When a charged particle transverses these different media it emits photons (transition radiation). The energy loss due to this radiation depends on the particle's Lorentz factor, $\gamma = E/m$. Therefore, electrons produce transition radiation at a lower energy than hadrons, such as pions. The transition radiation photons are absorbed by Xenon in the straw tubes, resulting in a higher voltage signal when transition radiation is present. Therefore, reading out signals at both high and low voltages from the TRT allows for the separation of energy deposits due to electrons and energy deposits due to charged hadrons.

The tracks used by physics analyses are found using an inside-outside tracking algorithm. This starts by looking for hits in the pixel detector and then searches for matching hits in the SCT and then the TRT. Back-tracking, where the tracking algorithm starts from hits in the TRT is also used in order to improve secondary vertex finding.

3.4 Calorimeter

There are two main ATLAS calorimeters: the electromagnetic calorimeter and the hadronic calorimeter. The electromagnetic calorimeter absorbs and measures the energy of photons and electrons. It also measures the energy of hadrons. Hadrons do not lose all of their energy in the electromagnetic calorimeter and therefore they pass through into the hadronic calorimeter. The hadronic calorimeter absorbs and measures the remaining energy of the hadrons. A diagram showing the different parts of the calorimetry system can be seen in Figure 3.4. The ATLAS calorimeters are sampling calorimeters, meaning that they use layers of material in which the particles shower and are absorbed (the absorber) and layers of material which measure the energy of the particles produced in the shower (the active material). The calorimeters are also non-compensating, meaning that a smaller energy is measured for a hadronic particle than for an electromagnetic particle of the same initial energy. The non-compensation is mainly due to the nuclear interactions of the hadrons: processes such as nuclear recoil, excitation and breakup absorb significant energy whilst producing little or no signal in the calorimeter. This is because scintillation light is emitted following excitation of atoms in the scintillating material by photon absorption or ionisation. Therefore, nuclear processes, such as those mentioned above, must subsequently cause ionisation or excitation of the scintillation atoms in order for the energy to be visible. These types of processes result in $\sim$20-40 % [24] of the energy of a hadronic shower being invisible. A further small fraction ($\sim$1%) is lost due to neutrinos, which are not detected. The remaining energy is visible energy, due to showering of the electromagnetic components of the shower, or ionisation energy from charged particles.

3.4.1 Electromagnetic Calorimeter

The electromagnetic (EM) calorimeters are divided into two sections: the barrel, covering $|\eta| < 1.475$; and the endcap, covering $1.375 < |\eta| < 3.2$. There are three layers for $|\eta| < 2.5$ and two layers for $|\eta| > 3.2$, allowing for more precise measurements within $|\eta| < 2.5$.

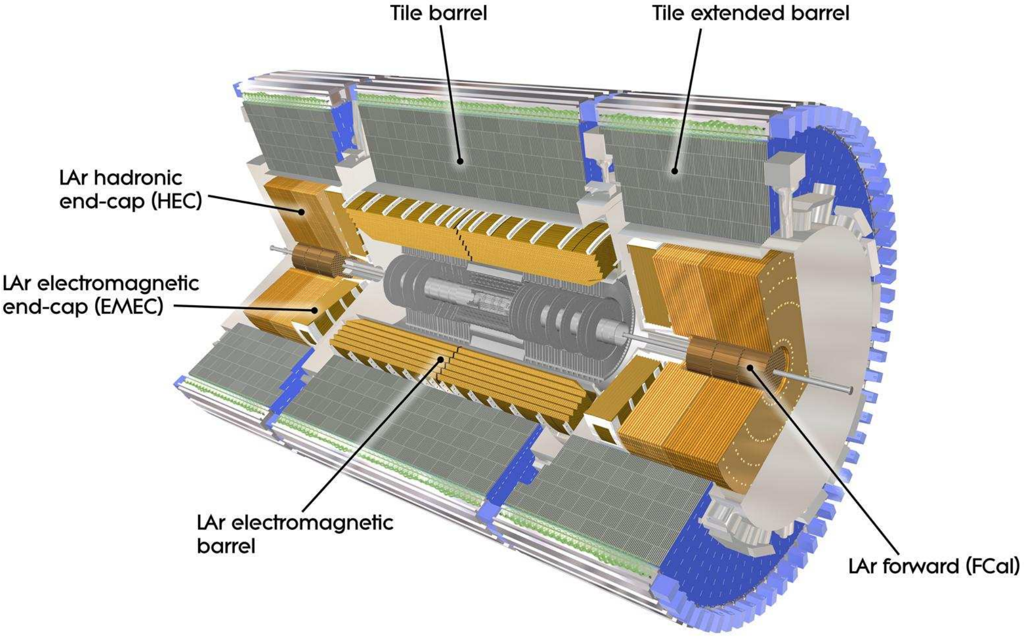

Figure 3.4: The ATLAS calorimetry system. ATLAS experiment copyright © 2014 CERN.

The EM calorimetry system is finely segmented into readout cells (which are also known as calorimeter cells) for precise energy and position measurement of electrons and photons. The EM calorimeter uses liquid Argon (LAr) for the active material with lead absorber in a unique accordion shaped geometry, providing full ϕ coverage with no azimuthal gaps. A module from the EM barrel showing the accordion geometry and the readout cells can be seen in Figure 3.5. It can be seen that the first layer has a high granularity of readout cells in the η direction, with decreasing granularity in the second and third layers. The EM calorimeters have $> 22(24)$ radiation lengths of material in the barrel (endcap) in order to fully absorb the electromagnetic showers of electrons and photons.

A LAr presampler is used for $|\eta| < 1.8$ to correct for energy lost before the calorimeter. The presampler is a layer of LAr with a thickness of 1.1 cm (0.5 cm) in the barrel (endcap). Additionally, scintillators are used in the region $1.0 < |\eta| < 1.6$ where there are gaps between the barrel and endcaps for cables and services for the inner detector and barrel calorimeter.

The signal produced by the LAr calorimeters is an analog signal that is sampled every 25 ns. The signal is shaped using a bi-polar pulse and converted to Analog-to-Digital Converter

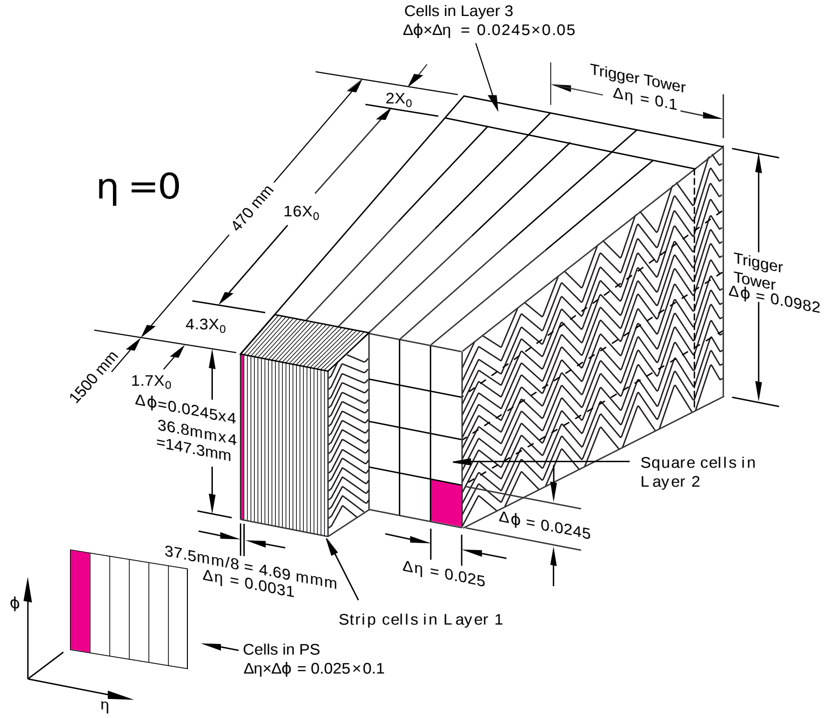

Figure 3.5: A diagram of a barrel module in the electromagnetic calorimeter. The accordion geometry and the three layers of the calorimeter are visible. The granularity of the readout cells is also shown, with the readout cells in the first layer having a much smaller size in the η direction than the readout cells in the second and third layers [8].

(ADC) counts. The resulting signal shape can be seen in Figure 3.6 a) for the first layer of the EM barrel calorimeter. As mentioned previously, the ATLAS calorimeters are sensitive to energy deposits in previous and future bunch crossings with respect to the current bunch crossing. This is due to the long integration time of the signal in the LAr calorimeters. The sensitivity is partly mitigated by the bipolar pulse shaping of the signal, which results in partial cancellation of in- and out-of-time pile-up.

3.4.2 Hadronic Calorimeter

The hadronic calorimeters utilise different technologies for different η regions. In the central region the Tile calorimeter covers $|\eta| < 1.0$ for the barrel and $0.8 < |\eta| < 1.7$ for the extended barrel. The Tile calorimeter consists of tiles of steel absorber interleaved with plastic scintillator for the active material. There are three layers of modules in both the barrel and the extended barrel. A module of the tile calorimeter can be seen in Figure 3.8,

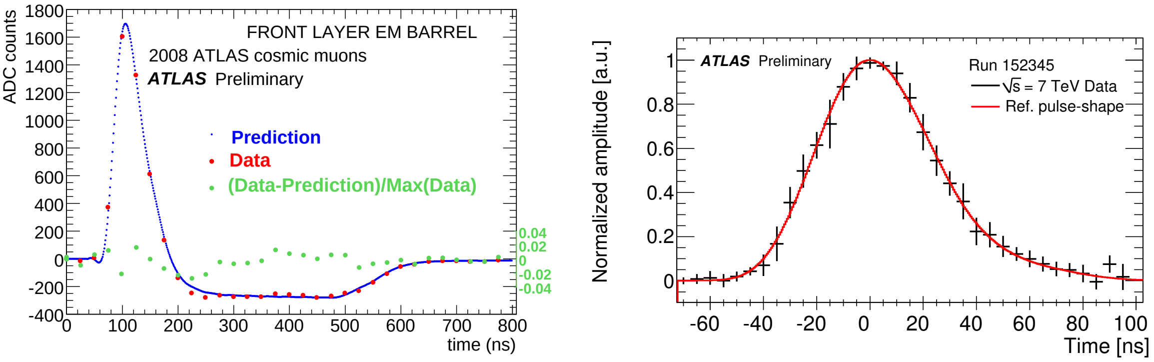

(a) (b)

Figure 3.6: The shape of the pulse for a) the first layer of the LAr EM calorimeter [64], b) the tile calorimeter [65].

including an illustration of the wavelength shifting fibres, which are used to collect the light at the edge of each scintillating tile. These fibres are grouped together in order to define a structure of readout cells. There are three layers of cells in the radial direction, with dimensions of $\Delta\eta \times \Delta\phi = 0.1 \times 0.1$ for the first two layers and $\Delta\eta \times \Delta\phi = 0.2 \times 0.1$ for the third layer, as illustrated in Figure 3.7.

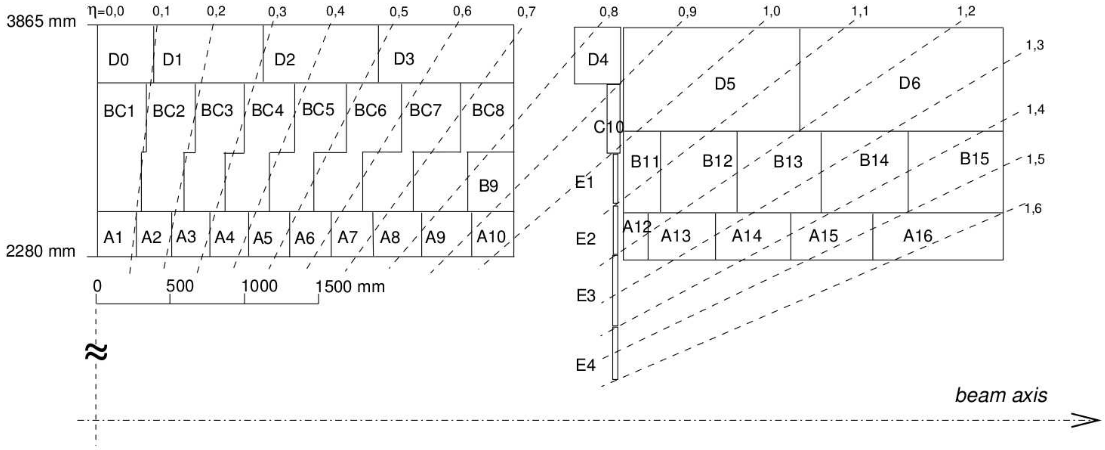

Figure 3.7: The segmentation of the Tile cal modules in the radial and η directions. Only half of the Tile calorimeter is shown since it is symmetrical about $\eta = 0$ [8].

The scintillation light is collected by the wavelength shifting fibres and detected using photomultipliers. This results in a pulse with a height proportional to the energy and a width of 50 ns as can be seen in Figure 3.6 b). The pulse shape is sampled 7 times and calibration constants that have been measured in a test beam are used to convert the ADC counts into an energy measurement. Due to the short integration time, which can be observed in

Figure 3.6 b), the Tile calorimeter is much less sensitive to out-of-time pile-up in comparison to the LAr calorimeters, being sensitive within only 75 ns [1]. Furthermore, the hadronic calorimeters are (in general) less affected by pile-up, since many of the low energy particles which are due to pile-up have already been absorbed by or lost significant amounts of their energy in the EM calorimeter.

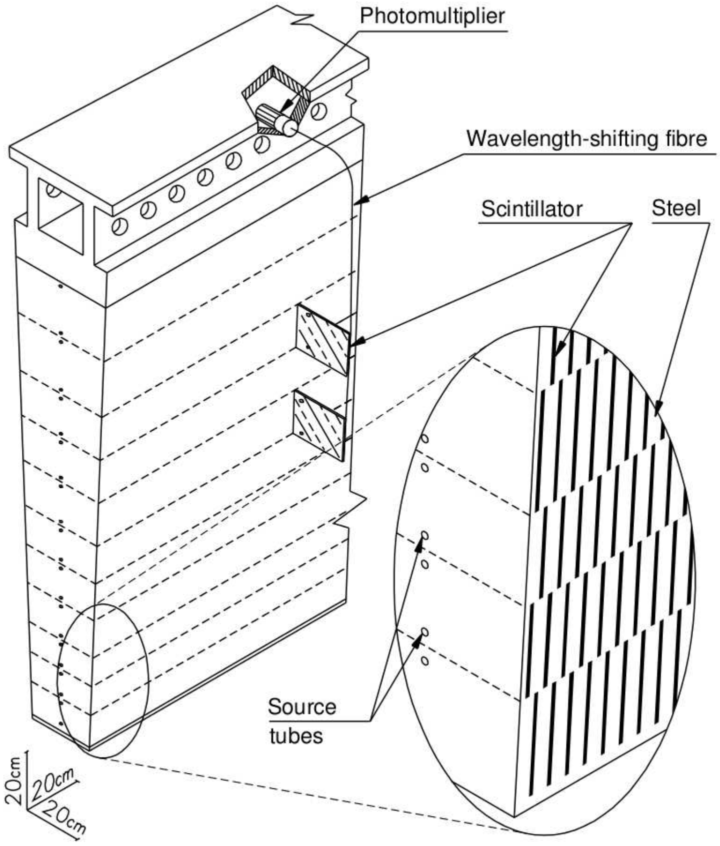

Figure 3.8: A diagram showing a module of the tile calorimeter. The layout of the steel absorber tiles and scintillating tiles can be seen [8].

The LAr hadronic endcap (HEC) extends the hadronic calorimeter to higher $|\eta|$, providing coverage of $1.5 < |\eta| < 3.2$. It uses copper for the absorber and LAr for the active material.

The forward regions ($3.1 < |\eta| < 4.9$) are covered by the LAr forward calorimeter (FCal). The FCal consists of 3 modules in each endcap. The first module uses copper for the absorbing material and it is mainly used for the measurement of electromagnetic showers. The other two modules use tungsten for the absorbing material and they mainly measure hadronic interactions.

3.4.3 Grouping of Calorimeter Cells using Topo-clusters

Various methods can be used to group calorimeter readout cells into groups which are used for the reconstruction of physics objects. A method which is of particular relevance for jet reconstruction is *topo-clustering*, which is used to build groups of calorimeter cells known as *topo-clusters* [66].

Topo-clusters are formed from calorimeter cells following a scheme that is designed to suppress calorimeter cells that are dominated by noise (from electronics or from pile-up). This is done by considering the signal-to-noise ratio of the calorimeter cells, E/σ, where E is the measured energy of the calorimeter cell and the estimated noise is $\sigma = \sqrt{\sigma^2_{electronics} + \sigma^2_{pile-up}}$. $\sigma_{electronics}$ is determined from measurements of the signal in the calorimeters when there are no collisions and it can be seen in Figure 3.9 a). $\sigma_{pile-up}$ is determined from Monte Carlo simulations [1]. The total noise, σ, can be seen in Figures 3.9 b) and c) for 2011 and 2012 respectively. By comparing Figure 3.9 a) to Figures 3.9 b) and c) it can be seen that the noise due to pile-up is either comparable to or greater than the electronic noise. The noise due to pile-up is particularly high in the Tile calorimeter and the hadronic endcaps due to the large size of the calorimeter cells in these detectors. Furthermore, the large increase in noise when going from the lower pile-up conditions of 2011 to the higher pile-up conditions of 2012 can be seen by comparing Figures 3.9 b) and c).

Using these noise measurements, the topo-clustering sequence starts by finding seed cells with $E/\sigma > 4$. Then surrounding cells with $E/\sigma > 2$ are added and finally a layer of cells with $E/\sigma > 0$ are added. A diagram showing examples of how topo-clusters can be formed can be seen in Figure 3.10.

Once all topo-clusters are formed a splitting algorithm is employed to divide topo-clusters with more than one energy maximum into smaller topo-clusters [66].

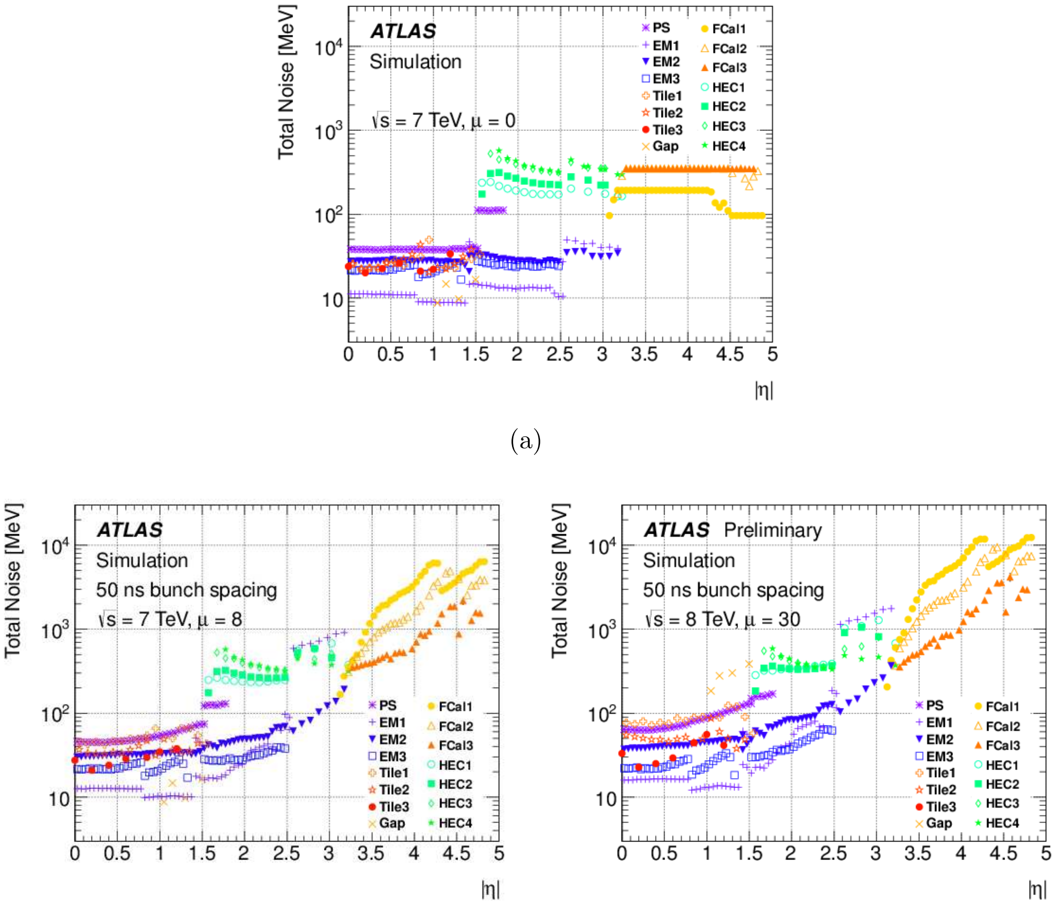

(a)

(b)

(c)

Figure 3.9: The noise thresholds in the calorimeters. a) The electronic noise, $\sigma_{electronics}$, which was used in 2011 and 2012 [1], b) the total noise for $\mu = 8$ (including the noise due to the electronics and pile-up) which was used for jet reconstruction in 2011 data and Monte Carlo [1] and c) the total noise for $\mu = 30$ (including the noise due to the electronics and pile-up) which was used for jet reconstruction in 2012 data and Monte Carlo [67].

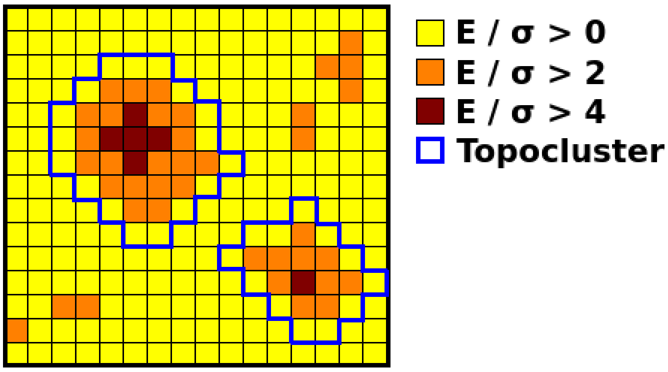

Figure 3.10: An illustration of topo-clusters. The grid represents calorimeter cells and the colours represent cells with $E/\sigma > 0$ (yellow), $E/\sigma > 2$ (orange), and $E/\sigma > 4$ (brown). The boundaries of the topo-clusters are shown in blue.

3.5 Muon System

The outermost component of the ATLAS detector is the muon system. It detects charged particles that pass through the rest of the detector and in particular it is designed for the detection of muons. The muon system has a coverage of $|\eta| < 2.7$ and it designed to detect muons with momenta above a few GeV [68]. The muon system uses large toroidal super-conducting magnets to bend the tracks of the charged particles. The muon tracks are measured using three layers of octagonal chambers in the barrel region and three layers perpendicular to beam axis in the endcap region. Monitored drift tubes (MDTs) are used for $0 < |\eta| < 2.7$ (except for the first layer where they cover $0 < |\eta| < 2.0$). The MDTs give a momentum resolution of 35 μm in the z-direction. Cathode Strip Chambers (CSCs) are used for the first layer in the region $2.0 < |\eta| < 2.7$, providing a momentum resolution of 40 μm in R and 5mm in ϕ. For triggering purposes the muon system also contains chambers covering $0 < |\eta| < 2.4$ that have a fast reaction time but lower momentum resolution. In the barrel these are Resistive Plate Chambers (RPCs) and in the endcap Thin Gap Chambers (TGCs) are used. These chambers are also useful for bunch crossing ID and they provide a position measurement orthogonal to that measured by the MDTs.

3.6 Data Acquisition and Triggers

The quantity of data that is produced by the ATLAS detector greatly exceeds the amount that can be stored or analysed. In order to reduce the data rate from $\sim$40 MHz to $\sim$200 Hz a *trigger* system is used to decide which events to store. The trigger primarily looks for events containing high p_{T} objects such as photons, electrons, jets and taus or events with large amounts of missing transverse momentum.

The ATLAS trigger system has three different stages: the Level 1 trigger (L1), the Level 2 trigger (L2) and the Event Filter (EF). The L2 and EF are collectively known as the High Level Trigger (HLT).

The Level 1 trigger is a hardware based trigger that uses information from the calorimeter and the muon system to reduce the event rate to a maximum of 75 kHz in 2.5 μs. L1 defines a Region of Interest (RoI), a slice of the detector where a high E_T energy deposit in the calorimeter or a high momentum track in the muon system has been measured. If L1 finds such a RoI then the event is passed to L2, which has access to detector information from all detector components in the RoI. L2 reduces the event rate to $\sim$3 kHz in approximately 40 ms/event. If the event passes the L2 trigger then the event is passed to the EF, which has access to information from all detector components in all regions of the detector. EF uses algorithms similar to those used for offline reconstruction in order to identify high p_{T} objects and reduce the data rate to 200 Hz in 4 s/event. The L2 and EF triggers are both software based triggers.

Even with the requirements placed on the triggers to identify high p_{T} objects the data rate would be too high. Therefore some triggers are *prescaled* which means that 1 out of N events (for a trigger with a prescale of N) is selected for storage. The triggers that are prescaled, and the value used for the prescale, is defined based on the instantaneous luminosity delivered to the detector and which objects are most needed by physics analyses. The prescales are accounted for by scaling the number of Monte Carlo events by the luminosity collected by the trigger.

Photon triggers are used for the γ-jet analyses presented in this thesis. These photon triggers are seeded at L1 using only calorimeter information to search for clusters of calorimeter cells with high E_T. Loose photon identification is applied in the HLT to discriminate between photons and jets with a high electromagnetic content. The identification is based on requirements relating to the shape of the shower in the electromagnetic calorimeter and leakage into the hadronic calorimeter [69, 70].

In the 2011 data events were selected using six single photon triggers with p_{T} thresholds ($p_T^{trigger}$) of 20, 40, 60 and 80 GeV. All of these triggers were prescaled except for the trigger with $p_T^{trigger}$ of 80 GeV. Following calibration the photons passing these triggers are required to have a $p_{\mathrm{T}} >$ 25, 45, 65 and 85 GeV for the triggers with $p_T^{trigger}$ of 20, 40, 60 and 80 GeV respectively. This requirement ensures that the trigger efficiency is $>$ 99 % [71]. The photons are required to have passed the triggers in non-overlapping p_{T} ranges, e.g. photons passing the 20 GeV threshold trigger are required to have $25 < p_T^{\gamma} < 45$ GeV, photons passing the 40 GeV threshold trigger are required to have $45 < p_T^{\gamma} < 65$ GeV etc.

Due to the higher luminosity of the LHC during 2012 operation compared to 2011, photon triggers with higher p_{T} thresholds and prescales were required. In addition to the triggers with $p_T^{trigger}$ of 20, 40, 60 and 80 GeV which were used for the 2011 analysis, two extra photon triggers were used with $p_T^{trigger}$ of 100 GeV and 120 GeV. These extra triggers had corresponding offline p_T^{γ} cuts of 105 GeV and 125 GeV respectively in order to ensure a trigger efficiency of $>$ 99% [72]. The only unprescaled trigger was the trigger with $p_T^{trigger}$ of 120 GeV.

A summary of the photon triggers used in 2011 and 2012 data is shown in Table 3.1.

Data collected by the detector and Monte Carlo simulations are replicated and distributed on the GRID, a worldwide computing network that are used to store and analyse data. Reconstruction of physics objects is performed centrally using the ATLAS software package, ATHENA, to produce, at the end of the chain, Derived Physics Datasets (D3PDs) that contain information about physics objects such as jets, as well as information about the hits, clusters and tracks in the event.

Trigger Name	Trigger p_T threshold [GeV]	p_T thresholds in analysis [GeV]		Prescaled ?	
		2011	2012	2011	2012
EF_g20_loose	20	$25 < p_T < 45$	$25 < p_T < 45$	Yes	Yes
EF_g40_loose	40	$45 < p_T < 65$	$45 < p_T < 65$	Yes	Yes
EF_g60_loose	60	$65 < p_T < 85$	$65 < p_T < 85$	Yes	Yes
EF_g80_loose	80	$p_T > 85$	$85 < p_T < 105$	No	Yes
EF_g100_loose	100	-	$105 < p_T < 125$	-	Yes
EF_g120_loose	120	-	$p_T > 125$	-	No

Table 3.1: Summary of the photons triggers and p_{T} thresholds used for the analyses presented in this thesis, for 2011 and 2012 data taking.

3.7 Data Quality

The quality of the data produced by the ATLAS detector is monitored and checked for any issues in the sub-detectors, for example noise bursts or occasions when the electronics needed to be reset for a particular detector component [73]. From this information a set of luminosity blocks in which the detector was operating well is defined, which is known as a Good Runs List (GRL). GRLs are used for the selection of good quality data for all studies shown in this thesis. Data quality requirements relating specifically to physics objects such as photons and jets are applied separately to this selection since they are dependent on which objects are of interest to an analysis.

3.8 Data Samples

Two different, non-overlapping sets of data collected by ATLAS were used for the studies presented in this thesis:

- 4.7 fb^{-1} of data collected in 2011 at $\sqrt{s} = 7$ TeV were used for the studies of the jet energy scale and its uncertainty (for anti-k_t $R = 0.4$ and $R = 0.6$ jets), which is presented in Chapter 6.
- 20.3 fb^{-1} of data collected in 2012 at $\sqrt{s} = 8$ TeV were used for the studies of the

jet energy scale uncertainty of large-R jets, which is presented in Chapter 7 and for the studies of the jet energy scale uncertainty of Variable R jets which is presented in Chapter 9.

These integrated luminosity values are the totals after the GRL has been applied and therefore they are slightly lower than the total integrated luminosity recorded by ATLAS, which was shown in Figure 3.2 b).

3.9 Monte Carlo Samples

Monte Carlo generators are used to simulate proton-proton interactions and the subsequent decay of particles into stable particles that are detected by the ATLAS detector. They provide a basis against which to compare data and they are used extensively for calibration purposes. In this thesis the processes of interest are events containing a photon and a jet in the final state (γ-jet events) and events containing at least two high p_{T} jets (di-jet events). The Monte Carlo generators that were used to simulate these types of event are briefly described below and details can be found in Table 3.2.

The stable particles produced by the Monte Carlo generators are passed on to GEANT4 [74], which simulates the interaction of the particles with the ATLAS detector and the tracks and energy deposits that they leave in the detector. The resulting simulated hits and energy deposits are reconstructed into physics objects using the same algorithms and software as are used for data.

In-time pile-up is modelled using minimum bias events, which are overlaid on top of the hard scatter events. The number of minimum bias events that are added to an event is sampled from a Poisson distribution with a mean of $\langle\mu\rangle$. Out-of-time pile-up is modelled by arranging the minimum bias events with the same bunch structure as the bunch structure in the LHC. The length of time for which each component of the detector is sensitive to out-of-time pile-up is used to select the number of events that must be taken into account on either side of the current bunch crossing. For the Monte Carlo samples simulated at $\sqrt{s} = 7$ TeV, to be compared to the 2011 dataset, the minimum bias events used for the pile-up modelling were generated using PYTHIA 8 [28] with the 4C [75] detector tune and the MRST LO** PDF set. For Monte Carlo samples simulated at $\sqrt{s} = 8$ TeV, for comparison to the 2012 dataset, the minimum bias events were generated using PYTHIA 8 with the A2M tune and the MSTW2008LO [76] PDF set.

In general, the simulated pile-up conditions do not exactly match the conditions in data as the exact conditions cannot be known until the data has been taken. The Monte Carlo samples are corrected for this by re-weighting events such that the μ distribution in Monte Carlo matches that seen in the data. It was also observed that the number of primary vertices in Monte Carlo for an event with a given value of μ was the same as for an event in data with $SF \times \mu$, where $SF = 0.97$ (1.11) for 2011 (2012) data and Monte Carlo. Therefore a scale factor (a multiplicative factor) is applied to the Monte Carlo such that $\mu_{\mathrm{MC}} = SF \times \mu_{\mathrm{data}}$.

3.9.1 γ-jet Monte Carlo Simulation

Inclusive γ-jet samples were generated for the studies presented in Chapter 6 and Chapter 7. For the simulation of events at $\sqrt{s} = 7$ TeV (for comparison to the 2011 dataset) the nominal Monte Carlo generator used was PYTHIA v6.425 [29]. Parameters used to model the underlying event and non-perturbative physics were derived from comparisons data and are known as the *detector tune*. The tune that was used is known as ATLAS AUET2B MRST LO** [77]. The MRST LO** PDF set was used.

For assessment of the systematic uncertainty due to the modelling of the underlying physics, HERWIG v6.510 [30] was used, also with the ATLAS AUET2B MRST LO** tune and the MRST LO** PDF set. HERWIG and PYTHIA use different models for the parton shower and hadronisation.

For assessment of the systematic uncertainty due to jets with a high electromagnetic content that are misidentified as a photon, an inclusive jet sample was generated using PYTHIA v6.425. A filter was applied to this sample of simulated events in order to select jets with a narrow shower profile, which are more likely to be misidentified as a photon.

For the simulation of inclusive γ-jet events at $\sqrt{s} = 8$ TeV the nominal Monte Carlo generator used was PYTHIA v8.165 [28] with the AU2 CTEQ6L1 detector tune [78] and CTEQ6L1 LO [79] PDF set. For the evaluation of the systematic uncertainty due to the modelling of the underlying physics HERWIG++ v2.5.2 [31] was used with the UE-EE-3 CTEQ6L1 detector tune and CTEQ6L1 LO PDF set.

3.9.2 Di-jet Monte Carlo Simulation

For the study and calibration of Variable R jets at $\sqrt{s} = 8$ TeV a di-jet Monte Carlo sample was used which was derived with the PYTHIA v8.165 generator with the AU2 CT10 detector tune and the CT10 [80] PDF set. The samples are sliced according to the leading anti-k_t $R = 0.6$ jet p_{T}. The events are weighted using the Monte Carlo event weight, the cross-section, filter efficiency and the number of events in each slice in order to restore the correct shape of the p_{T} distribution.

		Generator	$\sqrt{s}$ [TeV]	Detector tune	PDF
γ-jet nominal	2011	PYTHIA v6.425	7	ATLAS AUET2B	MRST LO**
	2012	PYTHIA v8.165	8	AU2	CTEQ6L1 LO
γ-jet uncertainty	2011	HERWIG v6.510	7	ATLAS AUET2B	MRST LO**
	2012	HERWIG++ v2.5.2	8	UE-EE-3	CTEQ6L1
Inclusive jet: filtered	2011	PYTHIA v6.425	7	ATLAS AUET2B	MRST LO**
Di-jet	2012	PYTHIA v8.165	8	AU2	CT10

Table 3.2: Summary of the Monte Carlo generators, detector tunes and PDFs used for event simulation for the results presented in this thesis.

Chapter 4

Object Reconstruction

The studies presented in this thesis mainly make use of two types of physics objects: photons and jets. This chapter gives an overview of the reconstruction of these objects. The reconstruction of the missing transverse momentum (E_T^{miss}) in an event and the reconstruction of electrons and muons are also briefly described.

4.1 Photon Reconstruction

Photons are built from electromagnetic calorimeter cells using a sliding window algorithm [66, 81]. The algorithm positions windows of size 3×5 in units of 0.025×0.025 in $|\eta \times \phi|$ space, maximising the energy contained within each window. Only calorimeter cells with $E_T > 2.5$ GeV are considered.

The clusters of calorimeter cells that are found using the sliding window algorithm are classified as either an electron, an *unconverted* photon or a *converted* photon, depending on the tracks, or lack of tracks, which are associated to the cluster [69].

Clusters with no matching tracks[1] are classified as unconverted photons. Clusters with

---

[1] A track is considered to be matched to a cluster if it is within a 0.05×0.10 window in $|\eta \times \phi|$ space around the centre of the photon cluster. A matching track is also required to have a momentum which is at least 10 % of the energy of the cluster.

matching tracks are either classified as an electron or a converted photon.

Converted photons are photons that have converted to an e^+e^- pair before reaching the calorimeter. They are differentiated from electrons by requiring that the tracks matching the cluster come from a conversion vertex (a tracking vertex consistent with the conversion of a photon to an e^+e^- pair). A dedicated tracking algorithm is used to find conversion vertices. The algorithm searches for pairs of opposite sign tracks and imposes requirements to select pairs consistent with a photon conversion. For example, the tracks must have a small angle between them at the point of conversion to account for the fact that photons are massless, so the opening angle of the e^+e^- pair produced in the conversion is zero [68]. Requirements are also placed on the number of high-threshold hits in the TRT compared to the total number of hits in the TRT, to ensure that the tracks are electron-like. Further requirements are placed on the reconstructed photon invariant mass and p_{T}. The clusters associated with the e^+e^- pair conversion are known as *double track conversions* if both of the tracks from the conversion are found.

Following reconstruction of pairs of tracks which are consistent with a photon conversion, the remaining tracks are studied since it is possible that one track from either the e^+ or e^- may not have been reconstructed. The remaining tracks must not have a hit in the first pixel layer, and they must pass stringent cuts on the number of high-threshold hits in the TRT compared to the total number of hits in the TRT. This ensures that only electron-like tracks are selected [68]. The clusters which have a single matching track that passes these requirements are known as *single track conversions.*

Following classification, the cluster is rebuilt with a size optimised to capture the energy of the photon whilst minimising contributions due to pile-up and noise. The optimal size depends on the position of the cluster in the calorimeter, and whether the cluster has been classified as a converted or unconverted photon. Electron clusters are expected to be wider than unconverted photon clusters as electrons are more likely to interact before reaching the calorimeter, and because they radiate soft photons due to Bremsstrahlung radiation. Electron trajectories are also bent in the ϕ direction by the magnetic field and therefore they form a wider cluster in the ϕ direction compared to unconverted photons. Converted photons are expected to have a wider cluster than unconverted photons since their energy is deposited in the calorimeter by the e^+e^- pair. In the EM barrel ($|\eta| < 1.475$), unconverted photons are reconstructed with a size of 3×5 in units of $0.025{\times}0.025$ in $|\eta \times \phi|$ space, whereas converted photons are reconstructed with a size of 3×7. In the EM endcap ($1.375 < |\eta| < 3.2$), both converted and unconverted photons have a size of 5×5 [66]. For converted photons, the size of the clusters in the endcaps is smaller in ϕ, compared to the size in the barrel, since the bending effect of the magnetic field is smaller for electrons travelling in the high η direction.

The energy of the photon is calculated by summing the energy of the constituent calorimeter cells, and the $\eta - \phi$ position is calculated from the energy weighted centre of the cluster. Photons with $1.37 < |\eta| < 1.52$ are not used as this region contains a significant proportion of material that is not instrumented.

4.1.1 Photon Identification

In order to distinguish photons from jets with a high electromagnetic content (e.g. due to $\pi^0 \rightarrow \gamma\gamma$), photons must pass criteria designed to ensure that the shape of the electromagnetic shower is consistent with the electromagnetic shower of a photon. For this purpose, requirements are placed on a set of variables that describe the shape of the shower and any leakage into the hadronic calorimeter. Two nominal sets of requirements are available: *tight* photon identification and *loose* photon identification.

The selection efficiency of tight photons is > 85 % and the background rejection is approximately 5000 [2] for tight photons with $E_T > 40$ GeV [69, 70]. The selection efficiency of loose photons is > 97 % and the background rejection is approximately 950 for loose photons with $E_T > 40$ GeV [69, 70]. For loose photon identification the same requirements are applied to converted and unconverted photon clusters. The requirements for tight photon identification are tuned separately for converted and unconverted photons.

---

[2] ie. 1 out of 5000 jets will be misidentified as a photon.

For the background studies shown in this thesis another definition of loose photon identification is used (denoted here as *loose*+ photon identification). The differences between the shower shape variables that are used for loose+ identification, loose identification and tight identification can be seen in Table 4.1.

Differences in the distributions of the variables shown in Table 4.1 are seen between data and Monte Carlo. The data-to-Monte Carlo differences observed between the mean values of the variables are used to shift the values of the variables in Monte Carlo, such that the means of the distributions in Monte Carlo match the means of the distributions in data. These shifts are applied before applying the photon identification requirements.

4.1.2 Photon Isolation and Object Quality

Photons are required to be isolated from other activity in the detector by considering the amount of energy deposited in a circle around the photon [82, 83]. There are two ways of measuring the energy surrounding the photon. The first method, known as cell-based isolation (shown in Figure 4.1 a)), sums the energy of all calorimeter cells in a circle of radius 0.4 around the photon. The second method, known as topo-cluster-based isolation (shown in Figure 4.1 b)), sums the energy of all positive energy topo-clusters within a circle of radius 0.4 around the photon. For both methods, the energy in a 5×7 window around the direction of the photon is then subtracted from the total energy. Corrections derived from Monte Carlo are used to account for any photon energy that was not contained in the 5×7 window and to account for pile-up, noise and the underlying event. The topo-cluster-based isolation is more robust against pile-up due to the inbuilt noise reduction of the topo-clustering algorithm and is used for the isolation energy (E^{γ}_{iso}) in analysis of 2012 data and Monte Carlo. For 2011 data and Monte Carlo the topo-cluster-based isolation was not available and so the cell-based isolation energy was used.

In addition to isolation requirements, photon cleaning requirements [84] are applied to reject photons that have been reconstructed from calorimeter cells with a high level of noise.

Category	Description	Name	Loose	Loose+	Tight
Acceptance	$\|\eta\| < 2.37$, $1.37 < \|\eta\| < 1.52$ excluded	-	✓	✓	✓
Hadronic Leakage	Ratio of E_T in the first sampling layer of the hadronic calorimeter to E_T of the EM cluster (used over the range $\|\eta\| < 0.8$ and $\|\eta\| > 1.37$)	R_{had1}	✓	✓	✓
	Ratio of E_T in all the hadronic calorimeter to E_T of the EM cluster (used over the range $0.8 < \|\eta\| < 1.37$)	R_{had}	✓	✓	✓
EM Middle Layer	Ratio of cell energies in 3×7 versus 7×7 cells in $\eta \times \phi$	R_η	✓	✓	✓
	Lateral width of the shower in η	$w_{\eta 2}$	✓	✓	✓
	Ratio of cell energies in 3×3 and 3×7 cells in $\eta \times \phi$	R_ϕ		✓	✓
EM Strip layer	Shower width for three strips around the strip with the maximum energy deposit	w_{s3}			✓
	Total lateral shower width	w_{stot}		✓	✓
	Energy outside the core of three central strips but within seven strips divided by energy within the three central strips	F_{side}			✓
	Difference between the energy associated with the ΔE second maximum in the strip layer, and the energy reconstructed in the strip with the minimal value found between the first and second maxima	ΔE			✓
	Ratio of the energy difference associated with the largest and second largest energy deposits over the sum of these energies	E_{ratio}			✓

Table 4.1: Table showing variables used for photon identification for loose+, loose and tight photon identification. The table is adapted from [70].

4.2 Electrons

The reconstruction and calibration of electrons is very similar to the reconstruction and calibration of photons. As described above the sliding window algorithm is used to identify

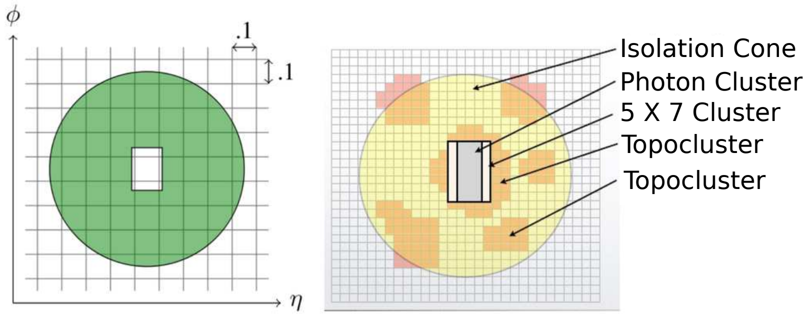

(a) (b)

Figure 4.1: Illustrations of the two ways of measuring the energy surrounding a photon. a) uses the energy of all cells within a circle of radius 0.4 around the photon [85] and b) uses the energy of all positive energy topo-clusters within a circle of radius 0.4 around the photon [86].

clusters of calorimeter cells that are electron or photon candidates. Electrons are then distinguished from photons by the presence of matching tracks that do not come from a conversion vertex. An overview of the reconstruction and identification of electrons can be found in Ref. [87].

Electron identification criteria are used to reject *non-prompt* electrons, which did not come directly from the hard scatter or from the decay of a W or Z boson or a top quark. The shower shape variables used for photon identification are also used for electron identification. Additionally, electron identification makes use of information about the tracks in the inner detector. The electron identification is optimised to reject fake electrons, which originate from jets with a high electromagnetic content, and non-prompt electrons from the semi-leptonic decay of B or D hadrons, the decay of charged pions, or converted photons. Three categories of electron identification criteria are available: loose++, medium++ and tight++, each of which have an increasing rejection power against fake electrons and non-prompt electrons.

4.3 Muons

Muons are reconstructed from tracks in the muon spectrometer and they also make use of tracks in the inner detector. Muons which have tracks in the muon spectrometer that are matched to tracks in the inner detector have the highest purity and they are known as *combined muons.* Quality criteria are applied to the MDT and inner detector tracks used for muon reconstruction, including cuts to ensure that the muons come from the primary vertex. An overview of all types of muons and their performance can be found in Ref. [88].

4.4 Missing Transverse Momentum (E_T^{miss})

Missing transverse momentum (E_T^{miss}) provides a measure of the energy which has not been detected due to weakly interacting particles (e.g. neutrinos). E_T^{miss} may also be present due to mis-calibration of the physics objects, pile-up or regions of the detector that are not functioning. E_T^{miss} is defined as $-\sum p_T^{\text{all objects}}$ where $\sum p_T^{\text{all objects}}$ is the vector p_T sum of calorimeter based objects (electrons, photons, taus and jets), muons and any energy deposits that are not associated to a reconstructed object.

The transverse momentum for each of the reconstructed objects is determined using the standard calibration procedures. Topo-clusters are used to measure the transverse momentum of energy deposits not associated to a reconstructed object.

4.5 Jet Reconstruction

4.5.1 Inputs for Jet Finding

The inputs for jet finding at the ATLAS detector and in the ATLAS software can either be calorimeter towers, topo-clusters, tracks or Monte Carlo truth particles. A brief description of each of these is given here and more details can be found in References [43, 46, 66].

Tower jets Calorimeter towers are formed from calorimeter cells from all layers of the calorimeter, projected onto an $\eta \times \phi$ grid. The cells are then grouped into towers with a size of $|\Delta\eta \times \Delta\phi| = 0.1 \times 0.1$. Jets built from towers are known as *tower* jets. Only towers with a positive energy are used for jet finding. Jets built from towers are used primarily in the trigger and are not used for any studies presented here.

Reconstructed jets Jets built from topo-clusters are known as *calorimeter* or *reconstructed* jets. Only topo-clusters with positive energy are used for jet finding and they are considered to be massless. Since the topo-clusters are considered to be massless the jet mass that is built from topo-clusters is a measure of the dispersion of the topo-clusters within the jet.

Track jets Jets built from tracks are known as *track jets*. Tracks used for jet finding must satisfy selection criteria based on their transverse impact parameter (the transverse distance from the primary vertex at their closest approach to it), transverse momentum and the number of hits in the pixel and silicon trackers [43]. These criteria are designed to select good quality tracks that come from the primary vertex. The track mass is taken to be the mass of the pion.

Truth jets Jets built from Monte Carlo particles are known as *truth* jets. They are said to be at *particle level*, meaning that they are built from the Monte Carlo particles produced by the hadronisation and subsequent decay of hadrons into particles with a sufficiently long lifetime to be detected. Particles from Monte Carlo generators are used for jet finding if they are stable, with a lifetime > 10 ps. The mass of the particles is used in the four-vector of the Monte Carlo particles (e.g. if the particle is a proton the mass is taken to be the proton mass). Muons and neutrinos are not included in the reconstruction of truth jets.

4.5.2 Jet Algorithms used at the ATLAS Detector

The most commonly used types of jet at the ATLAS detector are jets built using the anti-k_t algorithm (described in Section 2.2) with a distance parameter of either $R = 0.4$ or $R = 0.6$. These jets will be known here as *small-R* jets.

Physics analyses dealing with boosted objects, such as boosted top quarks, W or Z bosons make use of jets with a much larger distance parameter, known as *large-R* jets. Large-R jets used at ATLAS are built either with the anti-k_t algorithm with $R = 1.0$ or the Cambridge-Aachen algorithm with $R = 1.2$. The anti-k_t $R = 1.0$ jets which are used for the studies presented in this thesis are trimmed as described in Section 2.3.

In addition to the studies of small-R and large-R anti-k_t jets which are presented in this thesis the calibration of jets built with the VR jet algorithm, which was introduced in Sections 2.2 and 2.4, will be discussed. In particular, the anti-k_t version of the VR jet algorithm is used with the following parameters:

	R_{max}	R_{min}	ρ_{VR}
Small VR jets	0.4 for $p_{\mathrm{T}} < 150$ GeV	0.2 for $p_{\mathrm{T}} > 300$ GeV	60 GeV
Large VR jets	1.0 for $p_{\mathrm{T}} < 600$ GeV	0.2 for $p_{\mathrm{T}} > 3$ TeV	600 GeV

Table 4.2: The parameters for the small and large VR jet collections.

4.6 b-jets

Jets containing B-hadrons are identified using *b-tagging.* b-tagging uses tracks which are associated with jets according to their distance from the centre of the jet ($\Delta R = \sqrt{\Delta\eta^2 + \Delta\phi^2}$), to identify B-hadrons. B-hadron decays result in displaced vertices in the detector. A neural network (known as MV1) is used to identify B-hadrons. It makes use of three b-jet tagging algorithms: I3PD that uses the transverse and longitudinal distance parameters of the secondary vertex; SV1 that uses variables such as the distance of the secondary vertex from the primary vertex; and jet fitter that looks for a secondary and a tertiary vertex due to the $b \to c \to X$ decay chain [89, 90].

Chapter 5

Photon and Jet Calibration

Photons are used extensively as a reference object for the jet calibration studies that are presented in this thesis. It is, therefore, important that the photons are well calibrated in order to know their energy to a high precision. The photon calibrations and uncertainties described in this chapter are derived by the EGamma group, a group dedicated to studying the performance and calibration of electrons and photons at the ATLAS detector. Following the discussion of the photon calibration, an overview is given of the jet calibration schemes that are used to calibrate small and large R jets at the ATLAS detector.

5.1 Photon Calibration

There are three main steps used to calibrate photons [68]. The first is the calorimeter calibration to convert the electronic signal in the calorimeter into an energy measurement. The second step is a calibration derived from Monte Carlo, which uses simulations of the detector to correct for energy that has been lost in material in front of the calorimeter, energy lost due to dead material in the calorimeter, energy which was not captured by the photon reconstruction algorithm and energy lost out of the back of the electromagnetic calorimeter. The Monte Carlo calibration is optimised separately for converted photons and unconverted photons.

The final step of the calibration is an in-situ Z→ee calibration [68, 91, 92], which is used to correct the energy of photons in data. The calibration makes use of the well known value of the Z mass, and line-shape, to correct the energy of electrons. Since no in-situ method is available for the calibration of the photon energy, the Z→ee calibration factors are also applied to photons.

Any mis-calibration of the energy scale of the electrons seen in Z→ee events is parametrised by $E_{\text{measured}} = E_{\text{true}}(1 - \alpha)$. The electron (or photon energy) can therefore be corrected as follows:

$$E_{\text{corrected}} = \frac{E_{\text{uncorrected}}}{1 - \alpha}. \tag{5.1}$$

Where $E_{\text{uncorrected}}$ is the measured energy after the calorimeter calibration and Monte Carlo calibrations. The factor, $1/(1 - \alpha)$, is the electron (or photon) energy scale that is used to correct the energy of the electrons and photons in data. Correction factors of the order of 2 % in the barrel and 4 % in the endcaps were derived in 2010 data [93] and were applied to the calorimeter cells. In 2011 data, residual correction factors on the order of 0.5 % in the barrel and 1 % in the endcap were applied to the photons. In 2012 data the correction factors were similar to those in 2011, with differences on the order of a few per mil.

The Z→ee calibration factors depend on the modelling of the pre-sampler and the amount of material in front of the calorimeter. Photons interact with matter in a different way compared to electrons, and produce electromagnetic showers with different topologies. Therefore, when the Z→ee calibration factors are applied to photons a larger uncertainty is required on the photon energy. These additional uncertainties are evaluated in Monte Carlo by varying the pre-sampler energy scale and the amount of material in front of the calorimeter. The Z→ee calibration factors are then re-derived and applied to the photons. The uncertainty is evaluated by measuring the effect that this has on the reconstructed photon energy compared to the true photon energy.

The systematic uncertainty on α has three components: the uncertainty due to the derivation of the Z→ee calibration factors, the uncertainty on the photon energy scale due to the pre-sampler and the uncertainty on the photon energy scale due to material in front of the calorimeter. For 2011 data, only the quadratic sum of these uncertainties was available and in 2012 the components were available separately. The average uncertainty on α ($\Delta\alpha$) can be seen in Figure 5.1 [1] for converted and unconverted photons. The uncertainty is $\sim$0.5 % for $|\eta| < 0.8$, rising up to $\sim$1 % for $0.8 < |\eta| < 1.37$. The uncertainty for converted photons is significantly larger in the region $0.8 < |\eta| < 1.37$.

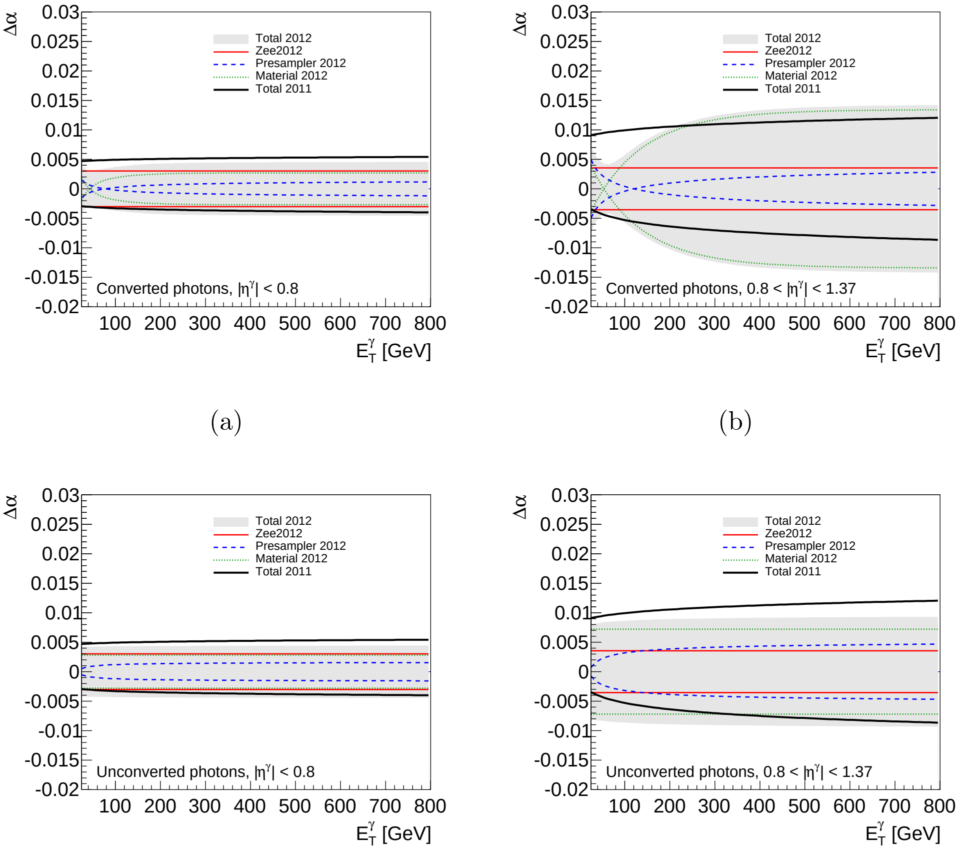

(a) (b)

(c) (d)

Figure 5.1: The uncertainty on α ($\Delta\alpha$) in 2011 and 2012 data for a) converted photons with $|\eta| < 0.8$, b) converted photons with $0.8 < |\eta| < 1.37$, c) unconverted photons with $|\eta| < 0.8$ and d) converted photons with $0.8 < |\eta| < 1.37$. The 2012 uncertainty is broken down into components due to the $Z \rightarrow ee$ calibration, material in front of the calorimeter and the pre-sampler. For 2011 only the total uncertainty is shown.

---

[1] These figures were produced for this thesis using the uncertainties on α, which are provided by the EGamma group.

The photon energy resolution, measured in Monte Carlo, is < 5 % (< 6 %) for photons with $E_T = 25$ GeV for converted (unconverted) photons. The photon energy resolution improves to < 2 % (< 1.5 %) for photons with $E_T > 100$ GeV for converted (unconverted) photons [81]. The energy resolution is measured in data using the width of the Z→ee distributions used for the calibration. A larger resolution is observed in data than in Monte Carlo. To account for this the photon energy in Monte Carlo is smeared in order to match the energy distribution observed in data.

5.2 Jet Calibration

5.2.1 Overview of the Jet Calibration Scheme

The four-vector of a reconstructed jet may be mis-measured due to several effects, including:

- Non-compensation of the calorimeter [2], which results in a hadron with a given energy depositing less visible energy in the calorimeter than an electromagnetically interacting particle with the same energy;
- Dead material in the calorimeter;
- Energy deposits that are not captured by the jet algorithm;
- Leakage of particles outside of the calorimeters;
- Noise thresholds and particle reconstruction efficiency;
- Additional energy deposits due to pile-up.

The aim of the jet calibration, known as the Jet Energy Scale (JES) calibration, is to correct for these effects. Two calibration schemes, known as the EM+JES and LCW+JES calibrations, are currently provided for use by physics analyses at ATLAS and will be described here. Further details about these calibrations in 2010 and 2011 data can be found in Refs. [1, 43].

---

[2] Non-compensation was introduced in Section 3.4

The energy of the reconstructed jets at the start of the JES calibration depends on the energy scale of the topo-clusters from which the jets were built. There are two different calibrations which are applied to topo-clusters before the jet algorithms are run: the electromagnetic (EM) calibration and the Local Cluster Weighting (LCW) calibration.

The EM scale calibration for topo-clusters calibrates the topo-clusters to the scale of an electromagnetic shower in the calorimeter. It is applied to the calorimeter cells before topo-clustering. For the LAr calorimeters, the EM calibration scheme described for photons in Section 5.1 is used for the electromagnetic calibration. This includes: LAr signal to energy conversion, Monte Carlo calibration and the application of the Z→ee calibration factors derived with 2010 data. The uncertainty on the EM scale is 3 % for the electromagnetic calorimeter. For the Tile calorimeter, the electromagnetic energy scale was verified using muons in the test beam [94] and cosmic ray data [95]. The uncertainty on the EM scale for the tile calorimeter is 3 %.

The LCW scale calibration [1, 96] for topo-clusters classifies the topo-clusters as either electromagnetic or hadronic. According to this classification, weights are applied to correct the topo-clusters for non-compensation of the calorimeter, out-of-calorimeter energy deposits and dead material.

Reconstructed jets are either at EM or LCW scale, depending on the scale of the topo-clusters that were used for the jet finding. The JES calibration for EM and LCW scale jets is derived according to the calibration scheme depicted in Figure 5.2. The calibration scheme is the same for EM and LCW scale jets, the only difference is the initial energy scale of the reconstructed jets.

The first step in the calibration is a pile-up correction to correct for additional energy in the jet that is due to pile-up. The second step is an origin correction to correct the direction of the jet to point to the primary vertex in the event instead of the centre of the detector. The third step is an energy and pseudorapidity calibration to correct the jet energy and pseudorapidity to particle level. The calibration is derived in Monte Carlo and applied to jets in data and Monte Carlo. The final step is an in-situ calibration to correct for residual differences in the jet energy scale between data and MC and it is applied to jets in data. Each of these steps is described in more detail in the following sections.

Jets at the LCW+JES scale are expected to have a better jet energy scale resolution since energy fluctuations due to non-compensation, dead material and out-of-calorimeter energy deposits have been corrected for by the LCW scale calibration [97]. However, the application of the LCW weights makes the overall calibration and study of LCW+JES jets more complicated. This resulted in ATLAS first providing the EM+JES calibration for use by physics analyses in 2010 and 2011 data and Monte Carlo and then, after further study, providing the LCW+JES calibration for use in 2011 and 2012 data and Monte Carlo [1, 43].

An additional step in the jet calibration, known as the Global Sequential Calibration (GSC), is currently under study by ATLAS for small-R jets for use in 2012 data and Monte Carlo. Initial studies of the GSC can be found in Ref. [43]. The GSC is implemented in-between steps three and four in Figure 5.2. For the calibration of LCW scale jets, GSC uses the width of the jet calculated using tracks, the number of tracks in the jet and the number of energy deposits in the muon system (punch-through) in order to further correct the energy of the jets. For the calibration of EM scale jets, the GSC uses these properties, plus the fraction of energy deposited in the first layer of the Tile calorimeter and the energy deposited in the third layer of the EM calorimeter. The purpose of these additional corrections is to further improve the jet energy resolution of the jets and to reduce differences between the measured jet energy of quark and gluon jets. However, at the time of writing the GSC and the corresponding uncertainties are not ready for use by physics analyses. GSC will not be discussed further in this thesis, since it was not applied for the results presented here.

In the case of large-R jets only LCW scale topo-clusters are used to reconstruct large-R jets. This is because the substructure of large-R jets is of great significance for performance studies and physics analyses. When studying the substructure of jets it is important that the energy profile within the jet is well known. The LCW calibration ensures that this is the case since it is a calibration applied to the topo-clusters rather than a global calibration of the whole jet.

For the JES calibration of large-R jets only step 3, the energy and pseudorapidity calibration, was available at the time of writing. Since the mass of large-R jets is used by physics analyses there is also an additional correction for large-R jets to correct the jet mass to particle level.

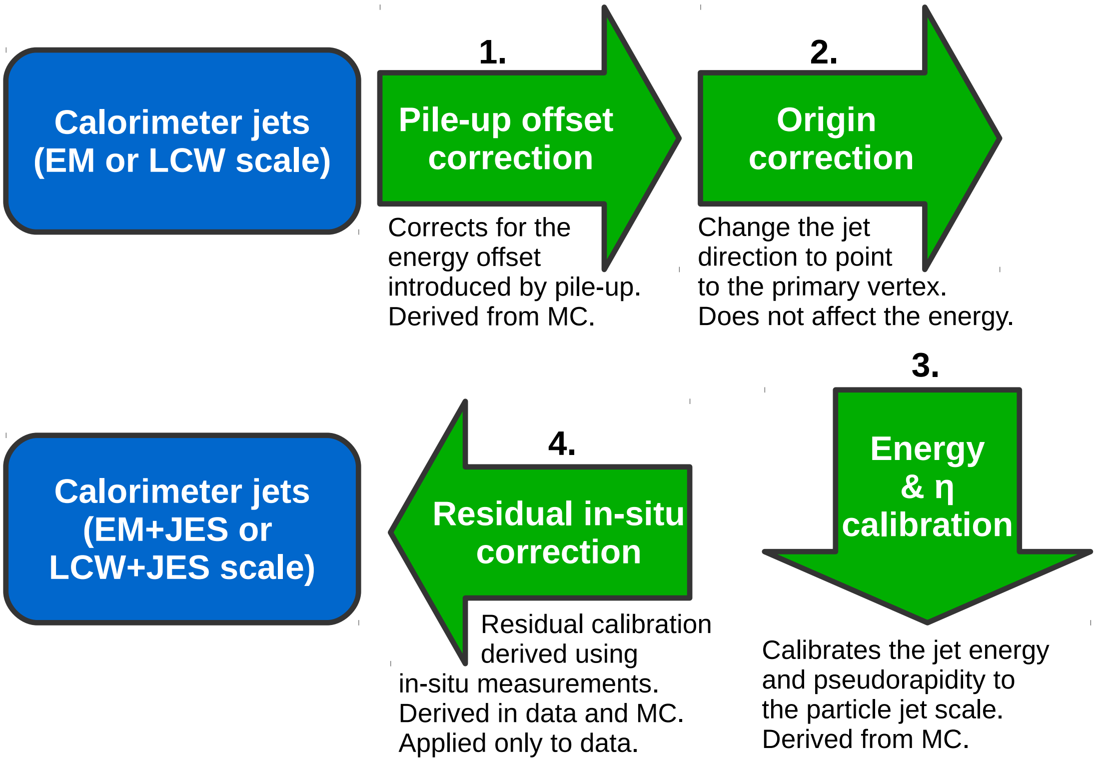

Figure 5.2: The EM+JES and LCW+JES calibration schemes for small-R jets. The figure is adapted from [1].

5.2.2 Pile-up Correction

Reconstructed jets contain energy deposits that are due to pile-up. The first step of the jet calibration corrects for these energy deposits. The pile-up corrections and uncertainties for small-R anti-k_t jets are derived by the JetEtMiss group (a group within ATLAS who are dedicated to the study and performance of jets and E_T^{miss}). The pile-up corrections are applied to the small-R jets used in Chapters 6 and 7. The methods discussed here also form the basis for the pile-up correction for VR jets which will be described in Chapter 8.

Two methods can be used to correct for pile-up: the average pile-up offset correction, and the jet area pile-up correction. The average offset pile-up correction was used for 2011 data. The recommended correction for 2012 data is the jet area pile-up correction, with an average offset pile-up correction to subtract the energy due to pile-up that was not accounted for by the jet area pile-up correction. An overview of the pile-up correction is given here and further details can be found in Refs. [1, 98].

The Average Offset Pile-up Correction

The average offset pile-up correction is designed to subtract the p_{T} of the jet due to pile-up from the total p_{T} of the reconstructed jet. The p_T to be subtracted is calculated with respect to a reference set of pile-up conditions, $\mathrm{NPV}^{\mathrm{ref}}$ and μ^{ref}, which are the average values of NPV and μ respectively, for the dataset under consideration. For the 2012 dataset $\mathrm{NPV}^{\mathrm{ref}}$ and μ^{ref} are 11.7 and 20.1 respectively and for the 2011 dataset $\mathrm{NPV}^{\mathrm{ref}}$ and μ^{ref} are 4.9 and 5.4 respectively.

The transverse momentum that needs to be subtracted is binned in η_{det} and parametrised in the following way:

$$\begin{aligned}\mathcal{O}(\mu, \mathrm{NPV}, \eta_{\mathrm{det}}) &= \frac{\partial p_T}{\partial \mathrm{NPV}}(\eta_{\mathrm{det}}) \cdot (\mathrm{NPV} - \mathrm{NPV}^{\mathrm{ref}}) + \frac{\partial p_T}{\partial \mu}(\eta_{\mathrm{det}}) \cdot (\mu - \mu^{\mathrm{ref}}) \\ &= \alpha(\eta_{\mathrm{det}})(\mathrm{NPV} - \mathrm{NPV}^{\mathrm{ref}}) + \beta(\eta_{\mathrm{det}})(\mu - \mu^{\mathrm{ref}}),\end{aligned} \tag{5.2}$$

where $\alpha(\eta_{\mathrm{det}}) = \frac{\partial p_T}{\partial \mathrm{NPV}}$ is the gradient of the distribution of jet p_{T} vs NPV and $\beta(\eta_{\mathrm{det}}) = \frac{\partial p_T}{\partial \mu}(\eta_{\mathrm{det}})$ is the gradient of the distribution of jet p_{T} vs μ. $\alpha(\eta_{\mathrm{det}})$ and $\beta(\eta_{\mathrm{det}})$ are derived from di-jet Monte Carlo samples as described in Ref. [1].

Using $\mathcal{O}$ the jet four-vector is scaled by $(p_T^{\mathrm{uncorrected}} - \mathcal{O})/p_T^{\mathrm{uncorrected}}$ as follows:

$$\mathbf{p}^{\text{corrected}} = \left(\frac{p_T^{\text{uncorrected}} - \mathcal{O}(\mu, \text{NPV}, \eta_{\text{det}})}{p_T^{\text{uncorrected}}} \right) \mathbf{p}_{\text{uncorrected}}, \tag{5.3}$$

where $p_T^{\text{uncorrected}}$ is the jet p_{T} before the pile-up correction and $\mathbf{p}$ is the four-vector of the jet. This means that the p_{T} of the jet, the energy of the jet and the mass of the jet are all scaled by the same factor $((p_T^{\text{uncorrected}} - \mathcal{O})/p_T^{\text{uncorrected}})$ whilst leaving the jet direction unchanged.

The systematic uncertainty on the average offset pile-up correction is derived by considering the difference in $\alpha(\eta_{\text{det}})$ and $\beta(\eta_{\text{det}})$ between data and Monte Carlo. For 2011 data and Monte Carlo these differences were studied in two different in-situ contexts. The first of these was in γ-jet events, where the photon is back-to-back with the jet. The jet in the event is used to calculate the difference in $\alpha(\eta_{\text{det}})$ and $\beta(\eta_{\text{det}})$ between data and Monte Carlo. The photon is used in order to parametrise the differences as a function of p_T^{γ}, which is stable against pile-up. The second method is to use jets in γ-jet events, where the reconstructed (calorimeter) jets in the event are matched to track jets using a geometrical matching criteria. The reconstructed jet can then be used to calculate the difference in $\alpha(\eta_{\text{det}})$ and $\beta(\eta_{\text{det}})$ between data and Monte Carlo, and the track jet can be used to parametrise the differences as a function of track jet p_{T}. Track jets are relatively stable against pile-up since they are constructed from tracks that originate from the primary vertex.

The differences derived in γ-jet events, and using track jets, were combined to give the final systematic shifts to be applied to α and β. In 2011 data and Monte Carlo the resulting systematic uncertainty is less than 0.3 (0.5) % for each reconstructed primary vertex for anti-k_t $R = 0.4(0.6)$ jets, and approximately 0.7 % for each unit of μ for $20 < p_T^{jet} < 30$ GeV. The fractional systematic uncertainty decreases as the p_{T} of the jets increases [1]. These uncertainties can be added in quadrature to obtain the uncertainty for particular values of NPV and μ.

The Jet Area Pile-up Correction

The average offset pile-up correction described above can be used to subtract the average energy due to pile-up. However, it does not take into account fluctuations of the pile-up from event to event. The jet area pile-up correction aims to address this issue by using a correction that takes into account these fluctuations.

The fraction of the p_{T} in a jet that is due to pile-up can be estimated by considering $\rho \cdot A$ where ρ is the p_{T} density of pile-up in the event and A is the area of the jet [99].

ρ is calculated on an event-by-event basis by clustering all topo-clusters in the event using the k_t algorithm with a distance parameter of 0.4. ρ can then be calculated as follows:

$$\rho = \text{median}\left(\frac{p_T^j}{A^j}\right), \tag{5.4}$$

where p_T^j is the transverse momentum of the j^{th} jet in the event formed by the k_t clustering and A^j is the area of the j^{th} jet. p_T^j/A^j is calculated on a jet-by-jet basis and 'median' denotes the fact that the median of the distribution of p_T^j/A^j is taken as the value of ρ. The median of the distribution is used so that the event density is not biased by high p_{T} jets from the hard scatter in the event rather than from pile-up. Only jets within $|\eta| < 2.0$ are used for the calculation of ρ. This is due to the fact that for higher $|\eta|$ the calorimeter cells are larger and as such there are fewer of them. Therefore the probability of energy deposits due to pile-up fluctuating above the the E/σ thresholds used for the topo-clustering is lower in this region. This results in the majority of cells used in the topo-clustering being due to the hard scatter. Therefore it is not possible to measure the mean pile-up density in the forward region with the current noise thresholds [98].

Two methods are used by ATLAS in order to calculate the jet area: the active area calculation and the Voronoi area calculation, both of which are described in detail in Ref. [100]. The active area calculation uses *ghosts* in order to determine the area of a jet. A ghost is an infinitesimally low energy, massless particle. Ghosts are added to the event before the jet algorithm is run in a uniform grid in the $\eta - \phi$ plane. The positions of the ghosts are fluctuated randomly about their initial positions. When the jet clustering is run, the ghost particles cluster with the real jet constituents. However, they do not affect the order in which the real jet constituents cluster, the final p_{T} of the jet or the direction of the jet. The jet area can then determined in the following way:

$$A(J|\{g_i\}) = \frac{N_g(J)}{\nu_g}, \tag{5.5}$$

where $N_g(J)$ is the number of ghosts jet J, ν_g is the density of ghosts in the event and $A(J|\{g_i\})$ is the area of jet J which contains a set of ghosts $\{g_i\}$. This is known as the *scalar active area.*

A *four-vector active area*, which takes into account the direction of the ghosts as well as the number of them, can be calculated using the four-vectors of the ghosts:

$$A_\mu(J|\,\{g_i\}) = \frac{1}{\nu_g}\sum_{g_i \in J} g_{\mu i}, \tag{5.6}$$

where $g_{\mu i}$ are the four-vectors of the ghosts in the jet, ν_g is the ghost density and $A_\mu(J|\,\{g_i\})$ is the four-vector active area of jet J containing a set of ghosts $\{g_i\}$. The active area of jets clustered with the anti-k_t algorithm can be seen in Figure 5.3 a). The circular nature of isolated anti-k_t jets is clearly visible.

The transverse component of the four-vector active area (A_T) is equal to the scalar active area for small jet sizes [99]. Using A_T and the event density ρ, the energy and momentum of the jet can be corrected for pile-up whilst leaving the jet direction unchanged:

$$\mathbf{p}^{\text{corrected}} = \left(\frac{p_T^{\text{uncorrected}} - \rho \cdot A_T}{p_T^{\text{uncorrected}}}\right)\mathbf{p}^{\text{uncorrected}}. \tag{5.7}$$

This is known as the *scalar jet area correction.* If instead of A_T the four-vector active area is used then the full four-vector of the jet can be corrected for pile-up:

$$p_{\mu i}^{\text{corrected}} = p_{\mu i}^{\text{uncorrected}} - \rho \cdot A_{\mu i}, \tag{5.8}$$

where $A_{\mu i}$ is the four-vector area and $p_{\mu i}$ is the four-vector of the jet. This is known as the *four-vector jet area correction.*

The active area calculation gives an accurate measure of the area of a jet and its sensitivity to pile-up since the ghosts cluster in the same way as soft particles from pile-up. However, the addition of a large number of ghosts has the adverse effect of slowing down the speed of the jet reconstruction. A fast alternative that can be used to find an approximate value for the area of a jet is the Voronoi area calculation [100]. The Voronoi area calculation starts by constructing a Voronoi diagram using the constituents of all the jets in the event [3]. The Voronoi diagram is constructed such that any point within a given Voronoi cell is closer to the jet constituent which is contained within that Voronoi cell than to any other jet constituent in the event. This is illustrated, for an example event, in Figure 5.3 b), where the Voronoi diagram is represented by the straight lines and the jet constituents are represented by the coloured bars.

To calculate the area of the jet, first of all the area of each of the jet constituents is calculated. This is done by taking the overlap of a circle of radius R_{eff} (where R_{eff} is the distance parameter of the jet algorithm) with each Voronoi cell. The intersection of the coloured areas with the Voronoi diagram in Figure 5.3 b) represent these areas. The area of a jet is then simply the sum of the area of the jet constituents that belong to that jet. This is illustrated in Figure 5.3 b), where the different colours correspond to the areas for different jets.

The disadvantage of the Voronoi area is that, for low density events, the Voronoi cells at the edge of the jet are large due to a lack of nearby constituents. Therefore, the jet area tends to be systematically overestimated in comparison to the jet area measured with the active area calculation. This effect can be seen by comparing the areas of the jets in

---

[3] The jet constituents are the constituents that the jet was reconstructed from. For example, the jet constituents of a reconstructed jet are the topo-clusters which the jet is made up of.

Figures 5.3, where it can be seen that the areas calculated with the active area calculation are significantly smaller than the areas calculated with the Voronoi areas calculation. Since low levels of pile-up result in less dense events than high levels of pile-up, this also means that the accuracy of the Voronoi area calculation is affected by the amount of pile-up in the event. Furthermore, the Voronoi area calculation can only provide a scalar area since it does not use any information about how soft particles cluster with the jet.

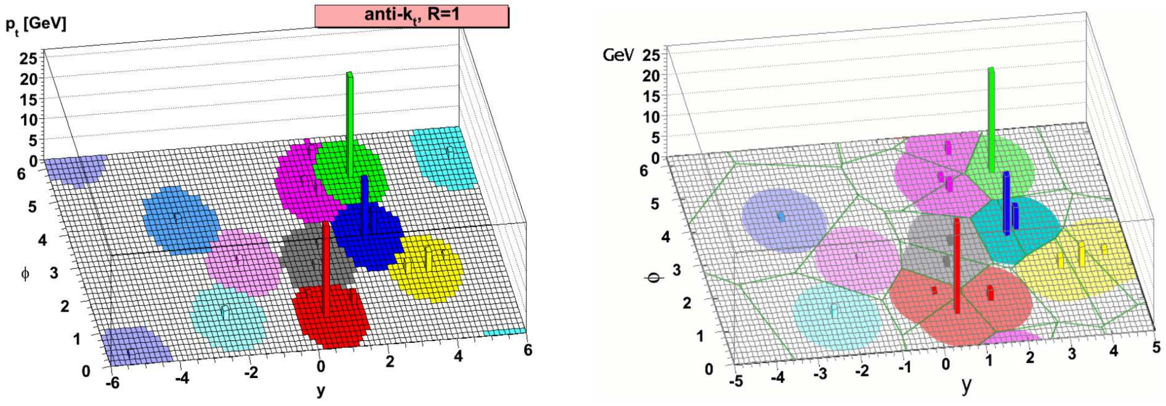

(a)

(b)

Figure 5.3: The area of jets clustered with the anti-k_t algorithm with $R = 1.0$ calculated using a) the active area calculation [41] and b) the Voronoi area calculation [100].

Both types of jet area calculation were tested by ATLAS for the calculation of ρ and the jet area. It was found that the difference between using the Voronoi area calculation and the active area calculation to measure ρ was small. Therefore the Voronoi area calculation, which is less time consuming, is used to measure ρ [98].

However, for the calculation of the jet area there is a significant difference between the areas obtained with the Voronoi area calculation and the active area calculation. It is also important that the accuracy of the calculation is not dependent on the level of pile-up in the event. Therefore the active area is used to calculate the jet area. At the time of writing, the scalar area correction (Equation 5.7) is used to correct the jets for pile-up. The issue of the speed and accuracy of the active area and Voronoi area calculations will be revisited in the context of the Variable R jet algorithm in Chapter 8.

The jet area pile-up correction significantly reduces the dependence of the jet p_{T} on NPV, as can be seen in Figure 5.4 a). For $|\eta| < 2.5$ there is an NPV dependence of 0.5 GeV per unit of NPV before the jet area correction, and an NPV dependence of less than 0.1 GeV per unit of NPV after the jet area correction. The increase in the NPV dependence for $|\eta| > 2.5$, both before and after the jet area correction, is due to the larger size of the calorimeter cells in the forward region, which are more sensitive to pile-up due to their larger size.

In Figure 5.4 b) the jet p_{T} dependence on μ is shown. It can be seen that the jet p_{T} has a negative dependence on μ both before and after the jet area correction, particularly for $|\eta| > 2.5$. This negative dependence is due to the fact that the bi-polar pulse shaping of the LAr calorimeters (which was introduced in Section 3.4) can result in calorimeter cells with a negative energy in the presence of out-of-time pile-up. If these negative energy cells are isolated from other activity in the calorimeter then they may form negative energy topo-clusters, which are not used for jet reconstruction. However, if the energy deposits due to pile-up overlap with the energy deposits from the primary interaction then the out-of-time pile-up can act to decrease the jet energy. This is more likely for larger calorimeter cells, such as those in the forward region of the LAr calorimeters, since there is a greater probability of overlap. These negative energy deposits are the reason for the negative dependence of the jet p_{T} on μ that can be seen for $|\eta| > 2.5$ in Figure 5.4 b).

It can also be seen that the jet area correction only makes a small impact on the dependence of the jet p_{T} on μ. This is due to the fact that the calculation of ρ is dominated by calorimeter cells in low occupancy conditions. As discussed above, the out-of-time pile-up sensitivity for high occupancy regions (such as those in the core of a jet) is different to that for low occupancy regions. Therefore, ρ does not provide a complete description of the out-of-time pile-up sensitivity.

In order to correct for the remaining dependence of the jet p_{T} on NPV and μ, the average offset pile-up correction is derived in the same way as described previously. In this context it is known as the *residual offset pile-up correction*. As can be seen in Figure 5.4, the combination of the jet area correction, followed by the residual offset pile-up correction, almost completely removes any dependence of the jet p_{T} on NPV and μ.

In 2012 data, the systematic uncertainty due to pile-up for anti-k_t $R = 0.4$ and $R = 0.6$ jets (after the jet area and residual offset pile-up corrections) is derived using Z-jet events. The jet is used to measure the dependence of the jet p_{T} on NPV and μ and the Z boson is used to parametrise the measurements as a function of p_{T}. The uncertainties are also derived using Z-jet events where the reconstructed jet is matched to a track-jet. The reconstructed jet is used to measure the dependence of the jet p_{T} on NPV and μ and the track jet is used to parametrise the measurements as a function of p_{T}. Track jets are relatively insensitive to pile-up since they are constructed from tracks which originate from the primary vertex. There are four components to the uncertainty: one due to the gradient of the jet p_{T} vs NPV, one due to the gradient of the jet p_{T} vs μ, one due to the p_{T} dependence of the gradients of the jet p_{T} vs NPV and μ and one due to the measurement of ρ. The total systematic uncertainties derived with 2012 data and Monte Carlo are less than 2 % for anti-k_t $R = 0.4$ jets in the central region for jets with $p_{\mathrm{T}} > 40$ GeV. The uncertainty increases at lower p_{T} and higher η up to 5.6 % [98]. For anti-k_t $R = 0.6$ jets the uncertainties are within ∼2 % for jets in the central region with $p_{\mathrm{T}} > 40$ GeV and the uncertainty increases at lower p_{T} and higher η up to ∼7-8 %.

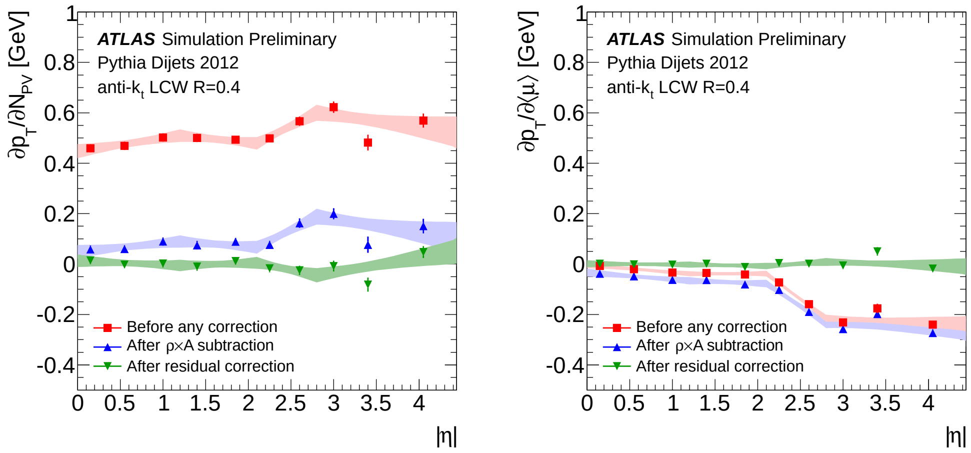

(a) (b)

Figure 5.4: a) $\frac{\partial p_T}{\partial \mathrm{NPV}}$ and b) $\frac{\partial p_T}{\partial \mu}$ as a function of $|\eta|$ with no pile-up correction, after the jet area pile-up correction and after the jet area and residual average offset pile-up correction for 2012 Monte Carlo [98]. The dependencies are derived for $p_T^{\text{truth jet}} = 25$ GeV.

The Jet Vertex Fraction

Energy deposits from pile-up can overlap with energy deposits from the primary interaction, but they can also form jets in which the majority of energy comes from pile-up rather than the primary interaction. A useful quantity that is used to suppress jets from additional proton-proton collisions in the event is the Jet Vertex Fraction [98], which is defined as:

$$\mathrm{JVF} = \frac{\sum p_T^{\text{tracks from PV}}}{\sum p_T^{\text{all tracks}}}, \tag{5.9}$$

where $p_T^{\text{tracks from PV}}$ is the scalar sum of the p_{T} of tracks associated with the jet coming from the primary vertex and $p_T^{\text{all tracks}}$ is the scalar sum of the p_{T} of all tracks associated with the jet. Since this quantity requires the presence of tracks, it is only available for jets within the tracking acceptance, ie. with $|\eta| < 2.5$. In 2011 data and Monte Carlo, jets were required to have JVF > 0.75 to ensure that only a small fraction of the jet's energy deposits were due to pile-up.

In 2012 data and Monte Carlo, the jet area correction results in $N^{\text{pile−up jets}}(20 < p_T < 50\ \text{GeV})/N^{\text{pile−up jets}}(p_T > 20\ \text{GeV}) \approx 99\ \%$ [98], where $N^{\text{pile−up jets}}(20 < p_T < 50\ \text{GeV})$ is the number of pile-up jets with $p_{\mathrm{T}} > 20$ GeV that also have $p_{\mathrm{T}} < 50$ GeV and $N^{\text{pile−up jets}}(p_T > 20\ \text{GeV})$ is the number of pile-up jets with $p_{\mathrm{T}} > 20$ GeV. Therefore, JVF is only applied to jets with $p_T < 50$ GeV in 2012 data and Monte Carlo and a looser requirement can be applied of JVF > 0.25.

5.2.3 Origin Correction

Topo-clusters used for jet finding are assumed to have come from the geometric centre of the ATLAS detector. A correction is applied after jet finding to correct the four-vector of the topo-clusters to point back to the primary vertex (defined as the vertex with the highest scalar $\sum p_T^{\text{track}}$ in the event). This is done using a vector pointing from the primary vertex to the centroid of the topo-cluster. The jet four-vector is then recalculated using the corrected topo-cluster four-vectors. This correction gives a small improvement of < 1 % to the angular resolution of the jets [43].

The jet origin correction was applied to 2011 data. However, at the time of writing the correction was not available for 2012 data.

5.2.4 Monte Carlo based Jet Energy, Pseudorapidity and Mass Scale Corrections

Following the pile-up and origin corrections, the jet energy and pseudorapidity of reconstructed jets are corrected to particle-level by comparing reconstructed jets to truth jets in Monte Carlo samples containing high p_{T} jets. For large-R jets, there is an additional correction for the jet mass. The derived calibration factors are applied to both data and Monte Carlo. The reader is referred to Refs. [1, 43] for further information about the small-R jet Monte Carlo calibration and to Ref. [46] for further information about the large-R jet Monte Carlo calibration. The Monte Carlo calibrations are derived by the JetEtMiss group within ATLAS, and they are applied to the anti-k_t jets used in Chapters 6 and 7. The methods discussed here form the basis for the Monte Carlo calibration of VR jets, which will be described in Chapter 8.

Jet Energy Correction

The jet energy calibration factors are derived by measuring the truth jet response:

$$\mathcal{R}(\mathrm{truth}) = \frac{\mathrm{E}^{\mathrm{reco}}}{\mathrm{E}^{\mathrm{truth}}}, \tag{5.10}$$

where E^{reco} is the energy of the reconstructed jets at EM or LCW scale and E^{truth} is the energy of the truth jets. $\mathcal{R}(\mathrm{truth})$ is measured in bins of E^{truth} and η_{det}. Truth jets are matched to reconstructed jets by looking for the highest p_{T} reconstructed jet which satisfies

$\Delta R(\text{truth jet} - \text{reco jet}) < 0.3$ [4].

The truth jet and the reconstructed jet are required to be isolated. For truth jets there must be no other truth jet with $p_{\text{T}} > 7$ GeV within $\Delta R < 2.5 \cdot R_{\text{eff}}$. For reconstructed jets there must be no other reconstructed jet with $p_{\text{T}} > 7$ GeV, after the pile-up correction has been applied, within $\Delta R < 1.5 \cdot R_{\text{eff}}$. R_{eff} is the distance parameter of the jet algorithm.

The mean $\mathcal{R}(\text{truth})$ in each E^{truth} and η_{det} bin ($\langle\mathcal{R}(\text{truth})\rangle$) is found by fitting a Gaussian to the $\mathcal{R}(\text{truth})$ distribution. For each η_{det} bin, the $\langle\mathcal{R}(\text{truth})\rangle$ vs E^{truth} distribution is translated into a $\langle\mathcal{R}(\text{truth})\rangle$ vs E^{reco} distribution using the arithmetic mean of E^{reco} in each E^{truth} bin.

The resulting $\langle\mathcal{R}(\text{truth})\rangle$ vs E^{reco} distribution is fit, separately for each η_{det} bin, using the following function:

$$\mathcal{F}_{\text{calib}}(E^{\text{reco}}) = \sum_{i=0}^{N_{\max}} \left(a_i \left(\ln E^{\text{reco}}\right)^i\right), \tag{5.11}$$

where a_i are free parameters of the fit. The fit is performed six times for $N_{\max} = 1 - 6$. The $N_{\max}$ which gives the smallest χ^2/NDF for the fit is used to define the JES calibration factors, $1/\mathcal{F}_{\text{calib}}$. The jet energy is then corrected as follows:

$$E^{\text{EM+JES}} = \frac{E^{\text{reco, EM}}}{\mathcal{F}_{\text{calib, EM}}}, \qquad E^{\text{LCW+JES}} = \frac{E^{\text{reco, LCW}}}{\mathcal{F}_{\text{calib, LCW}}}. \tag{5.12}$$

Values of $\mathcal{F}_{\text{calib}}$ as a function of $|\eta|$ and for different jet energies can be seen in Figure 5.5 [5] for the EM+JES and LCW+JES calibrations for anti-k_t $R = 0.4$ jets. The 2011 calibrations are shown in (a) and (b) and the 2012 calibrations are shown in (c) and (d). It can be seen that $\mathcal{F}_{\text{calib}}$ is significantly lower for EM jets than LCW jets, meaning that larger calibration factors will be applied to EM scale jets in comparison to LCW scale jets. This is expected since the topo-clusters that the LCW scale jets are built from have already been corrected

---

[4] $\Delta R = \sqrt{\Delta\eta^2 + \Delta\phi^2}$

[5] Figures (c), (d) and (e) were produced for this thesis, using the 2012 calibration factors provided by the JetEtMiss group.

for non-compensation, dead material and out-of-calorimeter energy deposits. Additionally, $\mathcal{F}_{\text{calib}}$ is smaller for lower energies where the effects of non-compensation are larger.

Also shown is the truth jet response for anti-k_t $R = 1.0$ trimmed LCW jets in Figure 5.5 (e). The calibration for large-R jets extends down to 50 GeV, although it can be seen that there are large fluctuations below 100 GeV. Therefore large-R jets are not recommended for use by physics analyses below 100 GeV.

Pseudorapidity Correction

The pseudorapidity of the jets is corrected by considering [43]:

$$\Delta\eta = \eta_{\text{reco}} - \eta_{\text{truth}}. \tag{5.13}$$

In 2011 data and Monte Carlo, η_{reco} is the η of the jet following the origin correction. In 2012 data and Monte Carlo, the origin correction was not available at the time of writing. Therefore, in this case, η_{reco} is the η of the jet without the origin correction. $\Delta\eta$ is measured in bins of the η^{reco} of the jet before the origin correction and as a function of E^{truth}. In each $(\eta^{reco}, E^{\text{truth}})$ bin a Gaussian distribution is fit to the $\Delta\eta$ distribution, and the mean of the fit is taken as the mean value of $\Delta\eta$. A function of the same form as Equation 5.11 is used to parametrise the $\langle\Delta\eta\rangle$ vs E^{truth} distribution. The jet pseudorapidity is then corrected as follows:

$$\eta_{\text{corrected}} = \eta_{\text{uncorrected}} + \mathcal{F}^{\eta}_{\text{calib}}. \tag{5.14}$$

Jet Mass Correction for Large-R Jets

For large-R jets, there is an additional correction to calibrate the mass of the jets. The jet mass correction follows the same procedure as the derivation of the jet energy calibration, using the truth jet mass response instead of the jet energy response:

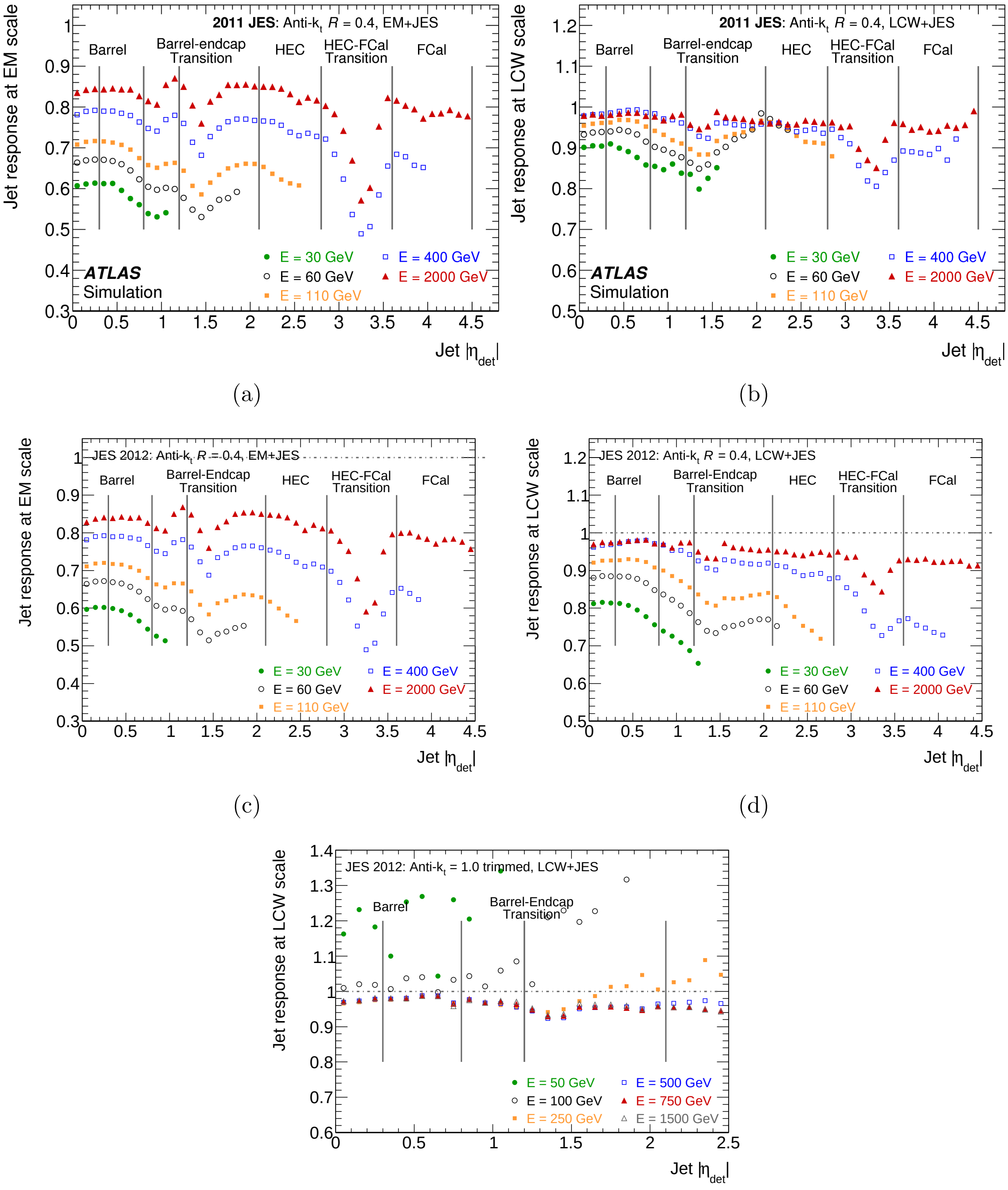

(a)

(b)

(c)

(d)

(e)

Figure 5.5: $\mathcal{F}_{\text{calib}}$ (labelled here as 'Jet response'), as a function of $|\eta|$ for different values of the jet energy for a) anti-k_t $R = 0.4$ EM jets in 2011 Monte Carlo [1] and b) anti-k_t $R = 0.4$ LCW jets in 2011 Monte Carlo [1], c) anti-k_t $R = 0.4$ EM jets in 2012 Monte Carlo, d) anti-k_t $R = 0.4$ LCW jets in 2012 Monte Carlo and e) anti-k_t $R = 1.0$ trimmed LCW jets in 2012 Monte Carlo. Different regions of the calorimeters are also shown.

$$\mathcal{R}(\text{truth, mass}) = \frac{m^{\text{reco}}}{m^{\text{truth}}}. \tag{5.15}$$

The jet mass calibration is derived in bins of E^{truth} and η^{reco}. Figure 5.6 [6] shows the jet mass response as a function of $|\eta|$ for different jet energies. As was observed for the jet energy response for large-R jets, there are large fluctuations in the jet mass response for $E < 100$ GeV.

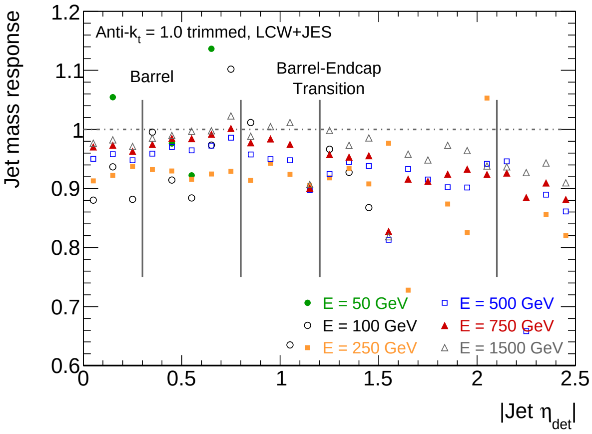

Figure 5.6: The truth jet mass response as a function of $|\eta|$ for different values of the jet energy for anti-k_t $R = 1.0$ trimmed LCW jets in 2012 Monte Carlo.

5.2.5 In-situ Calibration

The final step of the JES calibration is the in-situ calibration. As with the pile-up corrections and Monte Carlo calibrations, the in-situ calibrations are derived by the JetEtMiss group. The γ-jet direct balance in-situ calibration, which is introduced here and is the focus of the first part of this thesis, is described in further detail in Chapters 6 and 7. The γ-jet method will also be used in Chapter 9 to assess the performance of the VR jet calibration.

The in-situ analyses probe the JES in data and Monte Carlo after the pile-up corrections and Monte Carlo corrections described above have been applied. It is assumed that any residual differences between the data and Monte Carlo are due to mis-modelling of the

---

[6] This figure was produced for this thesis using the 2012 mass calibration factors provided by the JetEtMiss group.

detector. The data-to-MC differences that are observed are then used in order to apply a final correction to the data. The systematic uncertainties on these data-to-MC differences are taken to be the systematic uncertainty on the JES. The systematic uncertainties include systematics to account for residual physics effects, such as the modelling of additional radiation in the event.

In-Situ Calibration for Small Radius Jets

The in-situ calibration for small radius jets (jets with $R = 0.4$ or $R = 0.6$) proceeds using the following sequence of calibrations.

1. The first step in the in-situ calibration for small radius jets accounts for differences in the modelling of the jet energy in different η regions of the detector. It is known as the di-jet η-intercalibration method. In the simplest version of the analysis, di-jet events (where the two jets in the event have a back-to-back topology in the transverse direction) are used to probe $c_{ij} = p_T^{\mathrm{ref}}/p_T^{\mathrm{probe}}$, where p_T^{ref} is the p_T of the jet in the central region ($|\eta| < 0.8$) and p_T^{probe} is the p_{T} of the jet in the forward region ($|\eta| > 0.8$) for the i^{th} bin in η^{probe} and the j^{th} bin in $p_T^{\mathrm{avg}} = (p_T^{\mathrm{ref}} + p_T^{\mathrm{probe}})/2$. c_{ij} is measured in data and Monte Carlo and it is used to define calibration factors that are applied to data: $1/C_{ij} = c_{ij}^{\mathrm{MC}}/c_{ij}^{\mathrm{data}}$. A similar method (the matrix method) uses the same di-jet samples but retains events by not requiring a jet to be in the central region. This gives a more accurate measure of the calibration factors since a larger sample of events is available. The matrix method is the default method used to derive the η-intercalibration factors, full details of the method and the calibration factors can be found in [1].

   The η-intercalibration factors are applied to the jet energy and p_{T} in data before proceeding to the following steps.

2. In the second step of the in-situ calibration the JES is evaluated using a well calibrated reference object. One method used is the direct balance method [1, 43], where the p_{T} of the reference object is compared to the p_{T} of the jet in back-to-back events, using

the following response:

$$\mathcal{R}(\mathrm{DB}) = \frac{p_T^{\mathrm{jet}}}{p_T^{\mathrm{ref}}}, \tag{5.16}$$

where p_T^{jet} is the p_{T} of the jet following the pile-up correction, Monte Carlo calibrations, and η-intercalibration. p_T^{ref} is the p_{T} of a well calibrated reference object. The reference objects used at the ATLAS detector are the Z boson and the photon. The γ-jet and the Z-jet methods cover different (but overlapping) p_{T} ranges, which depend on the number of events available for the two different methods following event selection. The method using the Z boson covers the p_{T} range from 10 to 250 GeV and the method using the photon covers the p_{T} range from 25 to 800 GeV.

An alternative to the direct balance method is the Missing Energy Projection Fraction (MPF) method which utilises the hadronic recoil against the jet [1, 43]. This method assumes that any missing transverse energy in the event is due to calorimeter non-compensation, noise suppression and dead material in the detector. The MPF response is defined as:

$$\mathcal{R}(\mathrm{MPF}) = 1 + \frac{\mathbf{p_T^{\mathrm{ref}}} \cdot \mathbf{E_T^{miss}}}{|\mathbf{p_T^{\mathrm{ref}}}|^2} \tag{5.17}$$

where $\mathbf{p_T^{\mathrm{ref}}}$ is the transverse momentum vector of the reference object, $\mathbf{E_T^{miss}}$ is the missing transverse momentum vector and $|\mathbf{p_T^{\mathrm{ref}}}|$ is the absolute value of the transverse momentum of the reference object. The missing transverse momentum used for the MPF method is built using LCW or EM scale topo-clusters. Since Equation 5.17 does not directly use information from the jets in the event, it is independent of the jet algorithm and the size of the jets used. This method is also less sensitive to pile-up since, on average, pile-up is expected to be spherically symmetric and so will cancel out in the MPF response.

The response is evaluated in data and Monte Carlo for the direct balance Z-jet method, the direct balance γ-jet method and the MPF γ-jet method. For each of these methods the data-to-MC ratio of the response is calculated. For a perfect calibration it would be expected that the data-to-MC ratio of the response would be equal to one. However, this is not the case and the deviation of the data-to-MC ratio of the response from one is used to correct the jet energy and p_{T} in data. To define the correction factors that should be applied to the data, a single data-to-MC ratio must be derived. Information from the Z-jet and γ-jet methods is used to cover as wide a p_{T} range as possible.

Since the direct balance and MPF γ-jet methods are highly correlated one of the γ-jet methods is chosen to be combined with the Z-jet results. In order to decide which γ-jet method should be used, each is combined separately with the Z-jet results. The combination is performed by taking a weighted average of the data-to-MC ratio derived with the Z-jet method and either the direct balance or MPF γ-jet method. The weight used in the average is inversely proportional to the uncertainty of the method. Therefore, the method with the smallest uncertainty for a given p_{T} bin contributes the most to the final data-to-MC ratio of the response.

The systematic and statistical uncertainties on the average data-to-MC ratios are then derived by propagating the uncertainties of the Z-jet and γ-jet methods to the data-to-MC ratio using toy experiments, a full description of which can be found in [1]. The average data-to-MC ratio (either the one derived using the Z-jet and direct balance γ-jet methods, or the one derived using the Z-jet and MPF γ-jet methods) with the smallest uncertainty is chosen as the combined data-to-MC ratio of the Z-jet and γ-jet methods. This combined data-to-MC ratio of the response is used to correct the jet energy and p_{T} in data before the next step of the in-situ calibration.

3. The third step in the in-situ calibration uses the multi-jet balance method to evaluate the JES in the high p_{T} range from 210 GeV to 1.5 TeV. The multi-jet balance method compares the p_{T} of the leading (highest p_{T}) jet in the event to the vectorial sum of the p_{T}s of all other jets in the event:

$$\mathcal{R}(\mathrm{MJB}) = \frac{|\overrightarrow{p}_T^{\mathrm{leading}}|}{|\overrightarrow{p}_T^{\mathrm{recoil}}|}. \tag{5.18}$$

The calibration derived from the combination of the photon and Z boson methods described above is applied to all the non-leading jets in the event with $p_{\mathrm{T}} < 750$ GeV in the data. This provides a well calibrated system of jets against which the JES of the leading jet in the event can be evaluated. The difference in $\mathcal{R}(\mathrm{MJB})$ between data and Monte Carlo can then be used to iteratively extend the analysis to higher p_{T}s, applying the new calibration to the non-leading jets each time. In this way the measurement of the response extends up to 1.5 TeV. However, above 1 TeV in 2011 data and 1.2 TeV in 2012 data the number of events available in the multi-jet sample is insufficient for a precise measurement of the JES. Therefore, for $p_{\mathrm{T}} > 1$ (1.2) TeV the calibration factors at $p_{\mathrm{T}} = 1$ (1.2) TeV are used for the 2011 (2012) data and Monte Carlo.

4. The data-to-MC ratio of the response measured with either the MPF or direct balance γ-jet method (chosen as described in step two), the data-to-MC ratio of the response measured with the Z-jet method and the $\mathcal{R}(\mathrm{MJB})$ of the multi-jet method are combined. The same method which was described in step two is used for the combination. A full description of the combination can be found in [1]. The inverse of the combined data-to-MC ratio of the response is used as a calibration factor. The calibration factors are applied as a multiplicative factor to the jet four-vector in data to correct for the residual mis-calibration of the JES:

$$\mathbf{p}^{\mathrm{data}}_{\mathrm{corrected}} = \mathbf{p}^{\mathrm{data}}_{\mathrm{uncorrected}} \left(1 - \frac{\mathcal{R}_{\mathrm{MC}}}{\mathcal{R}_{\mathrm{data}}}\right), \tag{5.19}$$

where $\mathbf{p}^{\mathrm{data}}_{\mathrm{corrected}}$ is the fully calibrated jet four-vector, $\mathbf{p}^{\mathrm{data}}_{\mathrm{uncorrected}}$ is the four-vector of the jet after the Monte Carlo calibration and the η-intercalibration and $\frac{\mathcal{R}_{\mathrm{MC}}}{\mathcal{R}_{\mathrm{data}}}$ is the inverse of the data-to-MC ratio of the responses after combination.

Each uncertainty component of the Z-jet, γ-jet and multi-jet methods is propagated separately to the combined data-to-MC ratio of the response to give the final components of the JES uncertainties from the three methods.

5. Finally, the JES is studied using measurements of the calorimeter response to single

hadrons as described in [1]. These measurements are used as a cross-check of the data-to-MC ratio of the response over the full p_{T} range. For $p_T^{\mathrm{jet}} > 1$ TeV in 2011 data and Monte Carlo, and for $p_T^{\mathrm{jet}} > 1.2$ TeV in 2012 data and Monte Carlo, the single hadron response is used to define the JES uncertainty in the high p_{T} region where there is an insufficient number of events to measure the JES uncertainty using the other in-situ methods.

Summary of JES Uncertainties For Small R Jets

The final JES uncertainties for small-R jets are made up of the following components:

- **η-intercalibration:** The JES uncertainty from the η-intercalibration.
- **Z-jet,** γ-jet **and multi-jet:** The JES uncertainty resulting from the combination of the Z-jet, γ-jet and multi-jet methods.
- **Single hadrons:** The JES uncertainty derived using single hadron measurements is used for $p_{\mathrm{T}} > 1$ TeV in 2011 data and Monte Carlo and for $p_{\mathrm{T}} > 1.2$ TeV in 2012 data and Monte Carlo.
- **Pile-up uncertainties:** Uncertainties to account for the dependence of the jet p_{T} on in- and out-of-time pile-up.
- **Flavour uncertainties:** Quark and gluon jets have different shower shapes resulting in differences in the JES. The flavour uncertainties account for these differences and can be tuned according to the composition of quark and gluon jets in an analysis.
- **b-jet uncertainties** The JES of b-jets is studied in Monte Carlo, and also in-situ, in order to derive additional systematic uncertainties that are applied to b-tagged jets [1]. Additionally, corrections are available to calibrate the JES of b-jets that decay semi-leptonically, resulting in a large proportion of the energy being carried by neutrinos and muons, which is not accounted for by the standard JES calibration and uncertainties.
- **Close-by jet uncertainties (2011 only):** In 2011 data, an additional uncertainty was derived to account for differences in the JES for jets that are not isolated (jets

with another jet within $\Delta R < 2.5\ R_{\text{eff}}$) [1]. In 2012 data further studies indicated that differences in the JES for close-by jets are well modelled by the Monte Carlo. Therefore, the close-by JES uncertainty is considered to be negligible for 2012 data and Monte Carlo.

In-Situ Uncertainty Estimation for Large Radius Jets

Prior to the studies shown in this thesis, the JES uncertainty of large-R jets (jets with $R = 1.0$ or $R = 1.2$) had been evaluated using the track jet double ratio method [46]. For the track jet double ratio method, track jets are matched to calorimeter jets and the JES uncertainty is evaluated by measuring the track jet response:

$$\mathcal{R}(\text{track}, p_T) = \frac{p_T^{\text{calo jet}}}{p_T^{\text{track jet}}}, \tag{5.20}$$

where $p_T^{\text{calo jet}}$ is the transverse momentum of the calorimeter jet at LCW+JES scale and $p_T^{\text{track jet}}$ is the transverse momentum of the track jet [46]. The track jet response is measured in data and Monte Carlo and the track jet double ratio is calculated:

$$\mathrm{R}_{\text{track jet}} = \frac{\mathcal{R}(\text{track}, p_T)^{\text{data}}}{\mathcal{R}(\text{track}, p_T)^{\text{MC}}}. \tag{5.21}$$

$\mathrm{R}_{\text{track jet}}$ is measured using two Monte Carlo generators: PYTHIA 8 and HERWIG++ v2.5.2. The envelope of $\mathrm{R}_{\text{track jet}}$ measured with PYTHIA and HERWIG++ is used for the uncertainty. In addition to the uncertainty derived directly from $\mathrm{R}_{\text{track jet}}$ two additional sources of uncertainty on the method are evaluated, due to the uncertainty on the tracking efficiency (∼3 %), track merging (∼2 %) and the modelling of the charged component of the jet. This method covers a wide p_{T} range, up to 1.2 TeV. It is also used for the evaluation of the systematic uncertainty due to the Jet Mass Scale (JMS) and other substructure variables, such as $\sqrt{d_{12}}$ [46]. However, the precision of the systematic uncertainties derived with this method is limited to ∼ 2-7 % because of uncertainty on the tracking efficiency, the track merging and the modelling of the charged component of the jet [46].

It is also possible to measure the JES of large-R jets using the in-situ methods described above for small-R jets, which do not suffer from the large uncertainties which limit the precision of the track jet double ratio method. These methods can be used to improve the precision of the measurement of the uncertainty of the JES for large-R jets. The derivation of the JES uncertainty using the direct balance method in γ-jet events will be described in detail in Chapter 7. This is the first in-situ method other than the track jet double ratio method that has been used to measure the JES of large-R jets at the ATLAS detector. Additionally, the γ-jet method provided the first studies of the JES uncertainty of large-R jets with $|\eta^{\mathrm{jet}}| > 1.2$. Recently these forward region studies have been complemented by an extension of the track-jet double ratio studies in the region $1.2 < |\eta| < 2.0$.

5.2.6 Jet Energy Resolution

As well as the scale of the jet energy, the resolution of the jet energy is of great importance for any performance studies or physics analyses that make use of jets. At ATLAS the jet transverse momentum resolution is measured, normalised to jet p_{T}. It is parametrised using the following function:

$$\frac{\sigma(p_T)}{p_T} = \frac{N}{p_T} \oplus \frac{S}{\sqrt{p_T}} \oplus C \tag{5.22}$$

where $\frac{\sigma(p_T)}{p_T}$ is the fractional Jet Energy Resolution (JER). The first term parametrises the contributions to the JER that are proportional to $1/p_T$, e.g. due to effects such as pile-up and electronic noise. It is of the order of a few GeV. The second term is the stochastic term, which parametrises contributions to the JER that are due to statistical fluctuations (e.g. there are inherent statistical fluctuations in the number of particles in the electromagnetic and hadronic showers of a jet). Since this term is due to statistical effects it is proportional to $1/\sqrt{p_T}$ and it is of the order of 1 $\sqrt{\mathrm{GeV}}$. The third term is the constant term which accounts for effects which are p_T independent, such as detector effects including non-uniformities in the detector and non-linearities in photomultipliers, ADCs etc. It is of the order of 0.05.

The JER for small-R jets is measured in-situ using di-jet events [97]. The JER in 2011 data was found to agree with the JER observed in Monte Carlo to within 10 % as can be seen in Figure 5.7. Two techniques to measure the JER are shown; the di-jet method which exploits the asymmetry in di-jet events ($(p_{T,1} - p_{T,2})/(p_{T,1} + p_{T,2})$ where $p_{T,1}$ and $p_{T,2}$ are the scalar p_{T} of the two leading jets in the event, randomly ordered), and the bisector method which makes use of the vector p_{T} sum of the two leading jets in di-jet events. Further details of the methods can be found in Ref. [97]. The data-to-MC differences of the JER are included in the JER uncertainties [97]. In 2012 the JER observed in Monte Carlo agrees with that observed in data to within 10 % for anti-k_t $R = 0.4$ and $R = 0.6$ jets at EM+JES and LCW+JES scale for $|\eta| < 1.2$. At higher η differences of up to 20 % have been observed.

The JER and jet mass resolution (JMR) for large-R jets are known to less precision than the JER for small-R jets. Monte Carlo studies of the JER and JMS [101, 102] have been performed for large-R jets with $|\eta| < 2.0$. In these studies the the amount of dead material in the detector simulation was varied, different models were used for the hadronic shower in the calorimeters, and different Monte Carlo generators were used, which have different models of hadronisation and the underlying event. Differences of up to 20 % were observed.

Additionally, the JMS for large-R jets has been studied in-situ using the W mass peak [46, 103]. This analysis found that the JMR in data and Monte Carlo were consistent. However, there were uncertainties of up to 10 % on these measurements. Therefore, a value of 20 %, taken from the Monte Carlo studies, is used as conservative estimate of the uncertainty of the JER and JMS for large-R jets.

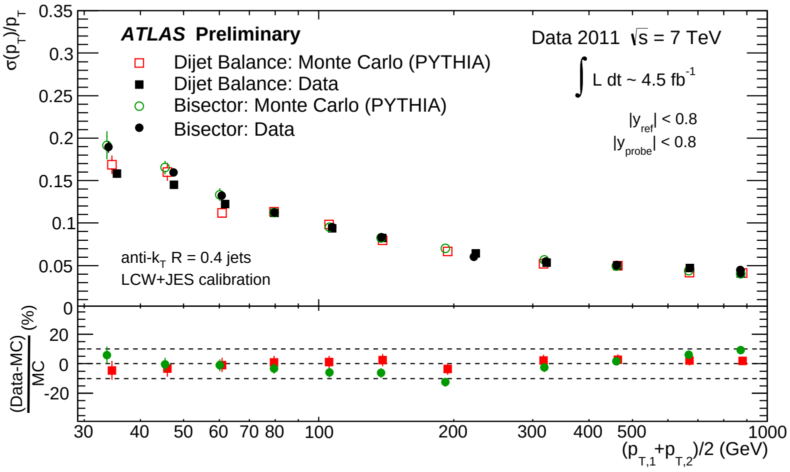

Figure 5.7: The JER of anti-k_t $R = 0.4$ jets at LCW+JES scale, measured with 4.7 fb^{-1} of data in 2011, compared to PYTHIA Monte Carlo. Two methods of measuring the JER using di-jet events are shown [104].

Chapter 6

The Jet Energy Scale of Small-R Jets Derived In-Situ Using γ-jet Events

This chapter describes the evaluation of the JES uncertainty and in-situ calibration for anti-k_t $R = 0.4$ and $R = 0.6$ jets using the γ-jet direct balance method at $\sqrt{s} = 7$ TeV. The 2011 data and Monte Carlo samples discussed in Sections 3.8 and 3.9 were used in the results presented here. The γ-jet direct balance method forms the basis for the evaluation of the JES uncertainties for large-R jets, which will be discussed in the following chapter.

The quantity of interest for the analysis is the direct balance response, which was introduced in Equation 5.16. In the context of the γ-jet method this equation is known as the photon response:

$$\mathcal{R}(\gamma,\ \mathrm{DB}) = \frac{p_T^{\mathrm{jet}}}{p_T^{\gamma}}, \tag{6.1}$$

where p_T^{jet} is the p_{T} of the reconstructed jet after the pile-up corrections and Monte Carlo calibrations[1] and p_T^{γ} is the p_{T} of the reconstructed photon, which is calibrated as described in Section 5.1.

A precise measurement of this quantity requires a clean sample of γ-jet events with a back-

---

[1] See Section 5.2 for details.

to-back topology. An important background is due to di-jet events, where one of the jets is misidentified as a photon. This background is accounted for using a systematic uncertainty, which requires knowledge of the fraction of photons in the γ-jet sample that contain a real photon. The estimation of the fraction of real photons in the γ-jet sample will be discussed below in Section 6.1 prior to discussion of the event selection for the γ-jet analysis. The measurement of the photon response and evaluation of the systematic uncertainties will then be presented.

Finally, these results will be put into context by comparing them to the photon response and systematic uncertainties obtained using the γ-jet MPF method [2] and a brief overview of how the γ-jet uncertainties are used for the final JES uncertainties will be given.

6.1 The Photon Purity

A jet can be incorrectly identified as a photon if the jet has a high electromagnetic content (for example, due to a jet containing a high p_{T} π^0 which decays to photons: $\pi^0 \rightarrow \gamma\gamma$). The number of events containing a correctly identified photon, as a fraction of the total number of events, is known as the *purity*, P:

$$P = \frac{\text{Number of reconstructed real photons}}{\text{Total number of reconstructed photons}} \tag{6.2}$$

The purity is estimated in data using a sideband technique, which is described in detail in Refs. [43, 82]. The method looks at the number of events falling into four regions, denoted by A, B, C and D. These regions are defined using the photon isolation, $E_{\mathrm{T}}^{\gamma\ \mathrm{Iso}}$, and the photon identification criteria that were described in Section 4.1. These two criteria help to reject jets which have been incorrectly identified as a photon. The regions A, B, C and D can be seen in Figure 6.1, where the regions are defined using $E_{\mathrm{T}}^{\gamma\ \mathrm{Iso}}$, the tight photon identification requirements and the loose+ photon identification requirements.

---

[2] The MPF method was introduced in Section 5.2.5.

The loose+ photon ID requirements used for the purity estimation differ from the standard loose photon ID requirements as described in Section 4.1. For estimation of the purity it is important that the shape of the $E_{\mathrm{T}}^{\gamma\ \mathrm{Iso}}$ distribution is the same for the tight photon requirements and for the loose photon requirements. This is the case for the loose+ photon ID requirements, but not for the standard loose photon requirements. Therefore, the loose+ requirements are used instead of the standard loose requirements [82].

For $E_{\mathrm{T}}^{\gamma\ \mathrm{Iso}}$, the loose requirement is $E_{\mathrm{T}}^{\gamma\ \mathrm{Iso}} > 8$ GeV. The tight requirement is chosen to be that of the signal region for the γ-jet analysis, which is $E_{\mathrm{T}}^{\gamma\ \mathrm{Iso}} < 3$ GeV.

In Figure 6.1, Region A corresponds to the signal region used for the γ-jet analysis and regions B, C and D are background dominated control regions. Regions C and D both require that the photons pass the loose+ photon requirements but fail the tight photon requirements, these photons will be known as *loose-not-tight* photons.

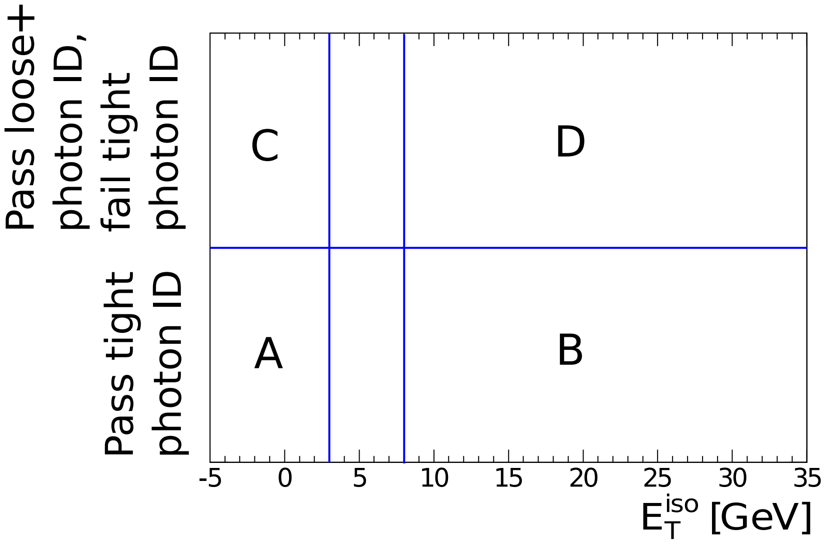

Figure 6.1: The diagram shows signal region (A) and control regions (B, C and D) which are used for the purity estimation. The figure is adapted from [82].

It is assumed that the number of signal events in the control regions is small and that the isolation distribution has the same shape for tight and loose+-not-tight photons. If it holds that the shape of the isolation distribution is the same for tight and loose+-not-tight photons then it is expected that $\mathrm{N}_{\mathrm{A\ bg}}/\mathrm{N}_{\mathrm{C\ bg}} = \mathrm{N}_{\mathrm{B\ bg}}/\mathrm{N}_{\mathrm{D\ bg}}$ where $\mathrm{N}_{\mathrm{A\ bg}}$ indicates the number of background events in region A, and similarly for B, C and D. Therefore, the number of background events in region A is:

$$\mathrm{N_{A\ bg}} = \mathrm{N_{C\ bg}} \frac{\mathrm{N_{B\ bg}}}{\mathrm{N_{D\ bg}}} \tag{6.3}$$

The purity can then be defined as:

$$P = 1 - \frac{\mathrm{N_{A\ bg}}}{\mathrm{N_A}} = 1 - \frac{\mathrm{N_{C\ bg}}}{\mathrm{N_A}} \frac{\mathrm{N_{B\ bg}}}{\mathrm{N_{D\ bg}}} \tag{6.4}$$

Where $\mathrm{N_A}$ is the total number of events in control region A (including both signal and background events). Monte Carlo prompt photon samples (samples containing only photons from the primary vertex) are used to correct the purity for the small number of signal events that fall into the control regions (which means that e.g. $\mathrm{N_C}$ is not equal to $\mathrm{N_{C,bg}}$). Further details of the method can be found in Refs. [43, 82, 105].

The purity found using this method is about 60% at $p_T^\gamma = 40$ GeV, rising to greater than 95% for $p_T^\gamma \gtrsim 200$ GeV, as be seen in Figure 6.2.

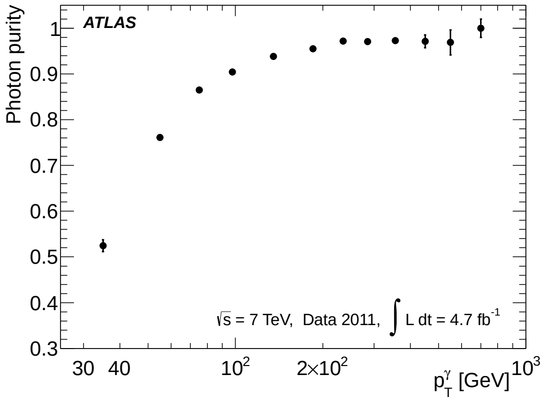

Figure 6.2: The purity of selected photons for the 2011 dataset [105].

6.2 γ-jet Event Selection for Small-R jets

This section describes the selection of γ-jet events for 2011 data at $\sqrt{s} = 7$ TeV. A summary of the selection can be found in Table 6.1.

Event Selection

Events are required to have a primary vertex with at least 5 tracks associated with it. The primary vertex is defined to be the vertex with the highest scalar $\sum p_T^{\text{track}}$. Events are rejected if there was a noise burst in the LAr calorimeter or a problem with data collection for the LAr calorimeter [106].

Photon Selection

The event must contain at least one reconstructed photon, which must pass the trigger requirements described in Section 3.6. The leading (highest p_{T}) photon is taken to be the photon from the hard scatter. This photon must pass the tight photon ID requirements and have an isolation energy of $E_{\mathrm{T}}^{\gamma\ \mathrm{Iso}} < 3$ GeV. The leading photon is required to have $p_{\mathrm{T}} > 25$ GeV, which is the lowest p_{T} available due to the trigger selection, and $|\eta| < 1.37$, so that it is contained within the EM barrel calorimeter.

As described in Section 4.1, photons can be either unconverted or converted, with converted photons falling into two categories: single track conversions (when there is one track matching the photon), or double track conversions (when there are two tracks matching the photon). The fraction of converted photons, compared to all photons after the event selection, for LCW+JES jets with $R = 0.6$ can be seen in Figure 6.3 a). $\sim 30 - 35$ % of photons are converted photons, with a significantly larger fraction of converted photons in data for $p_T^{\gamma} < 110$ GeV. Due to the presence of tracks, and the wider shower of a jet compared to a photon, it is more common for a jet with a high electromagnetic content to fake a converted photon compared to an unconverted photon. This background is suppressed by the tight photon ID requirements and isolation. But to further suppress this background a cut on $E_T^{\gamma\ \text{cluster}}/(\sum p_T^{\text{tracks}})$ was introduced for converted photons, where $E_T^{\gamma\ \text{cluster}}$ is the transverse energy of the converted photon cluster and $\sum p_T^{\text{tracks}}$ is the scalar sum of the p_{T} of the tracks associated with the converted photon cluster In order to define the values for this cut the distribution of $E_T^{\gamma\ \text{cluster}}/(\sum p_T^{\text{tracks}})$ was studied.

As can be seen in Figure 6.4 the $E_{\mathrm{T}}^{\gamma\ \mathrm{cluster}}/(\sum p_{\mathrm{T}}^{\mathrm{tracks}})$ distribution is centred around one, as expected for converted photons, with a narrower distribution for double track conversions compared to single track conversions. A narrower distribution for double track conversions is expected, since for single track conversions only one of the two tracks from the conversion has been found. At low p_T^{γ}, where the photon purity is low, the shapes of the tails of the distributions differ between data and Monte Carlo. At high p_T^{γ}, where the photon purity is high, the $E_{\mathrm{T}}^{\gamma\ \mathrm{cluster}}/(\sum p_{\mathrm{T}}^{\mathrm{tracks}})$ distributions agree within statistical uncertainties, when comparing data to Monte Carlo.

Requirements for $E_{\mathrm{T}}^{\gamma\ \mathrm{cluster}}/(\sum p_{\mathrm{T}}^{\mathrm{tracks}})$ are chosen to retain events in the central region of the $E_{\mathrm{T}}^{\gamma\ \mathrm{cluster}}/(\sum p_{\mathrm{T}}^{\mathrm{tracks}})$ distribution, where the data and Monte Carlo are in good agreement. They are chosen differently for single track conversions ($0 < E_{\mathrm{T}}^{\gamma\ \mathrm{cluster}}/(\sum p_{\mathrm{T}}^{\mathrm{tracks}}) < 2$) and double track conversions ($0.5 < E_{\mathrm{T}}^{\gamma\ \mathrm{cluster}}/(\sum p_{\mathrm{T}}^{\mathrm{tracks}}) < 1.5$) due to the different shapes of the distributions.

In Figure 6.5 it can be seen that the purity of the photon sample is increased by $\sim$ 4 - 5 % for $p_T^{\gamma} < 260$ GeV. For $p_T^{\gamma} > 260$ GeV, the cuts on $E_{\mathrm{T}}^{\gamma\ \mathrm{cluster}}/(\sum p_{\mathrm{T}}^{\mathrm{tracks}})$ have little impact on the photon purity. Also, as was illustrated in Figure 6.4, there is a good agreement between the $E_{\mathrm{T}}^{\gamma\ \mathrm{cluster}}/(\sum p_{\mathrm{T}}^{\mathrm{tracks}})$ distributions in data and Monte Carlo above 260 GeV. Therefore, the cuts on $E_{\mathrm{T}}^{\gamma\ \mathrm{cluster}}/(\sum p_{\mathrm{T}}^{\mathrm{tracks}})$ are only applied for $p_T^{\gamma} < 260$ GeV in order to retain events for $p_T^{\gamma} > 260$ GeV, even though this results in a discontinuity in the fraction of converted photons (which can be seen in Figure 6.3 b)).

Jet Selection

The event is also required to have at least one anti-k_t $R = 0.4$ or $R = 0.6$ jet, which must pass cuts to reject fake jets from noise bursts in the calorimeter and from non-collision backgrounds. The latest EM+JES or LCW+JES calibration is applied to all jets in the event. The η-intercalibration correction factors described in Section 5.2.5 are also applied, to correct for any residual differences in the response of jets in data and Monte Carlo at different η.

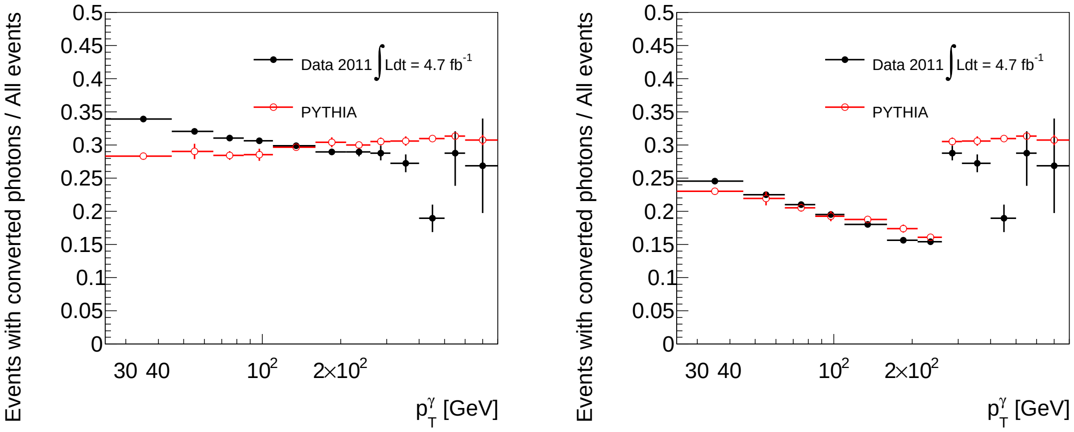

(a) (b)

Figure 6.3: The fraction of converted photons in the final sample in data and Monte Carlo (a) without the cuts on $E_{\mathrm{T}}^{\gamma\ \mathrm{cluster}}/(\sum p_{\mathrm{T}}^{\mathrm{tracks}})$ and (b) with the cuts on $E_{\mathrm{T}}^{\gamma\ \mathrm{cluster}}/(\sum p_{\mathrm{T}}^{\mathrm{tracks}})$.

During data processing, only jets with $p_T > 10$ GeV are retained. The jets are re-calibrated with the latest version of the calibration during the analysis. Therefore, events that may have migrated from below 10 GeV to above 10 GeV due to the calibration are not present in the sample of events available. To avoid any potential bias due to the re-calibration, the jets are first re-calibrated and then it is required that they have $p_T^{jet} >$ 12 GeV.

The leading (highest p_{T}) jet is taken to be that from the hard scatter and must have $|\eta| < 1.2$. Within this η region the calibration factors from the η-intercalibration method described in Section 5.2.5 are less than 1.5 % and the data-to-MC agreement of the response is seen to be stable [107].

If the leading or subleading jets fail jet cleaning cuts designed to reject fake jets from noise bursts in the calorimeter and from non-collision backgrounds [1], the event is rejected. Details of the jet cleaning procedure can be found in Ref. [1]. During 2011 data taking, the read-out in the EM calorimeter in the regions $0.0 < \eta < 1.4$ and $-0.8 < \phi < -0.6$ was not working between 30th April and 13th July 2011. For this time period the event is rejected if either the leading or subleading jets are within $\Delta R < 0.1$ of the affected regions of the calorimeter.

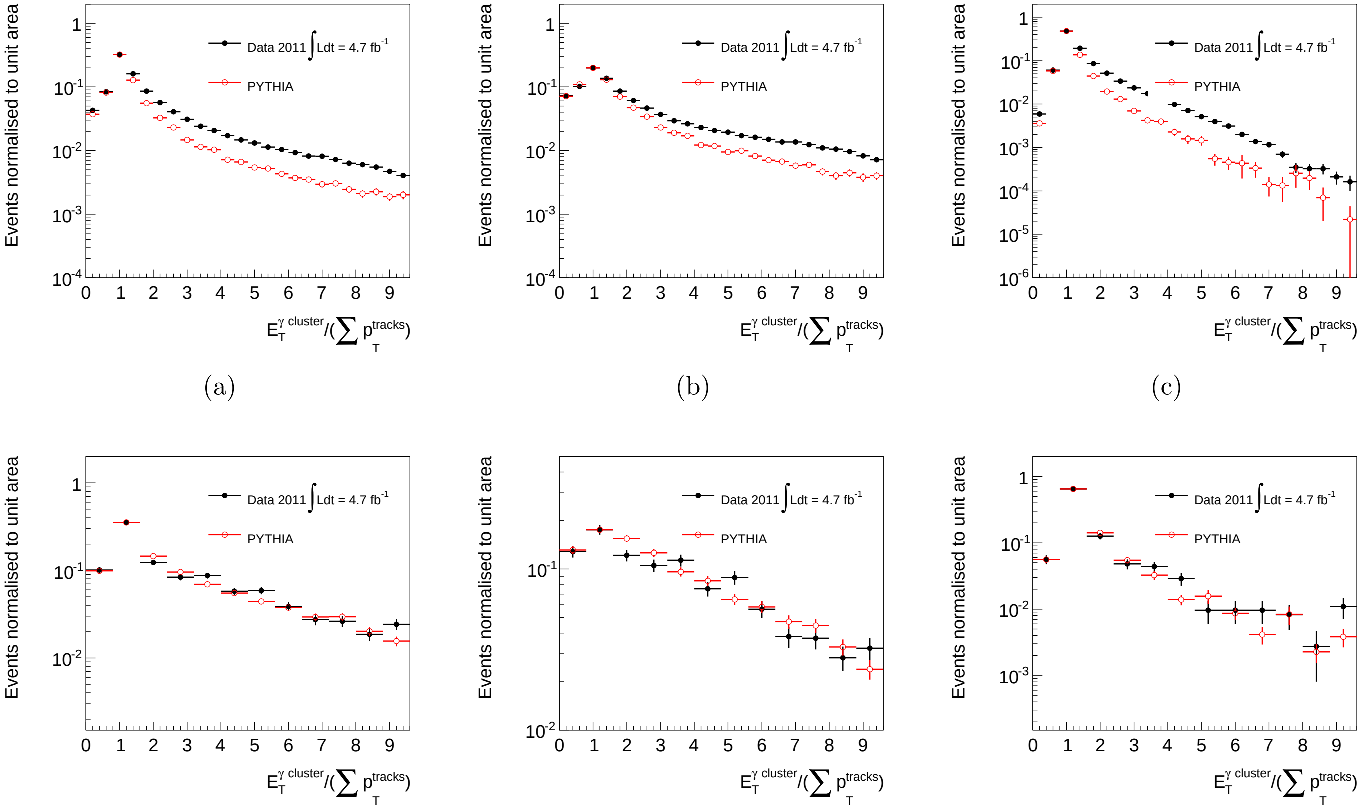

(a) (b) (c)

(d) (e) (f)

Figure 6.4: The $E_{\mathrm{T}}^{\gamma\ \mathrm{cluster}}/(\sum p_{\mathrm{T}}^{\mathrm{tracks}})$ distribution for photons with $25 < p_T^{\gamma} < 45$ GeV for (a) all converted photons, (b) converted photons with one matching track and (c) converted photons with two matching tracks and for photons with $260 < p_T^{\gamma} < 310$ GeV for (d) all converted photons, (e) converted photons with one matching track and (f) converted photons with two matching tracks.

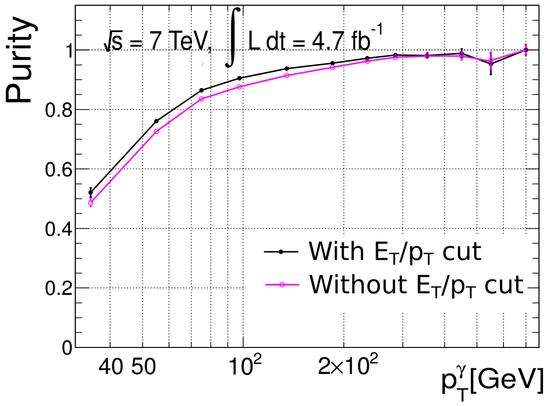

Figure 6.5: The purity of selected photons [2] for the nominal selection which includes the cut on $E_{\mathrm{T}}^{\gamma\ \mathrm{cluster}}/(\sum p_{\mathrm{T}}^{\mathrm{tracks}})$ of converted photons in black and for a selection without the cut on $E_{\mathrm{T}}^{\gamma\ \mathrm{cluster}}/(\sum p_{\mathrm{T}}^{\mathrm{tracks}})$ in pink.

Selection of a Back-to-Back γ-jet Topology

Events with additional hard radiation in the form of extra jets in the event would spoil the balance between the jet and the photon and also introduce additional Monte Carlo modelling uncertainties. Two cuts are applied to suppress events with hard radiation:

1. The leading photon and leading jet are required to be back-to-back: $\Delta\phi(\gamma - \mathrm{jet}) > 2.9$;

2. The p_{T} of the subleading jet in the event must be less than 20 % of the p_{T} of the leading photon: $\frac{p_T^{\mathrm{subleading\ jet}}}{p_T^{\gamma}} < 0.2$. To reduce the effect of pile-up on this cut the subleading jet must either have JVF > 0.75 or be outside of the tracking acceptance ($|\eta| > 2.5$), where it is not possible to calculate the JVF [3].

The photon p_{T}, photon η, jet p_{T} and jet η distributions following the full event selection can be seen in Figure 6.6 for anti-k_t $R = 0.4$ LCW+JES jets in data and Monte Carlo. In these figures the trigger prescales have been corrected for and the Monte Carlo distributions have been normalised to the data. The steeply falling spectrum of the photon and jet p_{T} can be seen as the p_{T} increases. The photon response is binned in p_T^{γ} using the following bins: `25, 45, 65, 85, 110, 160, 210, 260, 310, 400, 500,`

---

[3] JVF was introduced in Section 5.2.2

Variable	Threshold
$N^{\text{vertex}}_{\text{tracks}}$	> 4
p_T^{γ}	> 25 GeV
$\lvert\eta^{\gamma}\rvert$	< 1.37
$p_{\text{T}}^{\text{jet}}$	> 12 GeV
$\lvert\eta^{\text{jet}}\rvert$	< 1.2
$E_{\text{T}}^{\gamma\ \text{Iso}}$	< 3.0 GeV
$E_{\text{T}}^{\gamma\ \text{cluster}}/(\sum p_{\text{T}}^{\text{tracks}})$ for single track converted photons	$0 < E_{\text{T}}^{\gamma\ \text{cluster}}/(\sum p_{\text{T}}^{\text{tracks}}) < 2$
$E_{\text{T}}^{\gamma\ \text{cluster}}/(\sum p_{\text{T}}^{\text{tracks}})$ for double track converted photons	$0.5 < E_{\text{T}}^{\gamma\ \text{cluster}}/(\sum p_{\text{T}}^{\text{tracks}}) < 1.5$
$\Delta\phi(\gamma - \text{jet})$	> 2.9 rad
$p_T^{\text{subleading jet}}/p_T^{\gamma}$	< 0.2
Jet cleaning	The event is rejected if either the leading or subleading jet do not meet jet cleaning requirements

Table 6.1: Summary of the event selection criteria used for the direct balance γ-jet analysis in 2011.

`600, 800 GeV.` The first four bin boundaries correspond to the thresholds required in the analysis for the photon triggers, which were described in Section 3.6.

6.3 The Photon Response for the Direct Balance Method

The mean photon response in each p_T^{γ} bin is found using either a Gaussian or a Poisson fit, depending on the value of p_T^{γ}. In the first p_T^{γ} bin, 25 GeV $< p_T^{\gamma} <$ 45 GeV, the photon response distribution is non-Gaussian as can be seen in Figure 6.7 (a). This is due to the fact that only jets with a $p_{\text{T}} > 12$ GeV are considered in the analysis. Therefore, the low p_{T} jets are not present and the low response events in the first p_T^{γ} bin are not available. In order to find the peak of this distribution this bin is fit with a Poisson distribution extended to non-integer values [1]. For all p_T^{γ} bins with $p_T^{\gamma} > 45$ GeV, a Gaussian fit is used to find the peak of the distribution, an example of which can be seen in Figure 6.7 (b).

The photon response derived from these fits as a function of p_T^{γ} can be seen in Figure 6.8 as measured in data and Monte Carlo for anti-k_t $R = 0.4$ and $R = 0.6$ jets at EM+JES

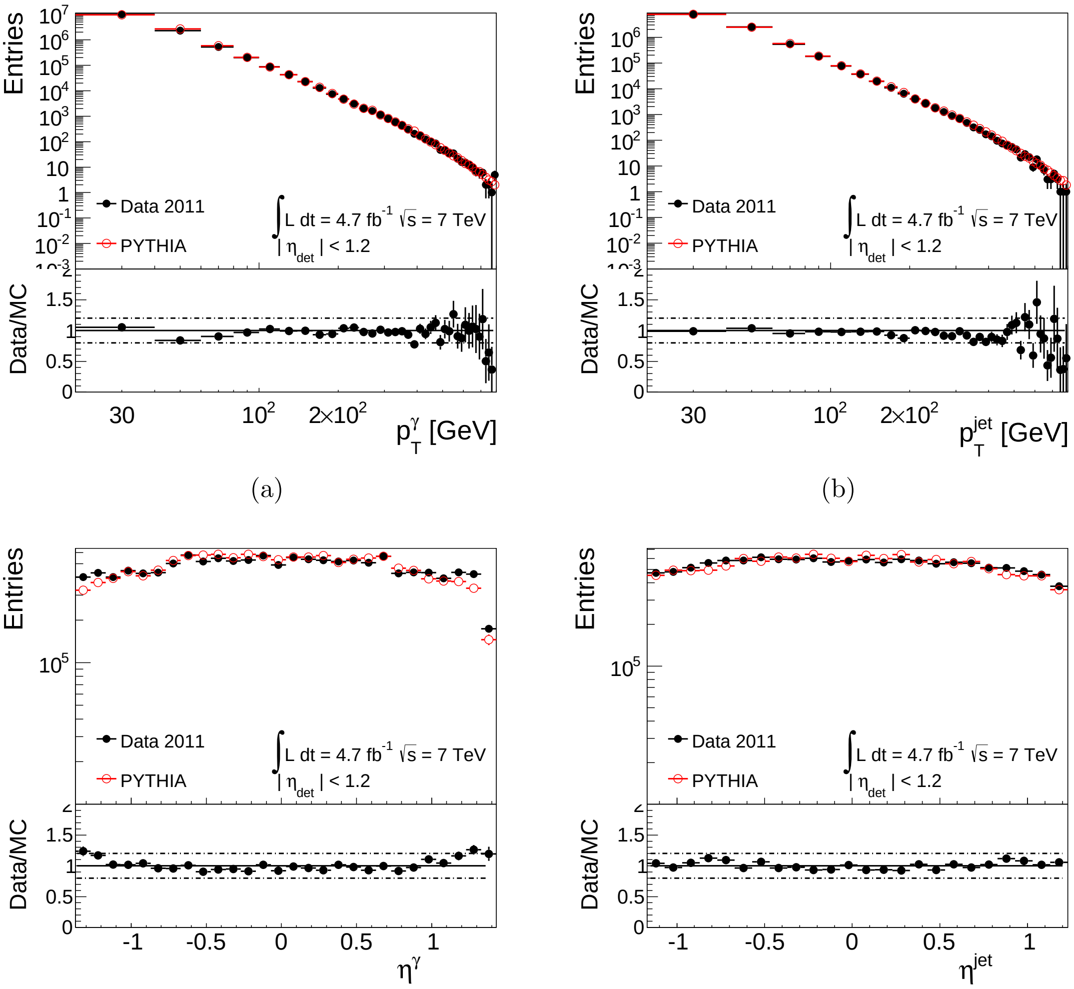

(a) (b)

(c) (d)

Figure 6.6: (a) The photon p_T distribution, (b) the jet p_T distribution, (c) the photon η and (d) the jet η after the event selection for anti-k_t $R = 0.4$ LCW+JES jets in data and Monte Carlo. The distributions are corrected for the trigger prescales and the Monte Carlo is normalised to the data.

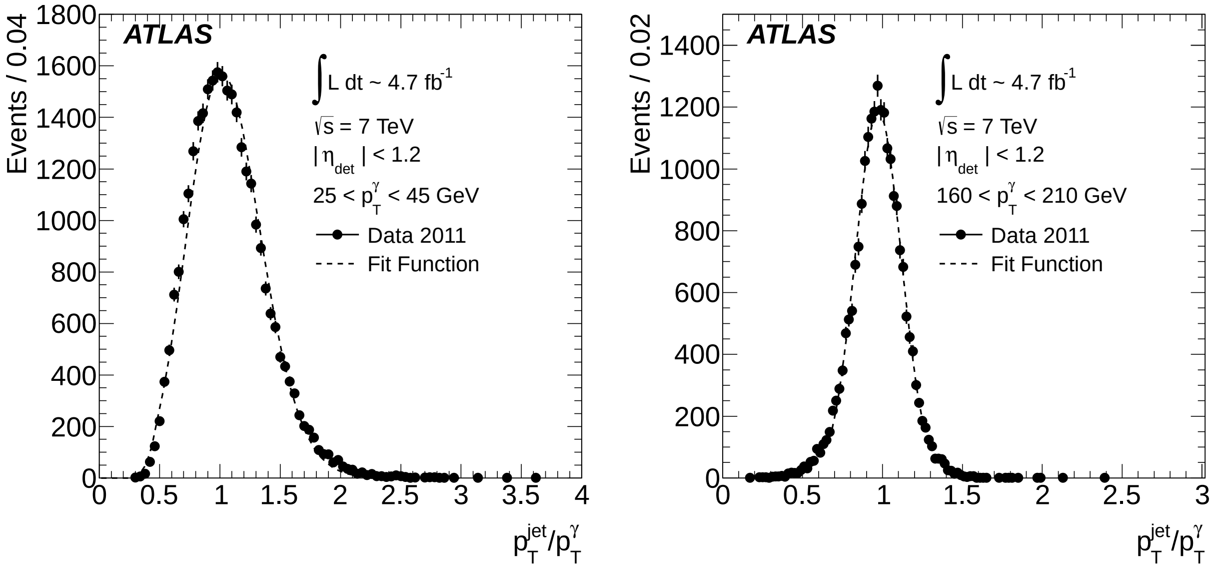

(a) (b)

Figure 6.7: Photon response distributions in data for anti-k_t EM+JES scale jets for (a) $25 < p_T^\gamma < 45$ GeV fit with a Poisson distribution and (b) $160 < p_T^\gamma < 210$ GeV fit with a Gaussian distribution [1].

and LCW+JES scale. It can be seen that the general trend is for the photon response for anti-k_t $R = 0.4$ jets to increase with increasing p_T^γ, whereas for anti-k_t $R = 0.6$ jets the photon response decreases with increasing p_T^γ. The shapes and absolute values of the photon response distributions are affected not only by the calibration of the jet but also by several other effects. One of these is the fraction of the hadronic shower that is contained by the jet (this fraction will be smaller for $R = 0.4$ jets than $R = 0.6$ jets due to their smaller size). Another is the amount of underlying event that is captured by the jet (less underlying event will be captured by the smaller $R = 0.4$ jets compared to the $R = 0.6$ jets). The accuracy with which these effects are modelled by the Monte Carlo will be accounted for by a systematic uncertainty, which will be discussed below in Section 6.4.7.

Additionally, for $p_T^\gamma < 260$ (65) GeV the photon purity in data is < 95 (80) % due to di-jet events where one jet has been incorrectly identified as a photon. The Monte Carlo contains only γ-jet events and it is therefore unaffected by this background. The inclusion of background events in data results in an increase in the photon response since a jet which has been reconstructed as a photon will contain only the central core of the hadronic shower of the jet. The background will also be accounted for by a systematic uncertainty, which is described below in Section 6.4.4.

For the in-situ calibration, the aim is to accurately measure the residual difference in the JES between data and Monte Carlo so that a correction can be applied to account for this difference. Therefore, the quantity of most importance is the data-to-MC ratio of the photon response, which can be seen in the bottom insets of Figure 6.8. It can be seen that the photon response is systematically lower in data than in Monte Carlo by up to $\sim 2\%$ above 100 GeV for all jet collections. The rise of the data-to-MC ratio of the photon response for $p_T^\gamma < 65$ GeV is attributed to the di-jet background in the data, which results in a higher photon response in data, thereby causing an increase in the data-to-MC ratio of the photon response.

6.3.1 The Effect of the Cut on $E_{\mathrm{T}}^{\gamma\ \mathrm{cluster}}/(\sum p_{\mathrm{T}}^{\mathrm{tracks}})$ for Converted Photons

As discussed previously, the photon purity is increased by placing requirements on the value of $E_{\mathrm{T}}^{\gamma\ \mathrm{cluster}}/(\sum p_{\mathrm{T}}^{\mathrm{tracks}})$ for converted photons. The effect of these requirements on the photon response can be seen in Figure 6.9. In Figure 6.9 (a) it can be seen that the response of converted photons in data is significantly lower for $p_T^\gamma < 65$ GeV with the application of the cut, as expected from a reduction in background events. This results in a slightly smaller data-to-MC ratio of the photon response as can be seen in Figure 6.9 (b).

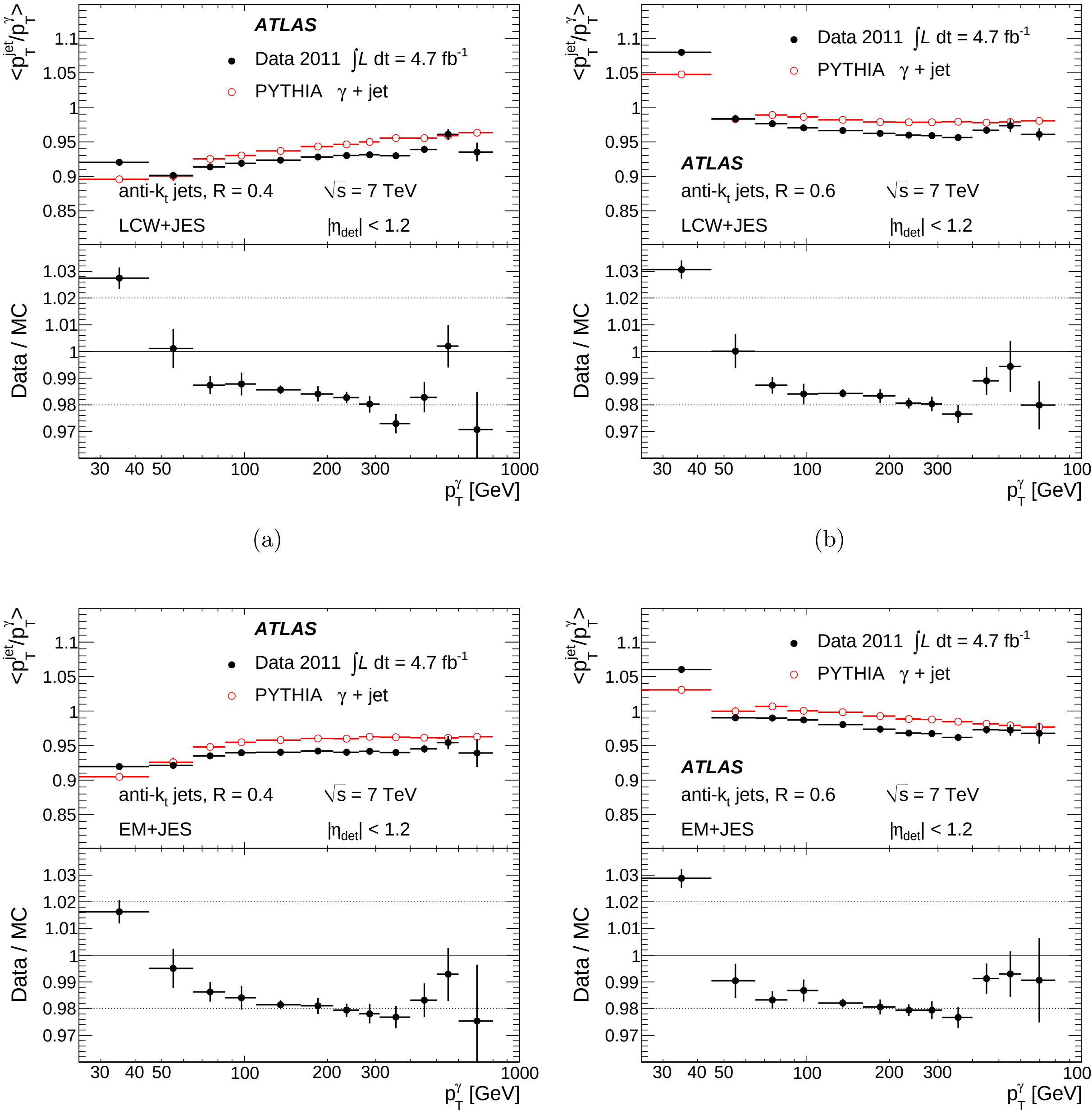

(a) (b)

(c) (d)

Figure 6.8: The average photon response for anti-k_t jets for (a) LC+JES scale jets with $R = 0.4$, (b) LC+JES scale jets with $R = 0.6$, (c) EM+JES scale jets with $R = 0.4$, and (d) EM+JES scale jets with $R = 0.6$. Only statistical uncertainties are shown [1].

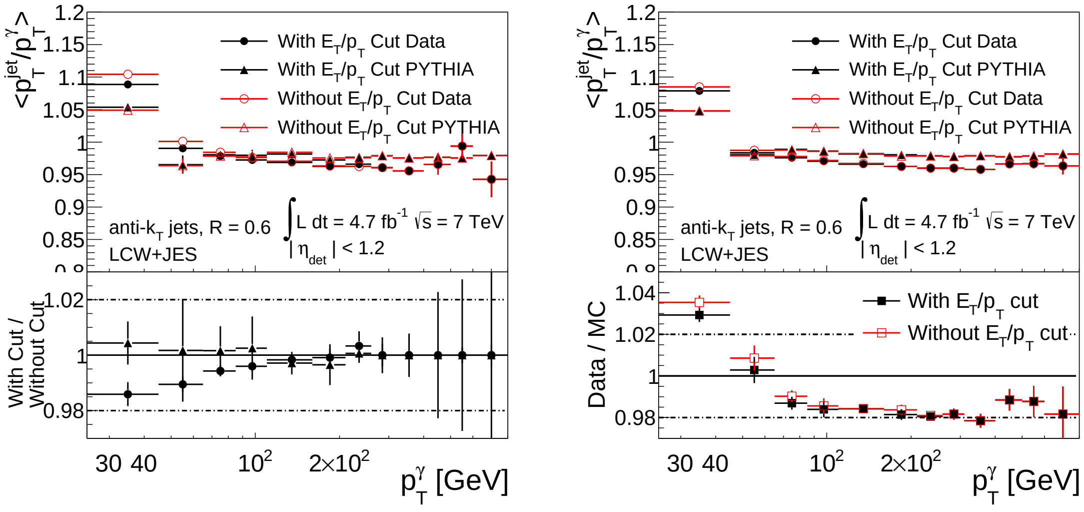

(a) (b)

Figure 6.9: The average photon response for anti-k_t jets for LCW+JES scale jets with $R = 0.6$, with and with out the $E_{\mathrm{T}}^{\gamma\ \mathrm{cluster}}/(\sum p_{\mathrm{T}}^{\mathrm{tracks}})$ cut on converted photons. (a) is for converted photons (including both single and double track conversions), where the bottom inset shows the ratio of the photon response with, compared to without, the $E_{\mathrm{T}}^{\gamma\ \mathrm{cluster}}/(\sum p_{\mathrm{T}}^{\mathrm{tracks}})$ requirement for data (circles) and Monte Carlo (triangles). (b) is for all photons, where the bottom inset shows the data-to-MC ratio of the photon response with (black squares) and without (red squares) the $E_{\mathrm{T}}^{\gamma\ \mathrm{cluster}}/(\sum p_{\mathrm{T}}^{\mathrm{tracks}})$ requirement.

6.4 Systematic Uncertainties of the γ-jet Direct Balance Method

The JES uncertainty of the jets under consideration is evaluated by considering the systematic and statistical uncertainties on the data-to-MC ratio of the photon response. Several sources of uncertainty are considered, as discussed below.

6.4.1 Effect of Pile-up on the Photon Response

The average offset pile-up correction is applied to the transverse momentum of the jet to subtract energy due to pile-up, as described in Section 5.2.2. Systematic uncertainties for this correction are available for use by physics analyses [1] to account for differences in the jet energy due to in-time (parametrised by NPV) pile-up and out-of-time pile-up (parametrised by μ). Figures 6.10 (a), (b), (c) and (d) show the effect on the photon response of propagating these uncertainties through the γ-jet analysis.

Figures 6.10 (e) and (f) show the variations in the photon response for events with a low, or high, μ and NPV (defined as $3.5 < \mu < 5.5$, NPV < 3 and $\mu > 7$, NPV > 5 respectively). The black points in the bottom inset of these figures are calculated as follows:

$$\frac{\mathcal{R}(\gamma, \mathrm{DB})_{\text{data, low PU}}/\mathcal{R}(\gamma, \mathrm{DB})_{\text{MC, low PU}}}{\mathcal{R}(\gamma, \mathrm{DB})_{\text{data, high PU}}/\mathcal{R}(\gamma, \mathrm{DB})_{\text{MC, high PU}}}, \tag{6.5}$$

where $\mathcal{R}(\gamma, \mathrm{DB})_{\text{data, low PU}}$ and $\mathcal{R}(\gamma, \mathrm{DB})_{\text{MC, low PU}}$ are the photon responses for the low pile-up regimes ($3.5 < \mu < 5.5$ in (e) and NPV < 3 in (f)) in data and Monte Carlo respectively and $\mathcal{R}(\gamma, \mathrm{DB})_{\text{high, low PU}}$ and $\mathcal{R}(\gamma, \mathrm{DB})_{\text{MC, high PU}}$ are the photon responses for the high pile-up regimes ($\mu > 7$ for (e) and NPV > 5 for (f)) in data and Monte Carlo respectively. The red band shown in the bottom insets of Figures 6.10 (e) and (f) is the uncertainty on the data-to-MC ratio of the photon response due to the shifts which were shown in Figures 6.10 (a), (b), (c) and (d).

It can be seen that, within the statistical uncertainty, the deviations of the data-to-MC ratio of the photon response for low and high μ and NPV are covered by the pile-up uncertainty. Therefore, in order to avoid double counting uncertainties in the final JES uncertainties, no systematic uncertainty for pile-up is considered for the γ-jet direct balance method.

6.4.2 Radiation Suppression

The cut on $\Delta\phi(\gamma - \text{jet})$, and the cut on the sub-leading jet in the event, are designed to suppress events with additional hard radiation. These cuts are varied in order to evaluate the systematic uncertainty due to additional radiation. The $\Delta\phi(\gamma - \text{jet})$ cut is varied to $\Delta\phi(\gamma - \text{jet}) > 2.7$ and $\Delta\phi(\gamma - \text{jet}) > 3.1$. The effect on the data-to-MC ratio of the photon response is found to be less than 0.5 % over the full p_T^{γ} range.

The cut on $\frac{p_T^{\text{subleading jet}}}{p_T^{\gamma}}$ is loosened and tightened according to the following definitions:

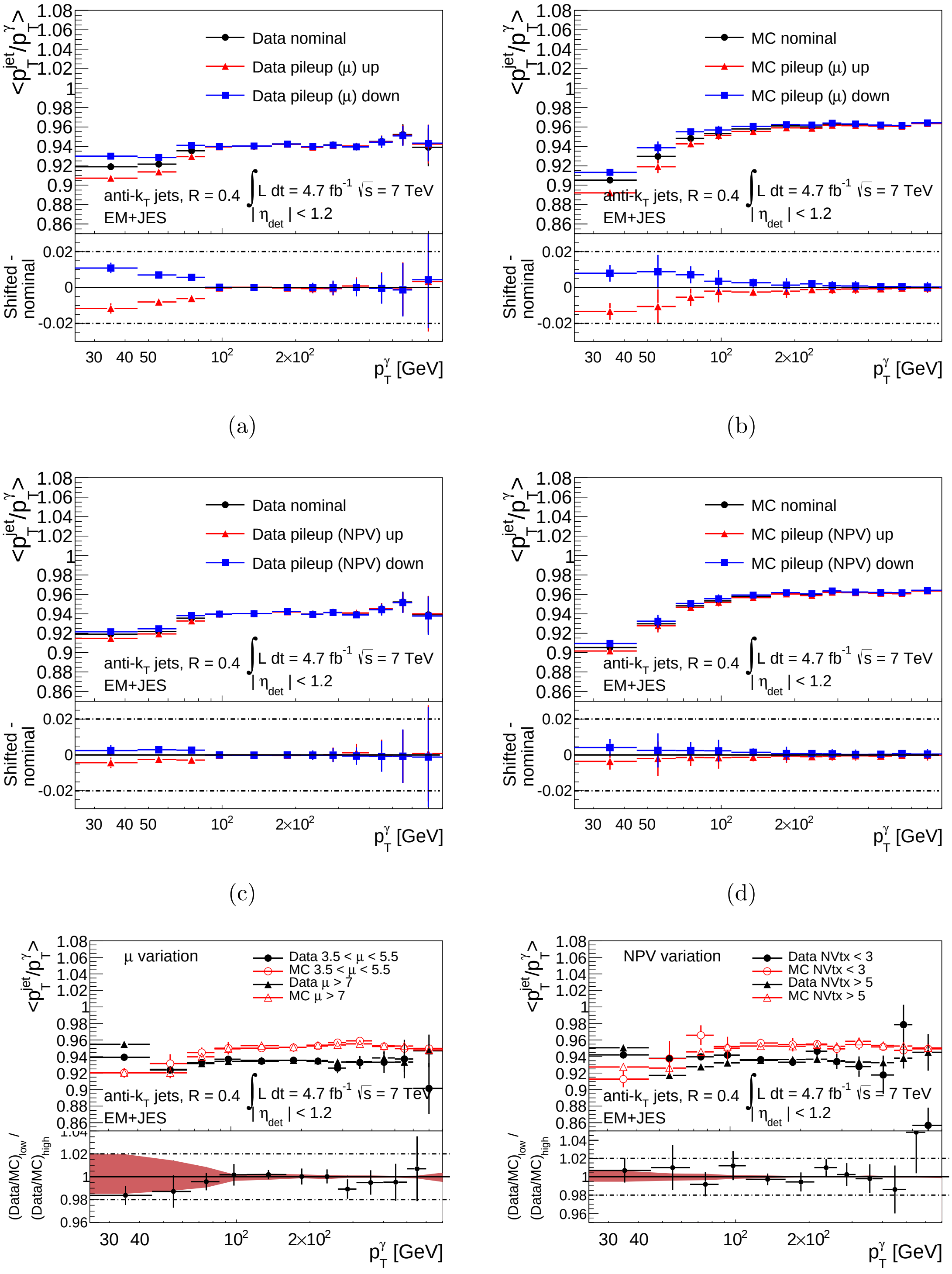

(a) (b)

(c) (d)

(e) (f)

Figure 6.10: The average photon response with the pile-up uncertainty shifted up and down due to the uncertainty on (a) μ in data, (b) μ in Monte Carlo, (c) NPV in data and (d) NPV in Monte Carlo. e) and f) show the variation of the photon response and the data-to-MC ratio of the photon response for high and low values of (e) μ and (f) NPV. The red band corresponds to the uncertainty on the pile-up when the shifts seen in (a), (b), (c) and (d) are propagated to the data-to-MC ratio of the photon response.

- **Loose:** $p_T^{\text{subleading jet}} \leq \max(12\text{ GeV},\ 0.2 \cdot \mathrm{p}_\mathrm{T}^{\gamma}) + 0.1 \cdot \mathrm{p}_\mathrm{T}^{\gamma}$
- **Tight:** $p_T^{\text{subleading jet}} \leq \max(10\text{ GeV},\ 0.1 \cdot \mathrm{p}_\mathrm{T}^{\gamma})$

In this way both the cut on $\frac{p_T^{\text{subleading jet}}}{p_T^{\gamma}}$ and the p_T threshold above which a sub-leading jet is accepted are varied to account for the effect of both of these aspects of the cut. The effect of these variations on the data-to-MC ratio of the photon response is found to be of the order of 0.5%.

6.4.3 Monte Carlo Generator

Uncertainty in the measurement of the photon response in Monte Carlo may be introduced due to the modelling of the parton shower, the jet fragmentation and multiple parton interactions in the event. In order to assess the effect of this uncertainty, the nominal Monte Carlo sample, generated and showered using PYTHIA v6.425 [29] is compared to HERWIG v6.510 [30], which uses a different parton shower and fragmentation model. More details of the Monte Carlo samples can be found in Section 3.9. The difference between the photon response in PYTHIA and HERWIG is taken as the systematic uncertainty and is found to be up to ∼ 1 %, as can be seen in Figure 6.11.

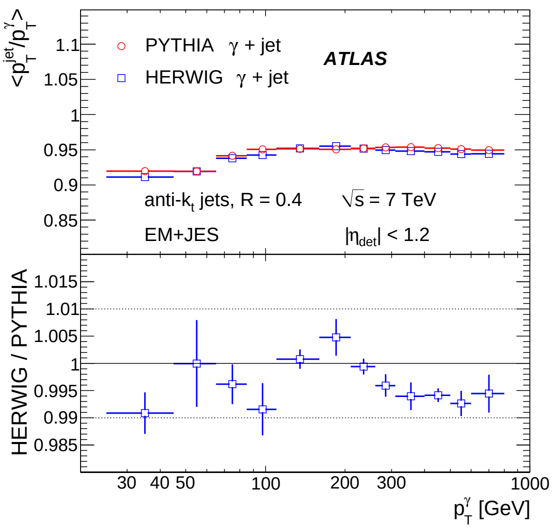

Figure 6.11: The photon response for anti-k_t $R = 0.4$ jets at EM+JES scale measured with PYTHIA and HERWIG [1].

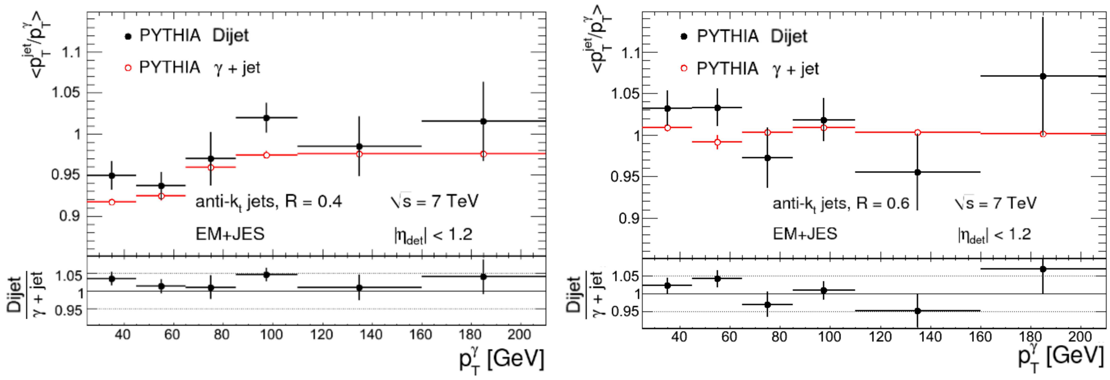

(a) (b)

Figure 6.12: The photon response of the nominal Monte Carlo sample which contains only signal, compared to the response of a sample of dijet events containing jets with narrow shower profiles which are more likely to fake a photon for a) anti-k_t $R = 0.4$ EM+JES jets and b) anti-k_t $R = 0.6$ EM+JES jets [2].

6.4.4 Background from Jet Events

The uncertainty due to the di-jet background is estimated to first order as:

$$(1 - P) \times \frac{(\mathcal{R}(\mathrm{di-jet}) - \mathcal{R}(\gamma\text{-jet}))}{\mathcal{R}(\gamma\text{-jet})}, \tag{6.6}$$

where P is the purity of the γ-jet sample, and $\mathcal{R}(\gamma\text{-jet})$ and $\mathcal{R}(\text{dijet})$ are the responses for the γ-jet signal and for the di-jet background events respectively.

$\mathcal{R}(\gamma\text{-jet})$ is taken to be the nominal photon response measured in the γ-jet Monte Carlo sample. The photon response of background events ($\mathcal{R}(\mathrm{di-jet})$) was estimated using a Monte Carlo di-jet sample enriched in jets with a narrow shower profile. Figure 6.12 shows the nominal photon response in the γ-jet Monte Carlo sample and the photon response in the di-jet Monte Carlo sample. There is a significant lack of statistics in the di-jet Monte Carlo sample and so the response could only be evaluated up to 210 GeV. However, it can be seen that, within statistical uncertainties, the difference between the response in the γ-jet Monte Carlo and the response in the di-jet Monte Carlo sample is ~5 % or less. Therefore $(\mathcal{R}(\text{dijet}) - \mathcal{R}(\gamma\text{-jet}))/\mathcal{R}(\gamma\text{-jet})$ was taken to be 5 % over the full p_{T} range.

6.4.5 Jet Energy Resolution

The effect of the Jet Energy Resolution is evaluated by comparing the nominal photon response in Monte Carlo to the photon response in Monte Carlo where the p_{T} of the jets has been smeared by a Gaussian centred at one, with a width of $\sigma = \sqrt{(\sigma_{\mathrm{data}} + \Delta\sigma_{\mathrm{data}})^2 - \sigma^2_{\mathrm{data}}}$ where σ_{data} is the Jet Energy Resolution in data and $\Delta\sigma^2_{\mathrm{data}}$ is its uncertainty.

The systematic uncertainty due to the JER is taken as the difference between the photon response in the nominal and smeared samples. As can be seen in Figure 6.13 variations of up to 1 % are seen below 110 GeV, falling to < 0.5 % at higher p_T^{γ}.

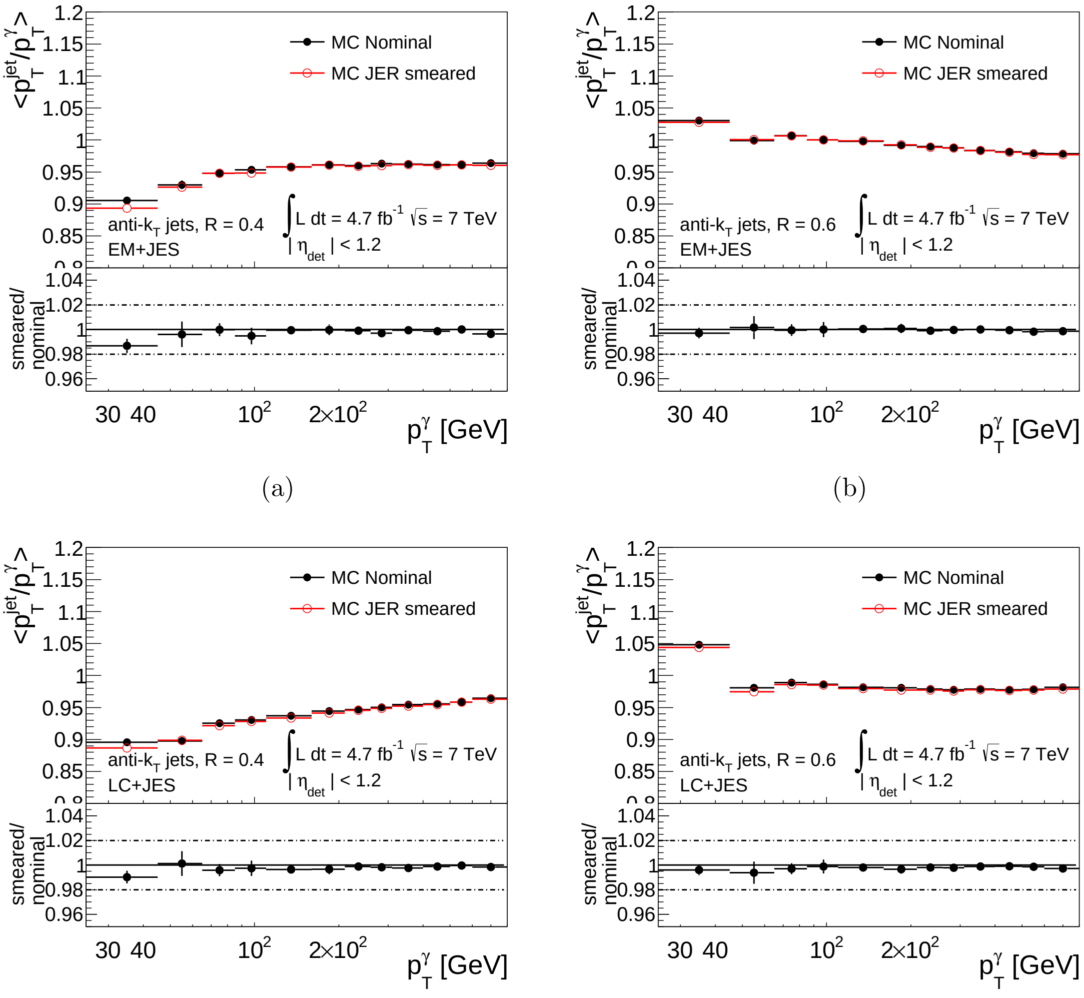

(a) (b)

(c) (d)

Figure 6.13: The photon response for the nominal Monte Carlo sample and the Monte Carlo with the smeared Jet Energy Resolution.

6.4.6 Photon Energy Scale

The calibration applied to photons is the same as that applied to electrons, as described in Section 5.1, with an increased uncertainty for the photon energy scale. The uncertainty consists of components due to the $Z \to ee$ calibration, energy losses due to interactions before the electrons or photons reach the calorimeter, and energy loss due to energy not captured in the photon clustering algorithm. The energy calibration is parametrised as shown previously in Equation 5.1.

The nominal photon energy is $p_T^{\gamma} = p_T^{\gamma,\text{uncorrected}}/(1-\alpha)$, as described in Section 5.1. To assess the impact of the photon energy scale uncertainty on the photon response, the shifted photon energy is taken to be $p_T^{\gamma} = p_T^{\gamma,\text{uncorrected}}/(1-(\alpha+\Delta\alpha))$ where $\Delta\alpha$ is the uncertainty on α. The photon response is then rederived using the shifted photon energy. The systematic uncertainty is taken as the difference between the shifted sample in data and the nominal sample in data. It is found to be $\sim +0.8\%$ and -0.5% as can be seen in Figure 6.14.

6.4.7 Out-of-cone Radiation and the Underlying Event

It is not expected that $p_T^{\gamma} \equiv p_T^{jet}$ even if it were possible to select events with a perfect 2 to 2 scatter. This is due to two effects:

1. The jet will contain more energy due to the underlying event in comparison to the photon, resulting in an increase in the photon response. The contribution of the underlying event to the reconstructed photon p_{T} is neglected since the photon has a small size [4] and therefore captures much less of the underlying event than a jet.
2. The jet does not contain all particles from the hadronic shower that balance the photon, since some will fall outside of the jet cone. This results in a decrease in the photon response.

---

[4] Photons with $|\eta| < 1.37$ have a size of 3×5 (3×7) for unconverted (converted) photons, in units of 0.025×0.025 in $|\eta \times \phi|$ space, as described in Section 4.1.

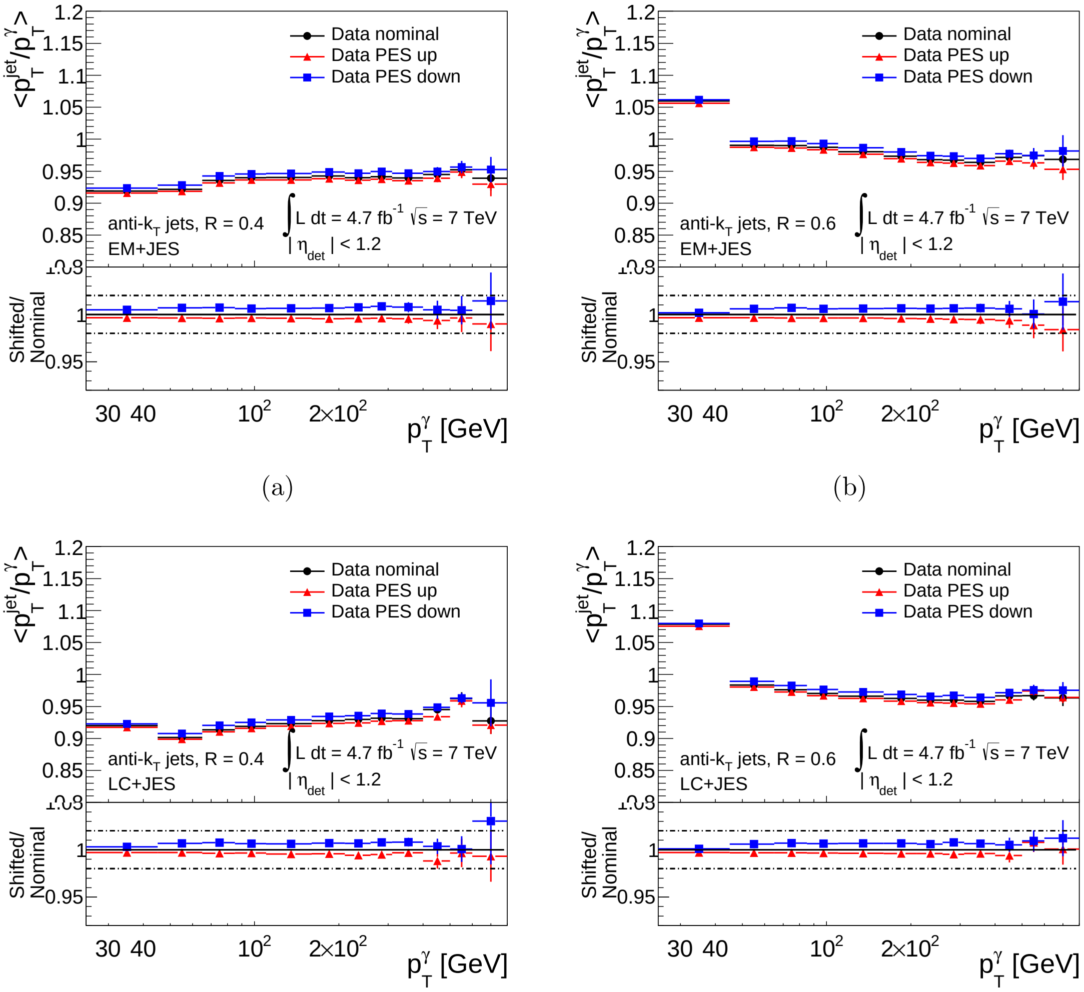

(a) (b)

(c) (d)

Figure 6.14: The the photon response in data using the nominal photon energy scale compared to the data using the photon energy scale with a $+1\sigma$ variation and with a -1σ variation for (a) anti-k_t $R = 0.4$ jets at EM+JES scale, (b) anti-k_t $R = 0.6$ jets at EM+JES scale, c) anti-k_t $R = 0.4$ jets at LCW+JES scale and d) anti-k_t $R = 0.6$ jets at LCW+JES scale.

In order to assess the impact of these two effects, a factor (known as the k-term) is defined, which is greater than 1 if the underlying event dominates and less than 1 if the out-of-cone radiation dominates. The k-term, k_{OOC}, is defined such that $p_T^{jet} \simeq k_{\mathrm{OOC}} \cdot p_T^{\gamma}$. The k-term is estimated by fitting the track transverse momentum profile of the charged particles around the jet. To reduce the effect of pile-up tracks are only selected if they are associated with the primary vertex assigned to the hard scatter in the event. The k-term is discussed in detail in Reference [1].

The k-term is defined as:

$$k_{\mathrm{OOC}} = \frac{p_{\mathrm{T}}^{\mathrm{IC,ALL}}}{p_{\mathrm{T}}^{\mathrm{IC+OC,ALL}} - p_{\mathrm{T}}^{\mathrm{IC+OC,UE}}} \tag{6.7}$$

where $p_{\mathrm{T}}^{\mathrm{IC,ALL}}$ is the average scalar p_{T} sum of all the tracks inside the jet cone with radius R, $p_{\mathrm{T}}^{\mathrm{IC+OC,ALL}}$ is the average scalar p_{T} sum of all the tracks inside a concentric cone with radius $R_0 \geq R$, where R_0 is the radius at which the average scalar track p_{T} sum distribution becomes approximately constant, and $p_{\mathrm{T}}^{\mathrm{IC+OC,UE}}$ is an estimation of the underlying event contribution. $p_{\mathrm{T}}^{\mathrm{IC+OC,UE}}$ is found by fitting the transverse momentum density profile of the tracks around the jet axis using the following function:

$$f(\Delta R) = \frac{a}{\Delta R^b + c} + C, \tag{6.8}$$

where ΔR is the distance from the jet axis and a, b, c and C are free parameters in the fit. C is taken to represent the contribution due to the underlying event and is used as an estimate for $p_{\mathrm{T}}^{\mathrm{IC+OC,UE}}$. A schematic representation of the k-term is shown in Figure 6.15.

The ratio of k_{ooc} in data and Monte Carlo is taken as a systematic uncertainty and is found to be $\sim$ 2 % for $25 < p_T^{\gamma} < 45$ GeV for jets with $R = 0.4$ and $\sim$ 1 % for jets with $R = 0.6$, falling to < 0.5 % for $p_T^{\gamma} > 160$ GeV as can be seen in Figure 6.16.

The larger amount of out-of-cone radiation for jets with $R = 0.4$, in comparison to jets with $R = 0.6$, is clearly visible when comparing Figures 6.16 (a) and (b). Since k_{ooc} is derived

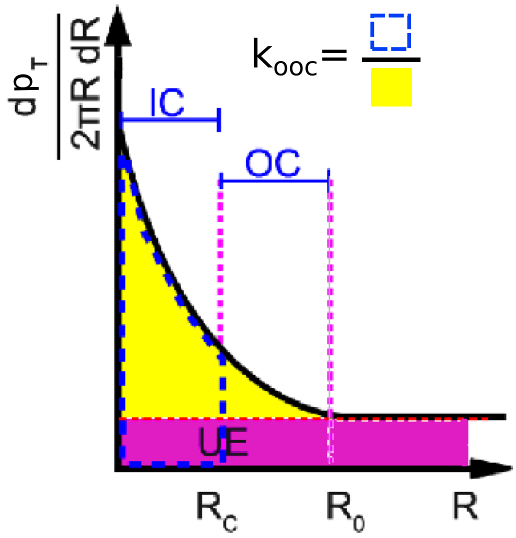

Figure 6.15: A schematic representation of the k-term, which is defined in Equation 6.8. The figure is adapted from [105]. The yellow area corresponds to $p_{\mathrm{T}}^{\mathrm{IC+OC,ALL}} - p_{\mathrm{T}}^{\mathrm{IC+OC,UE}}$ and the blue area corresponds to $p_{\mathrm{T}}^{\mathrm{IC,ALL}}$.

using tracks, this factor does not take into account the uncharged components of the jet and, therefore, provides only an estimate of the effect of the underlying event and the out-of-cone radiation.

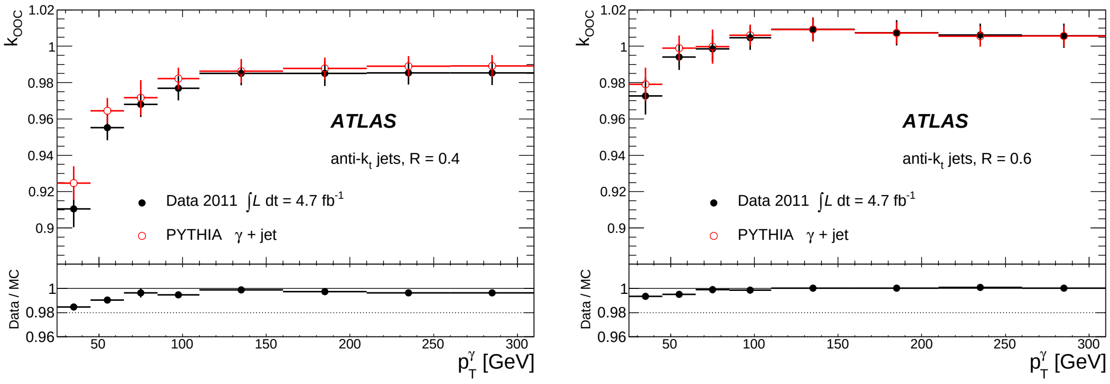

(a) (b)

Figure 6.16: k_{ooc} derived from data and Monte Carlo for (a) anti-k_t $R = 0.4$ jets and (b) anti-k_t $R = 0.6$ jets [1].

6.4.8 Summary of the Systematic Uncertainties

The sources of systematic uncertainty on the data-to-MC ratio of the γ-jet direct balance method for anti-k_t $R = 0.4$ and $R = 0.6$ jets at EM+JES and LCW+JES scale can be seen in Figure 6.17. The total uncertainty is obtained by adding all systematic uncertainties and the statistical uncertainty in quadrature.

The total uncertainty is found to be ∼ 1% between 100 GeV and 500 GeV, rising to ∼ 3 % below 100 GeV and ∼ 2 % above 500 GeV. The dominant uncertainty at low p_T^γ is due to background contamination and the out-of-cone radiation. The photon energy scale is a dominant source of systematic uncertainty at higher p_T^γ.

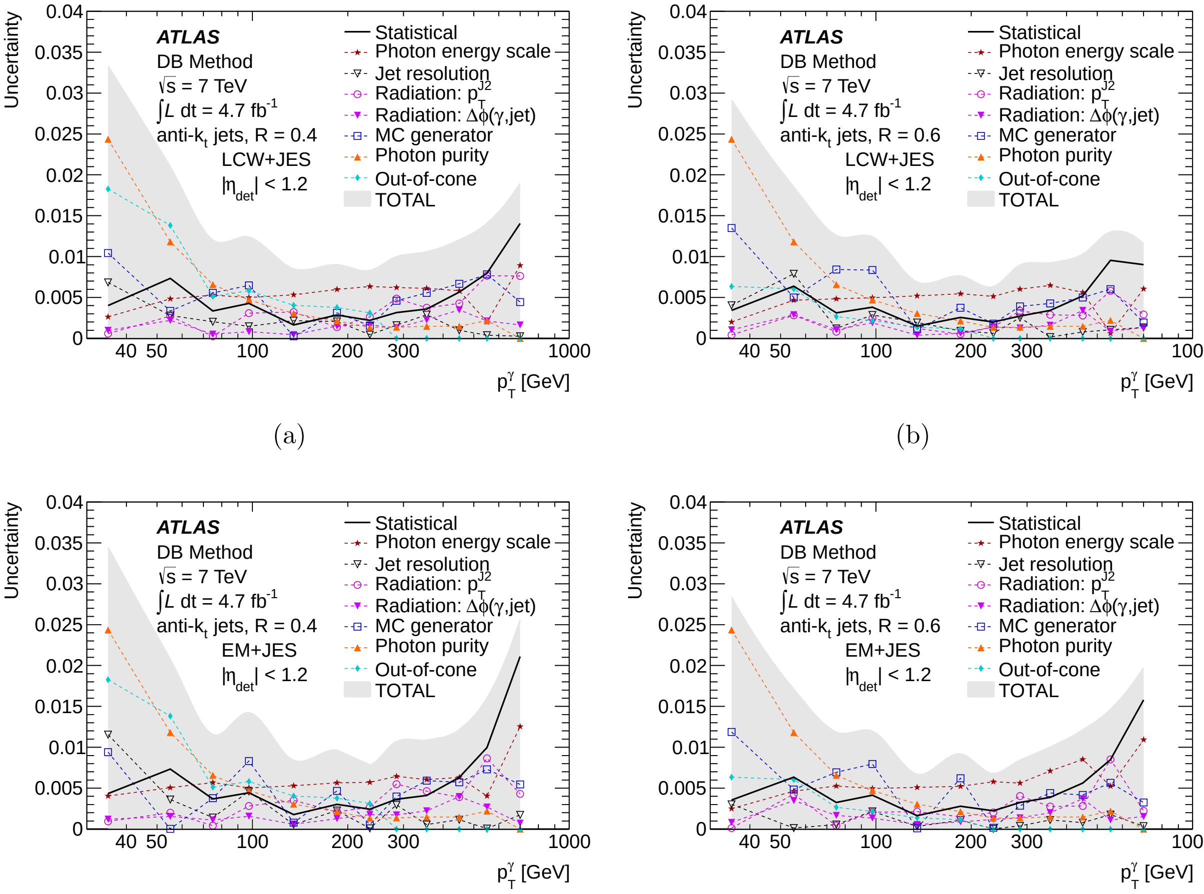

(a)

(b)

(c)

(d)

Figure 6.17: The JES uncertainties derived with the direct balance method for anti-k_t jets for (a) LC+JES scale jets with $R = 0.4$, (b) LC+JES scale jets with $R = 0.6$, (c) EM+JES scale jets with $R = 0.4$, and (d) EM+JES scale jets with $R = 0.6$[1].

Comparison to the Photon Response and Systematic Uncertainties Derived with the MPF Method

The photon response measured with the MPF method can be seen in Figure 6.18 for EM and LCW scales. The missing transverse energy used to derive $\mathcal{R}(\gamma,\ \mathrm{MPF})$ uses topo-clusters at the EM or LCW scales, rather than jets calibrated to EM+JES or LCW+JES scale. Therefore, the absolute value of the photon response measured with the direct balance and the MPF methods cannot be directly compared.

For the MPF method, the effect of the non-compensation of the calorimeters (which is larger at low p_T^γ) results in a lower $\mathcal{R}(\gamma,\ \mathrm{MPF})$ at low p_T^γ. This effect is not seen for the photon response measured with the direct balance method, shown in Figure 6.8, due to the fact that $\mathcal{R}(\gamma,\ \mathrm{DB})$ is derived using jets at the EM+JES and LCW+JES scales. Therefore, the effect of the non-compensation of the calorimeter on the jet p_{T} has already been corrected for.

Whilst the absolute values of the photon responses measured with the direct balance and the MPF methods cannot be directly compared, the data-to-MC ratio of the photon responses measured by the two methods can be compared. Any residual differences between the photon response in data and Monte Carlo are assumed to be due to mis-modelling of the calorimeter, of the electromagnetic and hadronic showers in the calorimeter, dead material or modelling of the physics of the γ-jet events. For the direct balance method, the same Monte Carlo JES factors are applied to both data and Monte Carlo. However, for the MPF method the JES is not propagated to the missing transverse energy. This is since it may mask the residual differences between the data and Monte Carlo that are due to detector effects, by introducing additional uncertainty, e.g. due to mis-modelling of the number of reconstructed jets or the underlying event.

In Figure 6.19 the difference between the data-to-MC ratio of the response measured with the direct balance and the MPF method is shown. It can be seen that there is good agreement between the two methods. Since the selection for the direct balance and MPF methods is almost exactly the same[5], the samples of events used to derive $\mathcal{R}(\gamma,\ \mathrm{DB})$ and $\mathcal{R}(\gamma,\ \mathrm{MPF})$ are almost exactly the same. Therefore, the statistical and systematic uncertainties are highly correlated between the two methods. The only uncertainty for which there is no correlation is that due to k_{OOC}, which is not accounted for by the MPF method because it doesn't use jets. To account for this the error bars shown in Figure 6.19 are calculated according to:

$$\sigma = \sqrt{|\sigma(\mathrm{MPF})^2_{\mathrm{stat}} - \sigma(\mathrm{DB})^2_{\mathrm{stat}}| + \sigma(\mathrm{DB})^2_{\mathrm{kooc}}}, \tag{6.9}$$

where $\sigma(\mathrm{MPF})_{\mathrm{stat}}$ is the statistical uncertainty on the data-to-MC ratio for the MPF method, $\sigma(\mathrm{DB})_{\mathrm{stat}}$ is the statistical uncertainty on the data-to-MC ratio for the direct balance method, and $\sigma(\mathrm{DB})_{\mathrm{kooc}}$ is the systematic uncertainty due to the k-term.

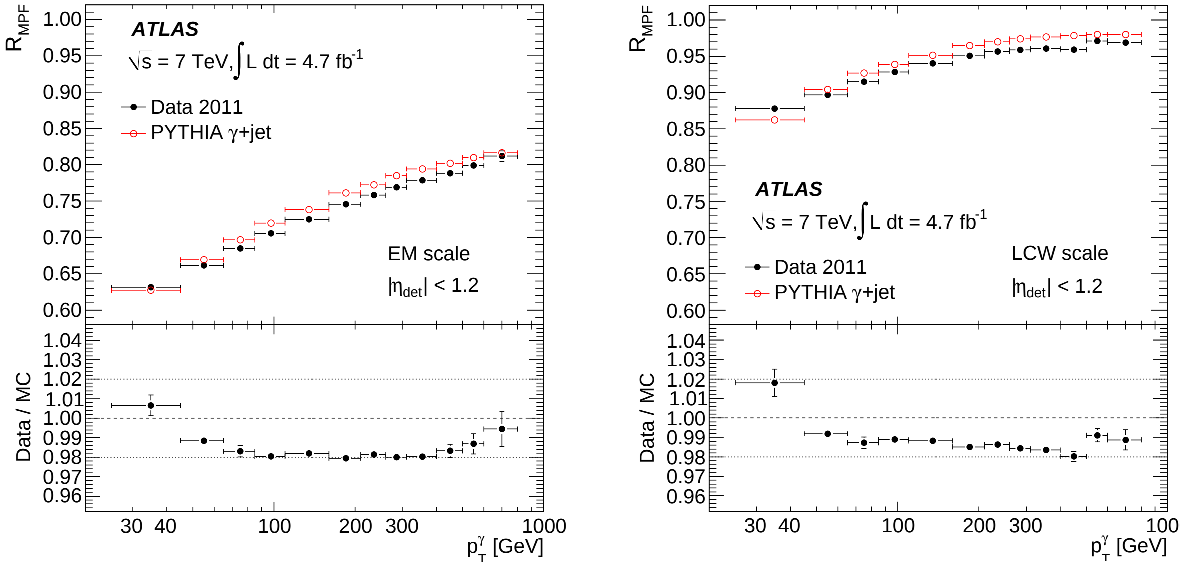

(a) (b)

Figure 6.18: The average jet response measured with the MPF method using γ-jet events at (a) EM scale and (b) LCW scale [1].

The JES uncertainties derived using the direct balance method (Figure 6.17) can be compared to those derived with the MPF method that are shown in Figure 6.20. For the MPF method no uncertainty due to k_{OOC} is shown since the method does not make direct use of jets. Since the MPF method does not directly use jets no correction is applied to

---

[5] The difference in the selection is that for the MPF method it is required that $\frac{p_T^{\mathrm{subleading\ jet}}}{p_T^{\gamma}} < 0.3$ (whereas it is 0.2 for the Direct Balance method, as described in Section 6.2.)

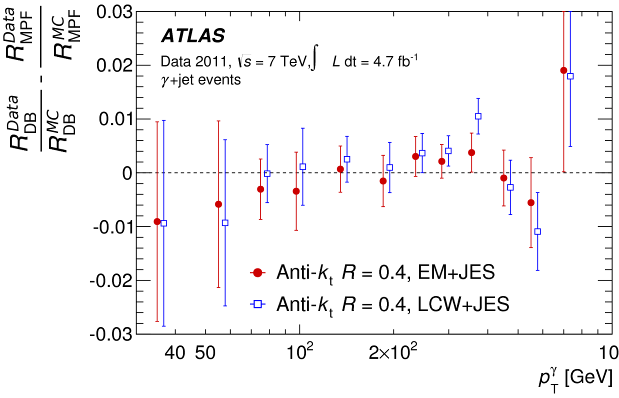

Figure 6.19: Difference between the data-to-MC ratio of the photon response measured with the direct balance method and the MPF method [1].

subtract energy deposits due to pile-up. Therefore, a pile-up uncertainty is included for the MPF method. The total JES uncertainties derived with the two methods are similar.

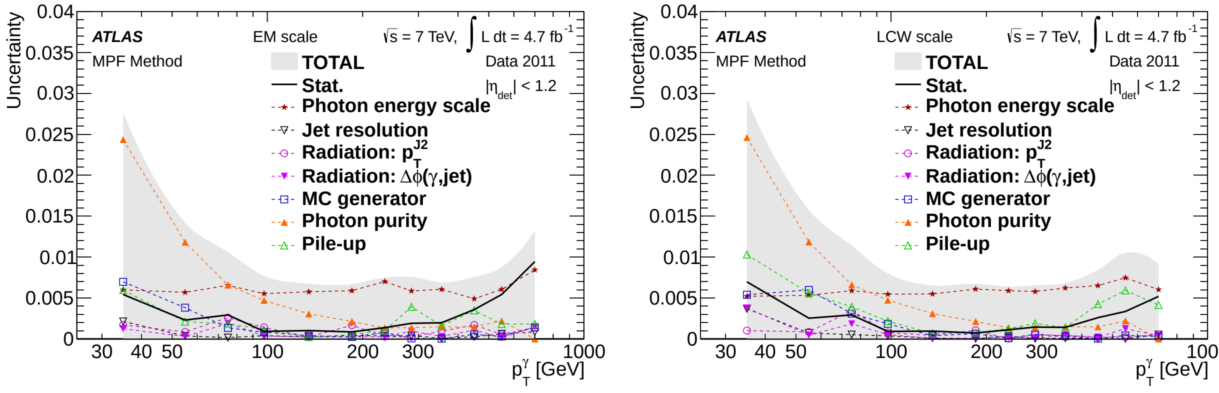

(a) (b)

Figure 6.20: The JES uncertainties derived with the MPF method at (a) EM scale and (b) LCW scale [1].

6.4.9 Use of the γ-jet Photon Response Measurements and Uncertainties

The data-to-MC ratio of the response and the total uncertainties derived using γ-jet events were combined with the Z-jet and the multi-jet measurements as described in full in Ref. [1] and briefly in Section 5.2.5. The combination was done separately with both the γ-jet direct balance method and the MPF method results.

As discussed previously, the MPF method does not make direct use of jets. However, the JES uncertainties will be applied to jets. Therefore, it is important to take into account the difference in the fraction of energy contained within the jet when comparing reconstructed to particle level jets. To account for the systematic uncertainty due to this effect, the k-term systematic uncertainty (which is derived in the direct balance γ-jet method) is added to the MPF systematic uncertainties.

Since the γ-jet direct balance and MPF methods are highly correlated, one method is chosen for use in the final JES uncertainties to simplify the evaluation of the correlations between the different components of the JES uncertainties. The two methods give very similar results and so, in order to choose one over the other, the direct balance and MPF methods are each combined separately with the Z-jet results. It was found that using the MPF method gave a smaller uncertainty (by up to one per mill [1]) after combination with the Z-jet method and so this method was chosen for the final combination.

The data-to-MC ratio of the response after the combination and the total combined uncertainties can be seen in Figure 6.21 for $R = 0.4$ EM+JES and LCW+JES scale jets. The data-to-MC ratio is used by physics analyses in order to apply a residual correction to the jet energy and p_{T} in data as described in Section 5.2.5. The combined uncertainties on the data-to-MC ratio are used for the in-situ JES uncertainties.

The total in-situ JES uncertainty as a function of jet p_{T} can be seen in Figure 6.22 (a). The uncertainty is broken down to show the components from the different in-situ methods for $\eta = 0.5$ for anti-k_t LCW+JES jets. In addition to the Z-jet, γ-jet and multi-jet balance methods, the uncertainty due to the η-intercalibration and due to the single particle methods are shown. The γ-jet method is the dominant component of the uncertainty for ∼100-700 GeV.

As discussed in Section 5.2.5 the total JES uncertainties are composed of the in-situ uncertainties, the pile-up uncertainty, the flavour uncertainty and the close-by jet uncertainty. These uncertainties can be seen in Figure 6.22 (b) for $\eta = 0.5$. It can be seen that the total in-situ uncertainty is a dominant uncertainty for the central η region, although the pileup uncertainty and flavour uncertainties are also important below ∼100 GeV.

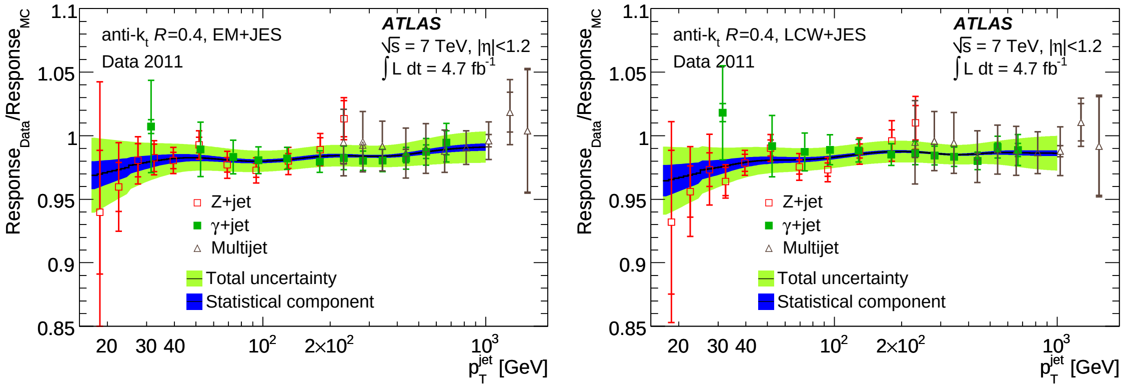

(a) (b)

Figure 6.21: The data-to-MC ratio of the response $(p_T^{\rm jet}/p_T^{\rm ref})$ derived with the Z-jet, γ-jet MPF and multi-jet methods, as a function of the $p_{\rm T}$ of the reference object for (a) anti-k_t $R = 0.4$ jets at EM+JES scale and (b) anti-k_t $R = 0.4$ jets at LCW+JES scale. The error bars show the statistical and systematic uncertainties added in quadrature for each method. The green band shows the total uncertainty obtained from the combination of the uncertainties of the three different methods and the blue band shows the statistical component of the uncertainty [1].

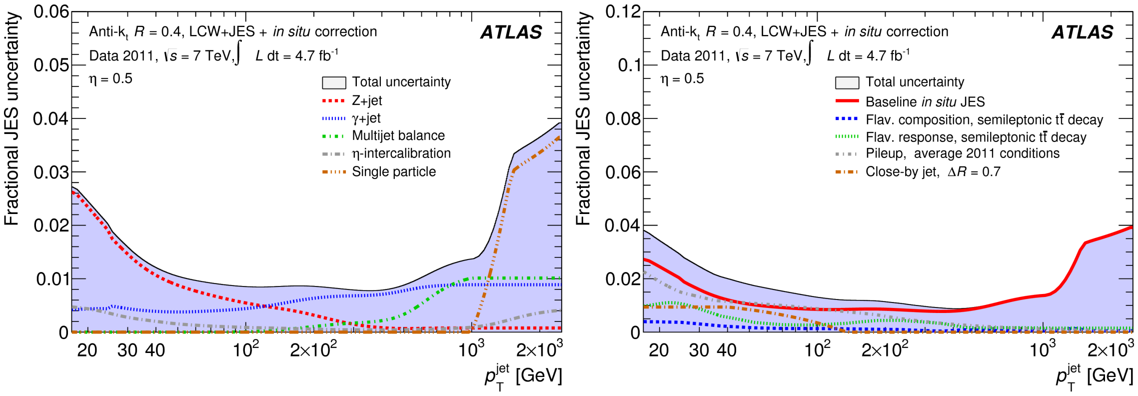

(a) (b)

Figure 6.22: (a) The in-situ JES uncertainties for $\eta = 0.5$, showing the total uncertainties from the Z-jet, γ-jet, multi-jet, η-intercalibration and single hadron methods and (b) the total JES uncertainties for $\eta = 0.5$ including the flavour uncertainties relevant for a semi-leptonic $t\bar{t}$ topology, the total in-situ uncertainty from (a), the pile-up uncertainty and an uncertainty due to close-by jets.

The direct balance γ-jet method provides a valuable cross check of the MPF γ-jet response and uncertainties, using a method that makes direct use of the jets used by physics analyses. The methods discussed here also serve as the basis for measuring the JES of large-R jets which will be discussed in the following chapter.

Chapter 7

The Jet Energy Scale Uncertainty of Large-R jets Derived In-Situ Using γ-jet Events

As discussed in Section 5.2.5, the JES uncertainties for large-R jets were previously evaluated using the track-jet double ratio method. However, the precision of the measurement of the JES uncertainty using track-jet events is limited to ∼2-7 %, due to the uncertainty on the tracking efficiency (∼3 %), track merging (∼2 %) and the modelling of the charged component of the jet [46]. To measure the JES uncertainty of large-R jets to a greater precision the direct balance γ-jet method is implemented for large-R jets. The large-R γ-jet analysis is based on the JES uncertainty studies for anti-k_t $R = 0.4$ and $R = 0.6$ jets that were described in Chapter 6.

The studies presented in this chapter make use of the 2012 data and γ-jet Monte Carlo samples, which were introduced in Sections 3.8 and 3.9. The event selection used to select $\gamma - \text{large} - \text{R}$ jet events with a back-to-back topology is discussed here in Section 7.1. The measurement of the photon response for large-R jets and the measurement of the γ-jet JES uncertainties for large-R jets are then presented in Sections 7.3, 7.4 and 7.5.

In addition to the in-situ JES uncertainty derived using γ-jet events, the uncertainty on the JES due to pile-up and the uncertainty on the JES due to the topology of the large-R jets are discussed. Finally, the impact of the new large-R JES uncertainties on the $t\bar{t}$ semi-leptonic resonance search will be shown.

7.1 γ-jet Selection for Large-R Jets

The selection of γ-jet events for the derivation of the photon response for large-R jets is based on the small-R jet selection described in Section 6.2. Differences in the event selection are described here and a summary of the selection can be seen in Table 7.1.

For large-R jets there is no $\eta-$intercalibration available to provide JES uncertainties for the forward η-region, as is the case for small-R jets. In order to provide JES uncertainties for the forward region, the γ-jet analysis can be extended up to $|\eta^{\text{jet}}| = 2.1$. Large-R jets are not used by physics analyses above $|\eta| > 2.1$ and therefore a measurement of the photon response is not required for $|\eta|$ values higher than this.

The following changes were made to the event selection with respect to that described in Section 6.2:

1. In addition to the rejection of events with a noise burst in the LAr calorimeters, events were rejected where there were problems in the Tile calorimeter, or where events were incomplete due to parts of the detector being restarted [108].
2. In order to reduce the background due to jets with a high electromagnetic content, which fake photons at low p_T^{γ}, a variable photon isolation threshold was introduced. These thresholds were optimised in the 2012 small R γ-jet analysis by comparing the $E_{\text{T}}^{\gamma\ \text{Iso}}$ distributions in data and Monte Carlo. More details about how these $E_{\text{T}}^{\gamma\ \text{Iso}}$ thresholds were derived can be found in [109]:
    - $E_{\text{T}}^{\gamma\ \text{Iso}} < 0.5$ GeV for $25 < p_T^{\gamma} < 45$ GeV
    - $E_{\text{T}}^{\gamma\ \text{Iso}} < 1.0$ GeV for $45 < p_T^{\gamma} < 65$ GeV
    - $E_{\text{T}}^{\gamma\ \text{Iso}} < 2.0$ GeV for $65 < p_T^{\gamma} < 85$ GeV

- $E_{\mathrm{T}}^{\gamma\ \mathrm{Iso}} < 3.0$ GeV for $p_T^\gamma > 85$ GeV

3. Due to the increased number of events available for the 2012 analysis, the cut on $E_{\mathrm{T}}^{\gamma\ \mathrm{cluster}}/(\sum p_{\mathrm{T}}^{\mathrm{tracks}})$ could be used over the full p_T^γ range.

4. The event is required to have at least one large-R jet, calibrated to LCW+JES scale. The performance of four large-R jet collections is routinely considered by the ATLAS experiment: anti-k_t $R = 1.0$ jets with and without grooming and Cambridge-Aachen $R = 1.2$ jets with and without grooming. However, at the time of writing, the LCW+JES calibration was only available for anti-k_t $R = 1.0$ trimmed jets. Therefore, the JES uncertainty has only been derived for this jet collection.

5. The requirement on $\frac{p_T^{\mathrm{subleading\ jet}}}{p_T^\gamma}$ is modified for the case of large-R jets to a requirement on:

$$\frac{p_T^{\mathrm{leading\ anti-k_T\ R\ =\ 0.4\ jet\ outside\ large-R\ jet}}}{p_T^\gamma} < 0.1, \tag{7.1}$$

where $p_T^{\mathrm{leading\ anti-k_T\ R\ =\ 0.4\ jet\ outside\ large-R\ jet}}$ is the transverse momentum of the leading anti-k_t LCW+JES $R = 0.4$ jet outside of the large-R jet. The anti-k_t $R = 0.4$ jet is considered to be outside of the large-R jet if the following criterion is satisfied:

$$\Delta R(\mathrm{anti-k_T\ R = 0.4\ jet,\ large\ R\ jet}) > D \cdot R_{\mathrm{eff}}, \tag{7.2}$$

where R_{eff} is the jet distance parameter of the jet collection under consideration (1.0 for anti-k_t $R = 1.0$ jets) and D is chosen to be 0.8 for the nominal selection. Any anti-k_t $R = 0.4$ jet with a ΔR greater than this will have a significant proportion of its energy deposits outside of the large-R jet. Using anti-k_t $R = 0.4$ jets for this cut, instead of large-R jets, is advantageous because it provides a consistent cut against radiation for any large-R jet collection that may be studied. Furthermore, the p_{T} of anti-k_t $R = 0.4$ jets is corrected for additional energy deposits due to pile-up. The leading anti-k_t $R = 0.4$ jet outside of the large-R jet is required to either have JVF > 0.25, to be outside of the tracking acceptance ($|\eta| > 2.5$) where JVF cannot be calculated, or to have $p_{\mathrm{T}} > 50$ GeV in order to reduce the effect of additional proton-proton interactions on the cut.

The value of the requirement for $p_T^{\text{leading anti}-\mathrm{k_T}\ \mathrm{R}\ =\ 0.4\ \text{jet outside large}-\mathrm{R}\ \text{jet}}/p_T^{\gamma}$ was changed from 20 %, which was used for the 2011 analysis, to 10 % for the 2012 analysis and the $\Delta\phi(\gamma - \text{jet})$ requirement was loosened from $\Delta\phi(\gamma - \text{jet}) > 2.9$ to $\Delta\phi(\gamma - \text{jet}) > 2.8$. These changes were made in order to harmonise the event selection for all the γ-jet and Z-jet in-situ analyses in 2012 data and Monte Carlo [3].

6. No quality criteria are available to reject fake large-R jets from noise busts in the calorimeter or non-collision backgrounds. As an alternative, if any anti-k_t $R = 0.4$ jet inside of the large-R jet or if the leading anti-k_t $R = 0.4$ jet outside of the large-R jet, which is used in the event selection, is identified as a fake jet [1, 110] then the event is rejected.

Variable	Threshold
$N_{\text{tracks}}^{\text{vertex}}$	> 4
p_T^{γ}	> 25 GeV
$\lvert\eta^{\gamma}\rvert$	< 1.37
$p_{\mathrm{T}}^{\text{jet}}$	> 8 GeV
$E_{\mathrm{T}}^{\gamma\ \text{Iso}}$	< 0.5 GeV if $25 < p_T^{\gamma} < 45$ GeV
$E_{\mathrm{T}}^{\gamma\ \text{Iso}}$	< 1.0 GeV if $45 < p_T^{\gamma} < 65$ GeV
$E_{\mathrm{T}}^{\gamma\ \text{Iso}}$	< 2.0 GeV if $65 < p_T^{\gamma} < 85$ GeV
$E_{\mathrm{T}}^{\gamma\ \text{Iso}}$	< 3.0 GeV if $p_T^{\gamma} > 85$ GeV
$E_{\mathrm{T}}^{\gamma\ \text{cluster}}/(\sum p_{\mathrm{T}}^{\text{tracks}})$ for single track converted photons	$0 < E_{\mathrm{T}}^{\gamma\ \text{cluster}}/(\sum p_{\mathrm{T}}^{\text{tracks}}) < 2$
$E_{\mathrm{T}}^{\gamma\ \text{cluster}}/(\sum p_{\mathrm{T}}^{\text{tracks}})$ for double track converted photons	$0.5 < E_{\mathrm{T}}^{\gamma\ \text{cluster}}/(\sum p_{\mathrm{T}}^{\text{tracks}}) < 1.5$
$\Delta\phi(\gamma - \text{jet})$	> 2.8 rad
$p_T^{\text{leading anti}-\mathrm{k_T}\ \mathrm{R=0.4}\ \text{jet outside large R jet}}/p_T^{\gamma}$	< 0.1
Jet cleaning	If any anti-k_t $R = 0.4$ jets contained within the large-R jet or the leading anti-k_t $R = 0.4$ jet outside of the large-R jet do not meet jet cleaning requirements then the event is rejected.

Table 7.1: Summary table of the event selection criteria used for the direct balance γ-jet analysis for large-R jets.

7.2 Basic kinematic variables and binning

The photon p_{T}, jet p_{T}, photon η and jet η distributions following the full event selection can be seen in Figure 7.1. It can be seen that there are few events for $p_T^\gamma \gtrsim$ 500-600 GeV and that the number of events for $|\eta^{\mathrm{jet}}| > 0.8$ is also reduced. The p_T^γ bins used for the small-R γ-jet analysis are retained for the large-R γ-jet analysis. However, the lowest p_T^γ bin is $45 < p_T^\gamma < 65$ (rather than $25 < p_T^\gamma < 45$ GeV) since the large-R jet Monte Carlo calibration only extends down to 50 GeV. The same $|\eta^{\mathrm{jet}}|$ bin boundaries are used as are used for the eta-intercalibration and other forward jet performance studies at ATLAS. The $|\eta^{\mathrm{jet}}|$ bin boundaries roughly reflect different parts of the calorimeter with different technologies or amounts of dead material. For $|\eta^{\mathrm{jet}}| < 0.8$ a sufficient number of events was available to extend the measurements up to 1 TeV. In $|\eta^{\mathrm{jet}}|$, wider bins are used for $p_T^\gamma < 85$ GeV, where the large trigger prescales reduce the number of events available, and for $p_T^\gamma >$500 GeV where the number of events is small due to the falling p_T^γ spectrum. The p_T^γ and $|\eta^{\mathrm{jet}}|$ bins used are illustrated in Figure 7.2.

7.3 Photon Response for Large-R Jets

The photon response, as measured for anti-k_t $R = 1.0$ trimmed jets, can be seen in Figure 7.3 for the five different $|\eta|$ regions. It can be seen that the photon response is stable for $p_T^\gamma > 110$ GeV and that its value is close to one. For $p_T^\gamma < 100$ GeV the photon response decreases by ~1-2 (3-5) % for $|\eta| < 0.8 (> 0.8)$.

For $|\eta| < 0.8$ the decrease in the photon response for $p_T^\gamma < 100$ GeV is not due to out-of-cone radiation, as is the case for anti-k_t $R = 0.4$ jets [1]. This is confirmed by evaluating the k-term for large-R jets (the k-term was introduced in Section 6.4.7) for $|\eta| < 0.8$, which can be seen in Figure 7.4. It can be seen that it is ~1 over the full range of p_T^γ, indicating that there is little out-of-cone radiation for large-R jets for $|\eta| < 0.8$. However, the k-term uses all tracks around the jet axis and, therefore, it does not take into account the effects

---

[1] The photon response for anti-k_t $R = 0.4$ LCW+JES scale jets was shown previously in Figure 6.8

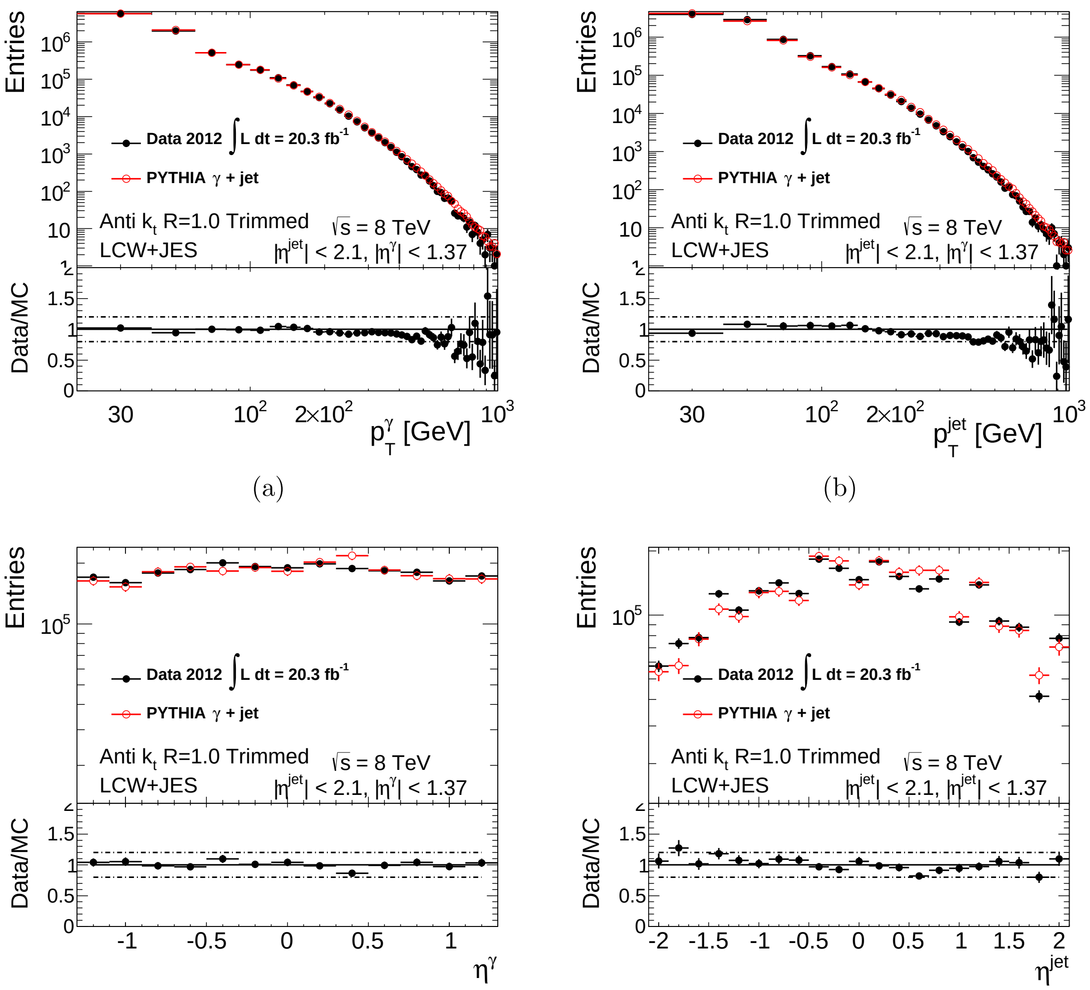

(a) (b)

(c) (d)

Figure 7.1: (a) The photon p_{T} distribution, (b) the jet p_{T} distribution, (c) the photon η and (d) the jet η after the event selection for anti-k_t $R = 1.0$ trimmed jets at LCW+JES scale in data and Monte Carlo. The distributions are corrected for the trigger prescales and the Monte Carlo is normalised to the data.

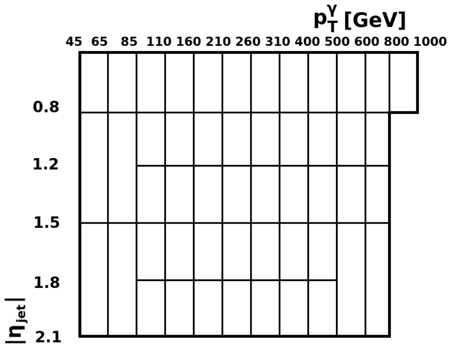

Figure 7.2: The $|\eta^{\mathrm{jet}}|$ and p_T^{γ} bins used for derivation of the γ-jet photon response and JES uncertainties for large-R jets.

of trimming, which would reduce the jet p_{T} with respect to the photon p_{T}. Furthermore, the k-term can only be calculated in the central $|\eta|$ region, since tracks are required for $\Delta R(\text{jet axis} - \text{ track}) < 2.5$. This makes it difficult to disentangle the effects of trimming, out-of-cone radiation and the underlying event for large-R jets.

The precision to which the photon response in data is modelled by the Monte Carlo is important for the evaluation of the JES uncertainties. For $|\eta| < 0.8$ it can be seen that the photon response in data is well modelled by the Monte Carlo, with differences of less than 1 % for $p_T^{\gamma} > 65$ GeV. For $|\eta| > 0.8$ the difference between the photon response in data and Monte Carlo rises to approximately 2 %.

7.4 Evaluation of the Systematic Uncertainties of the data-to-MC Ratio of the Photon Response

The systematic uncertainties on the data-to-MC ratio of the photon response are evaluated in the same way as described in Section 6.4. Changes to the systematic uncertainties and additional systematic uncertainties are as follows:

1. The cut on the first leading jet outside of the large-R jet does not reject events where more than one small radius ($R = 0.4$) jet is contained within the large-R jet. The inclusion of these events may result in additional uncertainties due to the modelling of the radiation. A systematic uncertainty is derived by comparing the nominal selection to a selection that minimises all additional jets from hard radiation in the event, regardless of whether or not they are contained within the large-R jet. This modified selection requires the p_{T} of the sub-leading anti-k_t $R = 0.4$ jet to be less than 10 % of p_T^{γ}, regardless of whether or not this jet is contained within the large-R jet.
2. The Jet Energy Resolution (JER) of large-R jets has not been extensively studied. However, variations of up to 20% have been observed in Monte Carlo studies, as discussed in Section 5.2.6. To assess the impact of these variations it is recom-

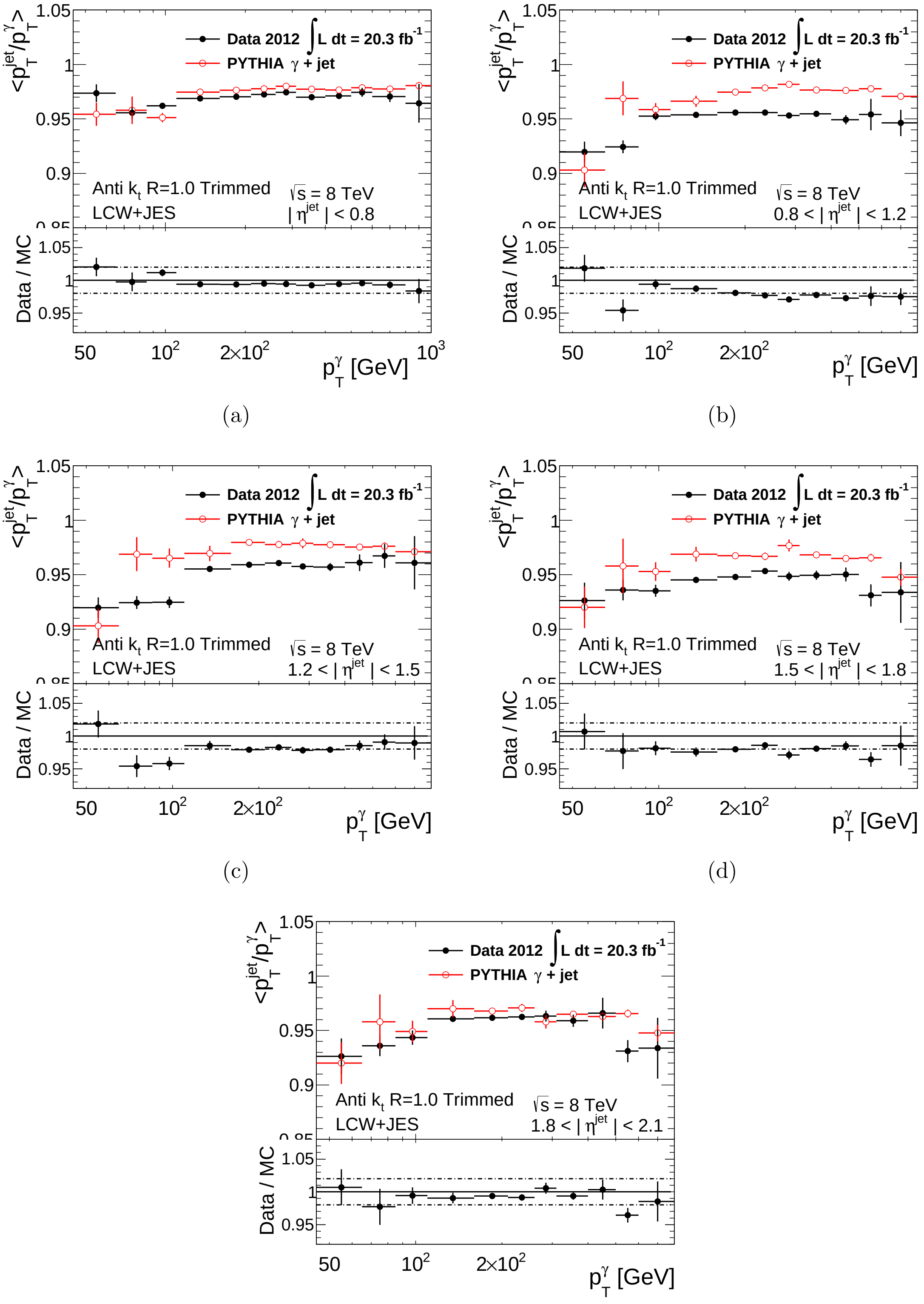

(a)

(b)

(c)

(d)

(e)

Figure 7.3: The average photon response for anti-k_t jets $R = 1.0$ trimmed jets for (a) $|\eta^{\text{jet}}| < 0.8$ (b) $0.8 < |\eta^{\text{jet}}| < 1.2$, (c) $1.2 < |\eta^{\text{jet}}| < 1.5$, (d) $1.5 < |\eta^{\text{jet}}| < 1.8$ and (e) $1.8 < |\eta^{\text{jet}}| < 2.1$. Only statistical uncertainties are shown.

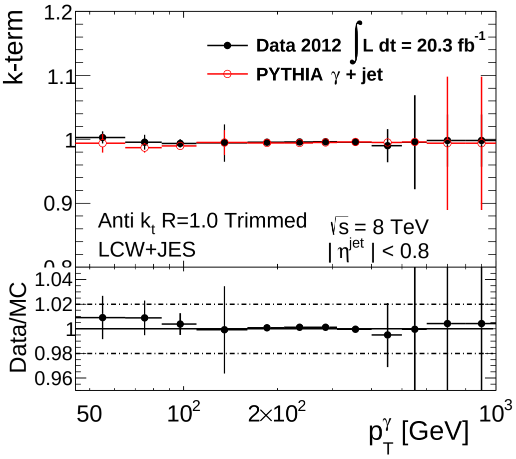

Figure 7.4: The k-term for anti-k_t $R = 1.0$ jets, calculated using jets with $|\eta^{\text{jet}}| < 0.8$ as a function of p_T^γ. Only statistical uncertainties are shown.

mended [111] that the jet p_{T} is smeared by a Gaussian centred at 1 with a width of $\sigma = \sqrt{(1.2\ \sigma_{\text{MC}})^2 - \sigma^2_{\text{MC}}}$ where $\sigma_{\text{MC}} = \sigma(p_T^{\text{reco jet}}/p_T^{\text{truth jet}})_{\text{MC}}$ is the truth JER measured in Monte Carlo, which can be seen in Figure 7.5. This smears the JER by 20 %, which is considered to be a conservative estimate of the uncertainty on the JER [101] based on the studies mentioned above.

3. As discussed in Section 6.4.4 the systematic uncertainty due to the background is estimated according to Equation 6.6 ($(1 - P) \times \frac{(\mathcal{R}(\text{di}-\text{jet}) - \mathcal{R}(\gamma\text{-jet}))}{\mathcal{R}(\gamma\text{-jet})}$). This requires a measurement of the photon purity (P), the response of the γ-jet sample ($\mathcal{R}(\gamma\text{-jet})$) and the response of background events ($\mathcal{R}(\text{di}-\text{jet})$).

   The photon purity was calculated using the same method as that described in Section 6.1, with 2012 data and the new $E_{\text{T}}^{\gamma\ \text{Iso}}$ requirements discussed above [3]. The resulting purity is ∼60 % for $p_T^\gamma = 40$ GeV, rising to > 95 % for $p_T^\gamma > 100$ GeV, as can be seen in Figure 7.6.

   For small-R jets in 2011, the background response was estimated using a Monte Carlo di-jet sample enriched with narrow jets, which are more likely to fake a photon. However, as was shown in Section 6.4.4, the number of events available in this sample is very low. As an alternative, the background response is estimated in data by selecting photons that pass the loose photon ID requirements but fail the tight photon ID requirements (loose-not-tight photons). The difference between the photon response in data for loose-not-tight photons and tight photons can be seen in Figure 7.7. As expected for background events, the photon response is significantly higher in data for p_T^{γ} <210 GeV, where the photon purity is < 95 %. The loose-not-tight sample has a photon response that is up to ∼10 % higher than the photon response for tight photons for $p_T^{\gamma} < 85$ GeV, decreasing to less than ∼1 % for $p_T^{\gamma} > 260$ GeV, within the statistical uncertainty.

The response of the loose-not-tight photons in data is taken as an estimate for $\mathcal{R}(\mathrm{di}-\mathrm{jet})$ and the response of tight photons in data is taken as an estimate for $\mathcal{R}(\gamma\text{-jet})$.

4. As discussed previously, the k-term can only be calculated for $|\eta^{\mathrm{jet}}| < 0.8$. For $|\eta^{\mathrm{jet}}| < 0.8$, the fractional difference of the k-term as measured in data and Monte Carlo is taken as a systematic uncertainty, to account for the modelling of out-of-cone radiation and the underlying event. This uncertainty is < 1 %, as can be seen in Figure 7.4, and it is also used for $|\eta^{\mathrm{jet}}| > 0.8$.

5. For 2012 data, the photon energy scale uncertainties are available in three separate components to account for the systematic uncertainties due to the material in front of the calorimeter, the presampler and the $Z \rightarrow ee$ energy scale, as discussed in Section 5.1. For each of these components, the photon energy scale in Monte Carlo is shifted by the uncertainty on that component. The fractional difference between the shifted and the nominal Monte Carlo samples is taken as the systematic uncertainty for the component under consideration. The systematic uncertainties from the three components are then added in quadrature to give the total photon energy scale systematic.

6. The cut on the leading anti-k_t $R = 0.4$ jet outside the large-R jet requires a definition of when an anti-k_t $R = 0.4$ jet is considered to be outside the large-R jet as given by Equation 7.2. The effect of this definition is evaluated by changing D from the nominal value of 0.8 to 1.4.

7. The track-jet double ratio uncertainties are derived in bins of $m^{\mathrm{reco\ jet}}/p_T^{\mathrm{reco\ jet}}$, which

accounts for variations of the JES due to the mass of the jet. In the γ-jet sample, the number of events is too low to be able to evaluate the photon response over the full $|\eta^{\text{jet}}|$ and p_T^{γ} range if an additional binning is performed in $m^{\text{reco jet}}/p_T^{\text{reco jet}}$. Instead, this dependency is taken into account using an additional systematic uncertainty. The data-to-MC ratio of the photon response in low $m^{\text{reco jet}}/p_T^{\text{reco jet}}$ events ($m^{\text{reco jet}}/p_T^{\text{reco jet}} < 0.15$) and high $m^{\text{reco jet}}/p_T^{\text{reco jet}}$ events ($m^{\text{reco jet}}/p_T^{\text{reco jet}} > 0.15$) is compared. The photon response for events with low and high $m^{\text{reco jet}}/p_T^{\text{reco jet}}$ can be seen in Figure 7.8. For $p_T^{\gamma} < 110$ GeV the photon response for jets with $m^{\text{reco jet}}/p_T^{\text{reco jet}} > 0.15$ is significantly higher than for jets with $m^{\text{reco jet}}/p_T^{\text{reco jet}} < 0.15$ for all $|\eta^{\text{jet}}|$, whereas for $p_T^{\gamma} > 110$ GeV the photon response tends to be lower for jets with $m^{\text{reco jet}}/p_T^{\text{reco jet}} > 0.15$.

A systematic uncertainty to account for the variation of the data-to-MC ratio of the photon response for high and low mass jets is defined as:

$$\frac{(\mathcal{R}(\gamma,\text{DB})_{\text{data}}/\mathcal{R}(\gamma,\text{DB})_{\text{MC}})_{\text{low m/pT}} - (\mathcal{R}(\gamma,\text{DB})_{\text{data}}/\mathcal{R}(\gamma,\text{DB})_{\text{MC}})_{\text{high m/pT}}}{(\mathcal{R}(\gamma,\text{DB})_{\text{data}}/\mathcal{R}(\gamma,\text{DB})_{\text{MC}})_{\text{nominal}}}. \tag{7.3}$$

The $m^{\text{reco jet}}/p_T^{\text{reco jet}}$ systematic uncertainty (calculated using Equation 7.3) is shown in Figure 7.8, where it can be seen that the changes in the photon response for jets with low and high $m^{\text{reco jet}}/p_T^{\text{reco jet}}$ are modelled by the Monte Carlo to within ~2-3 %, with larger deviations observed for $|\eta^{\text{jet}}| > 0.8$.

8. A deviation of the data-to-MC ratio of the photon response from unity indicates that there is a difference in the JES between data and Monte Carlo that has not been accounted for. For small R jets, the deviation of the data-to-MC ratio of the photon response from unity is used to correct the jet energy and p_{T} in data, as described in Chapter 6. However, this would require a full combination of the γ-jet and track-jet double ratio methods or the development of other techniques to measure the response at higher p_{T}. Therefore, for large-R jets any deviation of this ratio will not be corrected for. Instead the deviation of the data-to-MC ratio from unity is taken as an additional

uncertainty.

9. No pile-up corrections or uncertainties were available for large-R jets at the time of writing. Therefore an additional uncertainty to account for pile-up is required. This is discussed below in Section 7.7.

A summary of the systematic uncertainties on the data-to-MC ratio of the photon response can be seen in Figure 7.9 and the exact values can be found in Appendix A.1. It can be seen that there are significant fluctuations in the systematic uncertainties, particularly at low and high p_T^γ and for $|\eta^{\text{jet}}| > 0.8$. The statistical uncertainty on the data-to-MC ratio of the photon response is already accounted for and can be seen in Figure 7.9. It is desirable that the systematic uncertainties are due to real systematic effects rather than statistical fluctuations. In order to reduce the statistical fluctuations in the systematic uncertainties, p_T^γ and $|\eta^{\text{jet}}|$ bins are merged and the uncertainties are smoothed as discussed in the following section.

7.5 Statistical Treatment and Summary of the Systematic Uncertainties

7.5.1 Reducing Statistical Fluctuations by Merging p_T^γ and $|\eta^{\text{jet}}|$ Bins

In order to be able to distinguish between real systematic shifts and those due to statistical fluctuations, an accurate measure of the statistical uncertainty on the systematic uncertainty is required. For cases where the sample of events selected for the systematic evaluation overlaps with the nominal sample of events, the statistical uncertainty on the systematic uncertainty cannot be calculated by treating the two samples as independent. In this case the *bootstrap method* is used in order to evaluate the statistical uncertainty on the systematic uncertainty. A common ATLAS tool known as SystTool which is designed for the in-situ

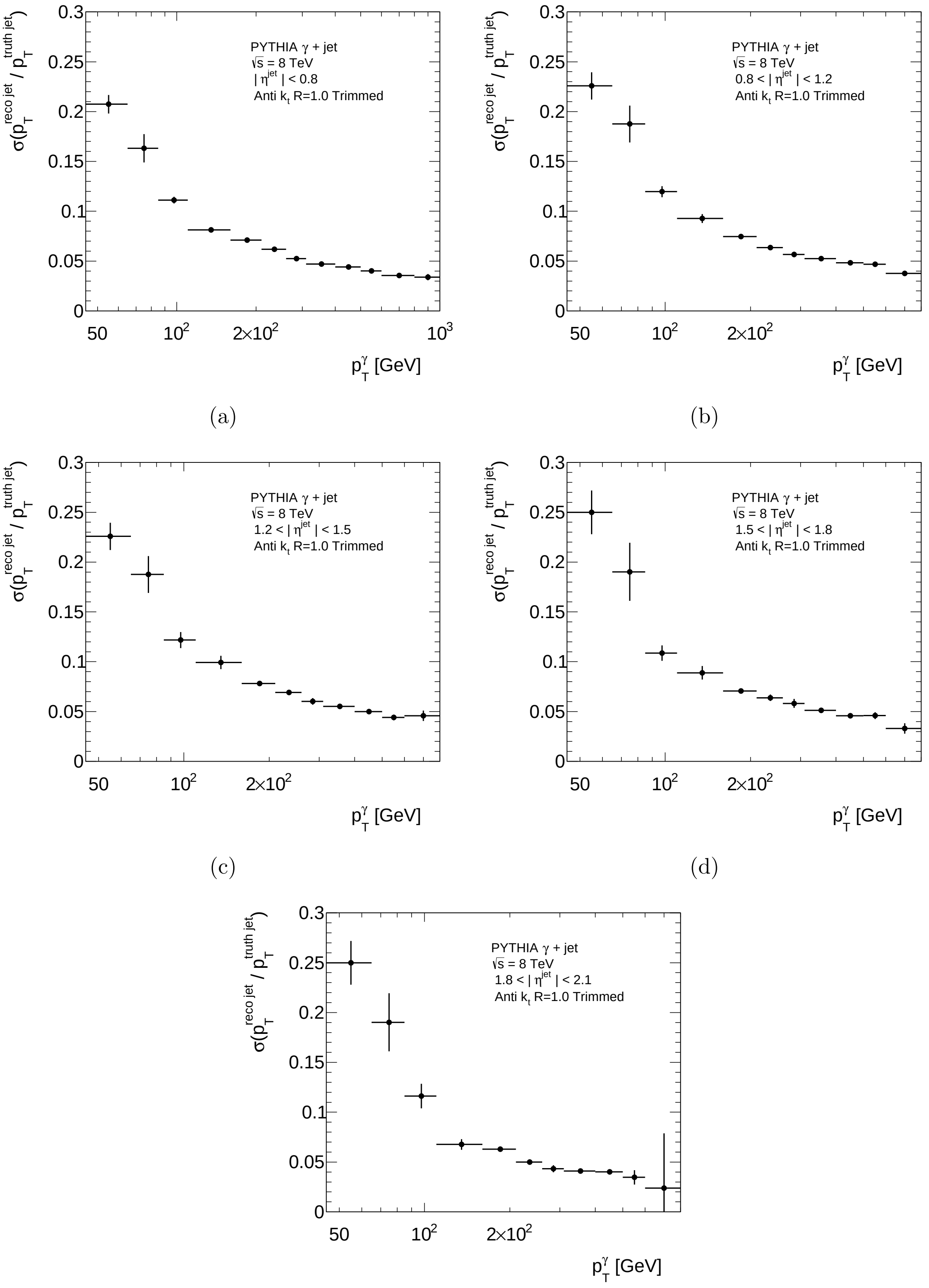

(a)

(b)

(c)

(d)

(e)

Figure 7.5: The truth JER ($\sigma(p_T^{recojet}/p_T^{truthjet})$) measured in Monte Carlo for anti-k_t jets $R = 1.0$ trimmed jets for (a) $|\eta^{\text{jet}}| < 0.8$ (b) $0.8 < |\eta^{\text{jet}}| < 1.2$, (c) $1.2 < |\eta^{\text{jet}}| < 1.5$, (d) $1.5 < |\eta^{\text{jet}}| < 1.8$ and (e) $1.8 < |\eta^{\text{jet}}| < 2.1$ as a function of the reconstructed photon p_{T}. Only statistical uncertainties are shown.

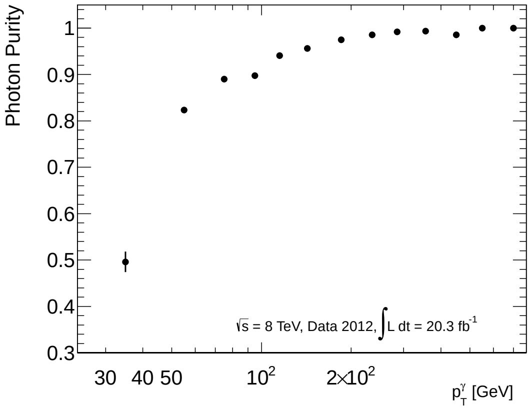

Figure 7.6: The purity of selected photons for the 2012 dataset [3].

JES analyses was used to implement the bootstrap method [2].

The bootstrap method works in the following way. For each p_{T} and $|\eta^{\mathrm{jet}}|$ bin the systematic uncertainty is defined as:

$$\text{Systematic uncertainty} = \frac{\left\langle\frac{\mathcal{R}(\gamma)^{\mathrm{data}}}{\mathcal{R}(\gamma)^{\mathrm{MC}}}\right\rangle_{\mathrm{shifted}} - \left\langle\frac{\mathcal{R}(\gamma)^{\mathrm{data}}}{\mathcal{R}(\gamma)^{\mathrm{MC}}}\right\rangle_{\mathrm{nominal}}}{\left\langle\frac{\mathcal{R}(\gamma)^{\mathrm{data}}}{\mathcal{R}(\gamma)^{\mathrm{MC}}}\right\rangle_{\mathrm{nominal}}} \tag{7.4}$$

For each $\mathcal{R}(\gamma)^{\mathrm{data}}/\mathcal{R}(\gamma)^{\mathrm{MC}}$ in Equation 7.4, a distribution is constructed that smears the photon response distribution by a Poisson distribution. For example, to construct $\left\langle\frac{R_\gamma^{\mathrm{data}}}{R_\gamma^{\mathrm{MC}}}\right\rangle_{\mathrm{shifted,bootstrap}}$ for a given $|\eta^{\mathrm{jet}}|$ and p_T^γ bin, every photon response value from the sample of events that pass the shifted selection is put into the distribution x times, where x is a random number sampled from a Poisson distribution with a mean of one. The means of the resulting distributions are then used to calculate the bootstrap distribution:

$$\text{Bootstrap} = \frac{\left\langle\frac{\mathrm{R}_\gamma^{\mathrm{data}}}{\mathrm{R}_\gamma^{\mathrm{MC}}}\right\rangle_{\mathrm{shifted,bootstrap}} - \left\langle\frac{\mathrm{R}_\gamma^{\mathrm{data}}}{\mathrm{R}_\gamma^{\mathrm{MC}}}\right\rangle_{\mathrm{nominal,bootstrap}}}{\left\langle\frac{\mathrm{R}_\gamma^{\mathrm{data}}}{\mathrm{R}_\gamma^{\mathrm{MC}}}\right\rangle_{\mathrm{nominal,bootstrap}}} \tag{7.5}$$

This process is repeated 1000 times and the RMS of the distribution of Equation 7.5 is taken as the statistical uncertainty on the systematic uncertainty.

Following the evaluation of the statistical uncertainty on the systematic uncertainties,

---

[2] SystTool-00-01-02 [112] was used for the results presented here.

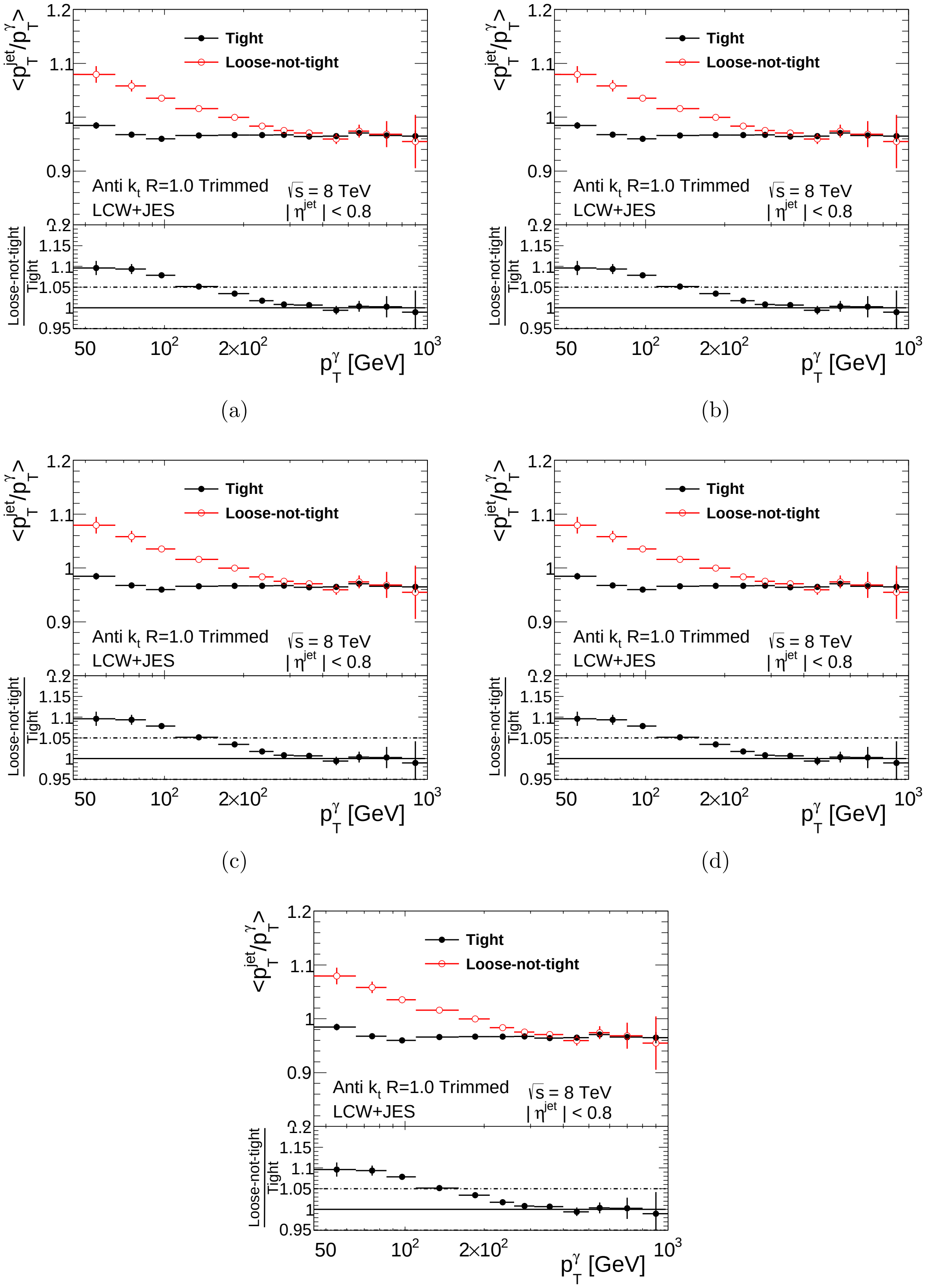

(a) (b) (c) (d) (e)

Figure 7.7: The photon response for loose-not-tight and tight photons in data for anti-k_t jets $R = 1.0$ trimmed jets for (a) $|\eta^{\text{jet}}| < 0.8$ (b) $0.8 < |\eta^{\text{jet}}| < 1.2$, (c) $1.2 < |\eta^{\text{jet}}| < 1.5$, (d) $1.5 < |\eta^{\text{jet}}| < 1.8$ and (e) $1.8 < |\eta^{\text{jet}}| < 2.1$ as a function of the reconstructed photon p_{T}. Only statistical uncertainties are shown.

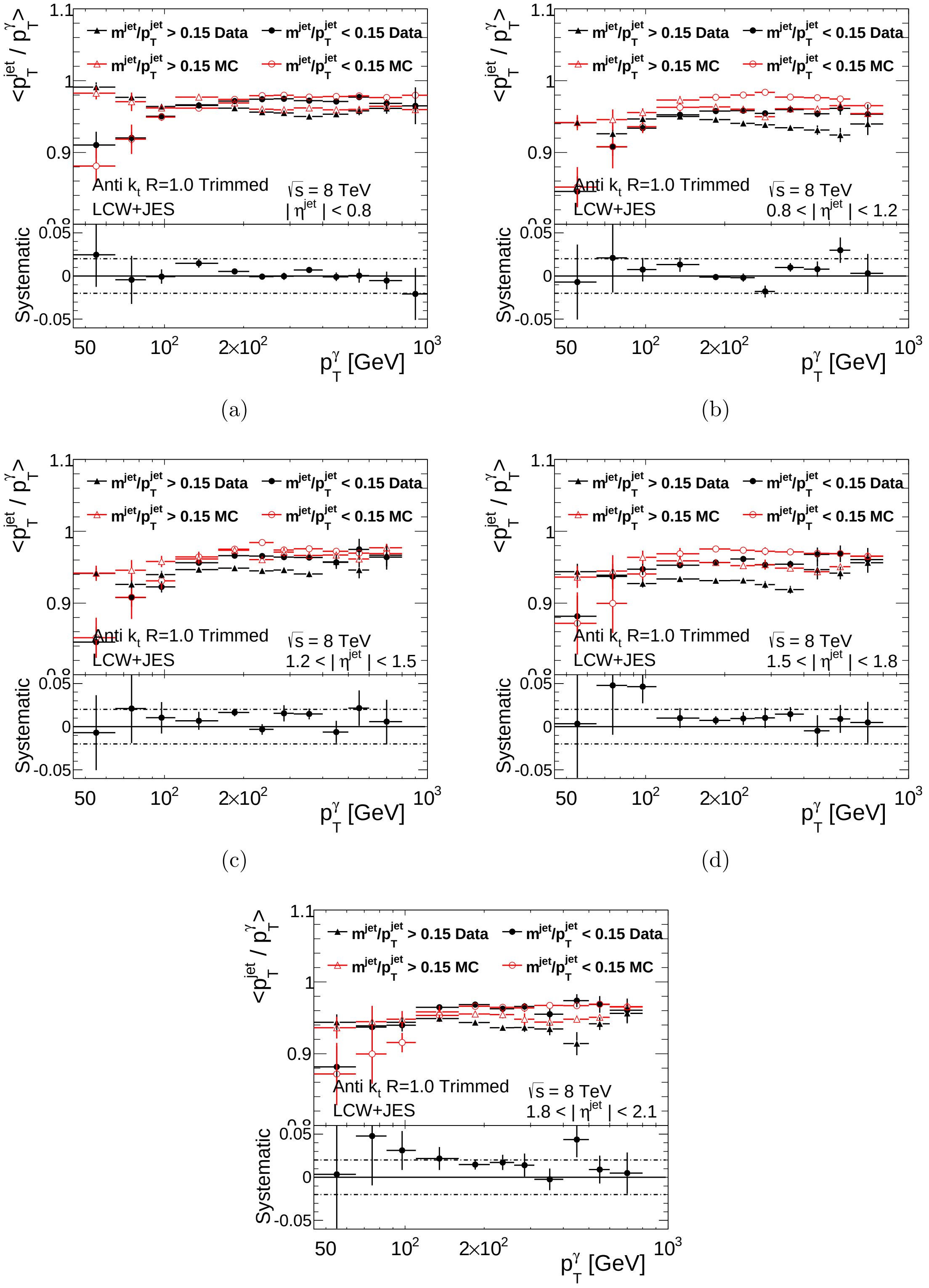

(a) (b)

(c) (d)

(e)

Figure 7.8: The average photon response for anti-k_t jets $R = 1.0$ trimmed jets with $m^{reco\ jet}/p_T^{reco\ jet} < 0.15$ (closed circles) and $m^{reco\ jet}/p_T^{reco\ jet} > 0.15$ (open circles) for (a) $|\eta^{\text{jet}}| < 0.8$ (b) $0.8 < |\eta^{\text{jet}}| < 1.2$, (c) $1.2 < |\eta^{\text{jet}}| < 1.5$, (d) $1.5 < |\eta^{\text{jet}}| < 1.8$ and (e) $1.8 < |\eta^{\text{jet}}| < 2.1$ as a function of p_T^{γ}. The systematic uncertainty is calculated according to Equation 7.3. The error bars represent the statistical uncertainty.

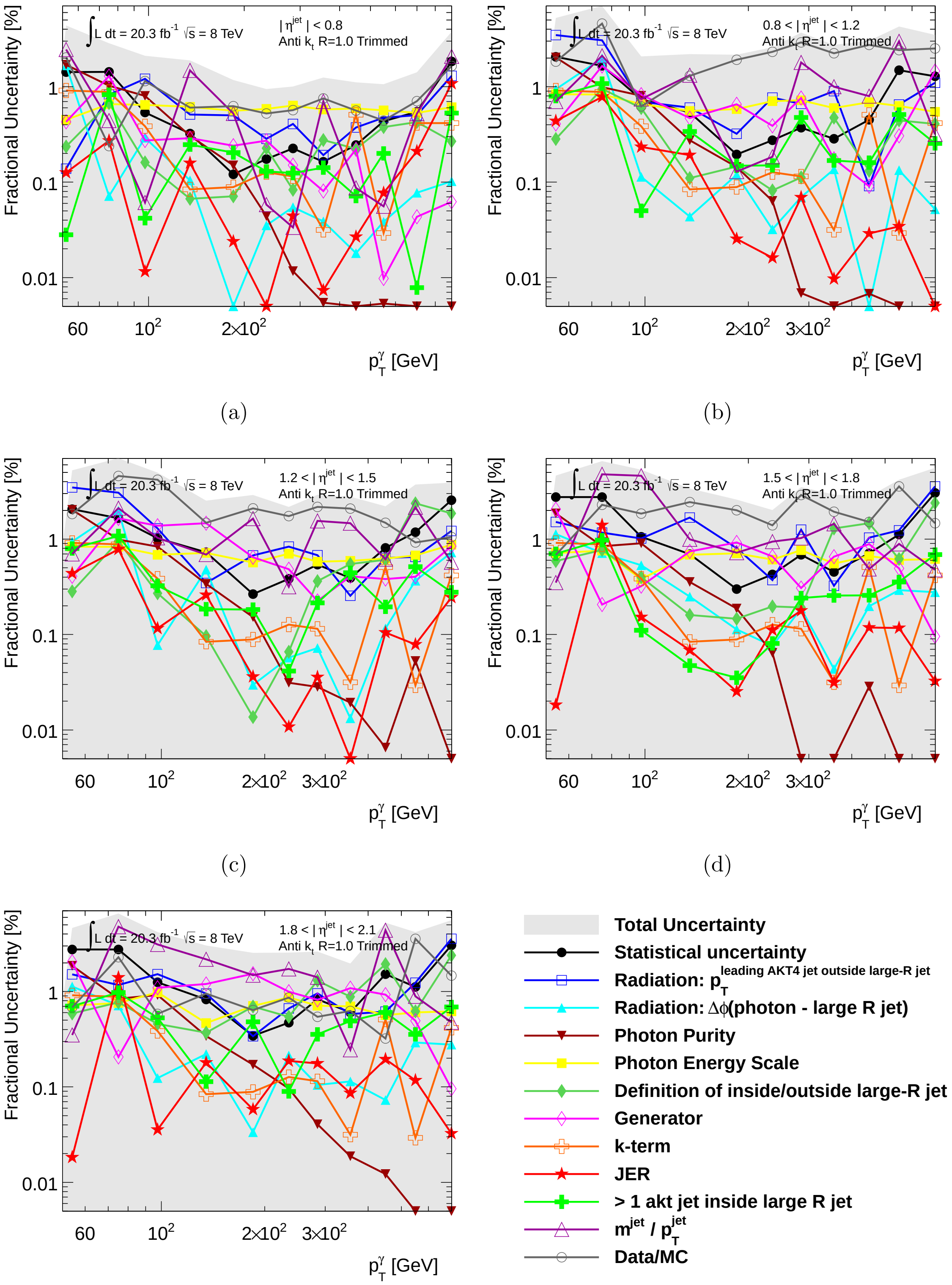

(a) (b)

(c) (d)

(e) (f)

Figure 7.9: The JES uncertainties for anti-k_t $R = 1.0$ trimmed jets derived using γ-jet events for (a) $|\eta^{\text{jet}}| < 0.8$, (b) $0.8 < |\eta^{\text{jet}}| < 1.2$, (c) $1.2 < |\eta^{\text{jet}}| < 1.5$, (d) $1.5 < |\eta^{\text{jet}}| < 1.8$ and (e) $1.8 < |\eta^{\text{jet}}| < 2.1$. The uncertainties are shown before any bin merging or smoothing is performed. Figure (f) is the legend for plots (a)-(e).

p_T^γ and $|\eta^{\mathrm{jet}}|$ bins are merged if $\sigma_{\mathrm{syst}} < 1.5\ \sigma_{\mathrm{stat}}$ where σ_{syst} is the systematic uncertainty and σ_{stat} is the statistical uncertainty. It is important that a balance is reached between too little merging, which results in large statistical fluctuations being incorporated into the final uncertainties, and too much merging, which may lead to an underestimation of the systematic uncertainties in regions with large statistical uncertainties. In order to achieve this balance, each systematic uncertainty is studied separately and bins are not merged over the full p_T^γ range or $|\eta^{\mathrm{jet}}|$ range if there is evidence that the systematic uncertainty is rapidly changing in a particular region of phase space.

For example, the systematic uncertainty derived by comparing the nominal data-to-MC ratio of the photon response to the data-to-MC ratio of the photon response with a looser requirement on $p_T^{\mathrm{leading\ anti-k_T\ R\ =\ 0.4\ jet\ outside\ large-R\ jet}}/p_T^\gamma$ can be seen in Figure 7.10. The systematic and the statistical uncertainties on the data, the Monte Carlo and the data-to-MC ratio can be seen for the five $|\eta^{\mathrm{jet}}|$ bins as a function of p_T^γ. The systematic uncertainty on the data-to-MC ratio is defined using Equation 7.4 and the statistical uncertainty is evaluated using the bootstrap method. For the data, the systematic uncertainty is defined as $\left(\mathcal{R}(\gamma)^{\mathrm{shifted}}_{\mathrm{data}} - \mathcal{R}(\gamma)^{\mathrm{nominal}}_{\mathrm{data}}\right)/\mathcal{R}(\gamma)^{\mathrm{nominal}}_{\mathrm{data}}$, and similarly for the Monte Carlo. It is observed that whilst the systematic uncertainty on the data and the Monte Carlo changes rapidly with p_T^γ, this dependence largely cancels when looking at the systematic uncertainty on the data-to-MC ratio. In this case no obvious $|\eta^{\mathrm{jet}}|$ dependence is observed and the systematic uncertainty is merged into two $|\eta^{\mathrm{jet}}|$ bins: $|\eta^{\mathrm{jet}}| < 1.5$ and $1.5 < |\eta^{\mathrm{jet}}| < 2.1$. The resulting uncertainty can be seen in Figure 7.11 in the black points.

Following the merging in $|\eta^{\mathrm{jet}}|$, bins are merged in p_T^γ. Boundaries for the merging are set such that bins cannot be merged outside of the following p_T^γ regions: $45 < p_T^\gamma <$110 GeV, $110 < p_T^\gamma <$(800) 1000 GeV for $|\eta^{\mathrm{jet}}| < 0.8 (> 0.8)$. The boundary is set at 110 GeV since there appears to be no systematic trend in the systematic uncertainty above this value. Inside each of these p_T^γ regions, the bins are merged until the systematic uncertainty has a statistical significance $> 1.5\ \sigma$. The resulting systematic uncertainty can be seen in red in Figure 7.11. The bin merging boundaries are *limits* on how many bins can be merged, sometimes not all bins within the defined bin boundaries need to be merged for the systematic uncertainty to become significant. For example, in Figure 7.11 b) the bins in the range 110 $< p_T^\gamma <$310 GeV become significant after merging 110 $< p_T^\gamma <$ 260 GeV and 260 $< p_T^\gamma <$310 GeV and therefore no further merging is performed in this region.

It can be seen that this procedure reduces statistical fluctuations. However the resulting systematic uncertainty is not statistically significant in all p_T^γ bins. Even though the systematic uncertainty has not become statistically significant for all p_T^γ, the values measured after bin merging are retained and not merged further, to avoid underestimation of the uncertainties. Table 7.2 gives the boundaries that are used for the bin merging for all the uncertainties.

All of the systematic uncertainties are shown after bin merging in Figure 7.12. It can be seen that the bin merging reduces the fluctuations in the systematic uncertainties, whilst retaining the overall shape of the systematic uncertainty distributions as a function of p_T^γ.

7.5.2 Smoothing of the Systematic Uncertainties

In order for the uncertainties to be continuous in η and p_{T}, the uncertainties need to be smoothed. This can be done using a 2D Gaussian kernel to smooth the results, as is done for the η-intercalibration analysis [107]. This works by constructing a smooth function using the data points of the systematic uncertainty under consideration:

$$F(p_T, \eta) = \frac{\sum_{i=1}^{N_{bins}} c_i w_i}{\sum_{i=1}^{N_{bins}} w_i} \tag{7.6}$$

Where c_i is the value of the uncertainty in the i^{th} η and p_T^γ bin and w_i is the weight, which is defined as:

$$w_i = \frac{1}{\Delta C_i^2} \times \mathrm{Gauss}\left(\frac{\ln(p_T) - \ln\langle p_{T,i}\rangle}{\sigma_{p_T}} \oplus \frac{\eta - \langle \eta_i \rangle}{\sigma_\eta}\right) \tag{7.7}$$

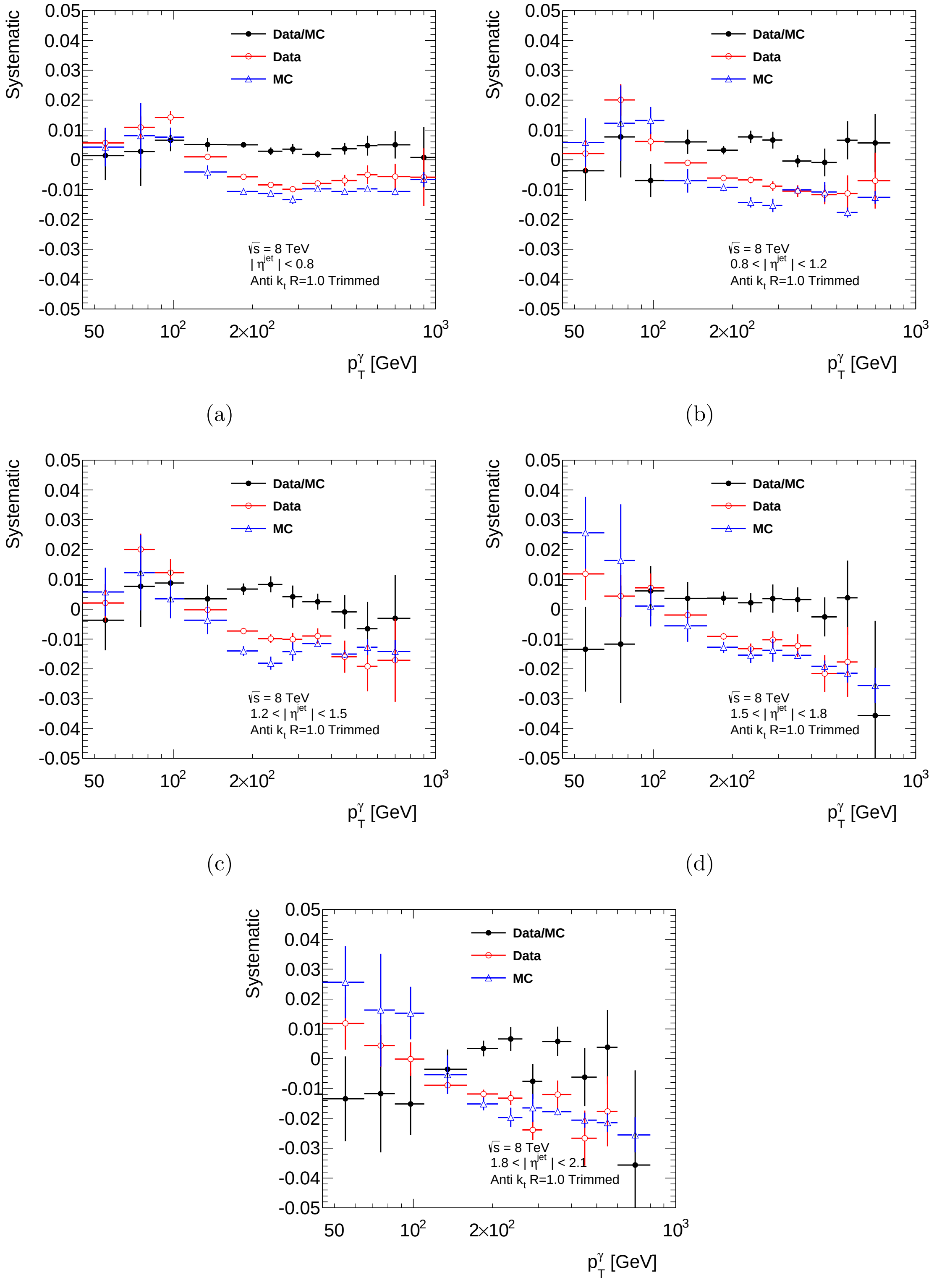

(a)

(b)

(c)

(d)

(e)

Figure 7.10: The systematic uncertainty for data (red), Monte Carlo (blue) and the data-to-MC ratio (black) when loosening the cut on $p_T^{\text{leading anti}-\text{k}_\text{T}\text{ R = 0.4 jet outside large}-\text{R jet}}/p_T^{\gamma}$ from the nominal cut of 0.1 to a cut of 0.2 for anti-k_t jets $R = 1.0$ trimmed jets for (a) $|\eta^{\text{jet}}| < 0.8$, (b) $0.8 < |\eta^{\text{jet}}| < 1.2$, (c) $1.2 < |\eta^{\text{jet}}| < 1.5$, (d) $1.5 < |\eta^{\text{jet}}| < 1.8$ and (e) $1.8 < |\eta^{\text{jet}}| < 2.1$. The error bars are the statistical uncertainties on the systematic uncertainty, calculated using the bootstrap method.

Uncertainty	$\lvert\eta^{\text{jet}}\rvert$ bins merged	Boundaries for p_T^{γ} bin merging
$m^{\text{jet}}/p_T^{\text{jet}}$	-	45 < p_T^{γ} <160 GeV, 160 < p_T^{γ} <1000 GeV
Generator	-	45 < p_T^{γ} <110 GeV, 110 < p_T^{γ} <310 GeV, 310 < p_T^{γ} <1000 GeV
PES: Material	$0 < \lvert\eta^{\text{jet}}\rvert < 2.1$	-
PES: Zee	$0 < \lvert\eta^{\text{jet}}\rvert < 2.1$	-
PES: Presampler	$0 < \lvert\eta^{\text{jet}}\rvert < 2.1$	45 < p_T^{γ} <110 GeV, 110 < p_T^{γ} <260 GeV, 260 < p_T^{γ} <400 GeV, 400 < p_T^{γ} <1000 GeV
Cut on leading anti-k_t $R = 0.4$ jet outside large-R jet	$0 < \lvert\eta^{\text{jet}}\rvert < 1.5$, $1.5 < \lvert\eta^{\text{jet}}\rvert < 2.1$	45 < p_T^{γ} <110 GeV, 110 < p_T^{γ} <1000 GeV
Cut on $\Delta\phi(\text{photon} - \text{jet})$	$0 < \lvert\eta^{\text{jet}}\rvert < 2.1$	45 < p_T^{γ} <110 GeV, 110 < p_T^{γ} <310 GeV, 310 < p_T^{γ} <1000 GeV
Photon Purity	-	-
JER	$0 < \lvert\eta^{\text{jet}}\rvert < 2.1$	45 < p_T^{γ} <260 GeV, 260 < p_T^{γ} <1000 GeV
Definition of inside/outside large-R jet	$0 < \lvert\eta^{\text{jet}}\rvert < 2.1$	45 < p_T^{γ} <110 GeV, 110 < p_T^{γ} <310 GeV, 310 < p_T^{γ} <1000 GeV
Cut on $p_T^{\text{subleading jet}}/p_T^{\gamma}$	$0 < \lvert\eta^{\text{jet}}\rvert < 2.1$	45 < p_T^{γ} <210 GeV, 210 < p_T^{γ} <1000 GeV
k-term	-	45 < p_T^{γ} <110 GeV, 110 < p_T^{γ} <260 GeV, 260 < p_T^{γ} <400 GeV, 400 < p_T^{γ} <1000 GeV

Table 7.2: Bin merging boundaries in $\lvert\eta^{\text{jet}}\rvert$ and p_T^{γ}. '-' means that no bin merging has been performed.

where ΔC_i^2 is the statistical uncertainty on the systematic uncertainty for each bin, $\langle p_{T,i}\rangle$ and $\langle\eta_i\rangle$ are the average p_{T} and η of the jets in the i^{th} η and p_T^{γ} bin, Gauss(x) is the amplitude of a Gaussian with a mean of 0 and a width of 1. Since the average reconstructed jet p_{T} and η in each η and p_T^{γ} bin are used for the smoothing, the uncertainties are now parametrised as a function of $p_T^{\text{reco jet}}$, rather than p_T^{γ}. σ_{p_T} and σ_η are the widths of the Gaussian kernel, which are chosen to be 0.22 and 0.15 respectively. σ_{p_T} and σ_η are optimised to give a minimal smoothing, where the χ^2 between the smoothed value and the original points is always less

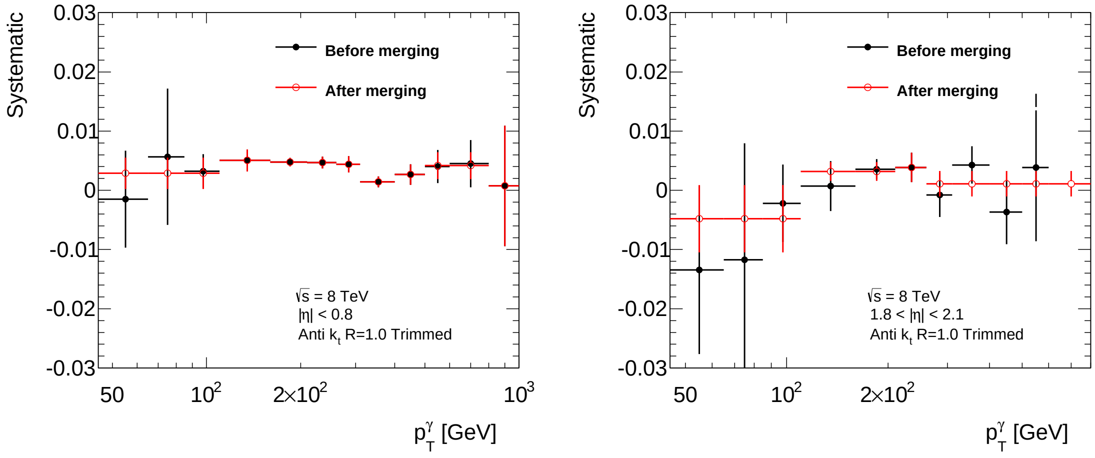

(a) (b)

Figure 7.11: The systematic uncertainty due to loosening the cut on $p_T^{\text{leading anti}-\text{k}_\text{T}\ \text{R}\,=\,0.4\ \text{jet outside large}-\text{R jet}}/p_T^\gamma$ from the nominal cut of 0.1 to a cut of 0.2 after merging into two $|\eta^{\text{jet}}|$ bins (black): a) $|\eta^{\text{jet}}| < 1.5$ and b) $1.5 < |\eta^{\text{jet}}| < 2.1$ and after merging p_T^γ bins (red).

than 5. A diagram to illustrate how the Gaussian kernel smoothing works in one dimension can be seen in Figure 7.13.

7.5.3 The Final Systematic Uncertainties Derived using the γ-jet Method

The final systematic uncertainties after the bin merging and smoothing can be seen in Figure 7.14 and the exact values can be found in Appendix A.2. The total uncertainty is the quadratic sum of the systematic uncertainties and the statistical uncertainty. It can be seen that the derived uncertainties are $\sim$ 1 % above 100 GeV for $|\eta^{\text{jet}}| < 0.8$, rising to $\sim$ 2-3 % for $|\eta^{\text{jet}}| > 0.8$. In all $|\eta^{\text{jet}}|$ regions the deviation of the data-to-MC ratio of the photon response from unity is a dominant systematic uncertainty. It is particularly dominant for $|\eta^{\text{jet}}| > 0.8$. Within $|\eta^{\text{jet}}| < 0.8$ the photon energy scale and the cuts against radiation give significant components to the total uncertainty. For $|\eta^{\text{jet}}| > 0.8$ the systematic uncertainties due to $m^{\text{reco jet}}/p_T^{\text{reco jet}}$ and the choice of Monte Carlo generator become important.

Future studies could investigate the possibility of correcting for the data-to-MC difference of the photon response, as is done for small-R jets. This would further reduce the

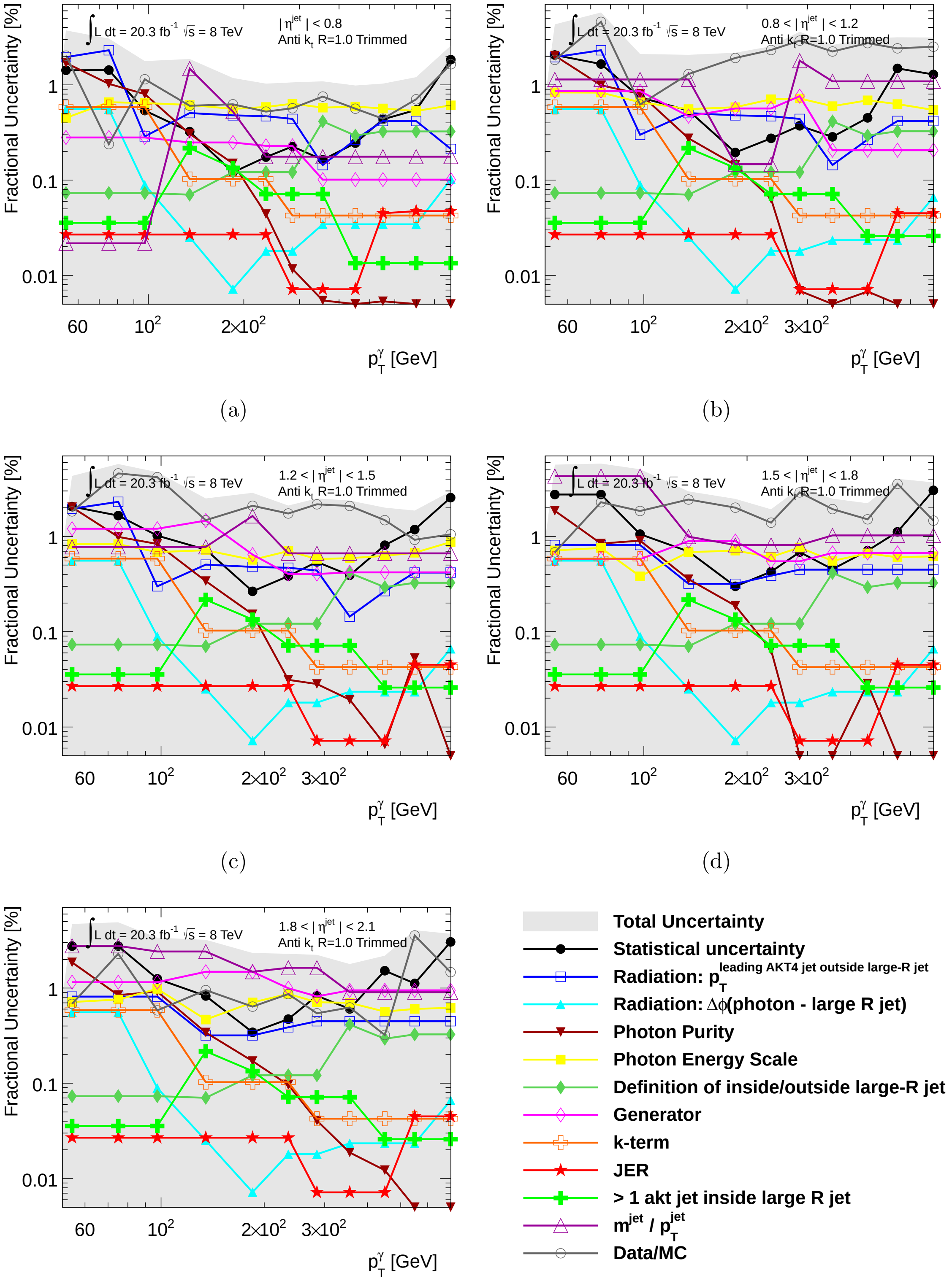

(a) (b)

(c) (d)

(e) (f)

Figure 7.12: The JES uncertainties for anti-k_t $R = 1.0$ trimmed jets derived using γ-jet events for (a) $|\eta^{\mathrm{jet}}| < 0.8$, (b) $0.8 < |\eta^{\mathrm{jet}}| < 1.2$, (c) $1.2 < |\eta^{\mathrm{jet}}| < 1.5$, (d) $1.5 < |\eta^{\mathrm{jet}}| < 1.8$ and (e) $1.8 < |\eta^{\mathrm{jet}}| < 2.1$. The uncertainties are shown after the bin merging and before the smoothing. Figure (f) is the legend for plots (a)-(e).

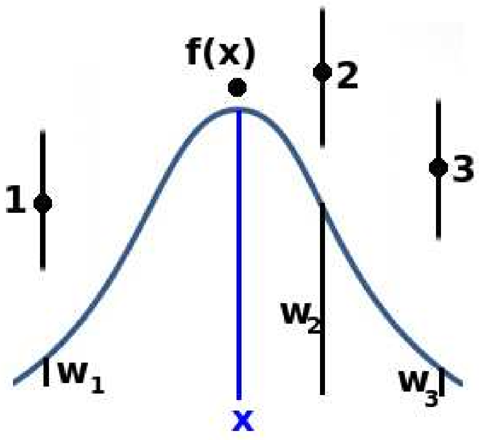

Figure 7.13: Illustration of Gaussian kernel smoothing. The Gaussian is centred at x and for each point (1,2 and 3) the weight (w_1, w_2 and w_3) is the amplitude of the Gaussian so that points further from the centre of the Gaussian get a smaller weight. The value of f(x) is then calculated as in Equation 7.6

.

JES uncertainty for large-R jets. However, studies would be required to combine the γ-jet uncertainties with the track-jet double ratio uncertainties for $p_{\mathrm{T}}>$ (800) 1000 GeV or the development of other methods such as multi-jet balance to measure the JES uncertainties for the high p_{T} region. Additionally, further studies into the dependence of the JES on the mass of the jet may help to find ways to reduce this component of the systematic uncertainty.

7.6 A Topology Uncertainty for Large-R Jets

The photon response measurements shown in Figure 7.3, and the uncertainties in Figure 7.14, are derived using γ-jet events where the large-R jet can contain more than one anti-k_t $R = 0.4$ jet. However, the uncertainties are used in a wide range of physics analyses where the large-R jet may contain the decay products of a W boson, Z boson, top quark or multiple quark or gluon jets. It is therefore important to consider whether an additional JES uncertainty is required to account for variations in the JES for large-R jets with these different topologies.

In the γ-jet sample used to derived the JES uncertainties, the large-R jets can encompass more than one small radius jet. The proportion of events where the large-R jet contains one

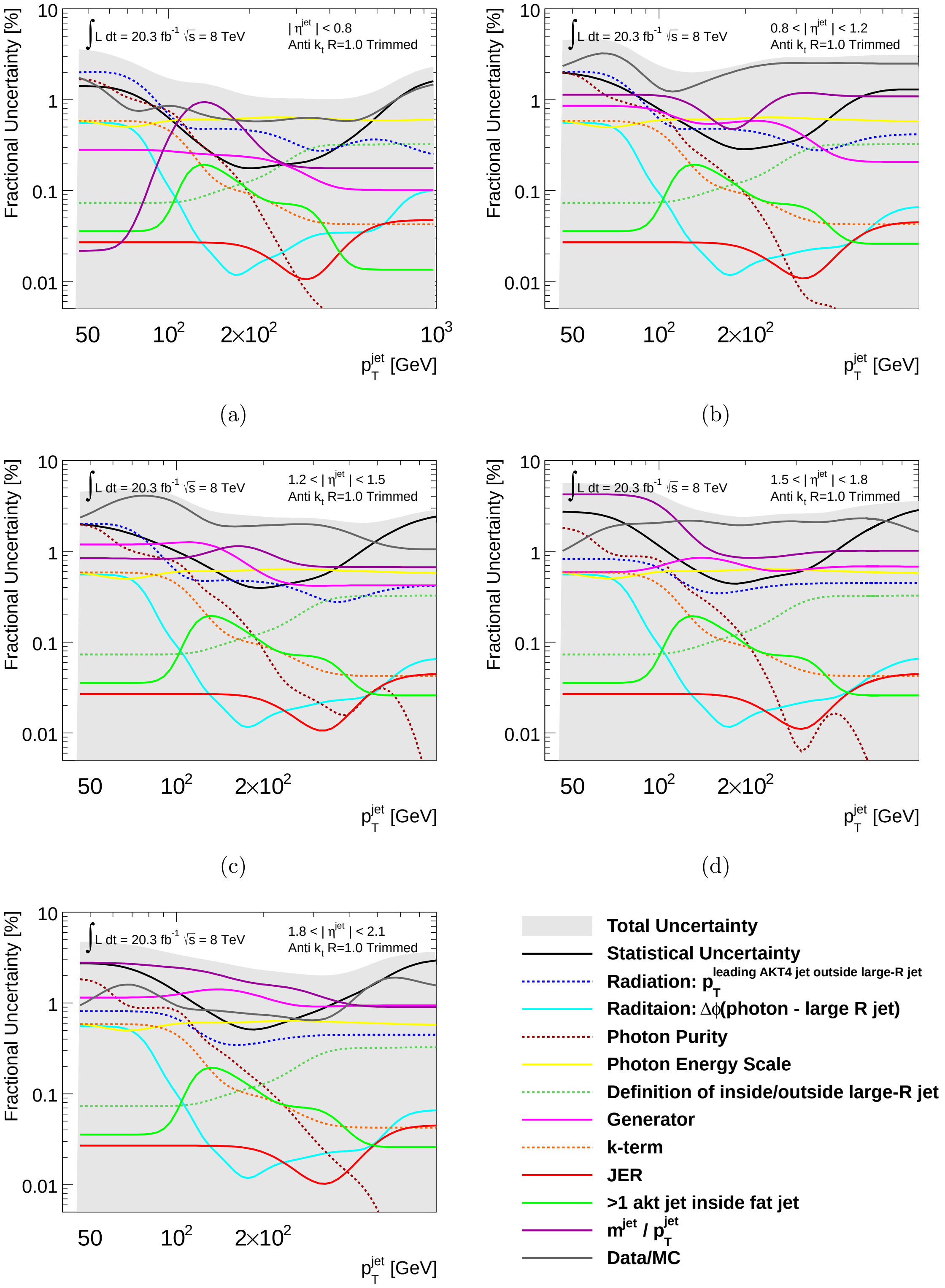

(a) (b)

(c) (d)

(e) (f)

Figure 7.14: The final JES uncertainties for anti-k_t jets $R = 1.0$ trimmed jets for (a) $|\eta^{\text{jet}}| < 0.8$ (b) $0.8 < |\eta^{\text{jet}}| < 1.2$, (c) $1.2 < |\eta^{\text{jet}}| < 1.5$, (d) $1.5 < |\eta^{\text{jet}}| < 1.8$ and (e) $1.8 < |\eta^{\text{jet}}| < 2.1$. Figure (f) is the legend for plots (a)-(e).

or more anti-k_t $R = 0.4$ jets can be seen in Figure 7.15. It can be seen that the number of large-R jets containing one anti-k_t $R = 0.4$ jet varies from ∼35 - 45 % depending on the value of p_T^γ, with a significant proportion of the remaining events containing two anti-k_t $R = 0.4$ jets or more. The photon response for events containing one, two or more than two anti-k_t $R = 0.4$ jets can be seen in Figures 7.16 a), b) and c) for $|\eta^{\text{jet}}| < 0.8$. The photon response for these different event topologies varies slightly in data and Monte Carlo, particularly for $p_T^\gamma < 100$ GeV. However, the data-to-MC ratio of the photon response is stable within statistical uncertainties.

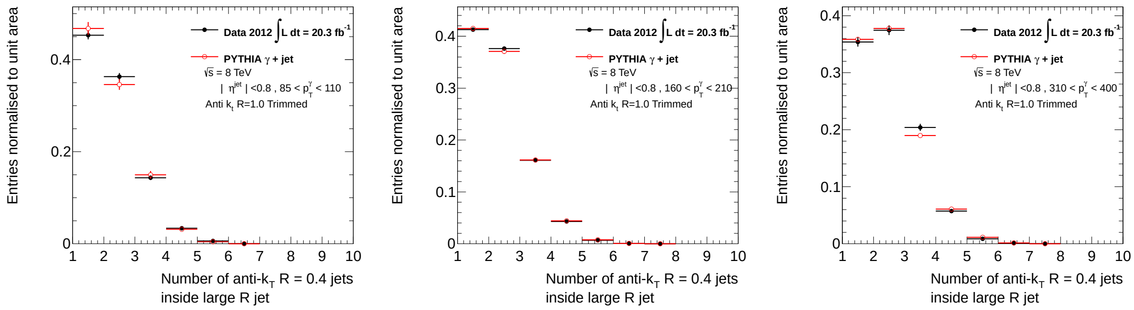

(a) (b) (c)

Figure 7.15: The fraction of anti-k_t $R = 0.4$ jets inside of the large-R jet in the bin $|\eta^{\text{jet}}| < 0.8$ for a) $85 < p_T^\gamma < 110$, b) $160 < p_T^\gamma < 210$ and c) $310 < p_T^\gamma < 400$.

The dependence of the JES uncertainties on the jet topology can also be studied by looking at the dependence of the photon response and the data-to-MC ratio of the photon response as a function of various jet substructure variables. In Figures 7.16 d), e) and f) the photon response as a function of $\sqrt{d_{12}}$ and τ_2/τ_1 [3] can be seen for $160 < p_T^\gamma < 210$ GeV and $|\eta^{\text{jet}}| < 0.8$. For this particular p_T^γ and $|\eta^{\text{jet}}|$ bin the general trends of the photon response are modelled by the Monte Carlo, with variations of up to ∼1-2 % between data and Monte Carlo.

Unfortunately, at high p_T^γ ($\gtrsim 300 - 400$ GeV) and high $|\eta^{\text{jet}}|$ ($\gtrsim 1.2$) the number of events available in the γ-jet sample is too low to be able to properly evaluate the dependence of the data-to-MC ratio of the photon response on these substructure variables. Furthermore, the number of events available in regions of phase space where the jet substructure is similar to that of jets used in physics analyses is particularly low. For example, in the $t\bar{t}$ semi-leptonic

---

[3] These substructure variables were introduced in Section 2.3

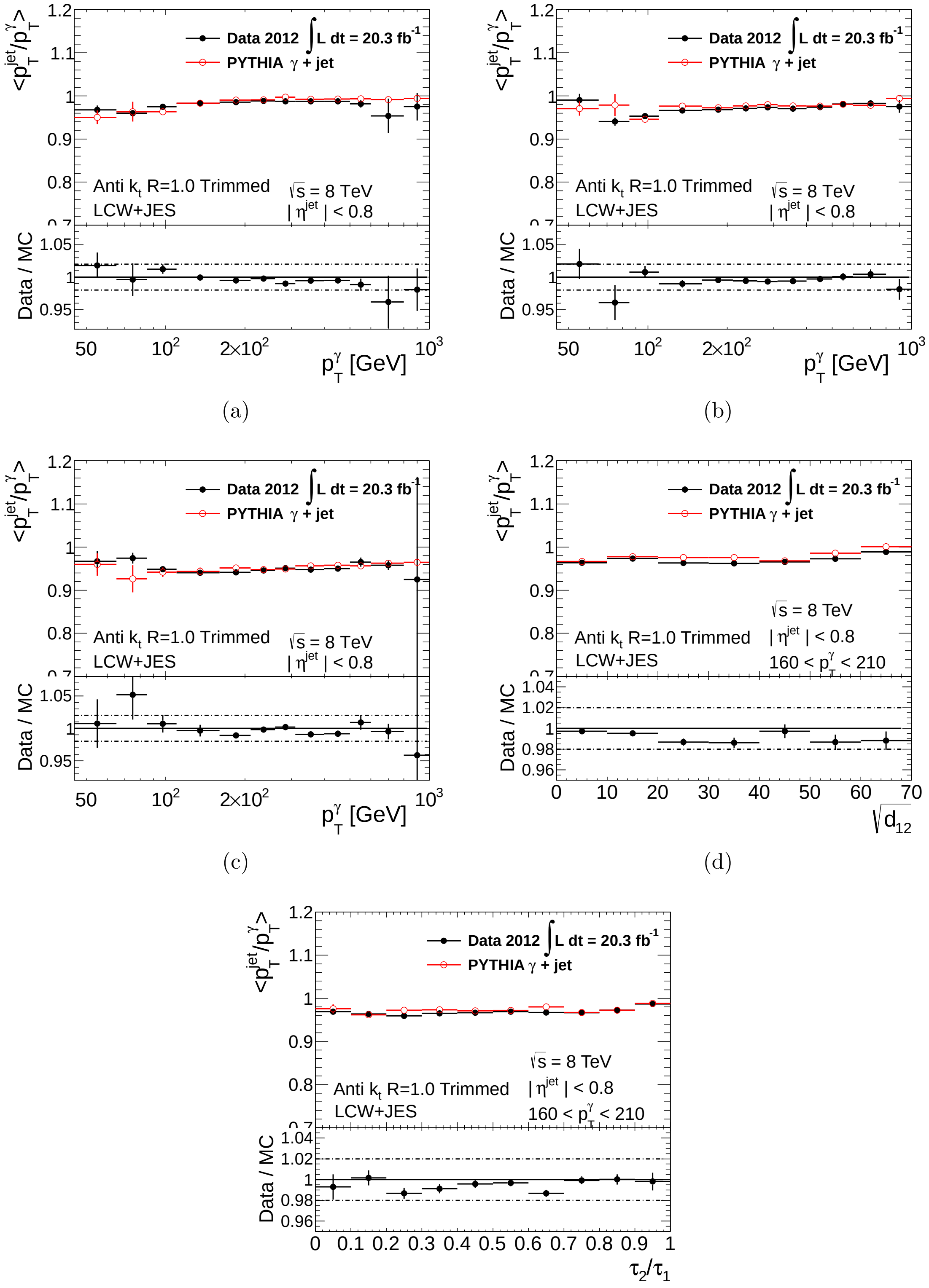

(a)

(b)

(c)

(d)

(e)

Figure 7.16: The average photon response for anti-k_t jets $R = 1.0$ trimmed jets for (a) events with 1 anti-k_t $R = 0.4$ jet inside the large-R jet as a function of p_T^γ, (b) 2 anti-k_t $R = 0.4$ jets inside the large-R jet as a function of p_T^γ, (c) > 2 anti-k_t $R = 0.4$ jets inside the large-R jet as a function of p_T^γ, (d) the average photon response as a function of $\sqrt{d_{12}}$ for $160 < p_T^\gamma < 210$ GeV, and (e) the average photon response as a function of $\tau_2/\tau 1$ for $160 < p_T^\gamma < 210$ GeV. All plots are for $|\eta^{\rm jet}| < 0.8$ and only statistical uncertainties are shown.

resonance search, large-R jets are required to have $\sqrt{d_{12}} > 40$ GeV, $p_T^{\rm jet} > 300$ GeV and $m^{\rm jet} > 100$ GeV in order to reduce background from QCD jets and accept top jets with real hard substructure. However, in the γ-jet sample few events are available in this region of phase space.

Differences in the JES between data and Monte Carlo for different event topologies are already accounted for by the systematic uncertainty on $m^{\rm reco\ jet}/p_T^{\rm reco\ jet}$. In order to further investigate the variation of the JES for different jet topologies the truth response, $(p_T^{\rm truth\ jet} - p_T^{\rm reco\ jet})/p_T^{\rm truth\ jet}$, was measured using $t\bar{t}$ and W+jets Monte Carlo events. The truth response was derived for the following topologies:

- $t\bar{t}$ events where the large-R jet contains all the decay products of the hadronically decaying top quark;
- $t\bar{t}$ events where the large-R jet contains only the decay products of the hadronicaly decaying W boson from the top quark;
- $t\bar{t}$ events where the large-R jet does not contain any of the decay products of the hadronically decaying top quark;
- W+jets events where the W decays leptonically and the large-R jet contains one or more of the jets in the event.

The resulting truth jet response can be seen in Figure 7.17. The envelope of the truth response measured in these different Monte Carlo samples is taken as an additional systematic uncertainty. The topology uncertainty is ~ 4 % for $p_{\rm T} < 300$ GeV, falling to 1-2 % for $p_{\rm T} > 300$ GeV. This topology uncertainty is specifically designed for the $t\bar{t}$ semi-leptonic resonance search and was only measured for $p_{\rm T} > 200$ GeV. Any physics analysis wishing to use large-R jets with $p_{\rm T} < 200$ GeV or with other topologies (e.g. large-R jets containing multiple quark or gluon jets) will need to assess the topology uncertainty for their particular event topology.

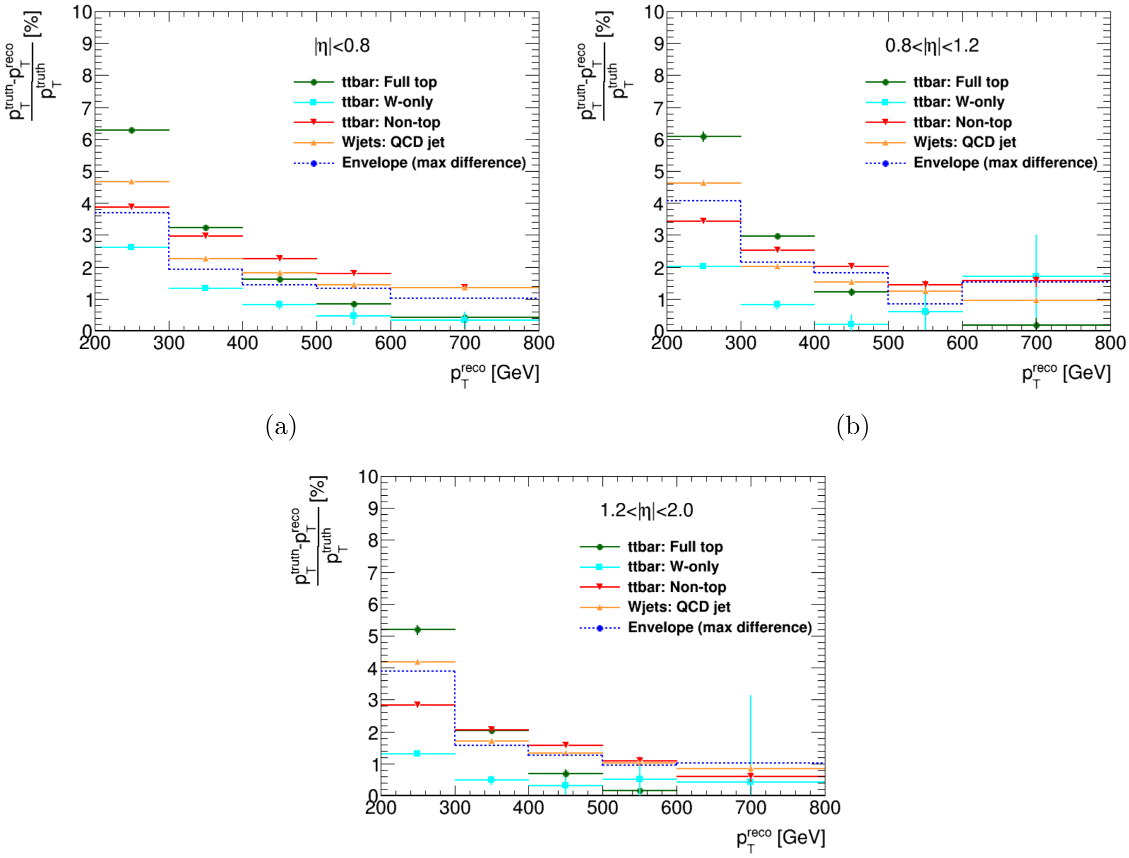

(a)

(b)

(c)

Figure 7.17: $(p_T^{truth\ jet} - p_T^{reco\ jet})/p_T^{truth\ jet}$ measured for large-R jets containing the decay products of the top quark in $t\bar{t}$ events, the hadronically decaying W boson from the top decay in $t\bar{t}$ events, large-R jets that do not contain any of the decay products of the top quark in $t\bar{t}$ events and large-R jets containing the jet(s) in W+jet events where the W decays leptonically for a) $|\eta^{\mathrm{jet}}| < 0.8$, b) $0.8 < |\eta^{\mathrm{jet}}| < 1.2$ and c) $0.8 < |\eta^{\mathrm{jet}}| < 2.0$ [113].

7.7 Pile-up Uncertainty for Large-R Jets

The derivation of the pile-up uncertainty for large-R jets is based on the procedure followed for anti-k_t $R = 0.4$ and $R = 0.6$ jets [98], which was briefly discussed in Section 5.2.2. In 2012 data the method [98] is designed for the case where the jets have been corrected for pile-up using the jet areas and the residual offset correction. However, for large-R jets no pile-up corrections are applied and therefore the uncertainties are modified accordingly.

Two components are derived for the large-R jet pile-up uncertainties: one to account for variations of the jet p_{T} due to out-of-time pile-up, parametrised by μ; and one to account for variations of the jet p_{T} due to in-time pile-up, parametrised by NPV. These components are defined as follows:

$$\Delta_{\mu} = \pm\Delta\left(\frac{\partial p_T^{\mathrm{jet}}}{\partial\mu}\right)\cdot(\mu - \mu_{\mathrm{ref}}), \tag{7.8}$$

$$\Delta_{\mathrm{NPV}} = \pm\Delta\left(\frac{\partial p_T^{\mathrm{jet}}}{\partial \mathrm{NPV}}\right)\cdot(\mathrm{NPV} - \mathrm{NPV}_{\mathrm{ref}}) \tag{7.9}$$

where μ and NPV are the μ and NPV of the event under consideration and μ_{ref} and $\mathrm{NPV}_{\mathrm{ref}}$ are the average values for the 2012 dataset (20.7 and 11.8 respectively). $\Delta\left(\frac{\partial p_T^{\mathrm{jet}}}{\partial\mu}\right)$ and $\Delta\left(\frac{\partial p_T^{\mathrm{jet}}}{\partial \mathrm{NPV}}\right)$ are the gradients of the jet p_{T} vs. μ and NPV respectively, as measured in data. In this way, Δ_{μ} and Δ_{NPV} are an estimation of the additional transverse momentum in a jet for an event with a given value of μ and NPV, when comparing to the p_{T} of jets reconstructed with the average pile-up conditions of the 2012 dataset. The gradients are measured in data and Monte Carlo in order to assess an uncertainty due to any differences between the way in which pile-up contributes to the jet p_{T} in data and Monte Carlo.

It is expected that the gradient of the jet p_{T} vs NPV and μ will be different in different p_{T} ranges since energy deposits due to pile-up contribute to a larger fraction of the jet p_{T} at lower p_{T} than at higher p_{T}. $\frac{\partial p_T^{\mathrm{jet}}}{\partial\mu}$ and $\frac{\partial p_T^{\mathrm{jet}}}{\partial \mathrm{NPV}}$ must, therefore, be measured as a function of p_{T}. Furthermore, they should be derived in p_{T} bins defined by the p_{T} of an object that is stable against pile-up in order to avoid biasing the measurement.

This can be done using Z-jet or γ-jet events with a back-to-back topology, where the jet is used to derive $\frac{\partial p_T^{\mathrm{jet}}}{\partial \mu}$ and $\frac{\partial p_T^{\mathrm{jet}}}{\partial \mathrm{NPV}}$ and the Z boson or photon are used in order to parametrise the gradients as a function of p_T^{γ} or p_T^{Z}. This requires the full event selection to select events with a back-to-back topology (as described for the γ-jet analysis in Section 7.1). However, after this selection the number of selected events mean that it is only possible to measure $\frac{\partial p_T^{\mathrm{jet}}}{\partial \mu}$ inclusively in NPV and $\frac{\partial p_T^{\mathrm{jet}}}{\partial \mathrm{NPV}}$ inclusively in μ. Ideally, $\frac{\partial p_T^{\mathrm{jet}}}{\partial \mu}$ should be measured for fixed values of NPV in order that it provides a measure of the dependence of the jet p_{T} on out-of-time pile-up and $\frac{\partial p_T^{\mathrm{jet}}}{\partial \mathrm{NPV}}$ should be measured for fixed values of μ in order that it provides a measure of the dependence of the jet p_{T} on in-time pile-up.

Therefore, in order to gain statistics, track-jets are used as the reference object, where the track-jet is matched to the reconstructed calorimeter jet using a geometrical matching criteria ($\Delta R(\text{track jet} - \text{reco jet}) < 0.7$). The reconstructed calorimeter jet is used to measure $\frac{\partial p_T^{\mathrm{jet}}}{\partial \mu}$ and $\frac{\partial p_T^{\mathrm{jet}}}{\partial \mathrm{NPV}}$ and the track-jet is used to parametrise the results as a function of $p_T^{\text{track jet}}$.

Since these studies are performed in data, a trigger must be used to select events. However, if a jet trigger is used then this may bias the results, since the jets that are used for the trigger may be sensitive to pile-up. Therefore, instead of jet triggers, the photon triggers used for the 2012 large-R γ-jet analysis are used [4] to select events and the photon selection criteria described in Sections 6.2 and 7.1 are used to select events containing a good photon. However, since the track-jet is used as a reference object, there is no need to ensure that the photon and the jet are back-to-back. Therefore, the requirements on $\Delta\phi(\gamma - \text{jet})$ and $p_T^{\text{leading anti}-k_{\mathrm{T}}\text{ R = 0.4 jet outside large}-\text{R jet}}/p_T^{\gamma}$ are not needed and a sufficient number of events remain following selection to allow for the results to be binned exclusively in NPV and μ.

A 3D binning is used with NPV and μ bins of width 2 and the following track jet p_{T} bins: `25,35,45,55,65,75,85,95,105,125,145,200,250 GeV`. The p_{T} bins are chosen to be as fine as possible, whilst retaining a sufficient number of events for the analysis of the pile-up dependencies. Above 250 GeV there is an insufficient number of events to derive the

---

[4] These triggers were introduced in Section 3.6.

gradients. The uncertainty is measured for $|\eta^{\text{jet}}| < 2.1$. In order to avoid overlap with the photons, calorimeter jets with $\Delta R(\text{reco jet} - \text{photon}) < 1.0$ are not considered.

Examples of $\frac{\partial p_T^{\text{jet}}}{\partial \mu}$ and $\frac{\partial p_T^{\text{jet}}}{\partial \text{NPV}}$ for $55 < p_T^{\text{track jet}} < 65$ GeV and $105 < p_T^{\text{track jet}} < 125$ GeV can be seen in Figure 7.18 and the straight line fit, which is used to extract the gradients, is shown in red. In Figure 7.19, $\frac{\partial p_T^{\text{jet}}}{\partial \text{NPV}}$ can be seen, as measured for different values of μ for $55 < p_T^{\text{track jet}} < 65$ GeV and $105 < p_T^{\text{track jet}} < 125$ GeV and $\frac{\partial p_T^{\text{jet}}}{\partial \mu}$ can be seen as measured for different values of NPV.

To define a single value of $\frac{\partial p_T^{\text{jet}}}{\partial \mu}$ and $\frac{\partial p_T^{\text{jet}}}{\partial \text{NPV}}$, for each track jet p_{T} bin $\frac{\partial p_T^{\text{jet}}}{\partial \mu}$ is averaged over NPV and $\frac{\partial p_T^{\text{jet}}}{\partial \text{NPV}}$ is averaged over μ. These averages and their corresponding error bands can also be seen in Figure 7.19. The resulting averages of $\frac{\partial p_T^{\text{jet}}}{\partial \mu}$ and $\frac{\partial p_T^{\text{jet}}}{\partial \text{NPV}}$, as a function of track jet p_{T}, can be seen in Figure 7.20 for data and Monte Carlo. The dependence of the jet p_{T} on NPV decreases rapidly with increasing track jet p_{T}. A much smaller dependence of the jet p_{T} on μ is observed.

In order to extract $\Delta\left(\frac{\partial p_T^{\text{jet}}}{\partial \mu}\right)$ and $\Delta\left(\frac{\partial p_T^{\text{jet}}}{\partial \text{NPV}}\right)$ from Figure 7.20, first the track jet p_{T} bins are translated into reconstructed jet p_{T} bins using the average reconstructed jet p_{T} in each track jet p_{T} bin. The distribution of the reconstructed jet p_{T}, as a function of track jet p_{T}, which was used for this translation, can be seen in Figure 7.21.

Next, the distribution of $\frac{\partial p_T^{\text{jet}}}{\partial \mu}$ and $\frac{\partial p_T^{\text{jet}}}{\partial \text{NPV}}$ vs reconstructed jet p_{T} in data is fit with an empirical function of the form $a + b\ log(\frac{p_T}{50\ GeV})$. This function is also used to parametrise the p_{T} dependence of the gradients for small radius jets [98]. The function of this function is to capture the p_{T} dependence of $\frac{\partial p_T^{\text{jet}}}{\partial \mu}$ and $\frac{\partial p_T^{\text{jet}}}{\partial \text{NPV}}$ and it can be seen in black in Figures 7.22 a) and b). The data is used for this fit rather than the Monte Carlo due to the much smaller statistical uncertainty. The red open points Figures 7.22 a) and b) are the quadratic sum of the statistical uncertainty in data, the statistical uncertainty in Monte Carlo and the data-to-MC difference of the gradients. The error bars on the red open points show only the statistical component of this uncertainty. This uncertainty is fit with a constant since no obvious p_{T} dependence is observed. The maximum of either the gradient in data or the value of the calculated uncertainty is used for the values of $\Delta\left(\frac{\partial p_T^{\text{jet}}}{\partial \text{NPV}}\right)$ and $\Delta\left(\frac{\partial p_T^{\text{jet}}}{\partial \mu}\right)$. This prevents

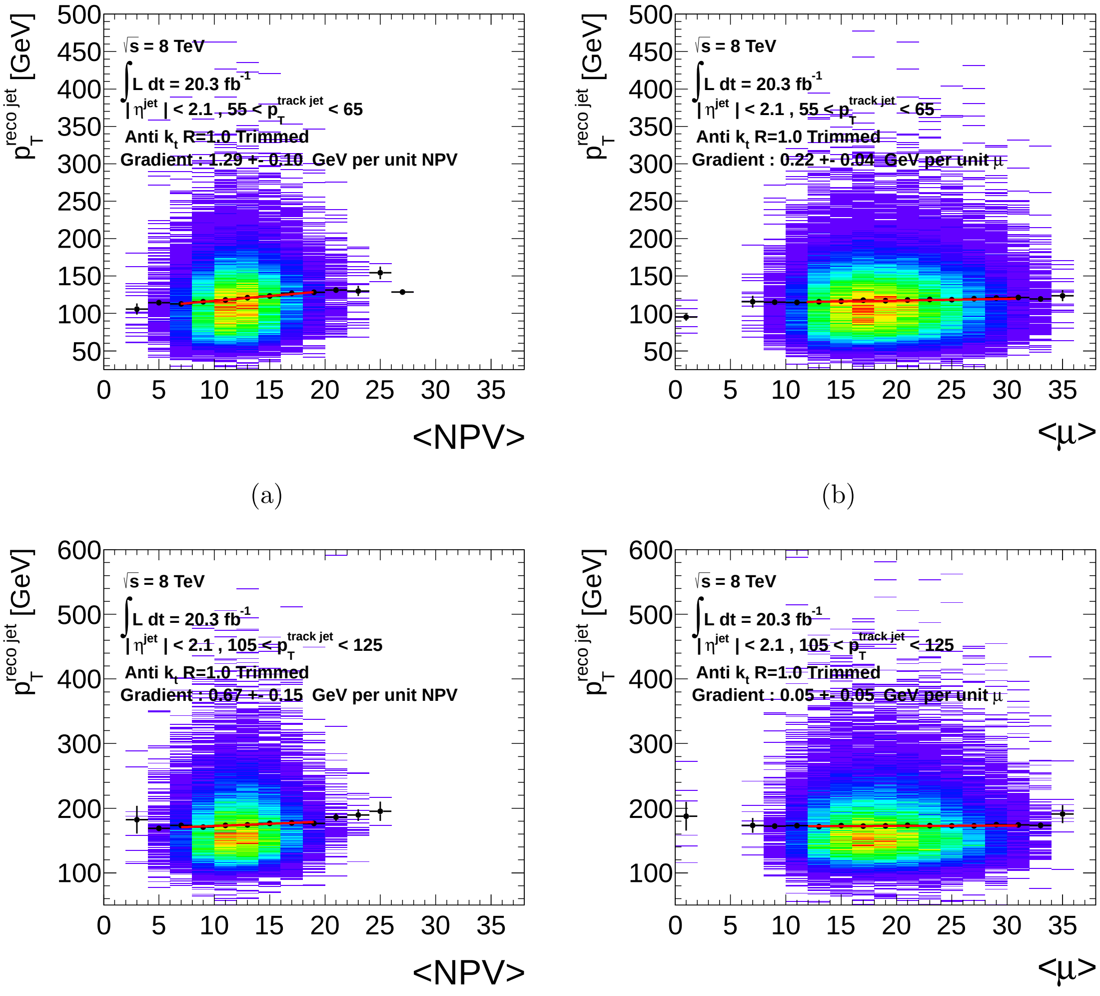

(a) (b)

(c) (d)

Figure 7.18: (a) The jet p_{T} vs NPV for jets with 55 GeV $< p_T^{\text{track jet}} <$ 65 GeV and $20 < \mu < 22$, (b) the jet p_{T} vs μ for jets with 55 GeV $< p_T^{\text{track jet}} <$ 65 GeV and 10 < NPV < 12, (c) the jet p_{T} vs NPV for jets with 105 GeV $< p_T^{\text{track jet}} <$ 125 GeV and $20 < \mu < 22$ and (d) the jet p_{T} vs μ for jets with 105 GeV $< p_T^{\text{track jet}} <$ 125 GeV and 10 < NPV < 12.

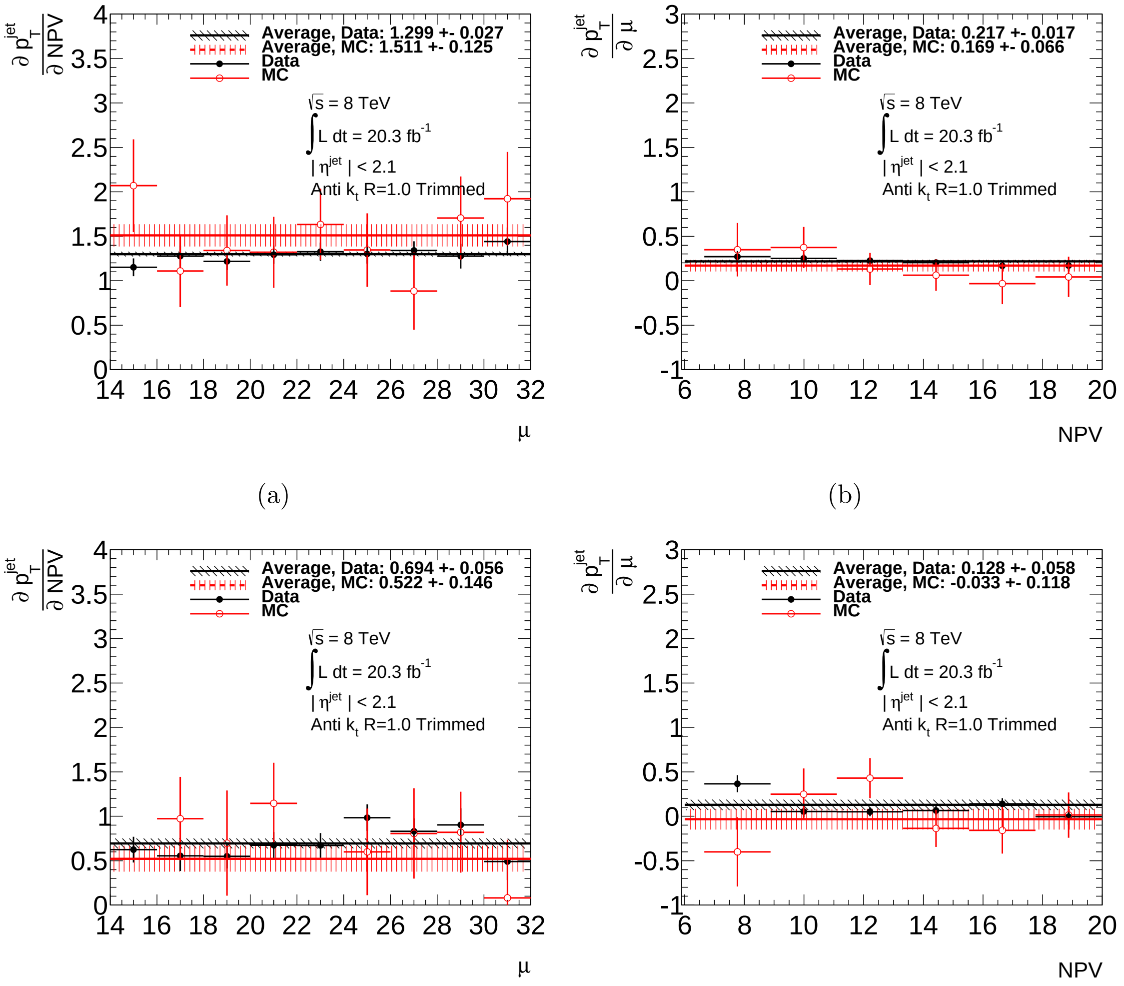

(a) (b)

(c) (d)

Figure 7.19: (a) $\partial p_T^{\rm jet}/\partial$NPV for different values of μ for 55 GeV $< p_T^{\rm track\ jet} <$ 65 GeV, (b) $\partial p_T^{\rm jet}/\partial\mu$ for different values of NPV for 55 GeV $< p_T^{\rm track\ jet} <$ 65 GeV, (c) $\partial p_T^{\rm jet}/\partial$NPV for different values of μ for 105 GeV $< p_T^{\rm track\ jet} <$ 125 GeV and (d) $\partial p_T^{\rm jet}/\partial\mu$ for different values of NPV for 105 GeV $< p_T^{\rm track\ jet} <$ 125 GeV.

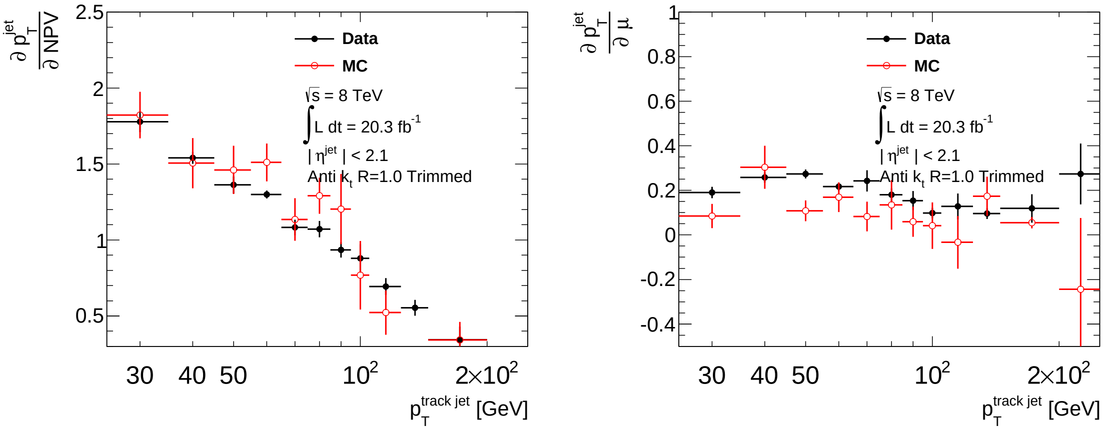

(a) (b)

Figure 7.20: The gradient of the jet p_{T} as a function of (a) NPV and (b) μ, in bins of track jet p_{T}.

$\Delta\left(\frac{\partial p_T^{\mathrm{jet}}}{\partial \mathrm{NPV}}\right)$ and $\Delta\left(\frac{\partial p_T^{\mathrm{jet}}}{\partial \mu}\right)$ becoming smaller than the uncertainty on the measurement, as can be seen in Figures 7.22 c) and d). For $p_{\mathrm{T}} > 262$ GeV the gradient vs NPV is 0.23 and for $p_{\mathrm{T}} > 187$ GeV the gradient vs μ is 0.14. The values shown in Figure 7.22 c) are used for $\Delta\left(\frac{\partial p_T^{\mathrm{jet}}}{\partial \mathrm{NPV}}\right)$ and the values shown in Figure 7.22 d) are used for $\Delta\left(\frac{\partial p_T^{\mathrm{jet}}}{\partial \mu}\right)$.

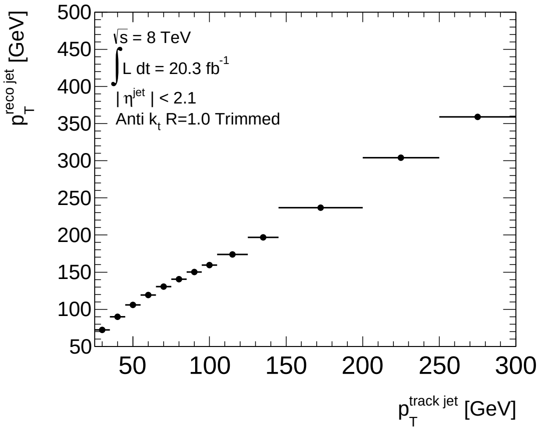

Figure 7.21: The average calorimeter jet p_{T} as a function of track jet p_{T}.

The uncertainty due to pile-up is propagated through analyses by taking Δ_μ and Δ_{NPV} from equations 7.8 and 7.9 on a jet-by-jet basis and shifting the jet p_{T} up and down accordingly. The size of Δ_μ and Δ_{NPV}, as a percentage of the jet p_{T}, and as a function of the NPV or μ of the event, can be seen in Figure 7.23 for two example jet p_{T} values of 100 and 300 GeV.

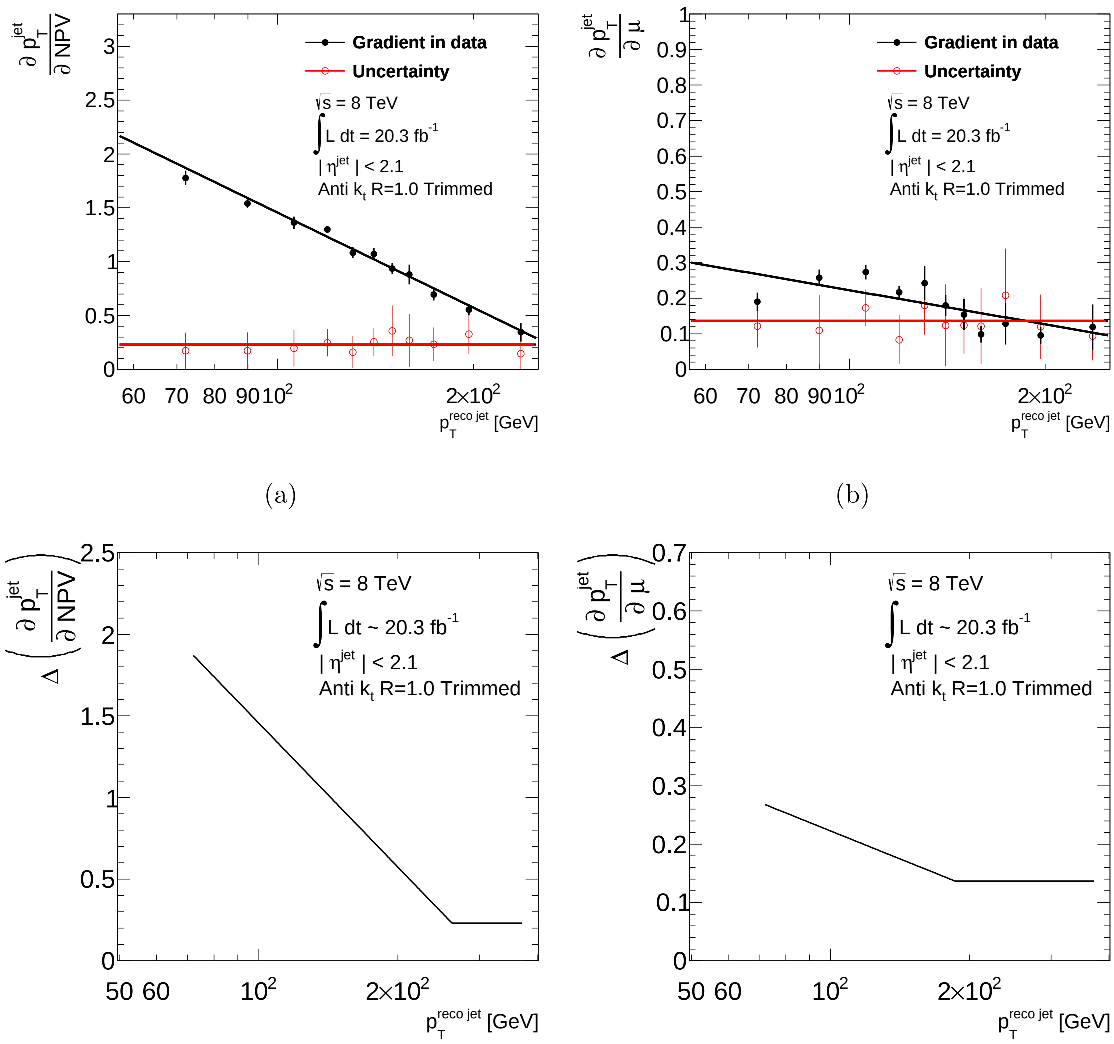

(a) (b)

(c) (d)

Figure 7.22: The gradient of the jet p_{T} vs (a) NPV and (b) μ in data (red line) and the difference of the gradients in data and Monte Carlo (black line) as a function of calorimeter jet p_{T}. (c) shows Δ_{NPV} derived using the fits from (a) and (d) shows Δ_{μ} derived using the fits from (b).

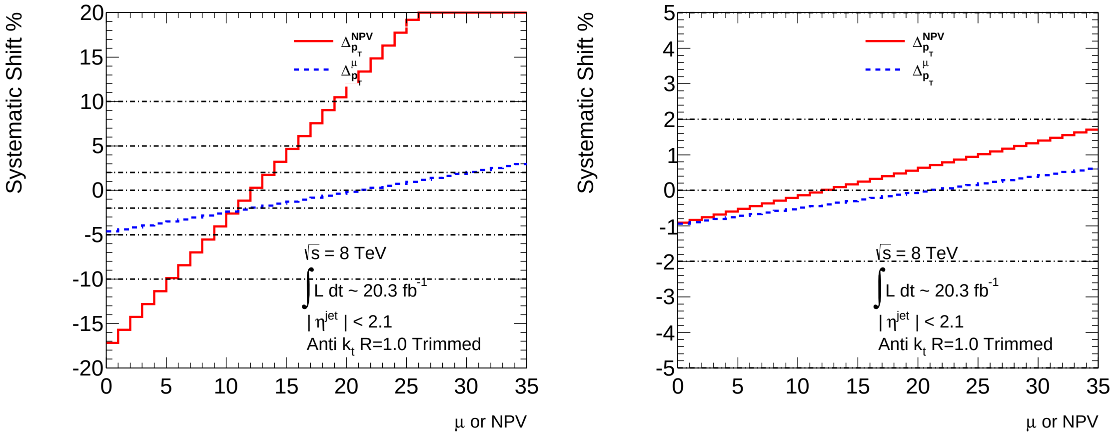

(a) (b)

Figure 7.23: The systematic shifts, calculated from Equations 7.8 and 7.9 as a function of μ and NPV of the event for (a) $p_T^{\text{jet}} = 100$ GeV and (b) $p_T^{\text{jet}} = 300$ GeV.

7.8 Comparison and Combination of Large-R JES Uncertainties Derived with the Track-Jet Double Ratio and γ-jet Methods

The large-R jet JES uncertainties, derived from the track-jet double ratio method and the γ-jet method, can be seen in Figure 7.24 for five different values of $|\eta^{\text{jet}}|$. The track-jet double ratio uncertainties are shown for three example values of $m^{\text{reco jet}}/p_T^{\text{reco jet}}$. It can be seen that the γ-jet uncertainties are significantly smaller than the track-jet double ratio uncertainties. For $|\eta^{\text{jet}}| = 0$, the uncertainty derived using γ-jet events is ~2.5 % smaller than the track-jet uncertainty. For $|\eta^{\text{jet}}| > 0.8$ there is a reduction of up to ~1.5 %.

The γ-jet uncertainties shown in Figure 7.24 are derived up to 1 TeV (800 GeV) for $|\eta^{\text{jet}}| < 0.8$ ($|\eta^{\text{jet}}| > 0.8$). However, a JES uncertainty is required for higher p_{T}. Therefore the γ-jet uncertainty is frozen at 1 TeV (800 GeV) for $|\eta^{\text{jet}}| < 0.8$ ($|\eta^{\text{jet}}| > 0.8$). For higher p_{T} an extra uncertainty is derived to account for the difference between the γ-jet uncertainty and the track-jet uncertainty (which is measured up to 1.2 TeV).

In order to provide a smooth transition for this additional uncertainty an interpolation is performed. The additional uncertainty (known as the interpolation component) is defined in the following way:

$$I = \begin{cases} 0 & : p_T^i < p_T^{\text{low interp}} \\ \frac{p_T^i - p_T^{\text{low interp}}}{p_T^{\text{high interp}} - p_T^{\text{low interp}}} \sqrt{\sigma(\text{track} - \text{jet})^2 - \sigma(\gamma - \text{jet})^2} & : p_T^{\text{low interp}} < p_T^i < p_T^{\text{high interp}} \\ \sqrt{\sigma(\text{track} - \text{jet})^2 - \sigma(\gamma - \text{jet})^2} & : p_T^i > p_T^{\text{high interp}} \end{cases} \tag{7.10}$$

where $\sigma(\text{track} - \text{jet})$ is the track jet double ratio uncertainty, $\sigma(\gamma - \text{jet})$ is the total γ-jet uncertainty and p_T^i is the p_{T} value under consideration in units of GeV. For $|\eta^{\text{jet}}| < 0.8$ the interpolation is performed between $p_T^{\text{low interp}} = 900$ GeV and $p_T^{\text{high interp}} = 1.1$ TeV. For $|\eta^{\text{jet}}| > 0.8$ the interpolation is performed between $p_T^{\text{low interp}} = 700$ GeV and $p_T^{\text{high interp}} = 900$ GeV. The uncertainties are also interpolated between $|\eta^{\text{jet}}|$ bins, which results in a gradual shift of $p_T^{\text{low interp}}$ ($p_T^{\text{high interp}}$) from 900 GeV to 700 GeV (1100 GeV to 900 GeV) in the region $0.7 < |\eta^{\text{jet}}| < 0.9$. This gives a smooth transition for the interpolation component over the full $|\eta^{\text{jet}}|$ range.

The quadratic sum of the γ-jet uncertainties and the interpolation component ($\sqrt{\sigma(\gamma - \text{jet})^2 + I^2}$) can be seen in Figure 7.24. The interpolation component is defined such that, when it is added in quadrature with the γ-jet uncertainties, it gives the total γ-jet uncertainty for $p_{\text{T}} < p_T^{\text{low interp}}$. For $p_T^{\text{low interp}} < p_T < p_T^{\text{high interp}}$ it gives the interpolation between the γ-jet and track-jet double ratio uncertainty. For $p_{\text{T}} > p_T^{\text{high interp}}$ it gives the track-jet double ratio uncertainty.

Previously, only the track-jet double ratio uncertainties were considered and they were sufficiently conservative that other sources of systematic uncertainty on the JES could be ignored. However, the new γ-jet uncertainties are much more precise (on the level of 1-3 %). It is, therefore, important to consider additional sources of uncertainty that effect the absolute value of the JES, as well as the data-to-MC differences which are evaluated using the γ-jet method. Therefore, the pile-up and topology uncertainties that were discussed in Sections 7.6 and 7.7 must also be considered.

The full set of new large-R jet uncertainties, including the pile-up and topology uncertainties, can be seen in Figure 7.25. For the pile-up uncertainty the systematic shift of the jet p_{T} for an NPV value evaluated at one σ from the average value of NPV is shown, and similarly for μ. It can be seen that the pile-up uncertainty gives a small contribution to the total uncertainty. The topology uncertainty is the dominant systematic uncertainty for $p_T < 500$ (300) GeV for $|\eta^{\mathrm{jet}}| < 0.8$ ($|\eta^{\mathrm{jet}}| > 0.8$).

The new total JES uncertainty (including the γ-jet, topology and pile-up uncertainties) for large-R jets, is reduced from ~3-4 % to ~2 % for $300 < p_T < 700$ GeV and $|\eta^{\mathrm{jet}}| < 0.8$, in comparison to the old JES uncertainties. A smaller reduction of $0.5 - 1$ % is seen for higher $|\eta^{\mathrm{jet}}|$.

7.8.1 The Effect of the Large-R JES Uncertainties in the $t\bar{t}$ Semi-leptonic Resonance Search

As discussed in Chapter 2, the JES uncertainty of large-R jets is a large source of systematic uncertainty for analyses using large-R jets. The effect of using the new anti-k_t $R = 1.0$ trimmed jet JES uncertainties, which have been discussed in this Chapter, is evaluated in the context of the $t\bar{t}$ semi-leptonic resonance search. In this analysis, anti-k_t $R = 1.0$ trimmed jets are used to capture the decay products of the hadronically decaying top quark, for events where the top quark is highly boosted. The JES uncertainty was found to be one of the dominant systematic uncertainties in previous iterations of the analysis. Full details can be found in Refs. [55–58].

The impact of the new uncertainties on the yield of the analysis has been assessed for the full 2012 dataset with 20.4 fb^{-1} of data [58]. These can be seen, along with the yield for the old track-jet double ratio uncertainties, in Table 7.3. The new JES uncertainties are propagated through the analysis using three different components: the deviation of the data-to-MC ratio from unity from the γ-jet analysis, the topology uncertainty, and all the other JES uncertainties summed in quadrature (ie. all γ-jet uncertainties except the data-to-

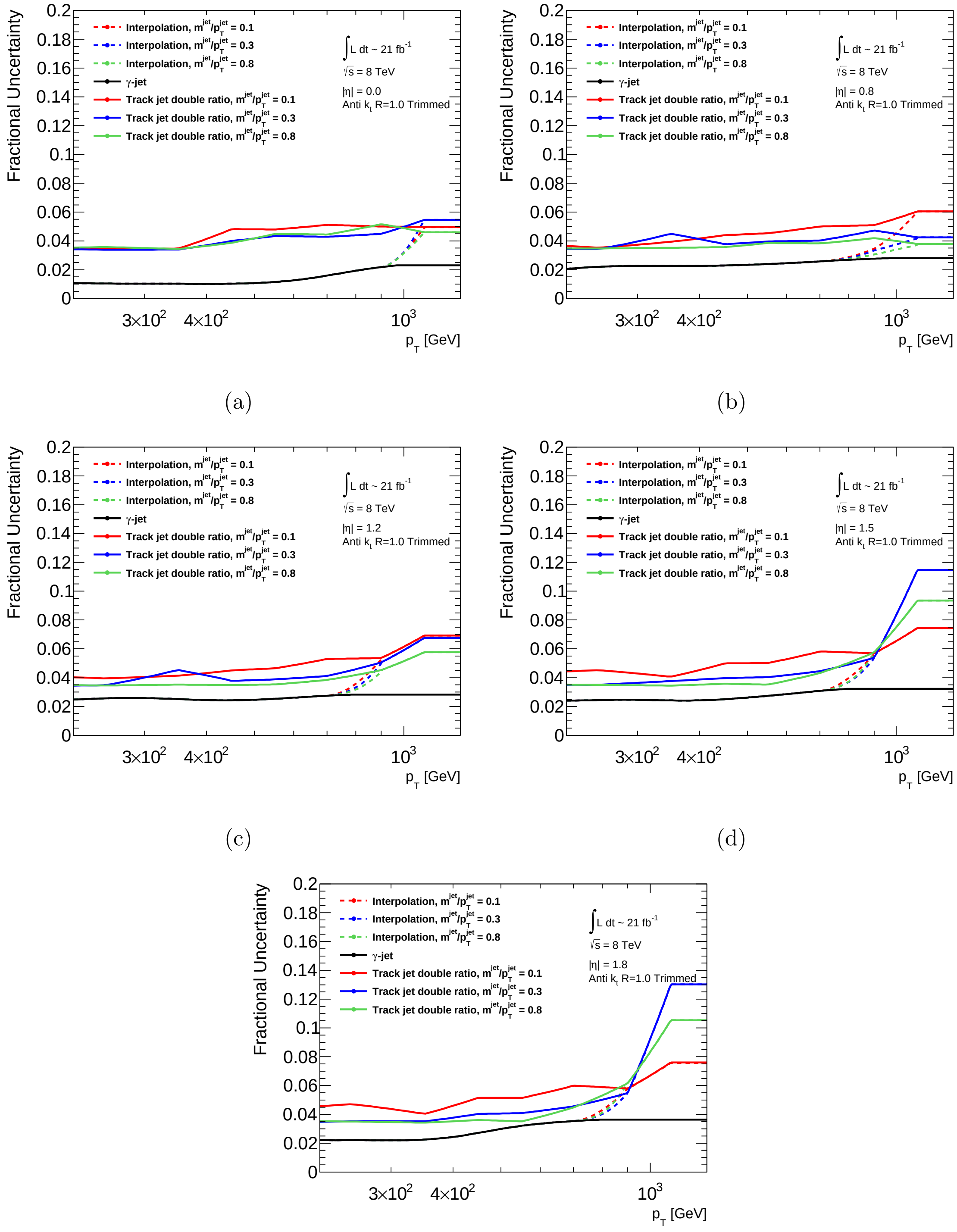

(a) (b)

(c) (d)

(e)

Figure 7.24: The γ-jet and track jet double ratio JES uncertainties for a) $|\eta^{\text{jet}}| = 0$, b) $|\eta^{\text{jet}}| = 0.8$, c) $|\eta^{\text{jet}}| = 1.2$, d) $|\eta^{\text{jet}}| = 1.5$ and e) $|\eta^{\text{jet}}| = 1.8$. The interpolation between the uncertainties of the two different methods is also shown.

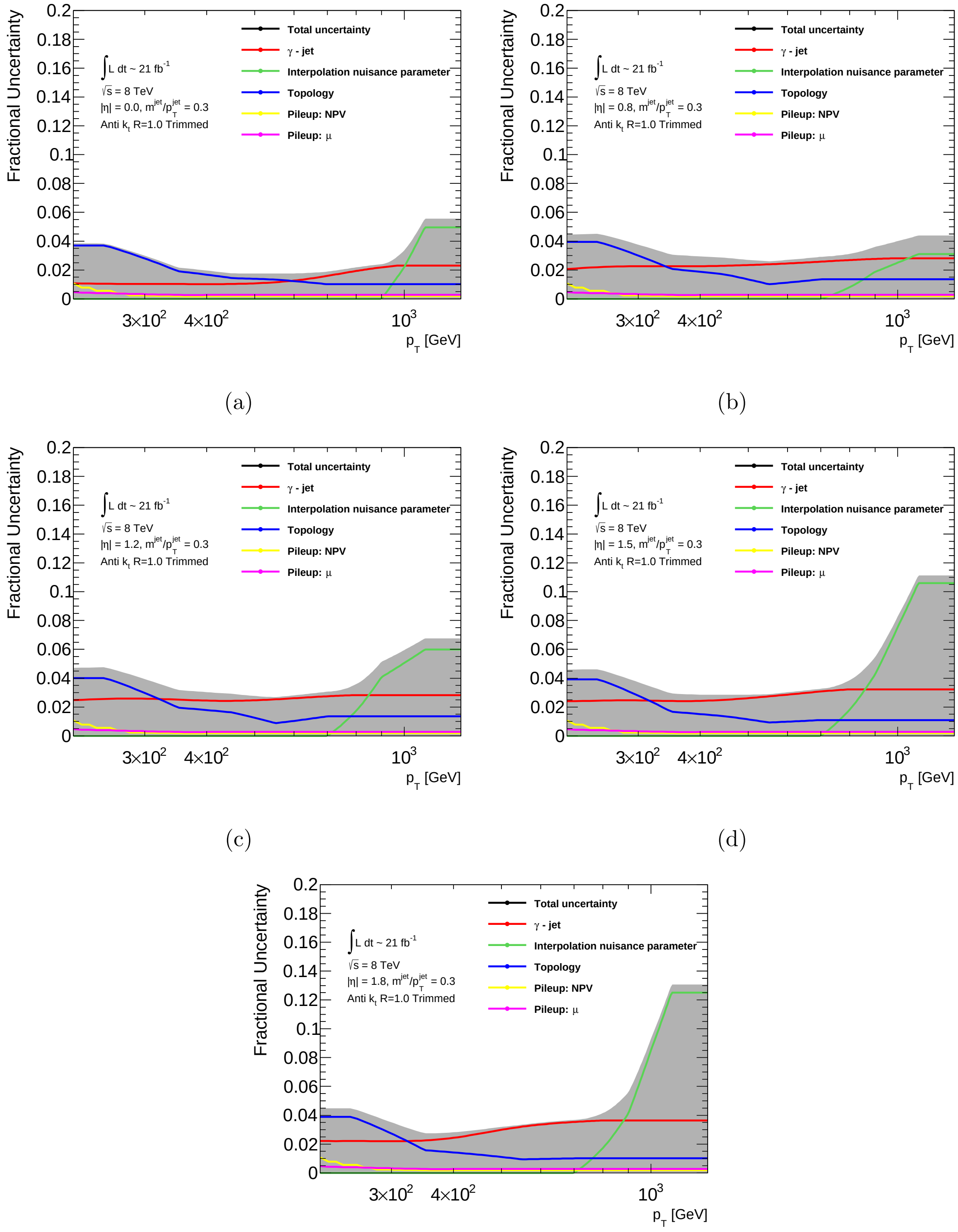

(a) (b) (c) (d) (e)

Figure 7.25: The combined γ-jet and track jet double ratio JES uncertainties, the topology uncertainty and the pile-up uncertainties for values of NPV and μ which are one σ from the average values for the 2012 dataset for a) $|\eta^{\text{jet}}| = 0$, b) $|\eta^{\text{jet}}| = 0.8$, c) $|\eta^{\text{jet}}| = 1.2$, d) $|\eta^{\text{jet}}| = 1.5$ and e) $|\eta^{\text{jet}}| = 1.8$.

MC component, the pile-up uncertainties and the interpolation uncertainty). The combined impact of the JMS and $\sqrt{d_{12}}$ uncertainties are also shown. It can be seen that the new JES uncertainties have an impact of 8.3 %, 4.3 % and 2.9 % on the yield of the analysis; for the data-to-MC uncertainty, the topology uncertainty and all other JES uncertainties respectively. These impacts are significantly smaller than the impact of the track-jet double ratio uncertainties, which were found to have an impact of 14.3 % on the yield (including a 3.5 % contibution from the JMS and $\sqrt{d_{12}}$ uncertainties).

The impact of the new and the old uncertainties on the $m_{t\bar{t}}$ distribution can be seen in Figures 7.26 and 7.27 respectively. For the new JES uncertainties, it can be seen that the data-to-MC γ-jet and topology JES uncertainties are the dominant components over the full range of $m_{t\bar{t}}$. The topology component is particularly dominant for $m_{t\bar{t}} < 1000$ GeV. When comparing to the old track-jet double ratio uncertainties in Figure 7.27, it can be seen that the new uncertainty components have a smaller impact on $m_{t\bar{t}}$ over the full range of $m_{t\bar{t}}$.

In the current iteration of the $t\bar{t}$ semi-leptonic resonance search, a technique known as profiling [114] is used during the limit setting procedure. This technique fits all nuisance parameters (including the JES and its uncertainties) by maximising a likelihood distribution so that these parameters best fit the particular dataset that is observed. The uncertainties are used to help constrain the range that the parameters vary over. It is interesting to look at the pull of the nuisance parameters $((\mathrm{X}_{\mathrm{post-fit}} - \mathrm{X}_{\mathrm{pre-fit}})/\sigma$, where $\mathrm{X}_{\mathrm{post-fit}}$ is the nuisance parameter (eg. the JES) after the fit, $\mathrm{X}_{\mathrm{pre-fit}}$ is the nuisance parameter before the fit and σ is the uncertainty on the nuisance parameter. The pulls for the large-R jet JES are shown in Figure 7.28. The error bars show $\sigma_{\mathrm{post-fit}}/\sigma_{\mathrm{pre-fit}}$, and therefore they are a measure of how much the JES uncertainties are constrained by the profiling. There is a small constraint (ie. the post-fit uncertainty is not much less than the pre-fit uncertainty) on the data-to-MC component of the γ-jet uncertainties and on the other γ-jet uncertainties. However, there is a large constraint on the topology component. This may be an indication that this uncertainty is over-conservative, for this particular analysis. More detailed studies of the topology dependence of the large-R JES may help to further constrain this uncertainty.

Furthermore, in the future, correcting for the data-to-MC differences observed in the JES would reduce, even further, the impact of the JES on the $t\bar{t}$ search, and other analyses making use of large-R jets.

Uncertainty	Impact on yield [%]
Track jet double ratio (JES,JMS and $\sqrt{d_{12}}$) for $p_{\mathrm{T}} < 500$ GeV	14.3
Track jet double ratio (JES,JMS and $\sqrt{d_{12}}$) for $p_{\mathrm{T}} > 500$ GeV	0.0
Topology	8.3
γ-jet data-to-MC	4.3
Other large-R JES	2.9
JMS and $\sqrt{d_{12}}$	3.5

Table 7.3: Impact of the old track jet double ratio JES, JMS and $\sqrt{d_{12}}$ uncertainties and the new uncertainties on the $t\bar{t}$ resonance search [58]. The other γ-jet uncertainties include all γ-jet uncertainties except the data-to-MC component, the pile-up and the interpolation uncertainties.

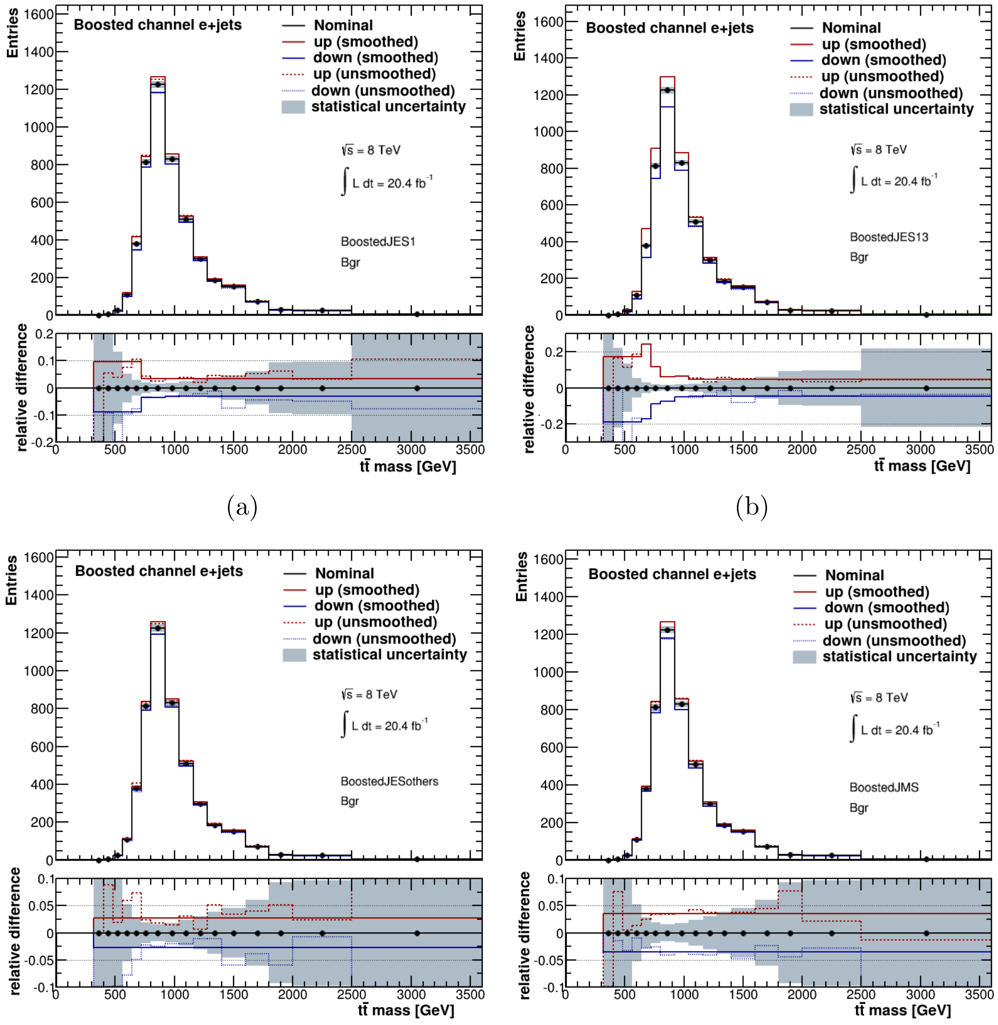

(a) (b)

(c) (d)

Figure 7.26: The impact of varying the large-R uncertainties up and down on the $m_{t\bar{t}}$ distribution for the $t\bar{t}$ semi-leptonic resonance search in the electron channel of the boosted analysis for the JES uncertainties for a) the data-to-MC component of the γ-jet uncertainties, b) the topology uncertainty, c) all the other γ-jet uncertainties (including pile-up and interpolation) and d) the JMS uncertainty [58].

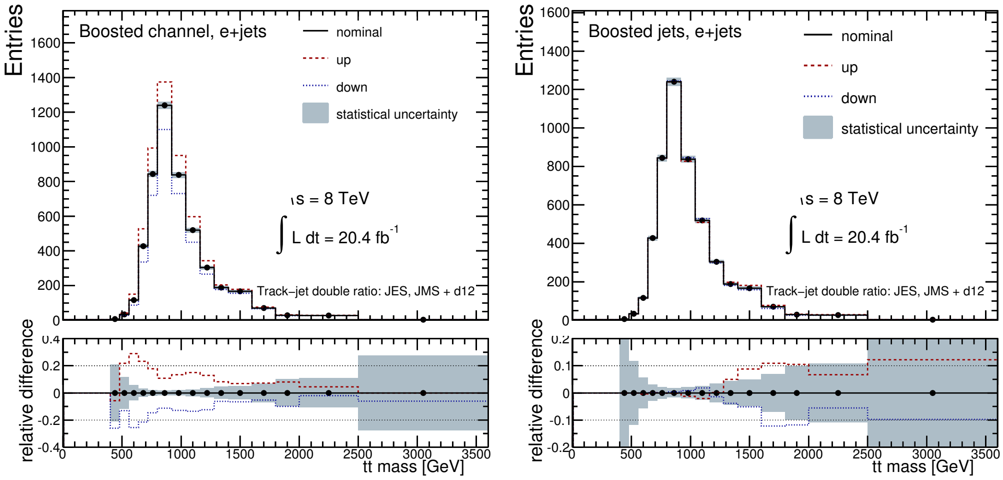

(a) (b)

Figure 7.27: The impact of varying the large-R uncertainties on the $m_{t\bar{t}}$ distribution, derived with the track-jet double ratio method for a) $p_T^{\text{jet}} < 500$ GeV and b) $p_T^{\text{jet}} > 500$ GeV. The JES, JMS and $\sqrt{d_{12}}$ uncertainties are treated as fully correlated (ie. they are all varied in the same direction, at the same time). The distribution is for the $t\bar{t}$ semi-leptonic resonance search in the electron channel of the boosted analysis [58].

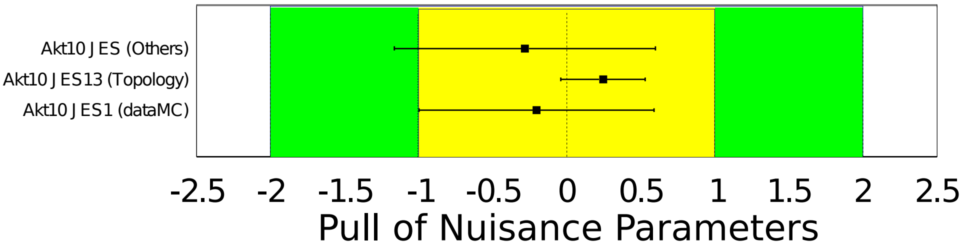

Figure 7.28: The pull of all nuisance parameters in the $t\bar{t}$ resonance search. The error bars represent the ratio of the errors post- and pre-fit [58].

Chapter 8

The Calibration of Variable R Jets

In this chapter the calibration of VR jets will be discussed. Calibrations are derived for the small and large VR jet algorithms that were introduced in Sections 2.4 and 4.5.2. The small VR jets shrink from $R_{\mathrm{max}} = 0.4$ at 150 GeV to $R_{\mathrm{min}} = 0.2$ at 300 GeV. The large VR jets shrink from $R_{\mathrm{max}} = 1.0$ at 600 GeV to $R_{\mathrm{min}} = 0.2$ at 3 TeV. The VR jets are constructed from topo-clusters at LCW scale. This is the first attempt to derive a calibration for these jet collections. A list of future studies, which could be performed in order to refine the calibration and provide a full set of systematic uncertainties, will be given at the end of Chapter 9.

8.1 Overview of the Calibration for VR Jets

A simplified version of the calibration scheme discussed in Section 5.2 has been investigated in order to calibrate small and large VR jets.

The calibration consists of two main steps, firstly a correction to subtract the transverse momentum due to pile-up from the jets and secondly a Monte Carlo based calibration to correct the jet energy and momentum to particle level. Additionally, a jet mass calibration is derived for large VR jets. The $\sqrt{s} = 8$ TeV di-jet Monte Carlo samples, which were described in Section 3.9, were used for these studies.

8.2 Pile-up Subtraction for VR Jets

The default method for pile-up subtraction at ATLAS for anti-k_t $R = 0.4$ and $R = 0.6$ jets is the scalar jet area correction (Equation 5.7), which was described previously in Section 5.2.2. The jet area pile-up correction is well suited for pile-up subtraction when using VR jets, since it takes into account the size of the jets on a jet-by-jet basis through the use of the jet area.

The scalar jet area correction corrects the transverse momentum of the jet for pile-up. However, it does not properly correct the mass of the jet: it simply scales the jet mass by the same factor as the transverse momentum. This is acceptable for small-R jets, since at the time of writing no mass calibration is derived for small-R jets and the small-R jet mass is not used extensively for physics analyses at ATLAS. However, for large-R jets the jet mass is an important substructure variable that is often used by physics analyses using large-R jets. Furthermore, the jet mass is directly correlated with the angular distribution of energy deposits within a jet (as discussed in Section 4.5.1) and so large-R jets will have larger masses due to their larger size. Therefore, it is desirable to be able to correct the mass of the large VR jets for pile-up as well as the transverse momentum. This can be achieved by using the 4-vector jet area correction (which was previously introduced in Equation 5.8), which uses the 4-vector jet area to subtract the contributions due to pile-up from the full 4-vector of the jet.

From Equations 5.7 and 5.8 it can be seen that the two key ingredients that are needed for the jet area pile-up correction are the median event density, ρ, and the jet area. The median event density is calculated on an event-by-event basis as described in Section 4.5. It is independent of the jet algorithm that is used and will not be discussed further here.

The default choice for calculating the area of anti-k_t $R = 0.4$ and $R = 0.6$ jets at ATLAS is the 4-vector active area calculation (Equation 5.6). The active area calculation provides an accurate measure of the area of a jet. However, the speed of reconstruction is significantly degraded when ghost particles are added to the event. For VR jets this problem is even more acute, since the speed of the VR jet algorithm degrades more rapidly with the number of constituents in the event compared to anti-k_t jets, for which the speed of the algorithm is extremely well optimised.

Two options were investigated to find a way of accurately measuring the jet area of VR jets without a significant degradation in the speed of the jet reconstruction. The first of these was to reduce the number of ghosts used in the active areas calculation. The default choice for ATLAS is to use a ghost area of 0.01, meaning that one ghost is placed in each 0.01 area of $\eta \times \phi$ space. Ghost areas of 0.1 and 0.05 were studied and compared to the default choice of 0.01. Due to the long reconstruction time for VR jets it was unfeasible to perform these studies with the full di-jet Monte Carlo samples and, therefore, only 1 out of every 100 events was used.

For small VR jets it was found that when the ghost area was increased from 0.01 the area distributions become discrete, as can be seen in Figure 8.1 a), b) and c). The discrete nature of the distributions is less obvious for Figure 8.1 b), since in this p_{T} range (150-200 GeV) the VR jets have different sizes ranging from $R = 0.4$ to $R = 0.3$, which results in a smearing of the distributions. These discrete distributions occur as it is possible that different jets of a similar size contain the same number of ghost particles. This is more likely for smaller jet sizes and for lower ghost densities (larger ghost areas). In the case of the scalar active area calculation this results in the jets having exactly the same area. In the case of the four-vector active area calculation they will not have exactly the same area since the calculation takes into account the direction of the ghosts, but the transverse area will be very similar. This effect is mitigated somewhat, since the initial positions of the ghosts are randomly fluctuated. The effect can be completely removed by re-running the active area calculation (with $\sim$5 repeats) using a different set of ghosts, with different initial positions each time, and taking the average jet area for each jet [53]. Unfortunately, this is not an option due to the increase in the CPU time that is required.

For large-R jets, the distributions remain continuous to higher p_{T} due to the larger jet sizes at low p_{T} as can be seen in Figure 8.2 a). However, the discrete nature of the jets becomes apparent as the large VR jets become smaller, as can be seen in Figure 8.2 b) for a ghost area of 0.1 (where the large VR jets have a size between 0.6 and 0.5) and in Figure 8.2 c) for ghost areas of 0.1 and 0.05 (where the large VR jets have a size between 0.3 and 0.24).

The second option that was investigated was to calculate the area of the jets using the Voronoi areas calculation instead of the active areas calculation. The Voronoi areas calculation is fast, since it does not involve the addition of ghosts to the event. However, as can be seen in Figure 8.3 the Voronoi area calculation systematically overestimates the area of the jet and has a broader area distribution than that calculated with the active area calculation. The cause of the overestimation of the jet areas, when using the Voronoi area calculation, is that for low density events the Voronoi cells at the edge of a jet are large due to a lack of nearby constituents. This also results in the Voronoi areas calculation being dependent on the level of pile-up in the event. For dense events with a high level of pile-up the Voronoi areas will be a more accurate measure of the jet area than for sparsely populated events with a low level of pile-up.

In order to improve the accuracy of the Voronoi area calculation ghosts were added to the event. This decreases the size of the Voronoi cells and increases the accuracy of the calculation of the jet area. This is illustrated in Figure 8.4, where the transverse jet area (normalised to πR^2) is shown as a function of NPV. It can be seen that for a Voronoi area calculation with no ghosts there is a significant increase in the jet area for events with NPV $<$ 20 (5) for small (large) VR jets, which is not observed for the active area calculation. The introduction of ghosts to the event reduces this dependence to a negligible level when using the Voronoi area calculation.

The more ghosts that are added to the event, the closer the Voronoi area calculation becomes in comparison to the active areas calculation. This can be seen in Figures 8.1 d), e) and f) for small VR jets and Figures 8.2 d), e) and f) for large VR jets, for some example p_{T} ranges. The fractional difference between the Voronoi areas calculation using ghosts, and the active area calculation with a ghost area of 0.01, on a jet-by-jet basis can be seen in Figure 8.5. Even introducing a small number of ghosts to the event (e.g. a ghost area of 0.1) significantly improves the accuracy of the Voronoi area calculation when comparing to the active area calculation.

The average CPU time that it takes to reconstruct one event when using the active area and the Voronoi area calculations can be seen in Table 8.1. The times were measured using ROOT's TStopwatch class in a standalone implementation of FastJet [53]. Therefore, these timings are likely to vary in comparison to the timings that may be measured when reconstructing jets using the ATLAS software. However, the aim here is to compare the time of reconstruction for the active area calculation (with a ghost area of 0.01) when using anti-k_t jets, to the time for reconstructing jets using the VR jet algorithm. Therefore, the accuracy of the absolute values is of less significance.

	Average time to reconstruct one event [sec]						
	Active Areas			Voronoi Areas			
Ghost area	0.01	0.05	0.1	0.01	0.05	0.1	No ghosts
Small VR	52.6	1.82	0.96	36.2	1.29	0.90	0.12
$R = 0.4$ anti-k_t	0.10	0.017	0.012	0.13	0.022	0.012	0.0071

Table 8.1: The average CPU time to reconstruct one event using small VR jets and anti-k_t $R = 0.4$ jets for the Active Areas and Voronoi Areas calculations with different ghost areas, the last column is for Voronoi Areas with no ghosts.

From the average times in Table 8.1 it can be seen that the active area calculation, with a ghost area of 0.01, takes ∼0.1 seconds per event for anti-k_t $R = 0.4$ jets. When using the VR jet algorithm the Voronoi areas calculation with no ghosts gives a similar reconstruction time. However, it was previously shown that the introduction of any number of ghosts to the event significantly improves the accuracy of the Voronoi areas calculation. Therefore, the Voronoi areas calculation with a ghost area of 0.1 is chosen, for use in the jet area correction, for the rest of the studies presented here. It should be noted that this may be particularly sub-optimal for large VR jets since the Voronoi area calculation is a scalar area calculation. A 4-vector is constructed from the scalar Voronoi area using the direction of the jet, rather than any information about the way pile-up clusters in the event. Therefore, when the Voronoi area is used in the context of the 4-vector jet area correction, it is not expected to exactly correct the mass of the jet for pile-up.

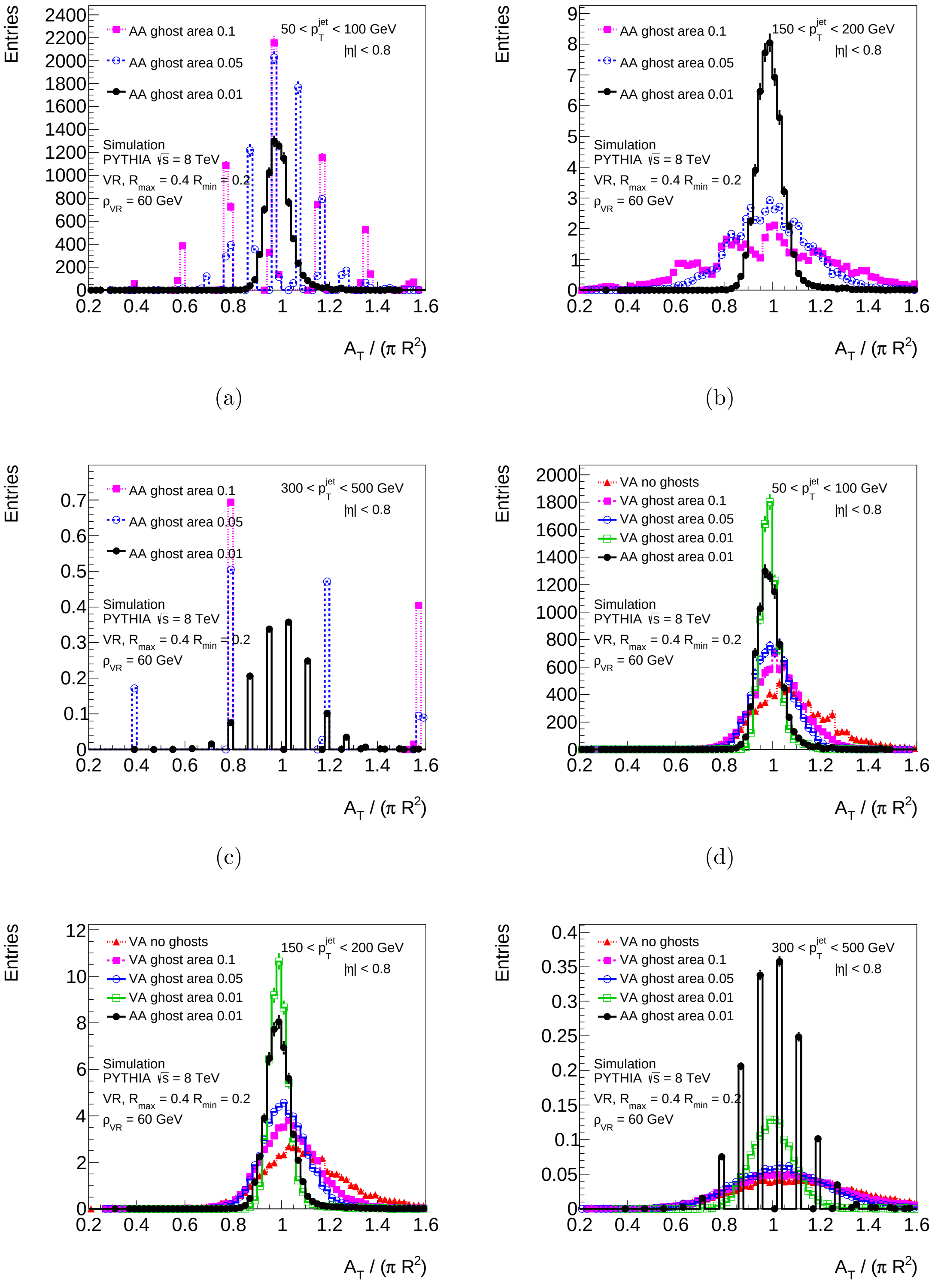

(a) (b) (c) (d) (e) (f)

Figure 8.1: Active areas (AA) for small VR jets with different ghost densities, normalised to πR^2, for a) 50 - 100 GeV, b) 150 - 200 GeV and c) 300 - 500 GeV and Voronoi Areas (VA) for small VR jets for d) 50 - 100 GeV, e) 150 - 200 GeV and f) 2000 - 2500 GeV. All the plots are for $|\eta| < 0.8$. Ghost areas of 0.1, 0.05 and 0.01 are shown for Voronoi areas and Active areas. The Voronoi area with no ghosts is also shown.

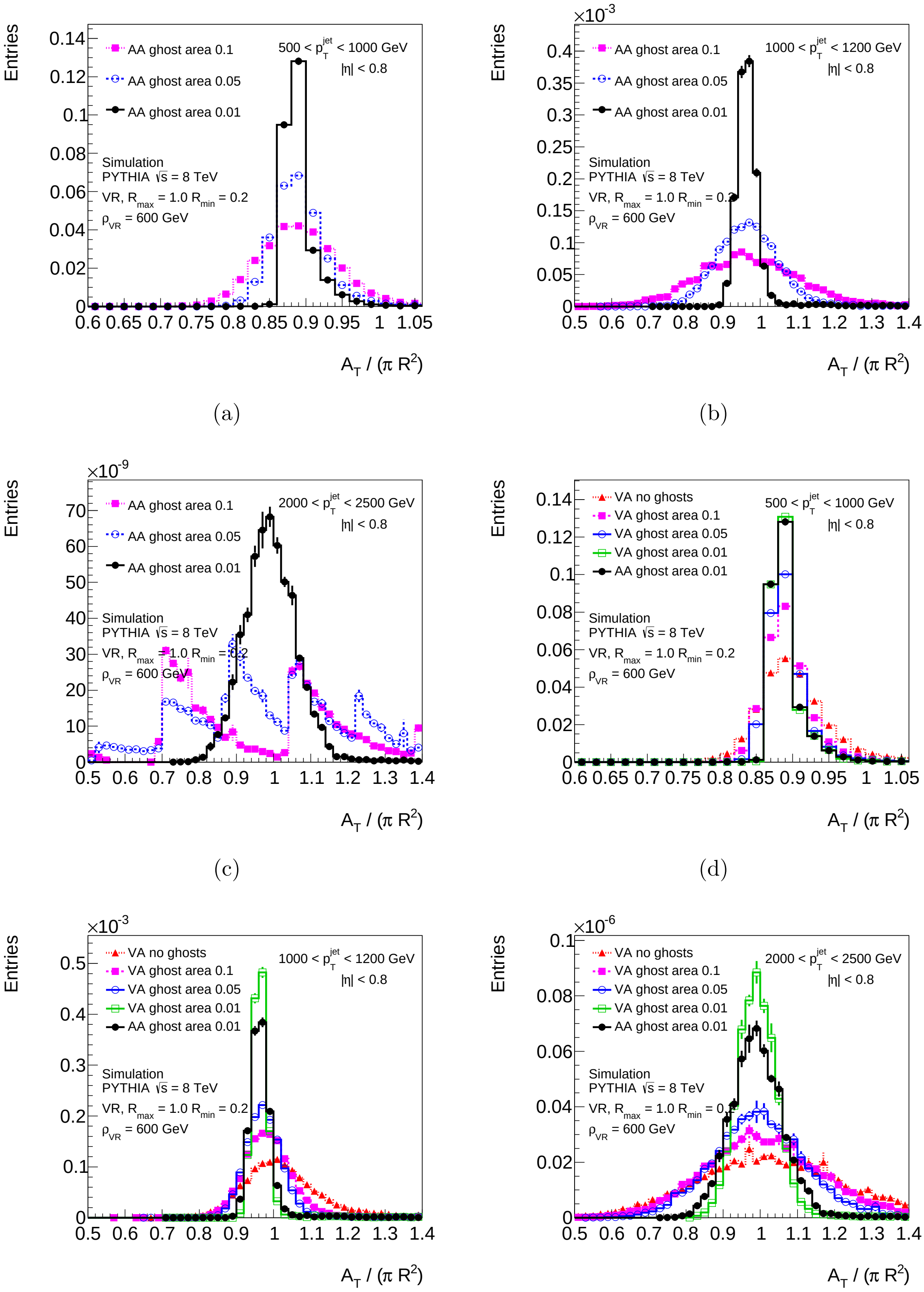

(a) (b) (c) (d) (e) (f)

Figure 8.2: Active areas (AA) for large VR jets with different ghost areas, normalised to πR^2, for a) 500 - 1000 GeV, b) 1000 - 1200 GeV and c) 2000 - 2500 GeV and Voronoi areas (VA) for large VR jets with d) 500 - 1000 GeV, e) 1000 - 1200 GeV and f) 2000 - 2500 GeV. All the plots are for $|\eta| < 0.8$. Ghost areas of 0.1, 0.05 and 0.01 are shown for Voronoi areas and Active areas. The Voronoi area with no ghosts isalso shown.

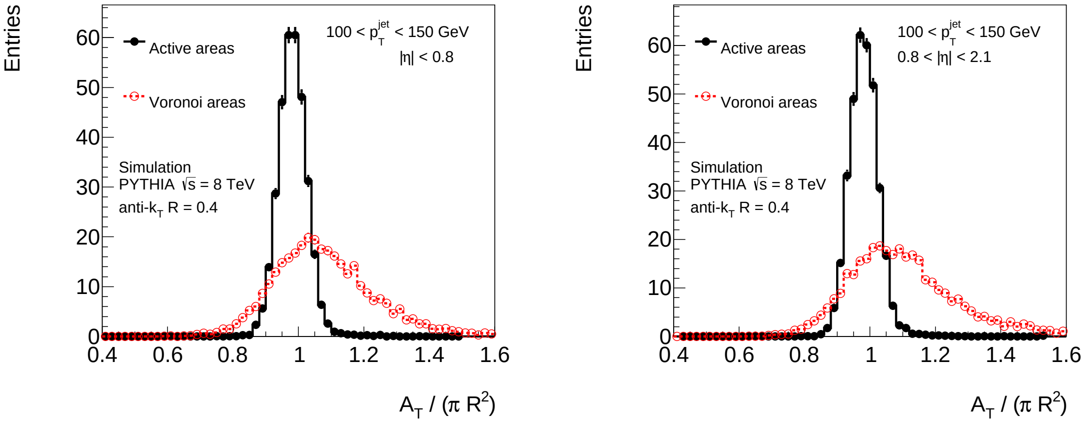

(a) (b)

Figure 8.3: The transverse area, normalised to πR^2, for anti-k_t $R = 0.4$ jets calculated with the active areas calculation and with the Voronoi areas calculation for $100 < p_T < 150$ GeV for a) $|\eta| < 0.8$ and b) $0.8 < |\eta| < 2.1$.

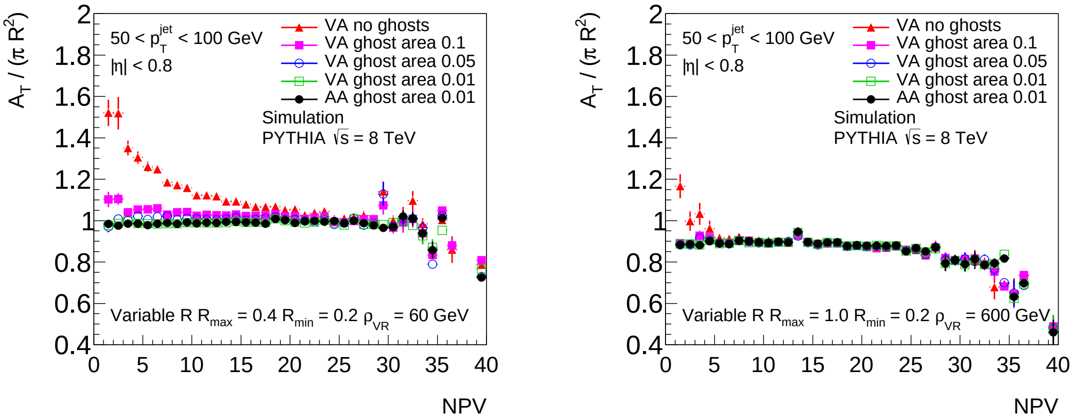

(a) (b)

Figure 8.4: The transverse area normalised to πR^2 as a function of NPV for a) small VR jets and b) large VR jets. Areas calculated with the Voronoi area calculation (VA) with ghost areas of 0.01, 0.05, 0.1 and no ghosts and the active area calculation (AA) with ghost areas of 0.01 are shown. The figures are for $|\eta| < 0.8$ and $50 < p_T^{\text{jet}} < 100$ GeV.

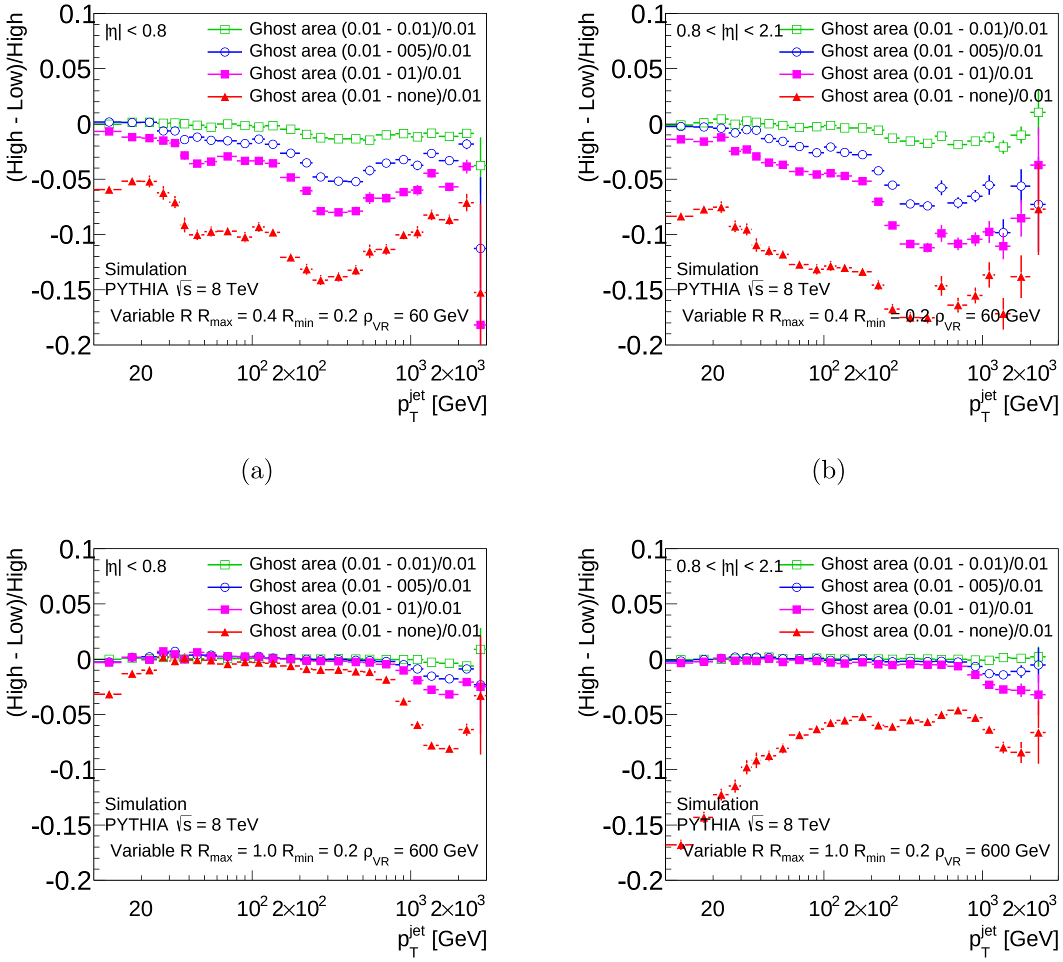

(a) (b)

(c) (d)

Figure 8.5: $(A_T^{\text{Active Areas ghost area 0.01}} - A_T^{\text{Voronoi Areas ghost area X}})/A_T^{\text{Active Areas ghost area 0.01}}$ with $X = 0.01$, 0.03, 0.05, 0.07, 0.1 and for Voronoi Areas with no ghosts for small VR jets with a) $|\eta| < 0.8$ and b) $0.8 < |\eta| < 2.1$, and large VR jets with c) $|\eta| < 0.8$ and d) $0.8 < |\eta| < 2.1$.

8.2.1 The Impact of Applying the Jet Area Correction to VR Jets

To assess the performance of the jet area correction, the gradients of the distributions of jet p_{T} vs. NPV and μ are derived. The scalar area correction is used for small VR jets and the four-vector area correction is used for large VR jets. In all cases the jet area is calculated using the Voronoi areas calculation with a ghost area of 0.1. The gradients are derived using a similar method as was used to derive the gradients for the pile-up uncertainty for large-R jets (Section 7.7). Since these are Monte Carlo based studies, the reference objects used to define the p_{T} ranges are truth jets rather than track jets. Truth jets are matched to reconstructed jets using a geometrical matching criterion: $\Delta R(\text{truth jet} - \text{reco jet}) < 0.75\ R_{\text{eff}}^{\text{jet}}$. A 4D binning in truth jet p_{T}, jet $|\eta|$, μ and NPV is used. In each p_{T} and $|\eta|$ bin $\partial p_T^{\text{jet}}/\partial\text{NPV}$ is averaged over μ and $\partial p_T^{\text{jet}}/\partial\mu$ is averaged over NPV. The full di-jet Monte Carlo samples were used for these studies.

In Figure 8.6 the resulting gradients can be seen as a function of $|\eta|$ for small VR jets with $20 < p_T^{\text{truth}} < 30$ GeV, and for large VR jets with $60 < p_T^{\text{truth}} < 80$ GeV. In Figure 8.7 the gradients can be seen as a function of p_T^{truth} for $|\eta| < 0.8$. For both small and large VR jets the jet area correction significantly reduces the dependence of the jet p_{T} on NPV. Additionally, the correction reduces the p_{T} dependence of $\partial p_T^{\text{jet}}/\partial\text{NPV}$. For small VR jets there is a residual dependence of less than ∼0.1 GeV per primary vertex for $|\eta| < 2.5$. For large VR jets there is a residual dependence of less than ∼0.4 GeV per primary vertex.

The jet area correction has little impact on the dependence of the jet p_{T} on μ. In fact, for small VR jets the correction slightly increases the dependence of the jet p_{T} on μ. This is also the case for fixed radius anti-k_t jets, as discussed in Section 5.2.2. For VR jets, within $|\eta| < 2.5$, the μ dependence is small and the residual dependence of the p_{T} on NPV and μ can be accounted for by systematic uncertainties. In the future it would be desirable to investigate the application of a residual offset correction, as is done for anti-k_t $R = 0.4$ and $R = 0.6$ jets. This would decrease the systematic uncertainty due to pile-up for VR jets, particularly in the forward region.

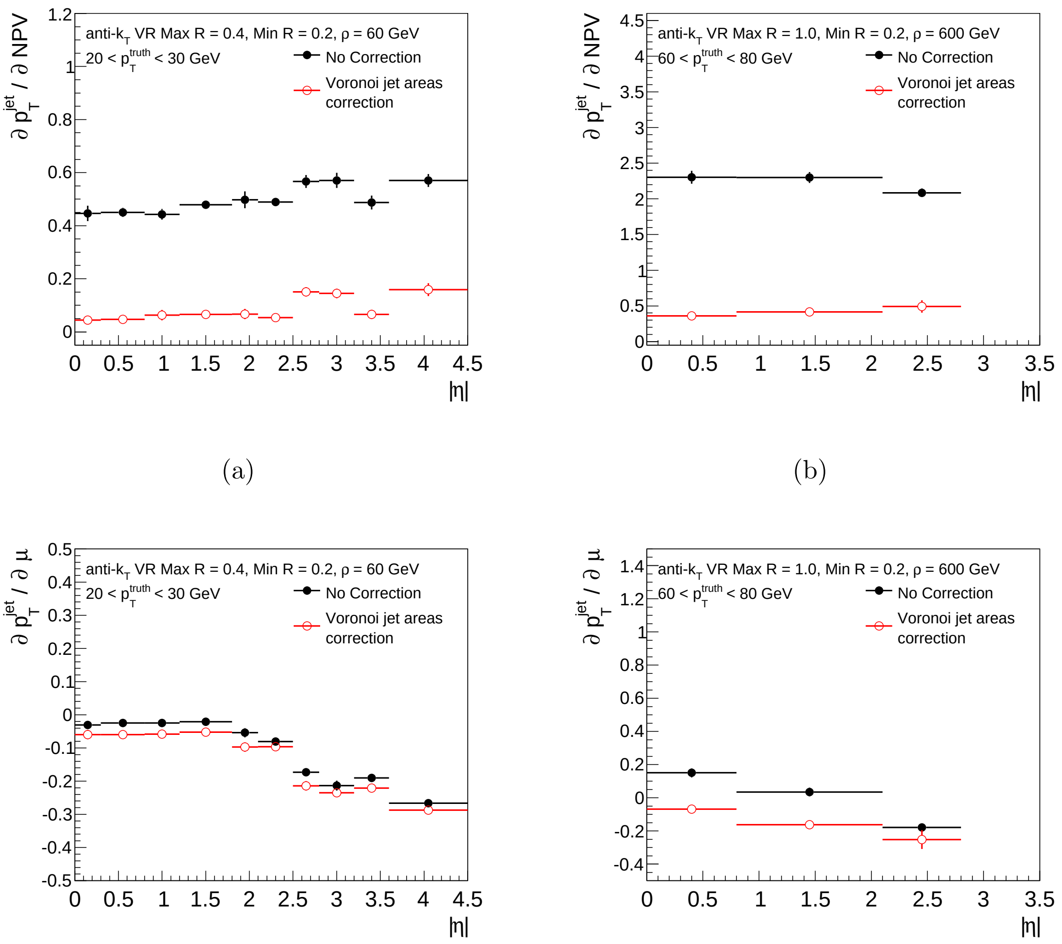

(a) (b) (c) (d)

Figure 8.6: $\partial p_T^{\text{jet}}/\partial NPV$ for a) small VR jets with $20 < p_T^{\text{truth}} < 30$ GeV and b) large VR jets with $60 < p_T^{\text{truth}} < 80$ GeV, and $\partial p_T^{\text{jet}}/\partial \mu$ for c) small VR jets with $20 < p_T^{\text{truth}} < 30$ GeV and d) large VR jets with $60 < p_T^{\text{truth}} < 80$ GeV. The jet p_{T} dependence is shown before and after the Voronoi jet area correction. All plots are shown as a function of $|\eta|$.

In order to assess the impact of the 4-vector jet area correction on the mass of large VR jets, the gradients of the jet mass vs. NPV and μ are derived as a function of jet p_{T}. The same method that was used to derive the jet p_{T} gradients is used. The resulting gradients can be seen before and after the jet area correction in Figure 8.8, for $|\eta| < 0.8$ and $0.8 < |\eta| < 2.1$. Despite the Voronoi area calculation not providing a true 4-vector area it can be seen that the area correction significantly reduces the dependence of the jet mass on NPV and μ, with NPV (μ) gradients of less than ~0.3 (0.1) following the correction.

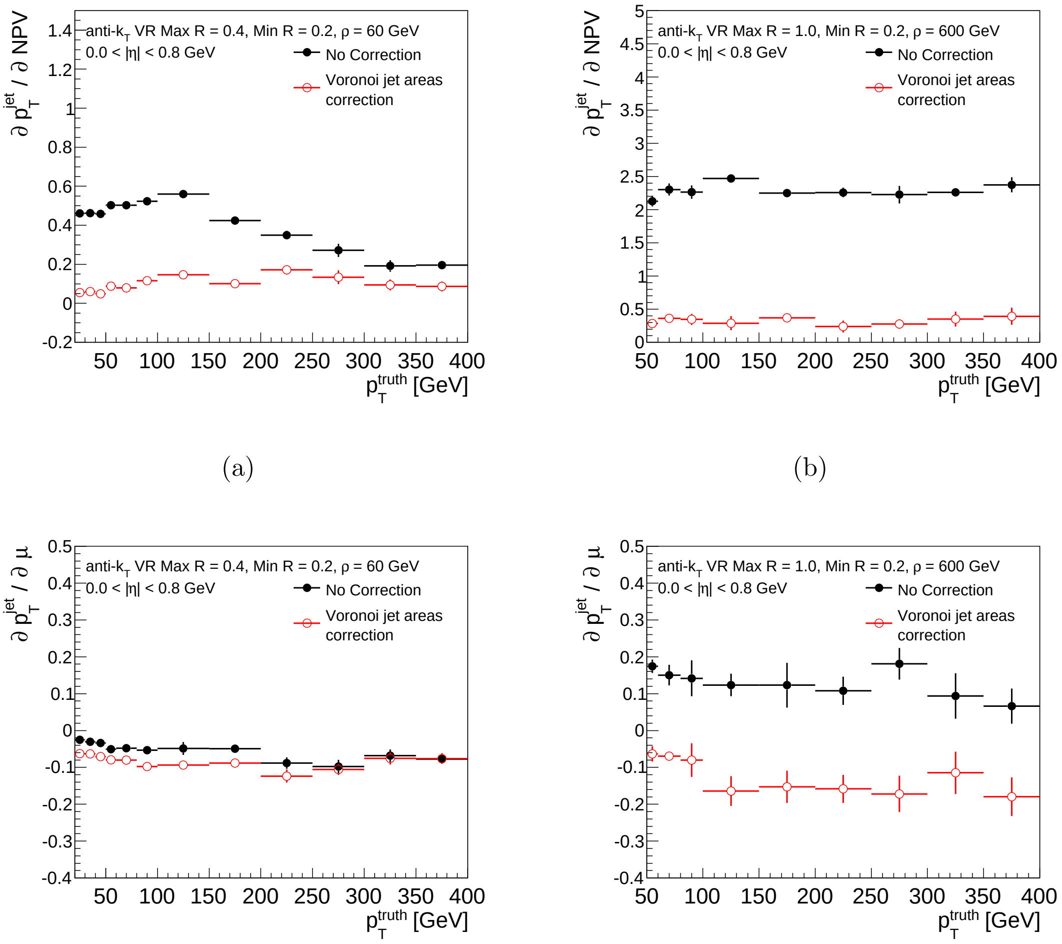

(a) (b)

(c) (d)

Figure 8.7: $\partial p_T^{\text{jet}}/\partial NPV$ for a) small VR jets and b) large VR jets, and $\partial p_T^{\text{jet}}/\partial \mu$ for c) small VR jets and d) large VR jets. The p_{T} dependence is shown before and after the Voronoi jet area correction. All plots are for $|\eta| < 0.8$, and are shown as a function of p_T^{truth}.

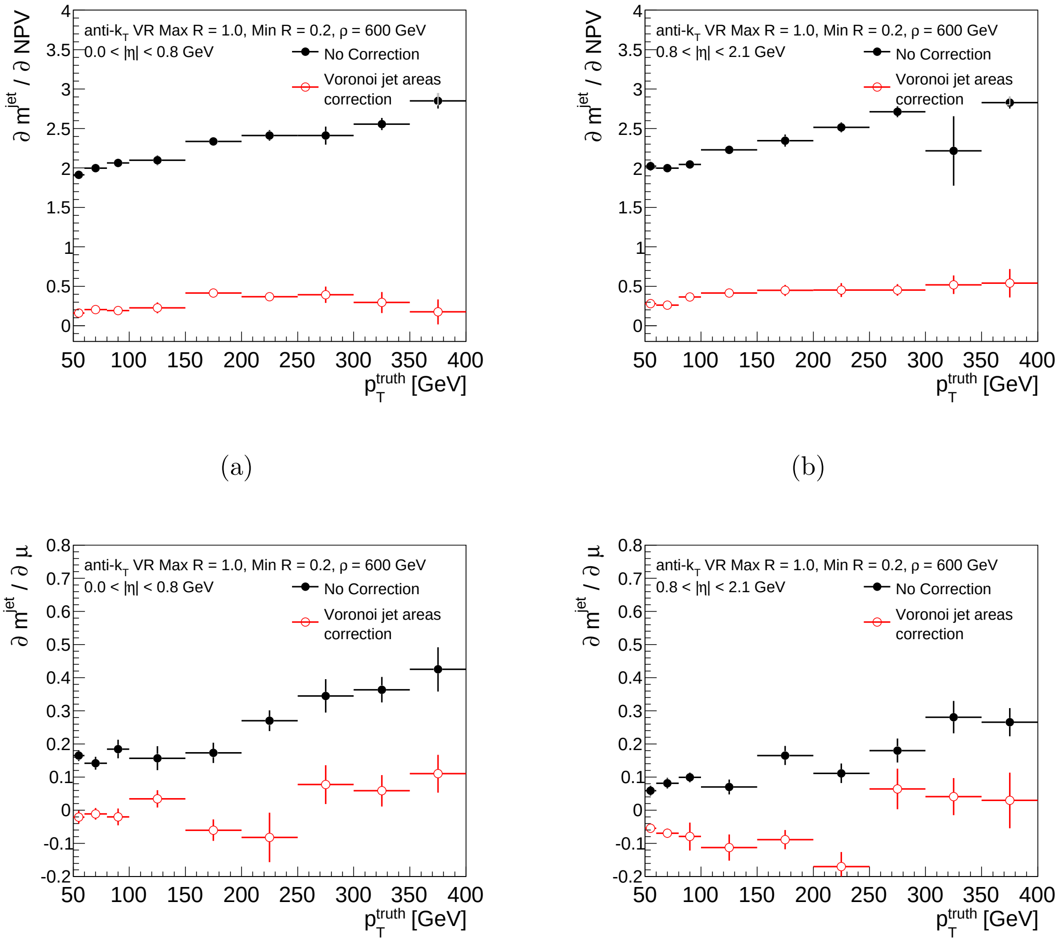

(a)

(b)

(c)

(d)

Figure 8.8: $\partial m^{\text{jet}}/\partial NPV$ for large VR jets for a) $|\eta| < 0.8$ and b) $0.8 < |\eta| < 2.1$, and $\partial m^{\text{jet}}/\partial \mu$ for large VR jets for a) $|\eta| < 0.8$ and b) $0.8 < |\eta| < 2.1$. The mass dependence is shown before and after the 4-vector jet area correction (using Voronoi areas). All plots are as a function of p_T^{truth}.

8.3 Monte Carlo Calibration of VR jets

The Monte Carlo calibration for VR jets follows the calibration scheme used for anti-k_t fixed radius jets (that was described in Section 4.5). For small VR jets, the energy and pseudorapidity are corrected to particle level. For large VR jets, the energy, pseudorapidity and mass are corrected to particle level.

For small VR jets, the scalar jet area pile-up correction is applied and for large VR jets the 4-vector jet area pile-up correction is applied. The pile-up corrections are applied before the Monte Carlo calibration. The full $\sqrt{s}$ = 8 TeV di-jet Monte Carlo samples that were described in Section 3.9 were used for these studies.

8.3.1 Energy and Pseudorapidity Corrections for VR Jets

The jet energy is corrected by considering the truth jet energy response from Equation 5.10 [1]. For anti-k_t fixed radius jets, $\mathcal{R}$(truth) is measured in bins of η^{reco} and E^{truth}. However, the size of VR jets is inversely proportional to the p_{T} of the jet and, therefore, for VR jets $\mathcal{R}$(truth) is measured in bins of η^{reco} and p_T^{truth}. In this way the calibration is parametrised as a function of jet size as well as p_{T}.

For this p_{T} parametrisation the following p_{T} bins are used:
`20,25,30,35,40,50,60,80,100,120,150,200,240,300,400,500,600,800,`
`1000,1200,1500,2000,2500,3000,3500 GeV.`
For large VR jets, only p_{T} bins above 50 GeV were used. For the η^{reco} parametrisation, bins with a width of 0.1 were used. The η^{reco} bins range from $\eta^{\mathrm{reco}} = -4.2$ up to $\eta^{\mathrm{reco}} = 4.2$ for small VR jets and from $\eta^{\mathrm{reco}} = -2.2$ up to $\eta^{\mathrm{reco}} = 2.2$ for large VR jets.

Truth jets are matched to reconstructed jets by taking the highest p_{T} reconstructed jet within $\Delta R(\text{truth jet} - \text{reco jet}) < 0.75{\cdot}\mathrm{R}_{\mathrm{eff}}^{\text{truth jet}}$, where $R_{\mathrm{eff}}^{\text{truth jet}}$ is the jet distance parameter of the truth jet. The truth jets and reconstructed jets are required to be isolated. For truth

---

[1] $\mathcal{R}(\text{truth}) = \frac{E^{\mathrm{reco}}}{E^{\mathrm{truth}}}$ where E^{reco} is the reconstructed jet energy after the pile-up correction.

jets there must be no other truth jet with $p_{\mathrm{T}} > 7$ GeV within $\Delta R < 2.5 \cdot R_{\mathrm{eff}}^{\mathrm{truth\ jet}}$. For reconstructed jets there must be no other reconstructed jet with $p_{\mathrm{T}} > 7$ GeV, after the pile-up correction has been applied, within $\Delta R < 1.5 \cdot R_{\mathrm{eff}}^{\mathrm{reco\ jet}}$.

The calibration factors are then derived as follows:

1. In each η^{reco} and p_T^{truth} bin the $\mathcal{R}(\mathrm{truth})$ distributions are fit with a Gaussian. Examples of these fits can be seen in Figures 8.10 a) and c). The mean of the Gaussian fits are used to determine the average values of $\mathcal{R}(\mathrm{truth})$ ($\langle\mathcal{R}(\mathrm{truth})\rangle$) in each p_{T} and η^{reco} bin.
2. In each η^{reco} bin $\langle\mathcal{R}(\mathrm{truth})\rangle$ is plot as a function of p_T^{reco}. The p_T^{truth} in each $(\eta^{\mathrm{reco}}, p_T^{\mathrm{truth}})$ bin is translated to p_T^{reco} using the arithmetic mean of p_T^{reco} in each p_T^{truth} bin.
3. In order to extract the JES calibration factors $(1/\mathcal{F}_{\mathrm{calib}}(p_T^{\mathrm{reco}}))$ the $\langle\mathcal{R}(\mathrm{truth})\rangle$ vs p_T^{reco} distributions are fit with the following function:

$$\mathcal{F}_{\mathrm{calib}}(p_T^{\mathrm{reco}}) = \sum_{i=0}^{N_{\mathrm{max}}} \left(a_i \left(\ln\ p_T^{\mathrm{reco}}\right)^i\right) \tag{8.1}$$

   where a_i are free parameters of the fit. The fit is performed six times for $N_{\mathrm{max}} = 1-6$. The N_{max} that gives the smallest χ^2/NDF for the fit is used to define the JES calibration factors. Examples of the $\langle\mathcal{R}(\mathrm{truth})\rangle$ vs p_T^{reco} distributions and the corresponding $\mathcal{F}_{\mathrm{calib}}(p_T^{\mathrm{reco}})$ fits can be seen in Figure 8.9 for small and large VR jets. $1/\mathcal{F}_{\mathrm{calib}}(p_T^{\mathrm{reco}})$ will be used to correct the JES in data and Monte Carlo as in Equation 5.12 ($E^{\mathrm{LCW+JES}} = E^{\mathrm{reco,\ LCW}}/\mathcal{F}_{\mathrm{calib}}$). The fits and parameters for all η^{reco} and p_{T} bins can be found in Ref. [5] and Ref. [6].

Following the JES calibration, the η of the jets is corrected to particle level by considering the difference in truth and reconstructed η ($\Delta\eta$ from Equation 5.13 [2]). The same procedure is used to derive the η calibration factors as was used to derive the JES calibration factors.

$\Delta\eta$ is measured in the same bins of η^{reco} and p_T^{truth} as $\mathcal{R}(\mathrm{truth})$. Examples of distributions of $\Delta\eta$ and the corresponding Gaussian fits that are used to define $\langle\Delta\eta\rangle$ can be seen in

---

[2] $\Delta\eta = \eta_{\mathrm{reco}} - \eta_{\mathrm{truth}}$

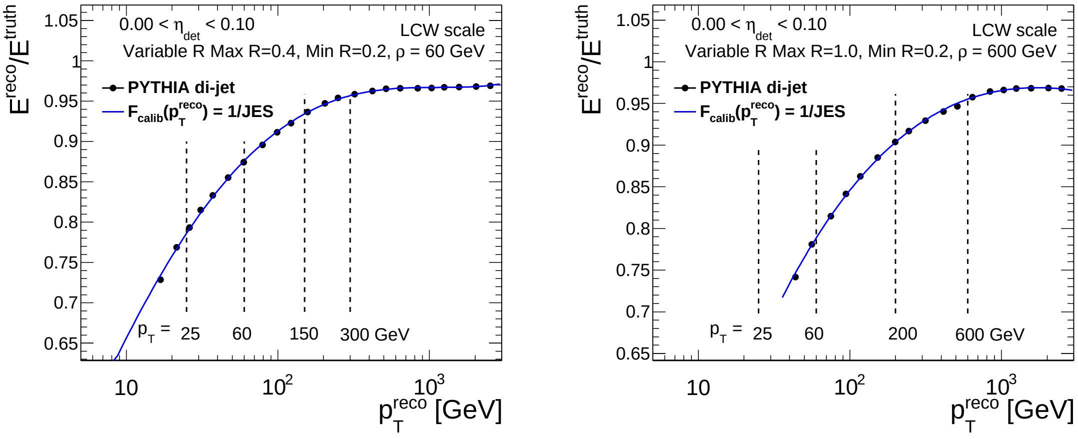

(a) (b)

Figure 8.9: $\langle\mathcal{R}(\text{truth})\rangle$ as a function of p_T^{reco} and the $\mathcal{F}_{\text{calib}}$ with the smallest χ^2/NDF for $0.0 < \eta^{\text{reco}} < 0.1$ for a) small VR jets ($R_{\text{min}} = 0.2$, $R_{\text{max}} = 0.4$ and $\rho = 60$ GeV) and b) large VR jets ($R_{\text{min}} = 0.2$, $R_{\text{max}} = 1.0$ and $\rho = 100$ GeV).

Figures 8.10 b) and d). The distribution of $\langle\Delta\eta\rangle$ vs p_T^{truth} is fit with a function of the same form as Equation 5.11 ($\mathcal{F}^{\eta}_{\text{calib}}(p_T^{\text{truth}}) = \sum_{i=0}^{N_{\text{max}}}\left(a_i\left(\ln\ p_T^{\text{truth}}\right)^i\right)$). An example of the resulting $\Delta\eta$ vs p_T^{truth} distribution can be seen in Figure 8.11 for $0.0 < \eta^{\text{reco}} < 0.1$, for small and large VR jets. The resulting $\mathcal{F}^{\eta}_{\text{calib}}$ function is used to correct the jet η according to Equation 5.14.

Energy and p_{T} Closure Following the JES and η Corrections

In order to assess the performance of the energy and pseudorapidity calibrations $\mathcal{R}(\text{truth})$ is measured after the application of the JES calibration factors. The p_{T} response ($\mathcal{R}(\text{truth},\ p_T) = p_T^{\text{reco}}/p_T^{\text{truth}}$) is also measured, following the application of the JES and η calibration factors. This is known as a closure test. For a perfect calibration $\mathcal{R}(\text{truth})$ and $\mathcal{R}(\text{truth},\ p_T)$ are expected to be equal to one, any deviation from unity is known as *non-closure*.

The resulting closure for $0.0 < \eta < 0.1$ can be seen in Figure 8.12. The energy closure after the JES calibration, the p_{T} closure after the JES calibration, and the p_{T} closure after the JES and η calibrations are shown. It can be seen that the energy and p_{T} closure for small VR jets is well within 1 % above 60 GeV. For $p_{\text{T}} < 60$ GeV there is a p_{T} non-closure, after both the JES and η calibrations, that rises up to 2 % for $p_{\text{T}} = 25$ GeV.

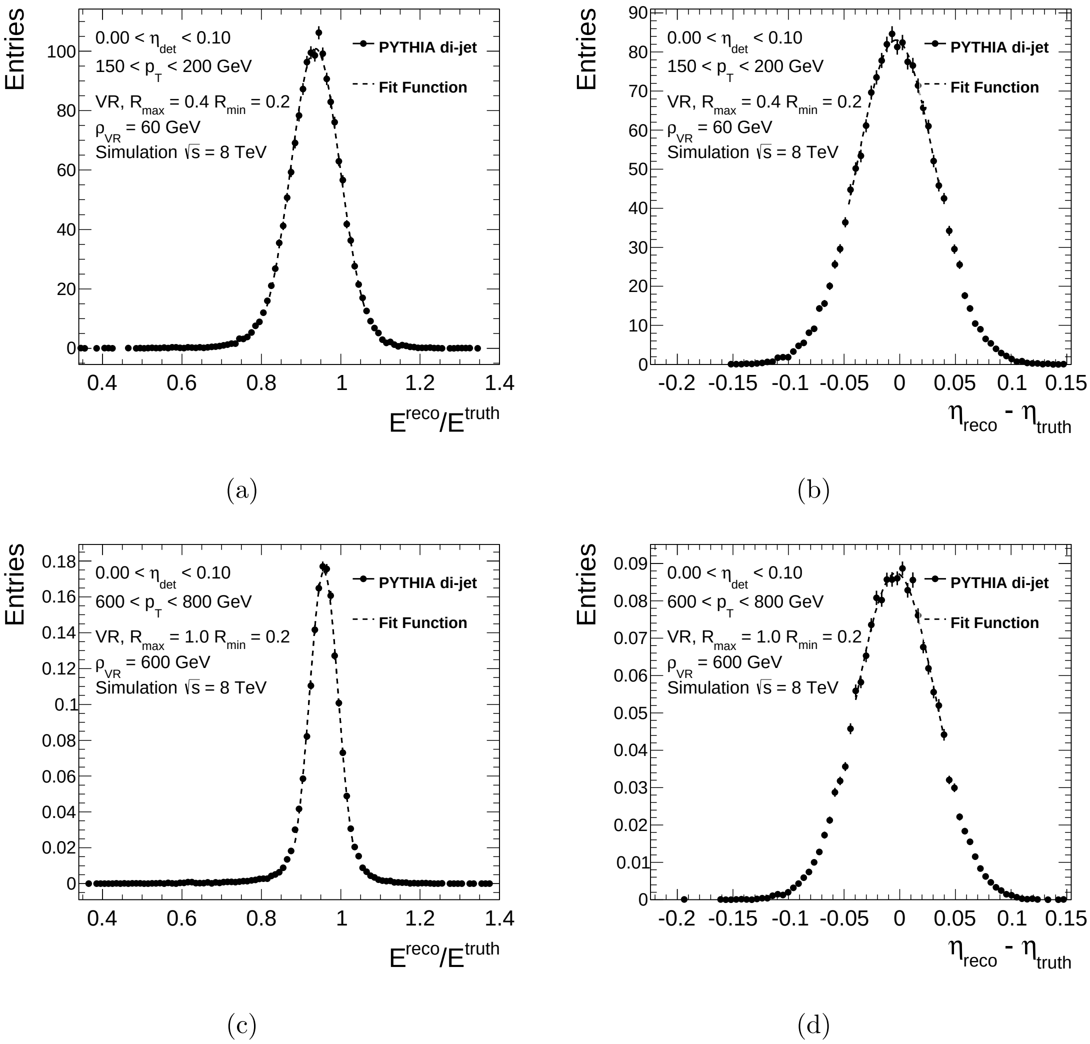

(a) (b)

(c) (d)

Figure 8.10: Examples of Gaussian fits for $0.0 < \eta^{\text{reco}} < 0.1$ for small VR jets with $150 < p_T < 200$ GeV for a) the energy response $\mathcal{R}$(truth) and b) $\Delta\eta$; and the Gaussian fits for large VR jets with $200 < p_T < 400$ GeV for c) the energy response $\mathcal{R}$(truth) and d) $\Delta\eta$.

For large VR jets, the energy closure is within 1 % over the full p_{T} range. However, there is a large p_{T} non-closure below $\sim$ 200 GeV. The mass calibration, which will be discussed further in Section 8.3.2, will help to correct for this non-closure.

Whilst the fit and the corresponding closure test is good for small VR jets for the η bin shown in Figures 8.11 and 8.12, some η bins exhibit a less stable response distribution. This results in deviations from unity in the corresponding closure tests. An example can be seen in Figure 8.13 for the bin $0.9 < \eta < 1.0$. It can be seen that the closure exhibits some instabilities in the region where the VR jets are of variable size ($150 < p_T^{jet} < 300$ GeV). This is a direct result of $\mathcal{F}_{\text{calib}}$ not fitting the response distribution well in this region. The

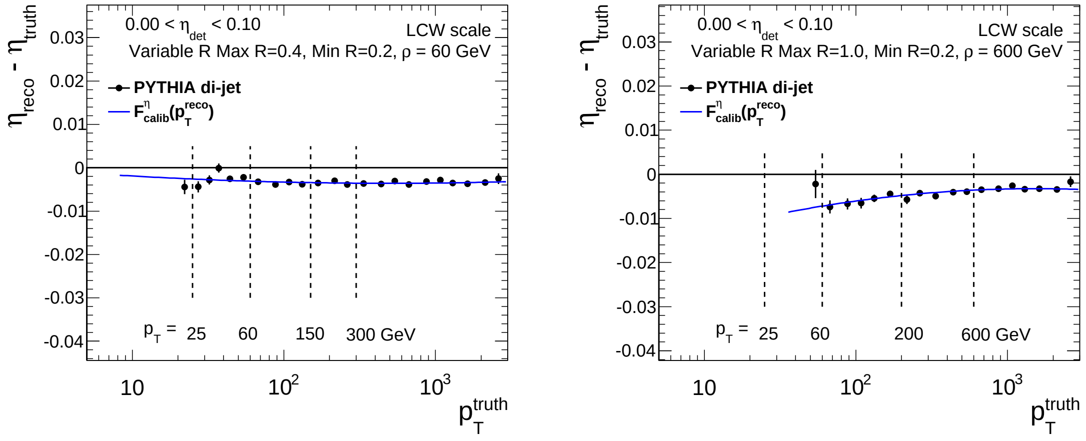

(a)

(b)

Figure 8.11: $\langle \mathcal{R}(\text{truth}) \rangle$ as a function of p_T^{reco} and the $\mathcal{F}_{\text{calib}}$ with the smallest χ^2/NDF for $0.0 < \eta^{\text{reco}} < 0.1$ for a) small VR jets ($R_{\text{min}} = 0.2$, $R_{\text{max}} = 0.4$ and $\rho = 60$ GeV) and b) large VR jets ($R_{\text{min}} = 0.2$, $R_{\text{max}} = 1.0$ and $\rho = 100$ GeV).

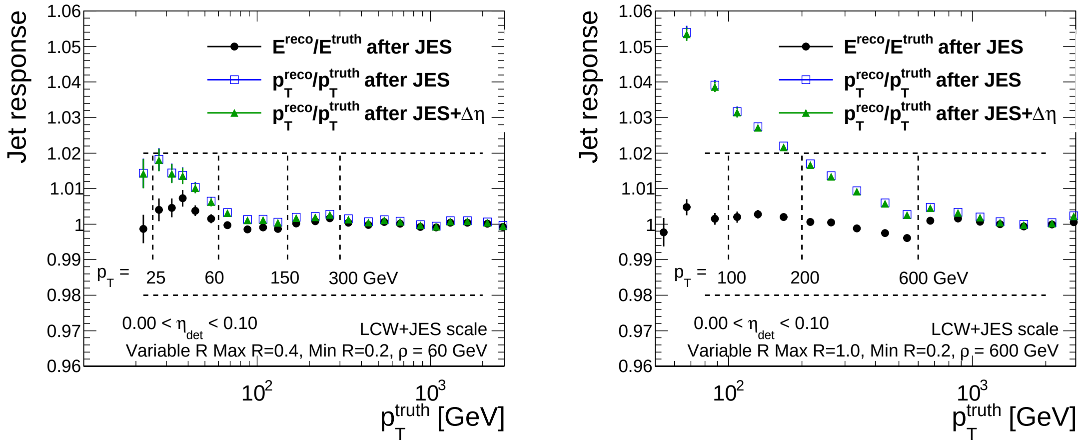

(a)

(b)

Figure 8.12: The energy ($E^{\text{reco}}/E^{\text{truth}}$) and p_{T} ($p_T^{\text{reco}}/p_T^{\text{truth}}$) closure for a) small VR jets and b) large VR jets with $0 < \eta < 0.1$. The energy closure is shown after the JES calibration (black points), the p_{T} closure is shown after the JES calibration (blue squares) and the p_{T} closure is also shown after the JES and η calibrations (green triangles).

size of these instabilities are small (< 0.5 %) and can be accounted for by an additional systematic uncertainty. However, it will be important to try to understand the source of these variations in future studies. Additionally, it can be seen that there are no data points above 1.5 TeV for this η bin, due to a lack of events above this value. At higher η the last data point is at an increasingly low value of p_{T}. For p_{T} greater than the p_{T} of the last data point the calibration is frozen. Improving the fit at high p_{T} would help to increase the accuracy of the calibration for high p_T jets.

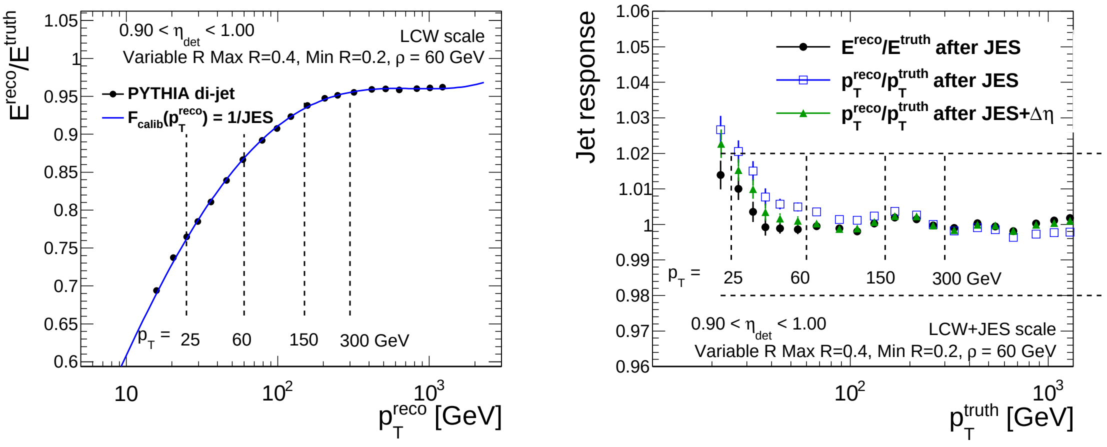

(a) (b)

Figure 8.13: a) shows the energy response distribution ($\mathcal{R}(\mathrm{truth}) = E^{\mathrm{reco}}/E^{\mathrm{truth}}$), that is used to derive the JES calibration factors, and $\mathcal{F}_{\mathrm{calib}}$, as a function of p_T^{reco}. b) shows the energy and p_T closure tests as a function of p_T^{truth}. b) shows $\mathcal{R}(\mathrm{truth}) = E^{\mathrm{reco}}/E^{\mathrm{truth}}$ after the JES calibration (black points), $\mathcal{R}(\mathrm{truth},\ p_T) = p_T^{\mathrm{reco}}/p_T^{\mathrm{truth}}$ after the JES calibration (blue squares) and $\mathcal{R}(\mathrm{truth},\ p_T) = p_T^{\mathrm{reco}}/p_T^{\mathrm{truth}}$ after the JES and η calibrations (green triangles). a) and b) are for small VR jets with $0.9 < \eta < 1.0$.

The calibration factors derived from the energy response distributions and $\Delta\eta$ distributions can be seen in Figure 8.14 for some example p_T values, as a function of η. Also shown is the p_T response following the JES and η calibrations. For small VR jets the p_T closure is within ∼2 % (1 %) for $p_T > 25$ GeV (50 GeV). For large VR jets there is a p_T non-closure of ∼2-3 % for $p_T = 100$ GeV.

8.3.2 Mass Correction for Large VR Jets

The mass calibration for large-R jets makes use of the same methods which are used to derive the JES and η calibrations. To derive the mass calibration, the jet mass response ($\mathcal{R}(\mathrm{truth},\ \mathrm{mass})$, from Equation 5.15 [3]) is measured. $\mathcal{R}(\mathrm{truth},\ \mathrm{mass})$ is measured in bins of η and p_T^{truth}. The same η and p_T^{truth} bins are used as were used to measure $\mathcal{R}(\mathrm{truth})$. It is observed that the $\mathcal{R}(\mathrm{truth},\ \mathrm{mass})$ distributions are highly non-Gaussian in many p_T and η bins, as can be seen in Figure 8.15. Therefore, only the very peak of the distributions

---

[3] $\mathcal{R}(\mathrm{truth},\ \mathrm{mass}) = m^{\mathrm{reco}}/m^{\mathrm{truth}}$

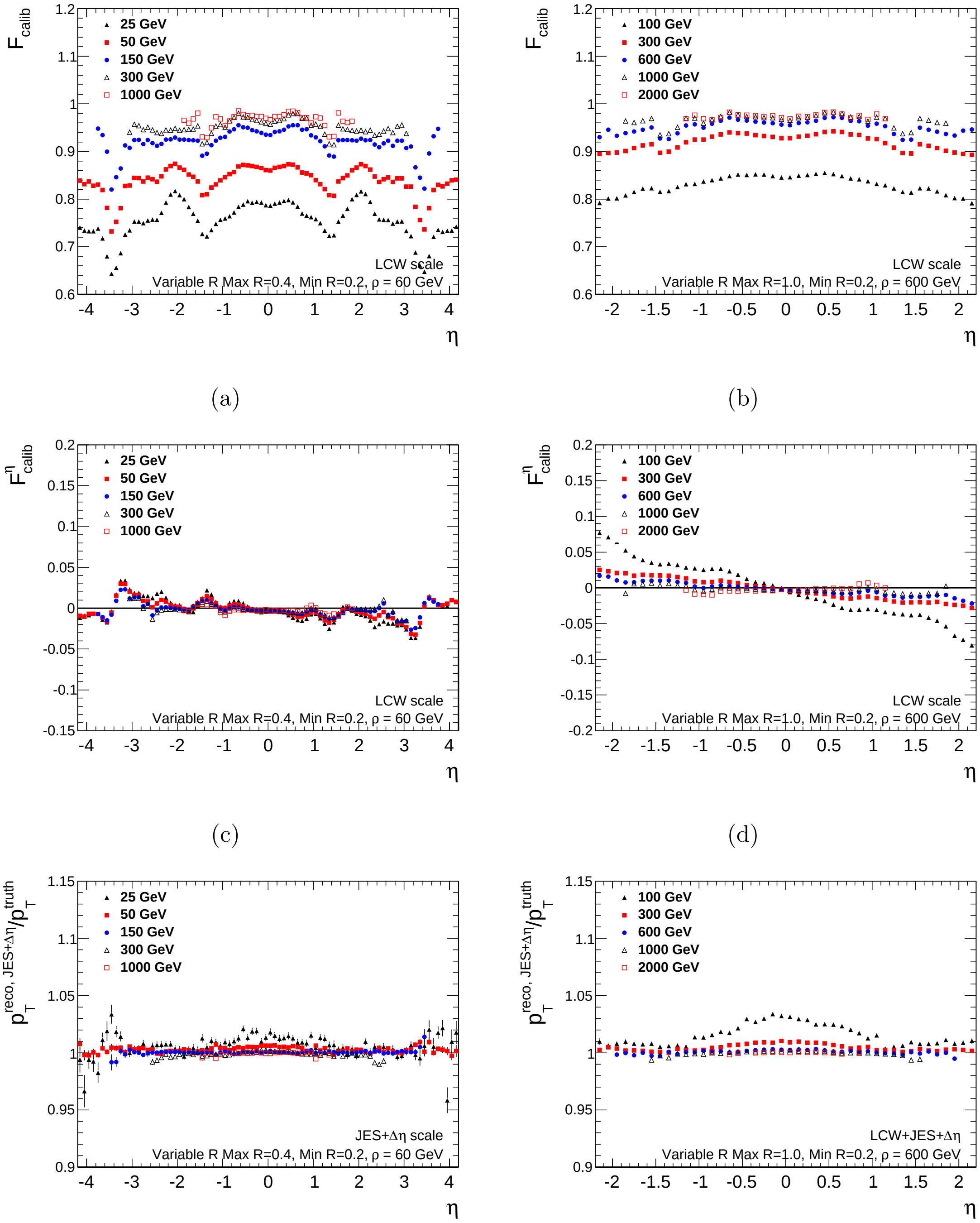

(a) (b)

(c) (d)

(e) (f)

Figure 8.14: The 1/JES calibration factors ($\mathcal{F}_{\text{calib}}$) as a function of η for a) small VR jets and b) large VR jets, the η calibration factors ($\mathcal{F}^{\eta}_{\text{calib}}$) as a function of η for c) small VR jets and d) large VR jets, and the p_{T} closure ($p_T^{\text{reco}}/p_T^{\text{truth}}$) following the JES and eta corrections for e) small VR jets and f) large VR jets. For small VR jets the calibration factors and closure are shown for $p_{\text{T}} = 25$, 50, 150, 300 and 1000 GeV. For large VR jets the calibration factors and closure are shown for $p_{\text{T}} = 100$, 300, 600, 1000 and 2000 GeV.

are fit with a Gaussian in order to find the position of the peak. The $\langle \mathcal{R}(\text{truth, mass}) \rangle$ vs p_T^{truth} distributions that result from these Gaussian fits are then fit with a function of the same form as Equation 8.1 ($\mathcal{F}^{\text{mass}}_{\text{calib}}(p_T^{\text{truth}}) = \sum_{i=0}^{N_{\max}} \left(a_i \left(\ln\ p_T^{\text{truth}}\right)^i\right)$). The jet mass scale is defined as JMS $= 1/\mathcal{F}^{\text{mass}}_{\text{calib}}$ and this is used to correct the jet mass: $m^{\text{reco}} = m^{\text{truth}}/\mathcal{F}^{\text{mass}}_{\text{calib}}$. An example of $\mathcal{F}^{\text{mass}}_{\text{calib}}$, for $0.0 < \eta < 0.1$, can be seen in Figure 8.16 a).

$\mathcal{R}(\text{truth}, \text{p}_\text{T})$ and $\mathcal{R}(\text{truth, mass})$, after the application of the JES, η and mass calibrations can be seen in Figure 8.16. Large fluctuations are seen in the mass closure due to the non-Gaussian nature of the mass responses, which will need to be accounted for by a systematic uncertainty. However, the mass calibration significantly improves the p_T closure for large VR jets with $p_T > 100$ GeV. Below 100 GeV the p_T closure increases up to 2-3 %.

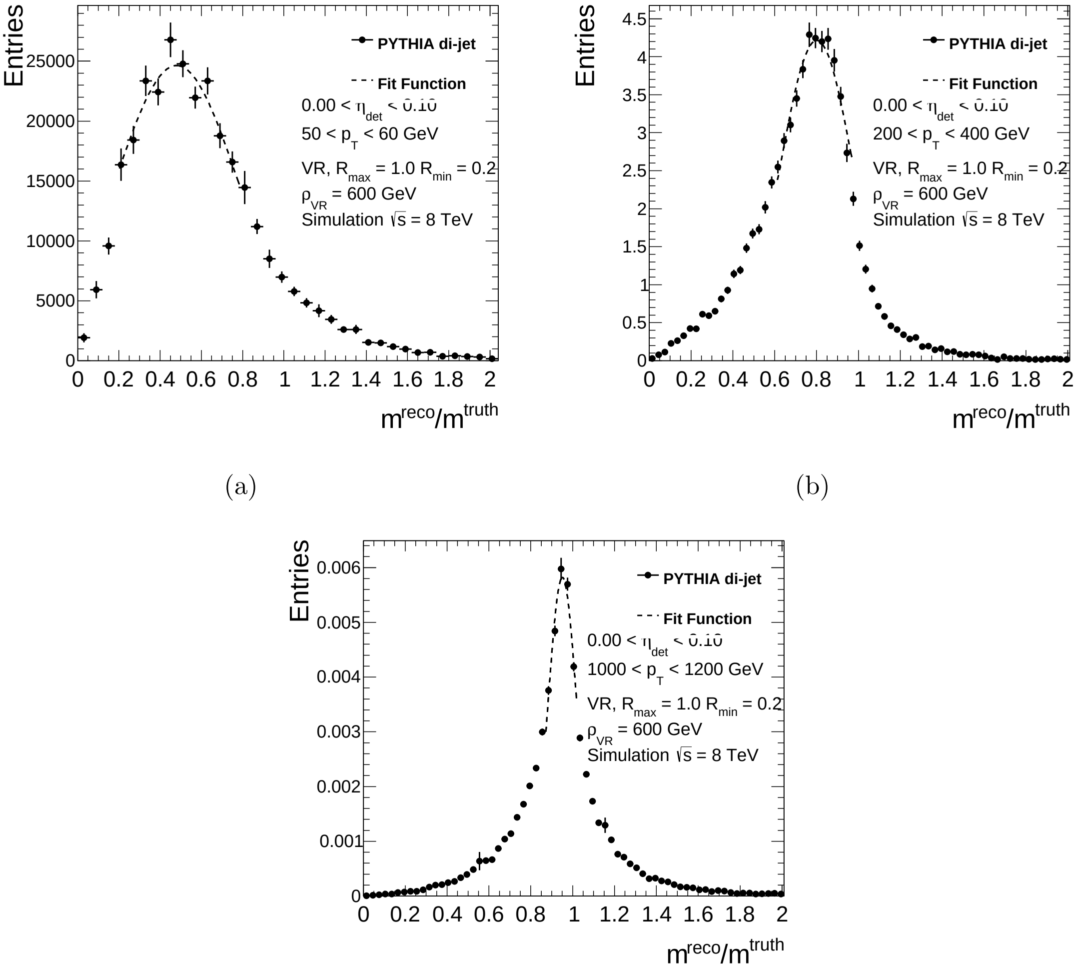

(a)

(b)

(c)

Figure 8.15: Examples of Gaussian fits of the mass response ($m^{\text{reco}}/m^{\text{truth}}$) for large VR jets with $0.0 < \eta < 0.1$ for a) $50 < p_T < 60$ GeV, b) $200 < p_T < 400$ GeV and c) $1000 < p_T < 1200$ GeV.

A summary of the mass calibration factors, the mass closure and the p_T closure following

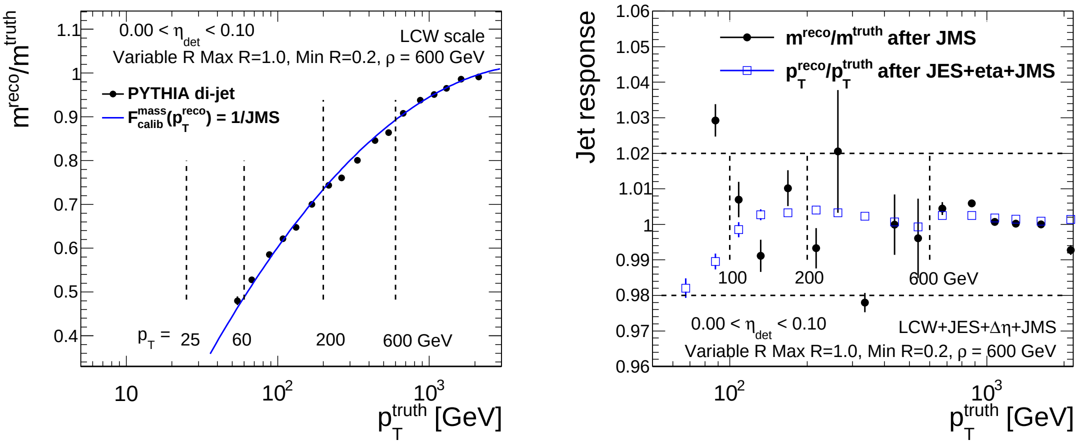

(a) (b)

Figure 8.16: a) shows $\langle\mathcal{R}(\text{truth, mass})\rangle$ as a function of p_T^{truth}, which is used to derive the JMS calibration factors, and the $\mathcal{F}_{\text{calib}}^{\text{mass}}$ with the smallest χ^2/NDF for $0.0 < \eta < 0.1$ for large VR jets. b) shows the mass closure following the application of the JES, η and JMS calibrations. b) shows the mass closure, $m^{\text{reco}}/m^{\text{truth}}$ following the JMS calibration (black points) and the p_{T} closure, $p_T^{\text{reco}}/p_T^{\text{truth}}$ after the JES, η and JMS calibrations (blue points).

the application of the mass calibration can be seen in Figure 8.17. It can be seen that the p_{T} closure is within ∼0.5-1% above 100 GeV and the mass closure is within ∼5 %.

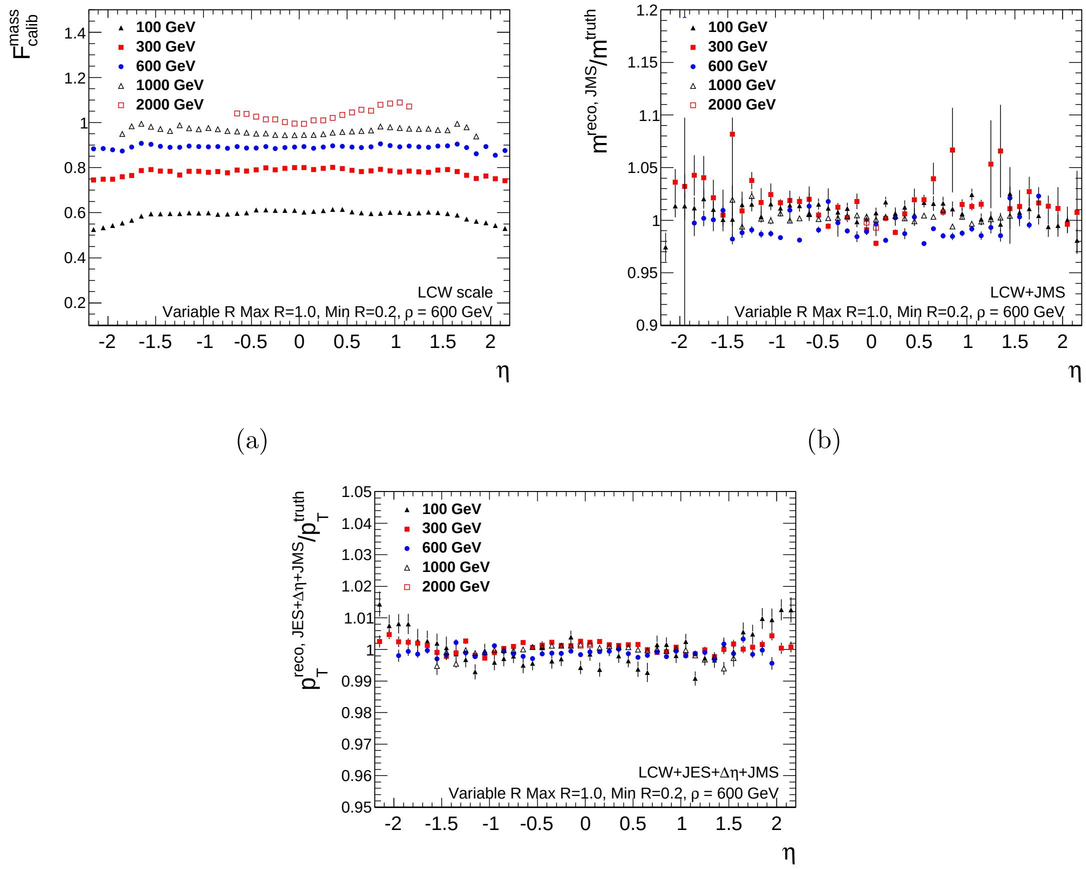

(a) (b)

(c)

Figure 8.17: a) The mass calibration factors ($\mathcal{F}_{\text{calib}}^{\text{mass}}$) as a function of η, b) the mass closure ($m^{\text{reco}}/m^{\text{truth}}$) after applying the JMS factors and c) the p_{T} closure ($p_T^{\text{reco}}/p_T^{\text{truth}}$) after applying the JES, η and mass corrections.

Chapter 9

Evaluation of the Jet Energy Scale Uncertainties for Variable R Jets

In this chapter the γ-jet direct balance method is used to evaluate the performance of the VR jet calibrations described in the previous chapter. The γ-jet JES uncertainties of small and large VR jets are also derived. The same techniques which were discussed in Chapters 6 and 7 were used for these studies. The 2012 data and γ-jet Monte Carlo samples described in Section 3.9 were used for the studies presented here, providing the first studies of Variable R jets in data.

The γ-jet method provides a measure of the JES uncertainty of jets by probing differences in the JES between data and Monte Carlo. However, uncertainties are also required to account for other sources of systematic uncertainty, such as the difference between the quark and gluon jet response or the topology of the jets. A list of further uncertainties and performance studies which will be needed to provide a full set of uncertainties for these jet collections is given at the end of this chapter.

9.1 The Jet Energy Scale Uncertainty of VR Jets Derived In-Situ using γ-jet Events

The Jet Energy Scale uncertainty of small and large VR jets has been evaluated in-situ using γ-jet events. The jet area pile-up correction and Monte Carlo calibrations described in the previous chapter are applied to the jets prior to the evaluation of these uncertainties. The event selection and analysis strategy is the same as that used to evaluate the JES uncertainties for large-R jets, which was described in Chapter 7. For small VR jets the uncertainty evaluation covers $25 < p_T^\gamma < 1000$ GeV and extends up to $|\eta^{\mathrm{jet}}| = 2.8$. For higher $|\eta^{\mathrm{jet}}|$ this there is an insufficient number of events to evaluate the uncertainties. Larger $|\eta^{\mathrm{jet}}|$ bins are used at low and high p_T^γ for $|\eta^{\mathrm{jet}}| > 0.8$. The binning used for small VR jets can be seen in Figure 9.1, the p_{T} binning is the same as for the large-R γ-jet analysis. The $|\eta^{\mathrm{jet}}|$ binning retains the same bin boundaries as for the large R γ-jet analysis with different bin merging at high and low p_T^γ in order to retain statistics and cover the wider $|\eta^{\mathrm{jet}}|$ range.

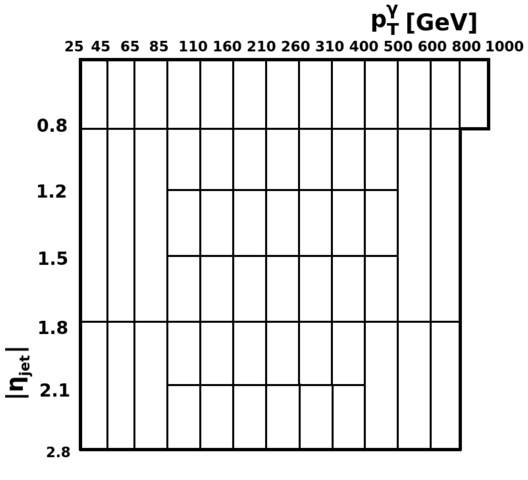

Figure 9.1: The p_T^γ and $|\eta^{\mathrm{jet}}|$ binning used to derive the small VR jet photon response and γ-jet JES uncertainties.

The binning for large VR jets is the same as that used for anti-k_t $R = 1.0$ jets, which was described in Chapter 7. It covers $45 < p_T^\gamma < 1000$ GeV and extends up to $|\eta^{\mathrm{jet}}| = 2.1$. Since the size of large VR jets only shrinks for $p_{\mathrm{T}} > 600$ GeV the large VR jets have a distance parameter of $R = 1.0$ for the majority of the p_{T} range which can be studied using

γ-jet events. Other in-situ techniques such as multi-jet balance and single hadron response measurements will be required to study the rest of the p_{T} region where large VR jets have a changing jet size.

The requirement that $p_T^{\text{leading anti}-\mathrm{k_T}\ \mathrm{R}\,=\,0.4\text{ jet outside jet}}/p_T^{\gamma} < 0.1$ is retained for small and large VR jets. An anti-k_t $R = 0.4$ jet is considered to be outside the VR jet if $\Delta R(\mathrm{anti-k_T\ R = 0.4\ jet,\ VR\ jet}) > D \cdot R_{\mathrm{eff}}$ where R_{eff} is the distance parameter of the VR jet and $D = 0.8$. This is the same procedure as was used for the large-R γ-jet analysis and it provides a veto against additional radiation in the event that is comparable for all VR jet collections.

9.1.1 The Photon Response for VR Jets

Figure 9.2 shows the photon response for small VR jets and Figure 9.3 shows the photon response for large VR jets. For small VR jets the photon response decreases for $p_{\mathrm{T}} < 110$ GeV, where the jets have a fixed radius ($R = 0.4$). The photon response also decreases in the region $160 < p_T^{\gamma} < 310$ GeV, where the radius of the small VR jets is decreasing. These decreases in the photon response for small VR jets are more pronounced for $|\eta^{\mathrm{jet}}| > 0.8$ compared to $|\eta^{\mathrm{jet}}| < 0.8$. For large VR jets, the photon response rises as p_T^{γ} decreases for $|\eta^{\mathrm{jet}}| < 0.8$. For $|\eta^{\mathrm{jet}}| > 0.8$ the photon response decreases for $p_T^{\gamma} < 100$ GeV.

As discussed previously, out-of-cone radiation and the underlying event can result in an imbalance between the momentum of the jet and the photon. The k-term (which was introduced in Section 6.4.7) can be used to assess whether there is significant out-of-cone radiation, or contributions from the underlying event that would affect the value of the photon response. The k-term for small and large VR jets, for $|\eta^{\mathrm{jet}}| < 0.8$, can be seen in Figure 9.4. For small VR jets (Figure 9.4 a)) it can be seen that there is a small decrease in the k-term for $p_T^{\gamma} < 100$ GeV and a significant decrease in the k-term for $160 < p_T^{\gamma} < 310$ GeV. This suggests that in the region $160 < p_T^{\gamma} < 310$ GeV there is an increasing and significant proportion of the hadronic shower that is not captured by the jet algorithm as the jet size decreases. This is consistent with the decrease in the photon response that is observed for this p_{T} region.

For large VR jets (Figure 9.4 b)) the k-term is stable over the full p_T^{γ} range. This suggests that there is little out-of-cone radiation, as expected for jets with such a large radius (large VR jets have $R = 1.0$ for $p_T^{\mathrm{jet}} < 600$ GeV).

Another source of imbalance between $p_T^{\mathrm{reco\ jet}}$ and p_T^{γ} is any residual bias in $p_T^{\mathrm{reco\ jet}}/p_T^{\mathrm{truth\ jet}}$, following the application of the Monte Carlo calibration factors. $p_T^{\mathrm{reco\ jet}}/p_T^{\mathrm{truth\ jet}}$ for small VR jets is shown in Figure 9.5, as a function of $p_T^{\mathrm{truth\ jet}}$. In Figure 9.5 a) only the leading jets which contribute to the photon response are used to calculate $p_T^{\mathrm{reco\ jet}}/p_T^{\mathrm{truth\ jet}}$. In Figure 9.5 b) $p_T^{\mathrm{reco\ jet}}/p_T^{\mathrm{truth\ jet}}$ is calculated using all jets in the γ-jet events (except for those with $\Delta R(\mathrm{jet},\ \gamma) < R_{\mathrm{eff}}$). It can be seen that for the leading jets there is a large non-closure of up to ~ 10 % at $p_T^{\mathrm{truth\ jet}} = 25$ GeV, for $|\eta^{\mathrm{jet}}| < 1.8$. However, for all jets in the γ-jet events the non-closure is significantly smaller, with deviations of up to ~ 3 % at $p_T^{\mathrm{truth\ jet}} = 25$ GeV for $|\eta^{\mathrm{jet}}| < 1.8$. A non-closure of up to ~ 3 % is consistent with the level of non-closure observed in the di-jet Monte Carlo samples where the calibration was derived.

It is expected that there will be differences in the JES for small VR jets in the γ-jet and di-jet samples. This is due to the fact that the leading jets in the γ-jet events are predominantly quark jets, whereas the jets in the di-jet sample are predominantly gluon jets. Since gluon jets have a wider shower shape than quark jets there are differences between the JES for quark and gluon jets. This is because a small radius jet will contain, on average, less of the hadronic shower of a gluon jet in comparison to a quark jet. It will be important to study the flavour uncertainty for small VR jets and to check whether the non-closure observed in the γ-jet sample can be explained by this uncertainty.

For large VR jets there is also a large non-closure for the leading jet in the γ-jet sample, as can be seen in Figure 9.6 a). However, it is not expected that large VR jets will have a significant flavour uncertainty. This is because the large radius of large VR jets results in little out-of-cone radiation for the p_{T} range that is studied here. However, there are significant differences between the non-closure for the leading jet in the γ-jet sample and all jets in the γ-jet sample, which can be seen in Figure 9.6 b). For all large VR jets in the

γ-jet sample it is observed that $p_T^{\text{reco jet}} < p_T^{\text{truth jet}}$. This large non-closure for all large VR jets in the γ-jet sample is due to the mass calibration. This can be seen in Figure 9.6 c), where $p_T^{\text{reco jet}}/p_T^{\text{truth jet}}$ for large VR jets is shown: with no Monte Carlo calibration; after the energy and pseudorapidity calibrations; and after the energy, pseudorapidity and mass calibrations.

Further investigation indicates that the non-closure caused by the mass calibration is due to differences in $p_T^{\text{reco jet}}/p_T^{\text{truth jet}}$ for jets with different mass. The mass calibration for large VR jets was performed as a function of p_{T}, inclusive of the jet mass. However, it can be seen in Figure 9.7 that the $m^{\text{truth jet}}/p_T^{\text{truth jet}}$ distributions in the γ-jet Monte Carlo sample tend to have lower values than the $m^{\text{truth jet}}/p_T^{\text{truth jet}}$ distributions in the di-jet Monte Carlo samples. This means that the mass calibration factors are derived for jets with a different substructure to those in the γ-jet sample.

Furthermore, $p_T^{\text{reco jet}}/p_T^{\text{truth jet}}$ in the γ-jet Monte Carlo sample is highly dependent on the value of $m^{\text{truth jet}}/p_T^{\text{truth jet}}$, as can be seen in Figure 9.8. It can also be seen that the $m^{\text{truth jet}}/p_T^{\text{truth jet}}$ distributions are more similar for higher p_{T}, and the dependence of $p_T^{\text{reco jet}}/p_T^{\text{truth jet}}$ on $m^{\text{truth jet}}/p_T^{\text{truth jet}}$ is smaller for higher p_{T} jets. This is consistent with the smaller non-closures which are observed at higher p_{T}. In future studies it will be important to derive the mass calibration for large VR jets as a function of jet mass or $m^{\text{jet}}/p_T^{\text{jet}}$ in order to account for these dependencies.

9.1.2 γ-jet JES Uncertainties for VR Jets

The JES uncertainties for small and large VR jets have been evaluated using the same methods and sources of uncertainty as were used for the small-R and large-R γ-jet analyses for fixed radius jets, which were described in Section 6.4 and 7.4. Despite the deviations observed in $p_T^{\text{reco jet}}/p_T^{\text{truth jet}}$ in the γ-jet sample following calibration, deriving these uncertainties is important in order to assess how well the JES in data corresponds to that measured in Monte Carlo.

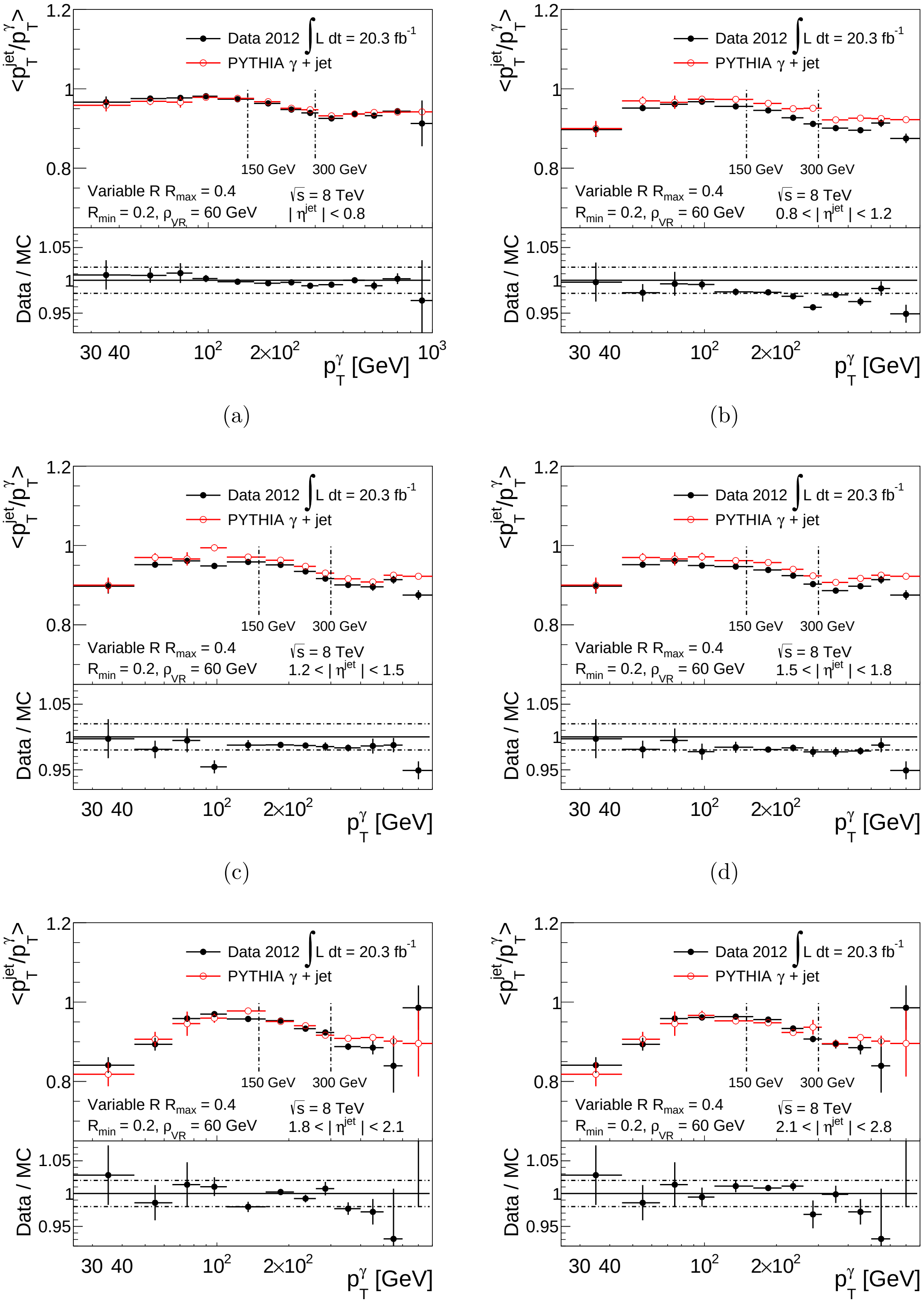

(a) (b)

(c) (d)

(e) (f)

Figure 9.2: Average photon response for small VR jets for (a) $|\eta^{\text{jet}}| < 0.8$ (b) $0.8 < |\eta^{\text{jet}}| < 1.2$, (c) $1.2 < |\eta^{\text{jet}}| < 1.5$, (d) $1.5 < |\eta^{\text{jet}}| < 1.8$, (e) $1.8 < |\eta^{\text{jet}}| < 2.1$, and f) $2.1 < |\eta^{\text{jet}}| < 2.8$. Only statistical uncertainties are shown.

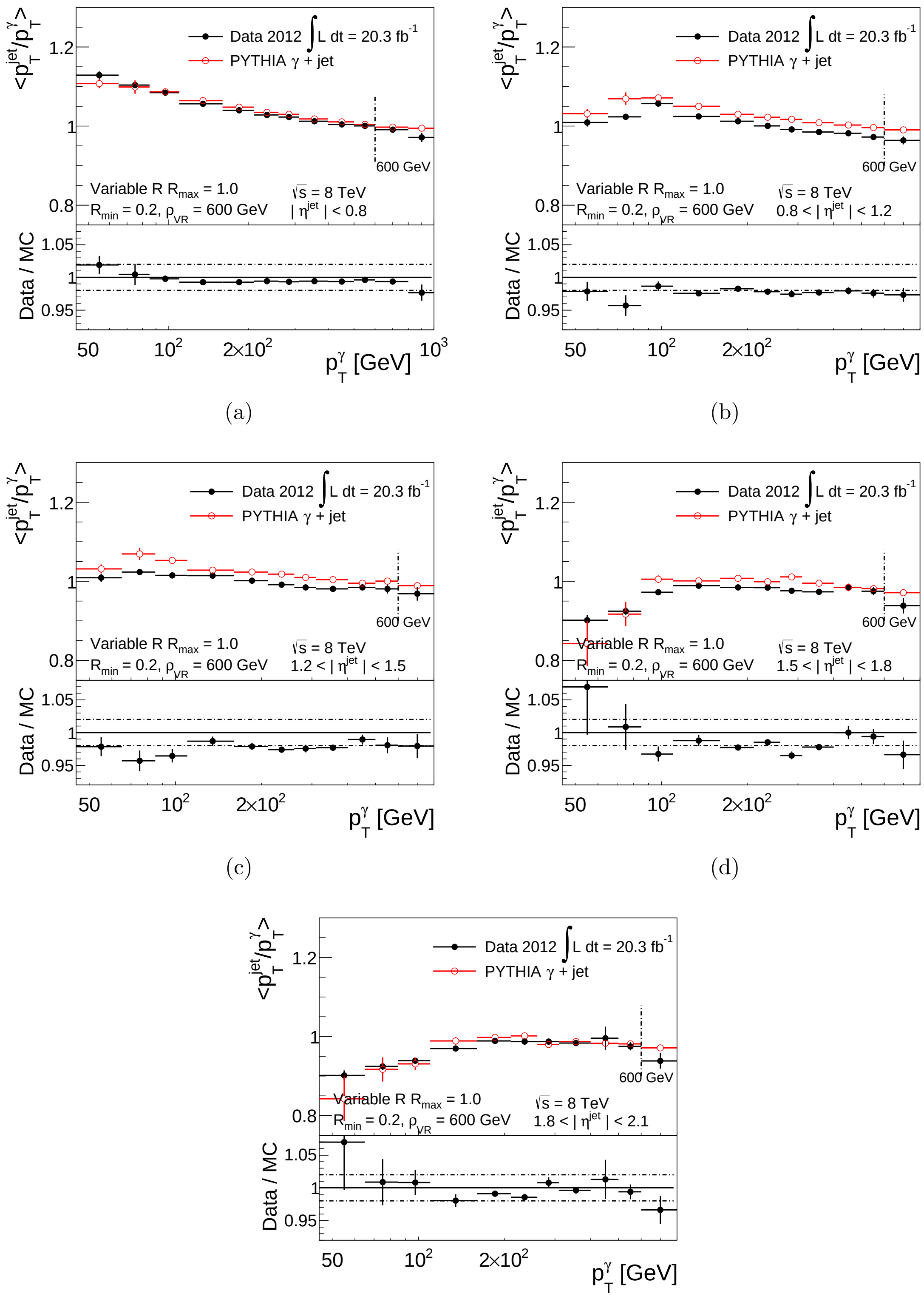

(a)

(b)

(c)

(d)

(e)

Figure 9.3: Average photon response for large VR jets for (a) $|\eta^{\text{jet}}| < 0.8$ (b) $0.8 < |\eta^{\text{jet}}| < 1.2$, (c) $1.2 < |\eta^{\text{jet}}| < 1.5$, (d) $1.5 < |\eta^{\text{jet}}| < 1.8$ and (e) $1.8 < |\eta^{\text{jet}}| < 2.1$. Only statistical uncertainties are shown.

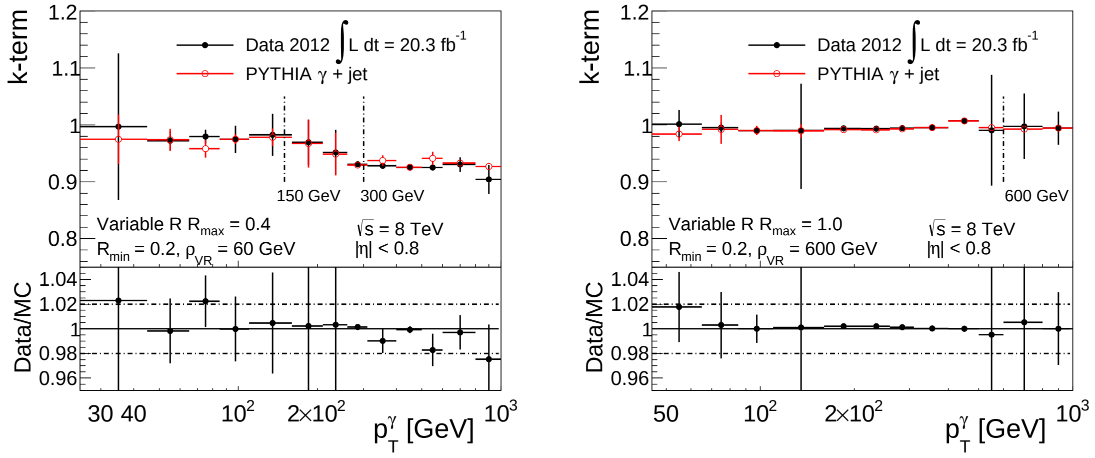

(a) (b)

Figure 9.4: The k-term for a) small and b) large VR jets. Only statistical uncertainties are shown.

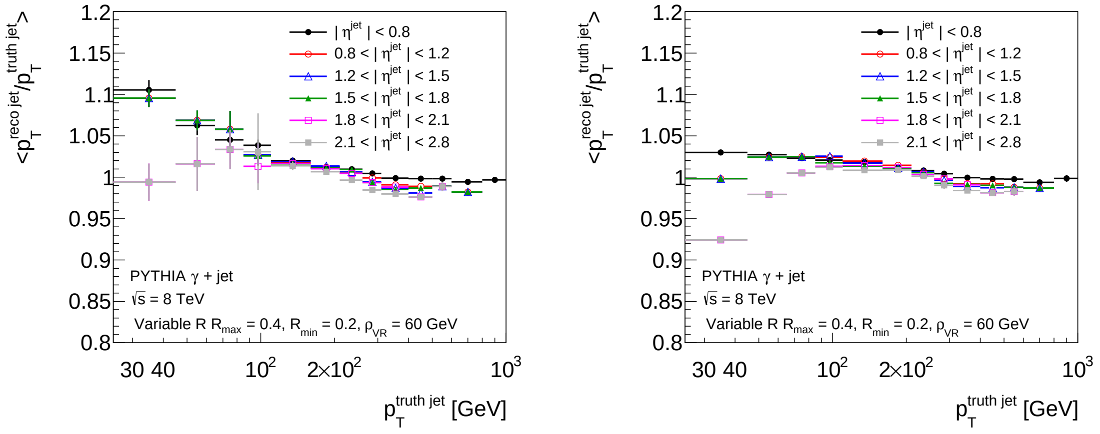

(a) (b)

Figure 9.5: $p_T^{\text{reco jet}}/p_T^{\text{truth jet}}$ vs $p_T^{\text{truth jet}}$ for (a) small VR jets for the leading jets in the γ-jet events which are back-to-back with the photon, (b) small VR jets for all jets in the γ-jet events.

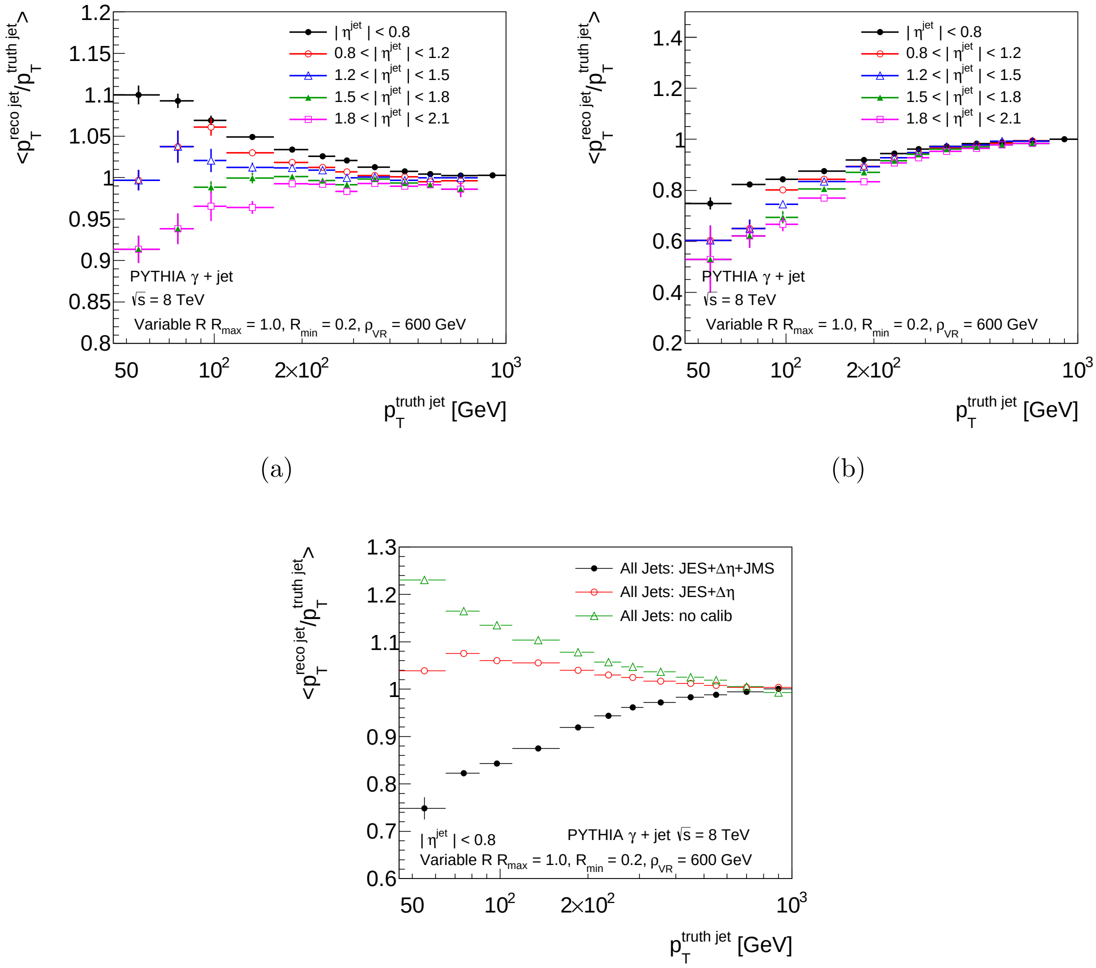

(a)

(b)

(c)

Figure 9.6: $p_T^{\text{reco jet}}/p_T^{\text{truth jet}}$ vs $p_T^{\text{truth jet}}$ for (a) large VR jets for the leading jets in the γ-jet events which are back-to-back with the photon and (b) large VR jets for all jets in the γ-jet events. (c) shows $p_T^{\text{reco jet}}/p_T^{\text{truth jet}}$ vs $p_T^{\text{truth jet}}$ for all large VR jets in the γ-jet sample with: no pile-up correction or Monte Carlo calibration (green triangles), after the JES and η calibrations and after the JES, η and JMS calibrations for $\eta^{\text{jet}} < 0.8$.

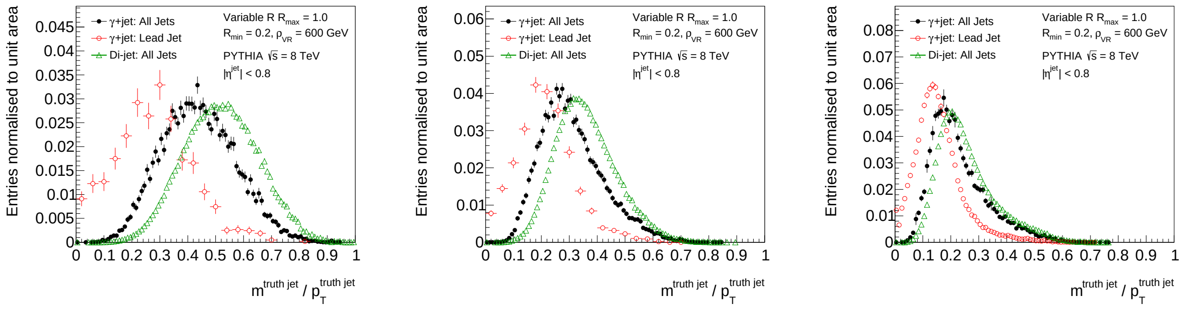

(a) (b) (c)

Figure 9.7: $m^{\text{truth jet}}/p_T^{\text{truth jet}}$ distributions for the leading jet in the γ-jet events, all jets in the γ-jet events and all jets in the di-jet Monte Carlo samples which were used to derive the Monte Carlo calibration for a) $45 < p_T^{\text{truth jet}} < 65$ GeV, b) $110 < p_T^{\text{truth jet}} < 160$ GeV and c) $310 < p_T^{\text{truth jet}} < 400$ GeV. All the distributions are for $|\eta^{\text{jet}}| < 0.8$. The distributions are similar for $|\eta^{\text{jet}}| > 0.8$ and can be found in [6].

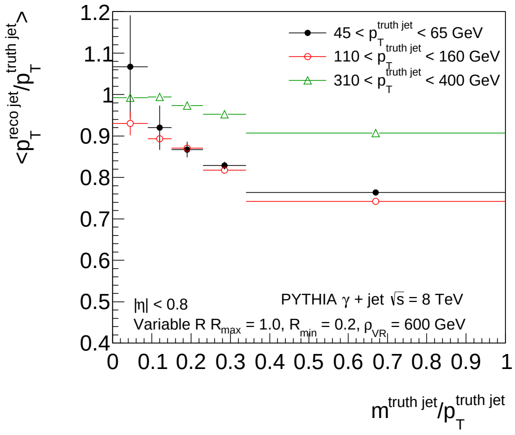

Figure 9.8: $p_T^{\text{reco jet}}/p_T^{\text{truth jet}}$ as a function of $m^{\text{truth jet}}/p_T^{\text{truth jet}}$ for all jets in the γ-jet events for $45 < p_T^{\text{truth jet}} < 65$ GeV, $110 < p_T^{\text{truth jet}} < 160$ GeV and $310 < p_T^{\text{truth jet}} < 400$ GeV. All the distributions are for $|\eta^{\text{jet}}| < 0.8$.

Two systematics which are derived for large VR jets (due to $m^{\text{jet}}/p_T^{\text{jet}}$ and due to the large VR jet encompassing more than one anti-k_t $R = 0.4$ jet), are not derived for small VR jets. The systematic uncertainty on $m^{\text{jet}}/p_T^{\text{jet}}$ is not derived for small VR jets since the mass of small VR jets is not calibrated or used for analysis. The systematic uncertainty to account for differences in the JES for jets encompassing more than one anti-k_t $R = 0.4$ jet is also not derived for small VR jets. Since small VR jets either have a size comparable to $R = 0.4$ or less than $R = 0.4$, they can not contain more than one anti-k_t $R = 0.4$ jet and therefore this uncertainty is not required.

Following bin merging and smoothing (which proceeds in the same way as described in Section 7.5) the total uncertainties can be seen in Figures 9.9 and 9.10 for small and large VR jets respectively. The deviation of data-to-mc ratio of the photon response from one is included in the total uncertainty. The total uncertainties are ~ 1 % for $p_T > 100$ GeV for $|\eta^{\text{jet}}| < 0.8$, increasing to 2-4 % at higher $|\eta^{\text{jet}}|$. The values for these uncertainties can be found in Appendix B and further details can be found in Refs. [5] and [6].

For small VR jets the photon energy scale is a dominant systematic uncertainty for $p_{\text{T}} > 100$ GeV and the generator systematic uncertainty becomes increasingly important as $|\eta^{\text{jet}}|$ increases. For $p_{\text{T}} < 50$ GeV the photon purity is a dominant systematic uncertainty for small VR jets since the photon purity is only ~50 % at $p_T^{\gamma} = 35$ GeV. The deviation of the data-to-mc ratio from one is an important source of uncertainty over the full $|\eta^{\text{jet}}|$ range and it would be desirable to correct for this difference, as is done for small-R anti-k_t jets.

For large VR jets the dominant sources of systematic uncertainty are similar to those for small VR jets. In addition, the uncertainty on $m^{\text{jet}}/p_T^{\text{jet}}$ is important for $|\eta^{\text{jet}}| < 1.2$ and it becomes a dominant source of systematic uncertainty for $|\eta^{\text{jet}}| > 1.2$. This suggests that there are significant data-to-MC differences in the JES due to the modelling of the substructure of the jet, as well as the absolute differences in the JES due to the jet mass that were discussed previously. Therefore, studies into the topology dependence of large VR jets, such as the Monte Carlo studies described in Section 7.6, will be important to ensure that the dependence of the JES on the substructure of large VR jets is well understood.

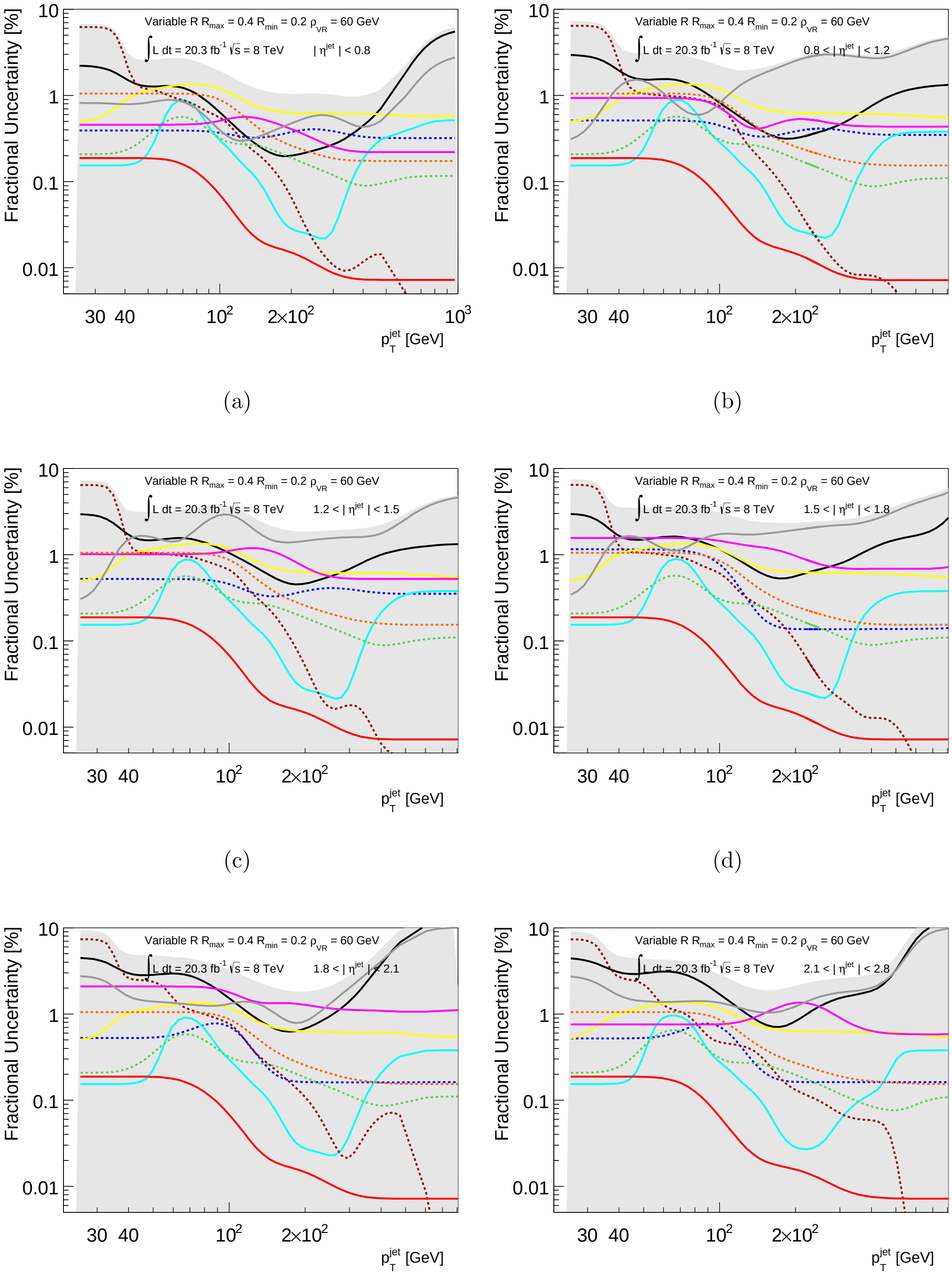

(a) (b)

(c) (d)

(e) (f)

Figure 9.9: JES uncertainties for small VR jets derived from γ-jet events for (a) $|\eta^{\text{jet}}| < 0.8$ (b) $0.8 < |\eta^{\text{jet}}| < 1.2$, (c) $1.2 < |\eta^{\text{jet}}| < 1.5$, (d) $1.5 < |\eta^{\text{jet}}| < 1.8$, (e) $1.8 < |\eta^{\text{jet}}| < 2.1$, and f) $2.1 < |\eta^{\text{jet}}| < 2.8$. The legend for these Figures can be seen in Figure 9.10 (f).

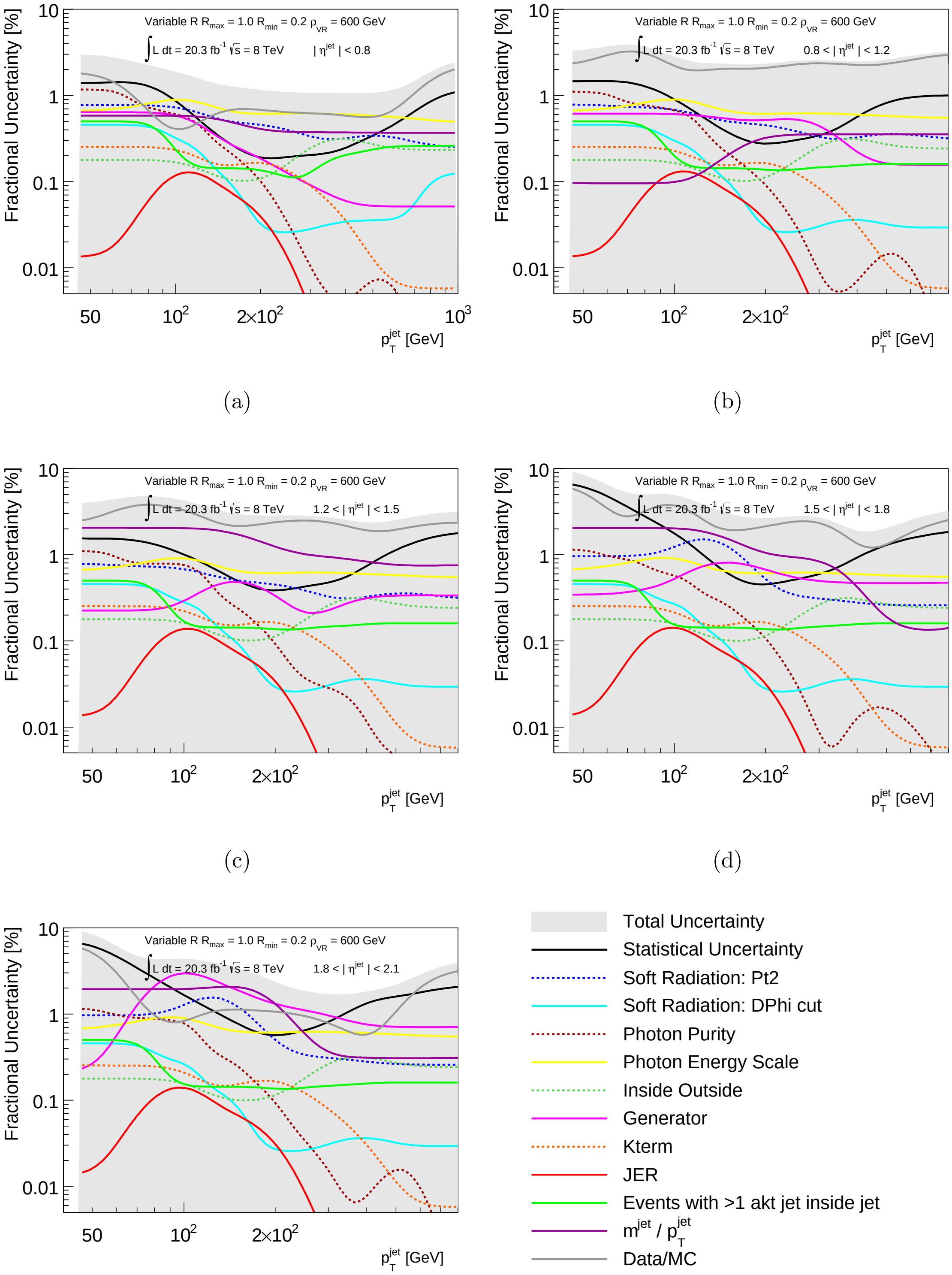

(a) (b)

(c) (d)

(e) (f)

Figure 9.10: JES uncertainties for large VR jets derived from γ-jet events for (a) $|\eta^{\mathrm{jet}}| < 0.8$ (b) $0.8 < |\eta^{\mathrm{jet}}| < 1.2$, (c) $1.2 < |\eta^{\mathrm{jet}}| < 1.5$, (d) $1.5 < |\eta^{\mathrm{jet}}| < 1.8$ and (e) $1.8 < |\eta^{\mathrm{jet}}| < 2.1$. Figure (f) shows the legend for the plots in this Figure and in Figure 9.9.

9.1.3 The JER for VR Jets

As well as measuring the JES, the jet energy resolution (JER) can be estimated in-situ in γ-jet events as follows [3]:

$$\mathrm{JER} = \sqrt{\sigma\left(\frac{\mathrm{p_T^{reco\ jet}}}{\mathrm{p_T^{\gamma}}}\right)^2 - \sigma\left(\frac{\mathrm{p_T^{truth\ jet}}}{\mathrm{p_T^{\gamma}}}\right)^2} \tag{9.1}$$

where $\sigma(p_T^{\text{reco jet}}/p_T^{\gamma})$ is the width of the photon response distribution using reconstructed jets and $\sigma(p_T^{\text{truth jet}}/p_T^{\gamma})$ is the width of the photon response distribution using truth jets. The truth photon response is subtracted from the reconstructed photon response in order to account for smearing of the jet p_{T} at truth level, e.g. due to having events in which the p_{T} of the jet does not exactly balance the p_{T} of the photon. However, in the case where the jet size becomes very small (such as for small VR jets where the jets can be as small as $R = 0.2$ for $p_{\mathrm{T}} > 300$ GeV), out-of-cone radiation results in significant low response tails in the photon response distribution. This is illustrated for small VR jets in Figure 9.11. It can be seen that the photon response using reconstructed jets ($p_T^{\text{reco jet}}/p_T^{\gamma}$) and the photon response using truth jets ($p_T^{\text{truth jet}}/p_T^{\gamma}$) have large low response tails. The tails are larger for $310 < p_T^{\gamma} < 400$ GeV than for $160 < p_T^{\gamma} < 210$ GeV since the VR jets are smaller for the former p_{T} range, and therefore have more out-of-cone radiation. These tails are not observed in the distributions of $p_T^{\text{reco jet}}/p_T^{\text{truth jet}}$ as can be seen in Figure 9.11 c) and f), since both the reconstructed and the truth jets have out-of-cone radiation and are of a similar size. Large asymmetric tails are also not seen for large VR jets, since they have little out-of-cone radiation, as can be seen in Figure 9.12.

The size of these tails can be evaluated on a more quantitative level using quantiles. The $\pm 1\sigma$ and $\pm 2\sigma$ quantiles have been evaluated for small and large VR jets and they are shown in Figure 9.13 for $|\eta^{\text{jet}}| < 0.8$. The -1σ quantile gives the value of the response distribution for which the integral from zero up to that value is equal to the mean minus the standard deviation of the distribution, and similarly for the other quantiles. It can be seen that there are significant tails for small VR jets in the $p_T^{\text{truth jet}}/p_T^{\gamma}$ distributions but not in the $p_T^{\text{reco jet}}/p_T^{\text{truth jet}}$ distributions (where both the reconstructed and truth jets have out-of-cone radiation) and not for large VR jets (where the majority of the hadronic shower is encompassed by the jet due to their large size).

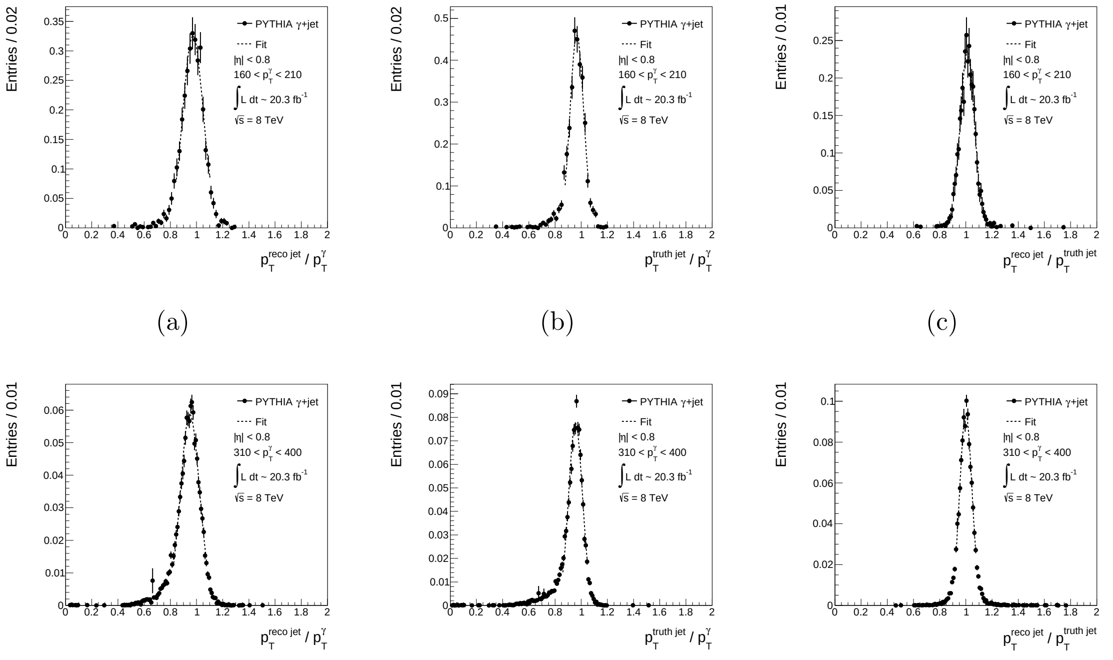

(a) (b) (c)

(d) (e) (f)

Figure 9.11: The response distributions for small VR jets for a) $p_T^{\text{reco jet}}/p_T^\gamma$ for $160 < p_T^\gamma < 210$ GeV, b) $p_T^{\text{truth jet}}/p_T^\gamma$ for $160 < p_T^\gamma < 210$ GeV, c) $p_T^{\text{reco jet}}/p_T^{\text{truth jet}}$ for $160 < p_T^\gamma < 210$ GeV, d) $p_T^{\text{reco jet}}/p_T^\gamma$ for $310 < p_T^\gamma < 400$ GeV, e) $p_T^{\text{truth jet}}/p_T^\gamma$ for $310 < p_T^\gamma < 400$ GeV and f) $p_T^{\text{reco jet}}/p_T^{\text{truth jet}}$ for $310 < p_T^\gamma < 400$ GeV.

These asymmetric tails will not be properly accounted for by the subtraction of $\sigma(p_T^{\text{truth jet}}/p_T^\gamma)$ in the JER since the widths are defined using a fit which does not take into account the asymmetric nature of the response distributions. These tails would need to be accounted for in order to provide a reliable measure of the JER in data and Monte Carlo using the direct balance γ-jet method.

Instead of measuring the JER according to Equation 9.1 the truth Monte Carlo JER ($\sigma(p_T^{\text{reco jet}}/p_T^{\text{truth jet}})$) is measured in the γ-jet samples, since it does not suffer from asymmetric tails in the response distributions. Unfortunately, this can not provide any information about the JER of VR jets in data. The truth JER can be seen in Figures 9.14 and 9.15 for small and large VR jets respectively, as measured using the PYTHIA and HERWIG++

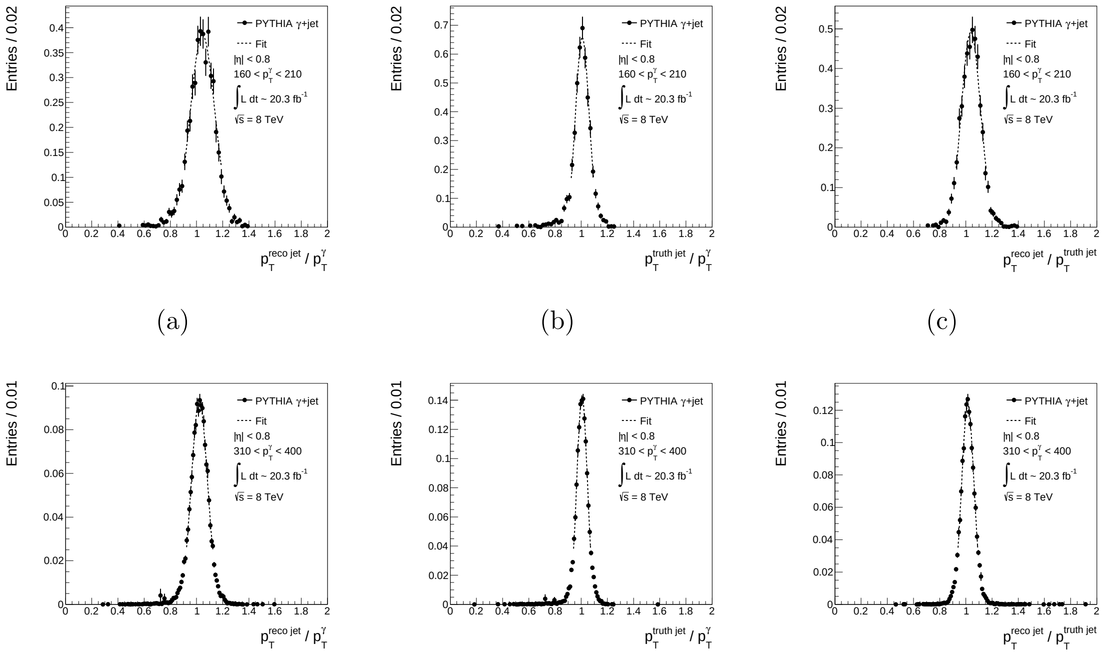

(a) (b) (c)

(d) (e) (f)

Figure 9.12: The response distributions for large VR jets for a) $p_T^{\text{reco jet}}/p_T^{\gamma}$ for $160 < p_T^{\gamma} < 210$ GeV, b) $p_T^{\text{truth jet}}/p_T^{\gamma}$ for $160 < p_T^{\gamma} < 210$ GeV, c) $p_T^{\text{reco jet}}/p_T^{\text{truth jet}}$ for $160 < p_T^{\gamma} < 210$ GeV, d) $p_T^{\text{reco jet}}/p_T^{\gamma}$ for $310 < p_T^{\gamma} < 400$ GeV, e) $p_T^{\text{truth jet}}/p_T^{\gamma}$ for $310 < p_T^{\gamma} < 400$ GeV and f) $p_T^{\text{reco jet}}/p_T^{\text{truth jet}}$ for $310 < p_T^{\gamma} < 400$ GeV.

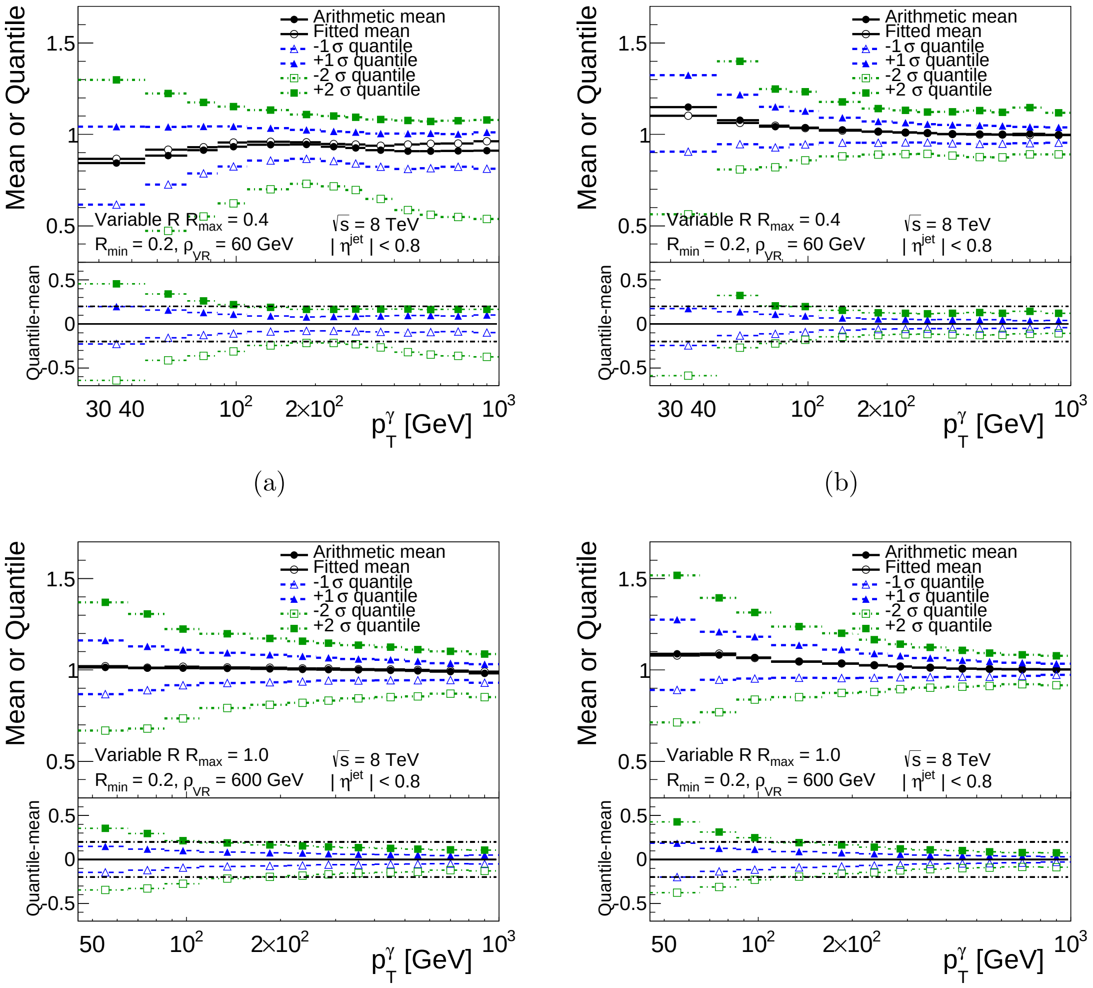

(a)

(b)

(c)

(d)

Figure 9.13: The arithmetic and fitted means of the response distributions and the quantiles for a) $p_T^{\text{truth jet}}/p_T^\gamma$ for small VR jets, b) $p_T^{\text{reco jet}}/p_T^{\text{truth jet}}$ for small VR jets, c) $p_T^{\text{truth jet}}/p_T^\gamma$ for large VR jets and d) $p_T^{\text{reco jet}}/p_T^{\text{truth jet}}$ for large VR jets. All the figures are for $|\eta^{\text{jet}}| < 0.8$. The bottom inset shows the arithmetic mean minus the quantiles.

Monte Carlo generators. It can be seen that the JER is < 0.1 for $p_{\mathrm{T}} > 45$ GeV and ~ 0.05 for $p_{\mathrm{T}} > 210$ GeV for small VR jets. For large VR jets the JER is < 0.1 for $p_{\mathrm{T}} \gtrsim 110$ GeV and < 0.05 for $p_{\mathrm{T}} > 300$ GeV. For large VR jets the JER does not plateau as it does for small VR jets, but continues to decrease for increasing p_{T} over the full p_{T} range which is studied. Within statistical uncertainties the JER estimated using PYTHIA is consistent with that measured with HERWIG++.

In order to probe the JER of VR jets in data and Monte Carlo di-jet events could be used. In this case both jets have out-of-cone radiation and so they are on an equal footing, unlike the photon and the jet in γ-jet events. It will still be important to account for differences in which particles are contained in the jet at truth and reconstructed level. The uncertainty due to these differences is likely to be larger for small jet sizes, and therefore have different effects for different p_{T} ranges for VR jets.

9.2 Future Performance Studies for VR Jets

The following list gives a selection of performance studies which could be performed, to understand the performance of VR jets better, and to provide a full set of uncertainties. This is not an exhaustive list of studies but it covers the most important areas of VR jet performance which still need to be addressed or investigated further.

- **Pile-up uncertainties.** The residual dependence of the jet p_{T} on pile-up, following the jet area correction, will need to be accounted for by a pile-up uncertainty. This can be derived in the same way as was done for $R = 1.0$ trimmed anti-k_t jets, as was discussed in Section 7.7 of this thesis. An additional component to account for the systematic uncertainty due to the median event density, ρ will also be required. The derivation of a correction to correct for the residual dependence of the jet p_{T} on pile-up after the jet area correction would significantly reduce this uncertainty.

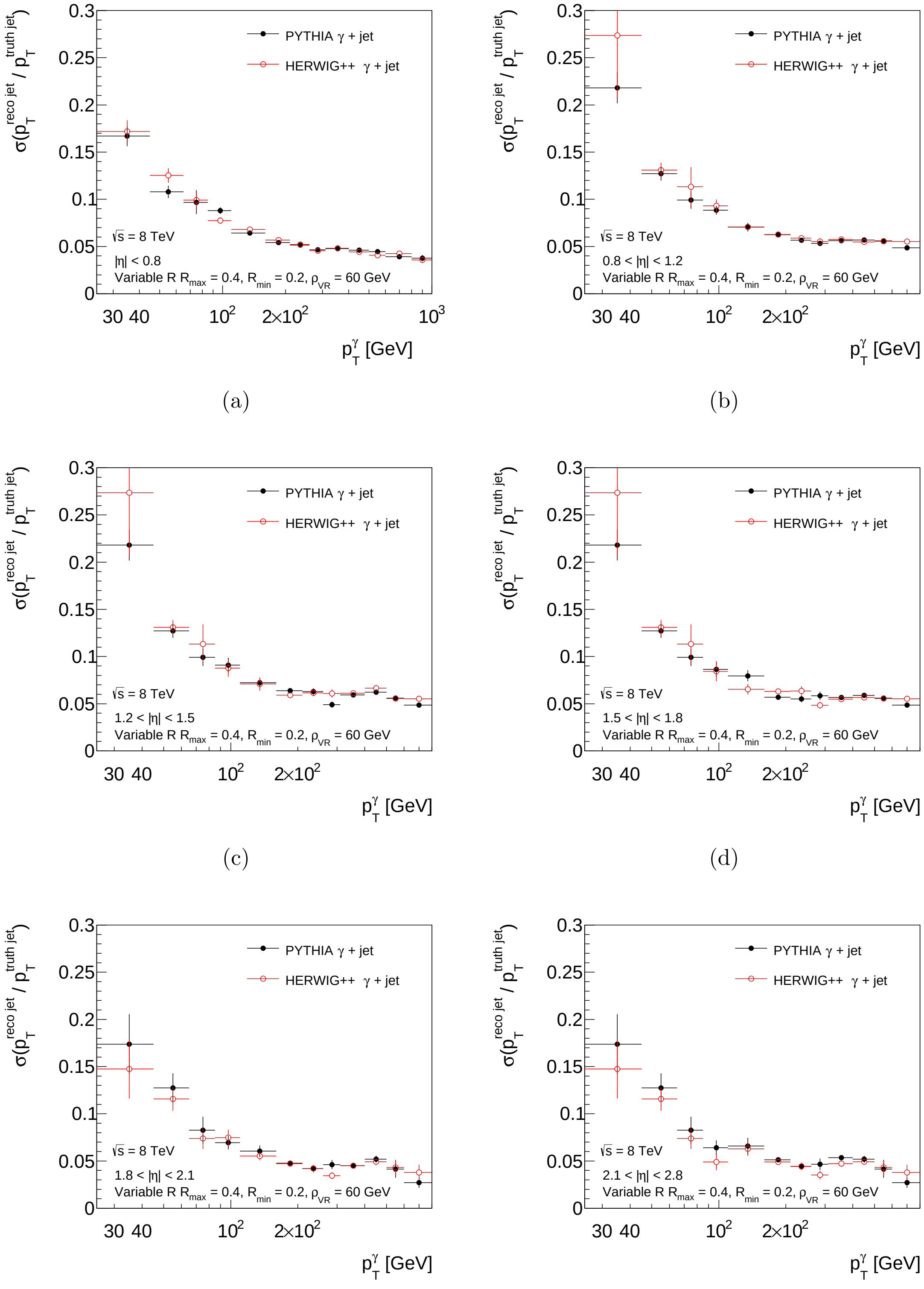

(a) (b) (c) (d) (e) (f)

Figure 9.14: The JER measured with γ-jet events for small VR jets for (a) $|\eta^{\text{jet}}| < 0.8$ (b) $0.8 < |\eta^{\text{jet}}| < 1.2$, (c) $1.2 < |\eta^{\text{jet}}| < 1.5$, (d) $1.5 < |\eta^{\text{jet}}| < 1.8$, (e) $1.8 < |\eta^{\text{jet}}| < 2.1$, and f) $2.1 < |\eta^{\text{jet}}| < 2.8$.Only statistical uncertainties are shown.

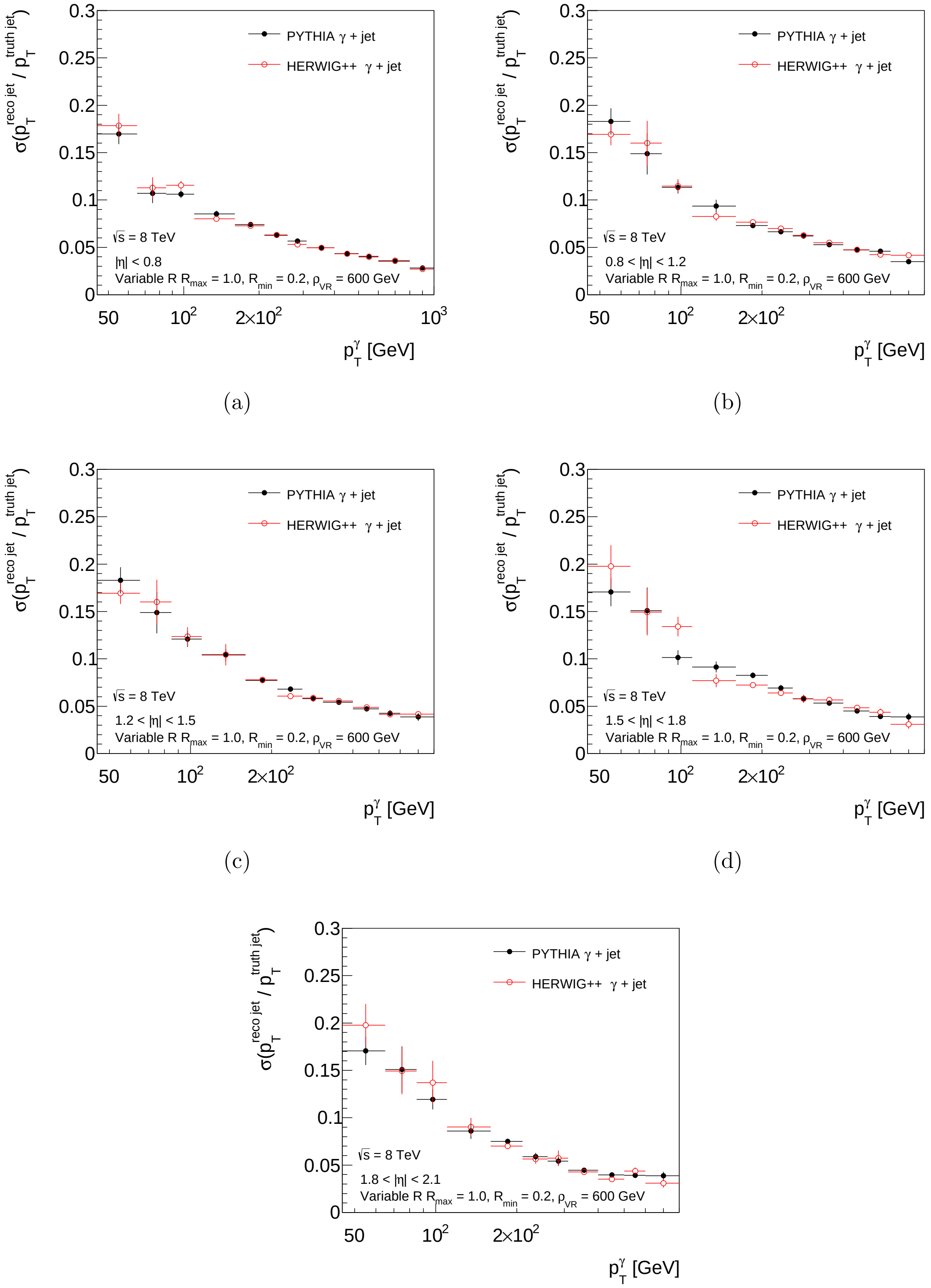

(a)

(b)

(c)

(d)

(e)

Figure 9.15: The JER measured with γ-jet events for large VR jets for (a) $|\eta^{\text{jet}}| < 0.8$ (b) $0.8 < |\eta^{\text{jet}}| < 1.2$, (c) $1.2 < |\eta^{\text{jet}}| < 1.5$, (d) $1.5 < |\eta^{\text{jet}}| < 1.8$ and (e) $1.8 < |\eta^{\text{jet}}| < 2.1$. Only statistical uncertainties are shown.

- **Further studies of the response distributions for the Monte Carlo JES calibration.** The response distributions used for the Monte Carlo JES calibration, which were discussed in the previous chapter, exhibit some instabilities in the region where the VR jets are changing in size. An example of this can be seen in Figure 8.13, for an example η bin of $0.9 < \eta < 1.0$, for small VR jets. The non-closure observed is small (< 0.5 %) and can be accounted for by systematic uncertainties of the same order. However, these instabilities and their causes should be investigated further. The fit function may need to be revisited in order to better fit the shape of the VR jet response distributions.

- **Dependence of the jet mass calibration on the jet mass.** As discussed in this chapter the jet mass calibration should be derived as a function of either jet mass or $m^{\text{jet}}/p_T^{\text{jet}}$ as well as p_T^{jet}. This will account for variations of the mass response for different jet masses. It is also expected to improve the non-Gaussian nature of the mass response that was observed in Figure 8.15, which will make the mass calibration more stable.

- **In-situ uncertainties at low and high p_{T}** The γ-jet studies presented here cover the p_{T} range from 25 - 1000 GeV. Studies making use of Z-jet events would improve the precision of the uncertainties for $p_{\text{T}} < 85$ GeV. At high p_{T}, the multi-jet balance technique could be used to extend the uncertainties into the TeV region. It will also be important to evaluate the JES uncertainties using single hadron studies. These would provide a valuable cross-check of the other in-situ methods, as well as providing uncertainties for $p_T > 1$ TeV.

- **Jet Mass Scale uncertainties for large VR jets.** The uncertainty on the JMS of large VR jets will need to be studied. Initially this can be done using the track-jet double ratio method. However, it would be desirable to develop methods of estimating the uncertainty using e.g. W-jet or $t\bar{t}$ events. These methods have the benefit of probing the JMS using events which are similar to those used in the $t\bar{t}$ resonance searches.

- **Flavour and topology uncertainties.** It will be important to study the dependence of the jet response on quark and gluon jets, and for different event topologies such as events containing W or Z bosons and top quarks. Since these uncertainties depend strongly on the containment of the hadronic shower by the jets they are likely to be significant for small VR jets and for large VR jets at high p_{T}.

- **Jet grooming for large VR jets.** Jet grooming could be investigated for large VR jets. This would help to reduce the impact of pile-up on the jets, which may make the calibration easier to derive. Additionally, jet grooming would improve the precision of the measurement of the jet substructure at low p_{T}.

- **JER of VR jets.** The JER of VR jets should be studied in-situ using di-jet events, which will not suffer from the problems of the asymmetric tails that are observed for small VR jets.

Chapter 10

Conclusions and Outlook

The Jet Energy Scale uncertainty of small and large-R jets and the calibration and Jet Energy Scale uncertainty of Variable R jets have been presented in this thesis. In Chapter 7 it was shown that the Jet Energy Scale uncertainty of large-R jets can be measured in-situ using the γ-jet direct balance method, which is also used to calibrate and derive the Jet Energy Scale uncertainty for small-R jets. The reduction in the Jet Energy Scale uncertainty from the level of 3-4 % to ∼2 % (2-3 %) for $|\eta| < 0.8$ ($|\eta| > 0.8$) between 300 and 700 GeV has been shown to significantly reduce the effect of the Jet Energy Scale uncertainty in the semi-leptonic $t\bar{t}$ resonance search. These uncertainties are now recommended for use by any physics analysis at ATLAS using anti-k_t $R = 1.0$ trimmed jets in the 2012 $\sqrt{s} = 8$ TeV dataset.

Looking forward to Run 2 of the LHC the γ-jet method will continue to provide an accurate measure of the Jet Energy Scale uncertainty for small- and large-R jets. For large-R jets correcting the data-to-MC differences that are observed in the photon response could help to further reduce the baseline Jet Energy Scale uncertainty in the future. Studies using the multi-jet balance and single hadron methods could be used to provide precision measurements of the Jet Energy Scale uncertainty for large-R jets to higher p_{T}. The jet area pile-up correction has been studied for large-R jets and shown, in conjunction with jet grooming, to provide a robust method with which to correct large-R jets for pile-up at the high levels of pile-up expected for Run 2 of the LHC and beyond [115]. In addition to exploiting techniques and methods which are used to probe the Jet Energy Scale uncertainty of small R jets, methods making use of W bosons [46] and $t\bar{t}$ events have been studied and are being developed. These techniques will be important in order to understand the Jet Energy Scale and Jet Mass Scale of large-R jets in topologies similar to those used in physics analyses.

The studies of the calibration and uncertainties for Variable R jets which were presented in Chapters 8 and 9 provide a basis for the calibration of Variable R jets. In this thesis it has been shown that the methods used to calibrate fixed radius jets can be applied to Variable R jets, with some modifications.

This new jet algorithm shows a lot of promise in the context of the $t\bar{t}$ semi-leptonic resonance search. Variable R jets may also be useful for other analyses, for use in jet substructure evaluation, or to construct track-jets for use in b-tagging studies. A reliable calibration and set of uncertainties for Variable R jets will make it possible for physics analyses to fully exploit these jets. A list of studies which could be performed to improve the understanding of the performance of Variable R jets was given at the end of Chapter 9.

Appendix A

Additional Information for the γ-jet Large-R Jet Uncertainties

A.1 The Uncertainties for anti-k_t $R = 1.0$ Trimmed Jets Derived using γ-jet Events Before any Bin Merging or Smoothing

	Uncertainty [%]					
p_T^γ [GeV]	45-65	65-85	85-110	110-160	160-210	210-260
1.0 - Data/MC	2.02±1.42	0.24±1.43	1.14±0.54	0.60±0.32	0.63±0.12	0.52±0.17
m^{jet}/p_T^{jet}	2.46±3.71	-0.44±2.78	-0.06±0.84	1.48±0.50	0.52±0.21	-0.06±0.30
Generator	0.43±1.55	-1.30±1.78	-0.27±0.58	-0.29±0.36	-0.24±0.14	-0.27±0.20
Photon Energy Scale	0.45±0.72	0.66±0.82	0.65±0.25	0.61±0.17	0.56±0.07	0.59±0.10
Cut on the leading anti-k_t $R = 0.4$ jet outside large R jet	0.14±0.82	0.83±1.26	1.21±0.68	0.51±0.23	0.50±0.09	0.28±0.12
Cut on $\Delta\phi(\text{photon} - \text{jet})$	1.67±0.75	0.07±0.72	0.29±0.19	0.10±0.09	0.00±0.03	0.04±0.05
Photon Purity	1.70±0.30	1.03±0.13	0.80±0.07	0.31±0.01	0.15±0.01	0.04±0.01
JER	0.13±0.47	0.27±0.58	-0.01±0.17	0.16±0.11	0.02±0.04	0.00±0.05
Definition of inside/outside large R jet	0.24±0.57	-0.68±0.74	-0.16±0.26	0.07±0.17	-0.07±0.07	-0.23±0.10
Cut on $p_T^{\text{subleading jet}}/p_T^\gamma$	-0.03±0.70	-0.83±0.86	-0.04±0.29	0.25±0.17	0.20±0.06	0.13±0.08
k-term	-0.91±1.75	-0.88±1.41	-0.38±0.89	0.08±3.55	-0.09±0.08	-0.13±0.11
Total uncertainty	4.37±5.11	2.85±4.63	2.11±1.77	1.89±3.65	1.18±0.35	0.94±0.50

Table A.1: γ-jet uncertainties for anti-k_t $R = 1.0$ trimmed jets for $45 < p_T^\gamma < 260$ GeV and $0.00 < |\eta| < 0.80$ before bin merging or smoothing.

	Uncertainty [%]					
Uncertainty [%]	260-310	310-400	400-500	500-600	600-800	800-1000
1.0 - Data/MC	0.57±0.23	0.75±0.16	0.56±0.24	0.44±0.44	0.71±0.55	1.65±1.84
m^{jet}/p_T^{jet}	-0.03±0.42	0.70±0.30	-0.09±0.49	0.06±0.82	-0.52±1.03	-2.08±3.01
Generator	-0.15±0.27	-0.08±0.20	-0.22±0.32	-0.01±0.55	0.04±0.69	-0.06±1.60
Photon Energy Scale	0.63±0.14	0.58±0.04	0.59±0.06	0.57±0.11	0.53±0.15	0.61±0.33
Cut on the leading anti-k_t $R = 0.4$ jet outside large R jet	0.41±0.28	0.19±0.16	0.37±0.20	0.47±0.33	0.50±0.46	1.30±1.00
Cut on $\Delta\phi(\text{photon} - \text{jet})$	0.05±0.06	0.04±0.02	0.02±0.05	0.04±0.08	0.08±0.05	0.10±0.08
Photon Purity	0.01±0.01	0.01±0.00	-0.00±0.01	0.01±0.02	0.00±0.01	-0.00±0.01
JER	0.04±0.06	-0.01±0.01	-0.03±0.02	-0.08±0.04	-0.21±0.14	-1.08±0.62
Definition of inside/outside large R jet	-0.08±0.16	-0.28±0.10	-0.22±0.20	-0.38±0.33	-0.43±0.55	-0.27±1.29
Cut on $p_T^{\text{subleading jet}}/p_T^{\gamma}$	-0.12±0.11	0.14±0.07	-0.07±0.13	-0.20±0.20	0.01±0.26	0.53±0.51
k-term	-0.11±0.11	0.03±0.11	0.51±2.61	0.03±7.39	-0.41±11.31	-0.41±11.31
Total uncertainty	1.00±0.71	1.25±0.49	1.11±2.72	1.06±7.50	1.42±11.43	3.77±12.24

Table A.2: γ-jet uncertainties for anti-k_t $R = 1.0$ trimmed jets for $260 < p_T^{\gamma} < 1000$ GeV and $0.00 < |\eta| < 0.80$ before bin merging or smoothing.

	Uncertainty [%]					
p_T^{γ} [GeV]	45-65	65-85	85-110	110-160	160-210	210-260
1.0 - Data/MC	1.84±2.06	4.59±1.66	0.62±0.74	1.30±0.54	1.92±0.19	2.32±0.27
m^{jet}/p_T^{jet}	-0.70±4.34	2.11±4.01	0.74±1.36	1.32±0.83	-0.13±0.33	-0.18±0.47
Generator	-0.41±1.85	-1.65±2.14	-0.82±0.90	0.47±0.58	-0.65±0.23	-0.39±0.32
Photon Energy Scale	0.84±0.60	0.83±0.75	0.66±0.33	0.56±0.19	0.58±0.11	0.71±0.15
Cut on the leading anti-k_t $R = 0.4$ jet outside large R jet	3.47±1.18	3.06±1.27	0.69±0.56	0.60±0.41	0.32±0.14	0.77±0.21
Cut on $\Delta\phi(\text{photon} - \text{jet})$	0.94±0.43	1.99±0.81	0.11±0.33	0.04±0.22	0.12±0.05	0.03±0.08
Photon Purity	2.03±0.31	0.99±0.15	0.80±0.10	0.28±0.02	0.14±0.01	0.06±0.01
JER	-0.44±0.54	0.78±0.63	0.23±0.26	-0.19±0.18	0.03±0.06	0.02±0.08
Definition of inside/outside large R jet	0.28±0.65	0.95±0.93	-0.60±0.38	0.11±0.29	-0.15±0.12	-0.08±0.17
Cut on $p_T^{\text{subleading jet}}/p_T^{\gamma}$	0.80±0.88	1.08±1.06	0.05±0.41	0.34±0.28	-0.15±0.10	-0.15±0.14
k-term	-0.91±1.75	-0.88±1.41	-0.38±0.89	0.08±3.55	-0.09±0.08	-0.13±0.11
Total uncertainty	5.27±6.11	7.03±5.78	2.07±2.34	2.20±3.82	2.17±0.55	2.60±0.78

Table A.3: γ-jet uncertainties for anti-k_t $R = 1.0$ trimmed jets for $45 < p_T^{\gamma} < 260$ GeV and $0.80 < |\eta| < 1.20$ before bin merging or smoothing.

	Uncertainty [%]				
Uncertainty [%]	260-310	310-400	400-500	500-600	600-800
1.0 - Data/MC	2.92±0.37	2.24±0.28	2.74±0.45	2.42±1.49	2.52±1.28
m^{jet}/p_T^{jet}	-1.79±0.69	1.00±0.50	0.80±0.89	2.98±1.47	0.32±2.24
Generator	-0.76±0.45	-0.18±0.34	-0.09±0.59	-0.31±1.08	-1.46±1.55
Photon Energy Scale	0.72±0.22	0.60±0.07	0.69±0.09	0.63±0.17	0.55±0.29
Cut on the leading anti-k_t $R = 0.4$ jet outside large R jet	0.66±0.28	0.90±0.29	0.09±0.47	0.65±0.63	1.10±0.95
Cut on $\Delta\phi(\text{photon} - \text{jet})$	0.07±0.12	0.14±0.07	0.00±0.08	0.13±0.16	0.05±0.06
Photon Purity	0.01±0.01	0.00±0.01	0.01±0.01	-0.00±0.03	0.00±0.01
JER	-0.07±0.10	0.01±0.03	-0.03±0.04	0.03±0.08	0.00±0.25
Definition of inside/outside large R jet	0.11±0.27	-0.47±0.17	-0.13±0.33	0.44±0.47	-0.41±0.94
Cut on $p_T^{\text{subleading jet}}/p_T^{\gamma}$	-0.48±0.19	0.17±0.12	-0.16±0.20	0.51±0.28	-0.26±0.60
k-term	-0.11±0.11	0.03±0.11	0.51±2.61	0.03±7.39	-0.41±11.31
Total uncertainty	3.70±1.11	2.75±0.82	3.03±2.96	4.28±7.95	3.49±11.87

Table A.4: γ-jet uncertainties for anti-k_t $R = 1.0$ trimmed jets for $260 < p_T^{\gamma} < 800$ GeV and $0.80 < |\eta| < 1.20$ before bin merging or smoothing.

	Uncertainty [%]					
p_T^{γ} [GeV]	45-65	65-85	85-110	110-160	160-210	210-260
1.0 - Data/MC	1.84±2.06	4.59±1.66	4.20±1.02	1.48±0.73	2.09±0.27	1.74±0.38
m^{jet}/p_T^{jet}	-0.70±4.34	2.11±4.01	1.03±1.82	0.69±1.04	1.64±0.44	-0.32±0.61
Generator	-0.41±1.85	-1.65±2.14	-1.38±1.15	-1.46±0.75	-0.64±0.30	-0.48±0.42
Photon Energy Scale	0.84±0.60	0.83±0.75	0.69±0.42	0.71±0.23	0.57±0.13	0.70±0.18
Cut on the leading anti-k_t $R = 0.4$ jet outside large R jet	3.47±1.18	3.06±1.27	1.29±1.29	0.35±0.47	0.67±0.19	0.83±0.27
Cut on $\Delta\phi(\text{photon} - \text{jet})$	0.94±0.43	1.99±0.81	0.08±0.42	0.48±0.20	0.03±0.08	0.06±0.10
Photon Purity	2.03±0.31	0.99±0.15	0.83±0.13	0.34±0.02	0.15±0.02	0.03±0.02
JER	-0.44±0.54	0.78±0.63	0.12±0.33	0.26±0.25	-0.04±0.08	-0.01±0.11
Definition of inside/outside large R jet	0.28±0.65	0.95±0.93	0.27±0.55	0.10±0.37	-0.01±0.15	0.07±0.22
Cut on $p_T^{\text{subleading jet}}/p_T^{\gamma}$	0.80±0.88	1.08±1.06	-0.32±0.56	0.18±0.35	0.18±0.13	0.04±0.18
k-term	-0.91±1.75	-0.88±1.41	-0.38±0.89	0.08±3.55	-0.09±0.08	-0.13±0.11
Total uncertainty	5.27±6.11	7.03±5.78	4.98±3.21	2.54±3.99	2.90±0.73	2.18±1.03

Table A.5: γ-jet uncertainties for anti-k_t $R = 1.0$ trimmed jets for $45 < p_T^{\gamma} < 260$ GeV and $1.20 < |\eta| < 1.50$ before bin merging or smoothing.

	Uncertainty [%]				
Uncertainty [%]	260-310	310-400	400-500	500-600	600-800
1.0 - Data/MC	2.17±0.54	2.08±0.39	1.48±0.81	0.92±1.18	1.05±2.55
m^{jet}/p_T^{jet}	1.55±0.94	1.47±0.63	-0.62±1.30	2.15±2.05	0.57±2.53
Generator	-0.22±0.62	-0.41±0.43	-0.38±0.85	-0.40±1.52	-0.84±1.83
Photon Energy Scale	0.58±0.32	0.59±0.07	0.62±0.12	0.67±0.24	0.87±0.34
Cut on the leading anti-k_t $R = 0.4$ jet outside large R jet	0.68±0.66	0.26±0.27	0.64±0.58	0.65±0.90	1.22±1.26
Cut on $\Delta\phi(\text{photon} - \text{jet})$	0.07±0.05	0.01±0.08	0.12±0.09	0.37±0.24	0.72±0.39
Photon Purity	0.03±0.01	0.02±0.01	0.01±0.01	0.05±0.05	-0.00±0.01
JER	-0.04±0.14	-0.00±0.04	0.11±0.06	-0.08±0.12	0.25±0.38
Definition of inside/outside large R jet	-0.36±0.33	-0.55±0.23	-0.61±0.57	-2.37±1.28	-1.86±1.76
Cut on $p_T^{\text{subleading jet}}/p_T^{\gamma}$	0.21±0.25	0.44±0.17	0.20±0.34	0.51±0.60	0.28±0.59
k-term	-0.11±0.11	0.03±0.11	0.51±2.61	0.03±7.39	-0.41±11.31
Total uncertainty	2.91±1.61	2.78±1.03	2.20±3.37	3.74±8.18	3.90±12.50

Table A.6: γ-jet uncertainties for anti-k_t $R = 1.0$ trimmed jets for $260 < p_T^{\gamma} < 800$ GeV and $1.20 < |\eta| < 1.50$ before bin merging or smoothing.

	Uncertainty [%]					
p_T^{γ} [GeV]	45-65	65-85	85-110	110-160	160-210	210-260
1.0 - Data/MC	0.68±2.75	2.29±2.75	1.85±1.06	2.44±0.70	2.01±0.30	1.40±0.43
m^{jet}/p_T^{jet}	0.35±6.28	4.78±5.71	4.62±1.92	1.00±1.15	0.72±0.49	0.94±0.75
Generator	-2.05±2.82	-0.21±3.29	-0.32±1.30	-0.74±0.79	-0.92±0.34	-0.66±0.51
Photon Energy Scale	0.71±0.82	0.76±0.72	0.38±0.47	0.68±0.28	0.71±0.13	0.61±0.20
Cut on the leading anti-k_t $R = 0.4$ jet outside large R jet	1.51±1.63	1.17±1.97	1.01±1.55	1.68±1.46	0.81±0.59	0.37±0.59
Cut on $\Delta\phi(\text{photon} - \text{jet})$	1.13±1.37	0.71±1.30	0.53±0.45	0.25±0.18	0.11±0.09	0.08±0.10
Photon Purity	1.86±0.40	0.84±0.22	0.91±0.14	0.36±0.02	0.19±0.02	0.06±0.02
JER	0.02±0.80	-1.40±1.20	0.15±0.38	0.07±0.24	-0.03±0.09	0.11±0.11
Definition of inside/outside large R jet	-0.59±0.98	-0.77±1.09	0.40±0.61	-0.16±0.41	-0.15±0.18	0.20±0.29
Cut on $p_T^{\text{subleading jet}}/p_T^{\gamma}$	-0.70±1.33	-0.97±1.65	0.11±0.60	-0.05±0.38	0.04±0.16	0.08±0.21
k-term	-0.91±1.75	-0.88±1.41	-0.38±0.89	0.08±3.55	-0.09±0.08	-0.13±0.11
Total uncertainty	4.64±8.62	6.57±8.49	5.35±3.49	3.39±4.25	2.59±0.99	2.01±1.32

Table A.7: γ-jet uncertainties for anti-k_t $R = 1.0$ trimmed jets for $45 < p_T^{\gamma} < 260$ GeV and $1.50 < |\eta| < 1.80$ before bin merging or smoothing.

	Uncertainty [%]				
Uncertainty [%]	260-310	310-400	400-500	500-600	600-800
1.0 - Data/MC	2.89±0.68	1.94±0.45	1.51±0.71	3.57±1.12	1.47±3.05
m^{jet}/p_T^{jet}	1.03±1.16	1.44±0.83	-0.49±1.83	0.89±1.62	0.48±2.38
Generator	-0.31±0.75	-0.66±0.58	-0.89±1.25	-0.49±1.79	-0.10±4.31
Photon Energy Scale	0.77±0.30	0.55±0.18	0.66±0.17	0.60±0.31	0.62±0.57
Cut on the leading anti-k_t $R = 0.4$ jet outside large R jet	1.26±0.79	0.33±0.41	1.03±0.88	1.23±1.15	3.56±3.18
Cut on $\Delta\phi(\text{photon} - \text{jet})$	0.19±0.13	0.04±0.11	0.20±0.12	0.29±0.62	0.28±0.39
Photon Purity	-0.00±0.02	0.00±0.01	-0.03±0.01	0.00±0.05	0.00±0.01
JER	-0.18±0.15	0.03±0.05	-0.12±0.08	0.12±0.14	-0.03±0.46
Definition of inside/outside large R jet	-0.19±0.51	-1.29±0.39	-1.47±0.86	-0.62±1.19	-2.39±2.97
Cut on $p_T^{\text{subleading jet}}/p_T^{\gamma}$	0.24±0.28	0.26±0.26	-0.26±0.62	-0.36±0.63	0.69±1.93
k-term	-0.11±0.11	0.03±0.11	0.51±2.61	0.03±7.39	-0.41±11.31
Total uncertainty	3.51±1.99	2.94±1.37	2.80±3.83	4.19±8.16	5.59±13.94

Table A.8: γ-jet uncertainties for anti-k_t $R = 1.0$ trimmed jets for $260 < p_T^{\gamma} < 800$ GeV and $1.50 < |\eta| < 1.80$ before bin merging or smoothing.

	Uncertainty [%]					
p_T^{γ} [GeV]	45-65	65-85	85-110	110-160	160-210	210-260
1.0 - Data/MC	0.68±2.75	2.29±2.75	0.58±1.25	0.95±0.83	0.64±0.34	0.87±0.47
m^{jet}/p_T^{jet}	0.35±6.28	4.78±5.71	3.11±2.25	2.17±1.33	1.48±0.58	1.72±0.88
Generator	-2.05±2.82	-0.21±3.29	-1.09±1.53	-1.20±0.96	-1.53±0.40	-0.99±0.61
Photon Energy Scale	0.71±0.82	0.76±0.72	0.98±0.80	0.47±0.36	0.71±0.18	0.87±0.29
Cut on the leading anti-k_t $R = 0.4$ jet outside large R jet	1.51±1.63	1.17±1.97	1.52±1.05	0.95±1.75	0.34±0.26	0.66±0.40
Cut on $\Delta\phi(\text{photon} - \text{jet})$	1.13±1.37	0.71±1.30	0.12±0.55	0.22±0.30	0.03±0.10	0.21±0.16
Photon Purity	1.86±0.40	0.84±0.22	0.92±0.15	0.34±0.02	0.17±0.02	0.10±0.03
JER	0.02±0.80	-1.40±1.20	0.04±0.40	0.18±0.27	0.06±0.09	0.19±0.13
Definition of inside/outside large R jet	-0.59±0.98	-0.77±1.09	0.46±0.77	0.37±0.60	-0.69±0.23	0.54±0.37
Cut on $p_T^{\text{subleading jet}}/p_T^{\gamma}$	-0.70±1.33	-0.97±1.65	0.53±0.77	0.11±0.41	0.48±0.18	0.09±0.25
k-term	-0.91±1.75	-0.88±1.41	-0.38±0.89	0.08±3.55	-0.09±0.08	-0.13±0.11
Total uncertainty	4.64±8.62	6.57±8.49	4.18±3.83	3.04±4.53	2.54±0.97	2.55±1.45

Table A.9: γ-jet uncertainties for anti-k_t $R = 1.0$ trimmed jets for $45 < p_T^{\gamma} < 260$ GeV and $1.80 < |\eta| < 2.10$ before bin merging or smoothing.

	Uncertainty [%]				
Uncertainty [%]	260-310	310-400	400-500	500-600	600-800
1.0 - Data/MC	0.54±0.83	0.62±0.60	0.32±1.52	3.57±1.12	1.47±3.05
m^{jet}/p_T^{jet}	1.41±1.34	-0.25±1.25	4.38±2.06	0.89±1.62	0.48±2.38
Generator	-0.82±0.92	-1.09±0.85	-0.93±1.48	-0.49±1.79	-0.10±4.31
Photon Energy Scale	0.71±0.42	0.70±0.10	0.57±0.21	0.60±0.31	0.62±0.57
Cut on the leading anti-k_t $R = 0.4$ jet outside large R jet	0.95±0.85	0.58±0.50	0.62±0.98	1.23±1.15	3.56±3.18
Cut on $\Delta\phi(\text{photon} - \text{jet})$	0.10±0.16	0.11±0.15	0.07±0.09	0.29±0.62	0.28±0.39
Photon Purity	0.04±0.02	0.02±0.03	-0.01±0.01	0.00±0.05	0.00±0.01
JER	0.18±0.22	-0.09±0.05	0.19±0.11	0.12±0.14	-0.03±0.46
Definition of inside/outside large R jet	-1.30±0.45	-0.88±0.46	-1.93±1.48	-0.62±1.19	-2.39±2.97
Cut on $p_T^{\text{subleading jet}}/p_T^{\gamma}$	0.35±0.38	-0.49±0.32	0.60±0.64	-0.36±0.63	0.69±1.93
k-term	-0.11±0.11	0.03±0.11	0.51±2.61	0.03±7.39	-0.41±11.31
Total uncertainty	2.63±2.31	1.97±1.90	5.25±4.63	4.19±8.16	5.59±13.94

Table A.10: γ-jet uncertainties for anti-k_t $R = 1.0$ trimmed jets for $260 < p_T^{\gamma} < 800$ GeV and $1.80 < |\eta| < 2.10$ before bin merging or smoothing.

A.2 The Uncertainties for anti-k_t $R = 1.0$ Trimmed Jets Derived using γ-jet Events after Bin Merging and Smoothing

	Uncertainty [%]					
p_T^{γ} [GeV]	45-65	65-85	85-110	110-160	160-210	210-260
Average p_T^{γ} [GeV]	52.3695	73.2248	98.6215	139.142	181.163	231.223
Average p_T^{jet} [GeV]	51.5045	70.8058	94.7053	134.414	175.148	223.533
1.0 - Data/MC	2.04	1.54	0.80	0.85	0.69	0.60
m^{jet}/p_T^{jet}	0.02	0.02	0.03	0.27	0.94	0.62
Generator	0.28	0.28	0.28	0.27	0.25	0.24
Photon Energy Scale	0.62	0.57	0.50	0.57	0.61	0.62
Cut on the leading anti-k_t $R = 0.4$ jet outside large R jet	1.97	2.02	1.74	0.82	0.48	0.48
Cut on $\Delta\phi(\text{photon} - \text{jet})$	0.56	0.56	0.50	0.14	0.03	0.01
Photon Purity	1.74	1.63	1.06	0.80	0.31	0.15
JER	0.03	0.03	0.03	0.03	0.03	0.03
Definition of inside/outside large R jet	0.07	0.07	0.07	0.07	0.09	0.11
Cut on $p_T^{\text{subleading jet}}/p_T^{\gamma}$	0.04	0.04	0.04	0.05	0.19	0.13
k-term	0.59	0.59	0.58	0.50	0.18	0.10
Statistics	1.43	1.41	1.20	0.72	0.31	0.19
Total uncertainty	3.76	3.48	2.67	1.82	1.51	1.23

Table A.11: γ-jet uncertainties for anti-k_t $R = 1.0$ trimmed jets for $45 < p_T^{\gamma} < 260$ GeV $0.00 < |\eta| < 0.80$ after bin merging and smoothing

	Uncertainty [%]					
p_T^γ [GeV]	260-310	310-400	400-500	500-600	600-800	800-1000
Average p_T^γ [GeV]	281.30	345.57	439.91	540.01	664.87	865.63
Average p_T^{jet} [GeV]	272.10	333.17	424.65	524.05	642.76	836.04
1.0 - Data/MC	0.58	0.61	0.63	0.59	0.61	0.84
m^{jet}/p_T^{jet}	0.29	0.20	0.18	0.18	0.18	0.18
Generator	0.22	0.19	0.15	0.11	0.10	0.10
Photon Energy Scale	0.64	0.64	0.62	0.61	0.60	0.59
Cut on leading anti-k_t $R = 0.4$ jet outside large R jet	0.44	0.37	0.29	0.30	0.35	0.36
Cut on $\Delta\phi(\text{photon} - \text{jet})$	0.02	0.02	0.03	0.03	0.03	0.04
Photon Purity	0.05	0.02	0.01	0.00	0.00	0.00
JER	0.02	0.01	0.01	0.02	0.03	0.04
Definition of inside/outside large R jet	0.14	0.20	0.28	0.32	0.32	0.32
Cut on $p_T^{\text{subleading jet}}/p_T^\gamma$	0.08	0.07	0.06	0.02	0.01	0.01
k-term	0.08	0.06	0.05	0.04	0.04	0.04
Statistics	0.18	0.19	0.21	0.30	0.46	0.78
Total uncertainty	1.07	1.04	1.03	1.02	1.10	1.39

Table A.12: γ-jet uncertainties for anti-k_t $R = 1.0$ trimmed jets for $260 < p_T^\gamma < 1000$ GeV $0.00 < |\eta| < 0.80$ after bin merging and smoothing

	Uncertainty [%]					
p_T^γ [GeV]	45-65	65-85	85-110	110-160	160-210	210-260
Average p_T^γ [GeV]	52.37	73.23	98.34	138.99	181.15	231.45
Average p_T^{jet} [GeV]	48.99	67.81	92.76	132.22	172.38	219.96
1.0 - Data/MC	1.85	2.69	3.07	1.54	1.45	1.96
m^{jet}/p_T^{jet}	1.14	1.14	1.14	1.12	0.82	0.48
Generator	0.86	0.86	0.85	0.78	0.56	0.56
Photon Energy Scale	0.62	0.55	0.50	0.58	0.61	0.62
Cut on the leading anti-k_t $R = 0.4$ jet outside large R jet	1.97	2.03	1.68	0.73	0.48	0.47
Cut on $\Delta\phi(\text{photon} - \text{jet})$	0.56	0.56	0.48	0.12	0.02	0.01
Photon Purity	2.13	1.85	1.00	0.78	0.27	0.14
JER	0.03	0.03	0.03	0.03	0.03	0.03
Definition of inside/outside large R jet	0.07	0.07	0.07	0.07	0.09	0.11
Cut on $p_T^{\text{subleading jet}}/p_T^\gamma$	0.04	0.04	0.04	0.05	0.19	0.13
k-term	0.59	0.59	0.58	0.49	0.17	0.10
Statistics	2.07	1.91	1.45	0.88	0.46	0.30
Total uncertainty	4.35	4.63	4.26	2.60	2.01	2.27

Table A.13: γ-jet uncertainties for anti-k_t $R = 1.0$ trimmed jets for $45 < p_T^\gamma < 260$ GeV $0.80 < |\eta| < 1.20$ after bin merging and smoothing

	Uncertainty [%]				
p_T^γ [GeV]	260-310	310-400	400-500	500-600	600-800
Average p_T^γ [GeV]	282.05	345.11	436.77	535.26	662.67
Average p_T^{jet} [GeV]	267.40	327.76	413.10	509.20	628.28
1.0 - Data/MC	2.38	2.53	2.53	2.54	2.52
m^{jet}/p_T^{jet}	0.73	1.09	1.19	1.11	1.09
Generator	0.58	0.52	0.36	0.23	0.21
Photon Energy Scale	0.64	0.64	0.62	0.61	0.60
Cut on leading anti-k_t $R = 0.4$ jet outside large R jet	0.43	0.36	0.28	0.31	0.37
Cut on $\Delta\phi(\text{photon} - \text{jet})$	0.02	0.02	0.02	0.02	0.04
Photon Purity	0.06	0.02	0.01	0.00	0.00
JER	0.02	0.01	0.01	0.02	0.03
Definition of inside/outside large R jet	0.15	0.21	0.29	0.32	0.32
Cut on $p_T^{\text{subleading jet}}/p_T^\gamma$	0.08	0.07	0.06	0.03	0.03
k-term	0.08	0.06	0.05	0.04	0.04
Statistics	0.30	0.33	0.42	0.77	1.13
Total uncertainty	2.69	2.92	2.95	2.98	3.07

Table A.14: γ-jet uncertainties for anti-k_t $R = 1.0$ trimmed jets for $260 < p_T^\gamma < 800$ GeV $0.80 < |\eta| < 1.20$ after bin merging and smoothing

	Uncertainty [%]					
p_T^γ [GeV]	45-65	65-85	85-110	110-160	160-210	210-260
Average p_T^γ [GeV]	52.24	72.91	98.25	138.96	180.92	231.13
Average p_T^{jet} [GeV]	48.72	67.18	91.93	132.08	173.11	220.96
1.0 - Data/MC	1.81	2.75	4.02	3.66	2.02	1.90
m^{jet}/p_T^{jet}	0.84	0.84	0.83	0.83	1.02	1.13
Generator	1.19	1.19	1.19	1.24	1.14	0.73
Photon Energy Scale	0.62	0.55	0.50	0.59	0.61	0.62
Cut on the leading anti-k_t $R = 0.4$ jet outside large R jet	1.95	2.01	1.65	0.72	0.48	0.47
Cut on $\Delta\phi(\text{photon} - \text{jet})$	0.56	0.56	0.47	0.11	0.02	0.01
Photon Purity	2.13	1.84	1.00	0.81	0.32	0.15
JER	0.03	0.03	0.03	0.03	0.03	0.03
Definition of inside/outside large R jet	0.07	0.07	0.07	0.07	0.09	0.11
Cut on $p_T^{\text{subleading jet}}/p_T^\gamma$	0.04	0.04	0.04	0.05	0.19	0.13
k-term	0.59	0.59	0.58	0.49	0.17	0.10
Statistics	2.08	1.92	1.53	1.08	0.62	0.41
Total uncertainty	4.33	4.67	5.02	4.31	2.76	2.50

Table A.15: γ-jet uncertainties for anti-k_t $R = 1.0$ trimmed jets for $45 < p_T^\gamma < 260$ GeV $1.20 < |\eta| < 1.50$ after bin merging and smoothing

	Uncertainty [%]				
p_T^{γ} [GeV]	260-310	310-400	400-500	500-600	600-800
Average p_T^{γ} [GeV]	281.37	345.11	438.52	540.84	663.45
Average p_T^{jet} [GeV]	269.08	329.16	419.74	520.95	640.86
1.0 - Data/MC	1.96	2.00	1.89	1.48	1.18
m^{jet}/p_T^{jet}	0.87	0.71	0.68	0.67	0.67
Generator	0.48	0.42	0.42	0.42	0.42
Photon Energy Scale	0.64	0.64	0.62	0.61	0.60
Cut on leading anti-k_t $R = 0.4$ jet outside large R jet	0.43	0.36	0.29	0.30	0.37
Cut on $\Delta\phi(\text{photon} - \text{jet})$	0.02	0.02	0.02	0.02	0.03
Photon Purity	0.05	0.03	0.02	0.02	0.03
JER	0.02	0.01	0.01	0.02	0.03
Definition of inside/outside large R jet	0.15	0.21	0.29	0.32	0.32
Cut on $p_T^{\text{subleading jet}}/p_T^{\gamma}$	0.08	0.07	0.06	0.03	0.03
k-term	0.08	0.06	0.05	0.04	0.04
Statistics	0.42	0.47	0.57	0.93	1.45
Total uncertainty	2.37	2.34	2.25	2.07	2.18

Table A.16: γ-jet uncertainties for anti-k_t $R = 1.0$ trimmed jets for $260 < p_T^{\gamma} < 800$ GeV $1.20 < |\eta| < 1.50$ after bin merging and smoothing

	Uncertainty [%]					
p_T^{γ} [GeV]	45-65	65-85	85-110	110-160	160-210	210-260
Average p_T^{γ} [GeV]	53.05	72.83	98.38	138.80	180.99	230.45
Average p_T^{jet} [GeV]	50.10	67.82	91.77	130.58	170.57	218.07
1.0 - Data/MC	0.71	1.22	1.92	2.05	2.17	1.97
m^{jet}/p_T^{jet}	4.25	4.26	4.22	3.53	1.35	0.89
Generator	0.59	0.59	0.59	0.66	0.85	0.77
Photon Energy Scale	0.62	0.56	0.51	0.58	0.61	0.62
Cut on the leading anti-k_t $R = 0.4$ jet outside large R jet	0.83	0.83	0.82	0.70	0.38	0.35
Cut on $\Delta\phi(\text{photon} - \text{jet})$	0.56	0.56	0.47	0.12	0.02	0.01
Photon Purity	1.95	1.69	0.91	0.85	0.34	0.17
JER	0.03	0.03	0.03	0.03	0.03	0.03
Definition of inside/outside large R jet	0.07	0.07	0.07	0.07	0.09	0.11
Cut on $p_T^{\text{subleading jet}}/p_T^{\gamma}$	0.04	0.04	0.04	0.05	0.19	0.13
k-term	0.59	0.59	0.58	0.48	0.16	0.10
Statistics	2.76	2.71	2.25	1.30	0.62	0.45
Total uncertainty	5.65	5.64	5.41	4.54	2.89	2.46

Table A.17: γ-jet uncertainties for anti-k_t $R = 1.0$ trimmed jets for $45 < p_T^{\gamma} < 260$ GeV $1.50 < |\eta| < 1.80$ after bin merging and smoothing

	Uncertainty [%]				
p_T^{γ} [GeV]	260-310	310-400	400-500	500-600	600-800
Average p_T^{γ} [GeV]	280.86	345.07	435.99	536.82	637.53
Average p_T^{jet} [GeV]	264.34	323.52	417.75	504.81	586.38
1.0 - Data/MC	2.01	2.14	2.10	2.21	2.31
m^{jet}/p_T^{jet}	0.85	0.89	0.96	1.01	1.02
Generator	0.64	0.61	0.64	0.68	0.68
Photon Energy Scale	0.64	0.64	0.62	0.61	0.59
Cut on leading anti-k_t $R = 0.4$ jet outside large R jet	0.40	0.43	0.44	0.45	0.45
Cut on $\Delta\phi(\text{photon} - \text{jet})$	0.02	0.02	0.02	0.03	0.04
Photon Purity	0.06	0.02	0.01	0.02	0.01
JER	0.02	0.01	0.01	0.02	0.04
Definition of inside/outside large R jet	0.15	0.21	0.29	0.32	0.32
Cut on $p_T^{\text{subleading jet}}/p_T^{\gamma}$	0.08	0.07	0.06	0.03	0.03
k-term	0.08	0.06	0.05	0.04	0.04
Statistics	0.49	0.55	0.65	1.09	1.68
Total uncertainty	2.45	2.59	2.62	2.86	3.21

Table A.18: γ-jet uncertainties for anti-k_t $R = 1.0$ trimmed jets for $260 < p_T^{\gamma} < 800$ GeV $1.50 < |\eta| < 1.80$ after bin merging and smoothing

	Uncertainty [%]					
p_T^{γ} [GeV]	45-65	65-85	85-110	110-160	160-210	210-260
Average p_T^{γ} [GeV]	52.89	72.93	98.29	138.85	180.97	230.08
Average p_T^{jet} [GeV]	49.11	69.11	92.63	132.66	172.94	218.62
1.0 - Data/MC	0.66	1.15	1.58	1.02	0.83	0.77
m^{jet}/p_T^{jet}	2.78	2.78	2.68	2.49	2.11	1.72
Generator	1.15	1.15	1.15	1.21	1.41	1.29
Photon Energy Scale	0.63	0.56	0.50	0.58	0.61	0.62
Cut on the leading anti-k_t $R = 0.4$ jet outside large R jet	0.81	0.81	0.81	0.72	0.39	0.35
Cut on $\Delta\phi(\text{photon} - \text{jet})$	0.56	0.56	0.48	0.13	0.02	0.01
Photon Purity	1.94	1.72	0.90	0.87	0.33	0.17
JER	0.03	0.03	0.03	0.03	0.03	0.03
Definition of inside/outside large R jet	0.07	0.07	0.07	0.07	0.09	0.11
Cut on $p_T^{\text{subleading jet}}/p_T^{\gamma}$	0.04	0.04	0.04	0.05	0.19	0.13
k-term	0.59	0.59	0.58	0.49	0.17	0.10
Statistics	2.76	2.72	2.32	1.49	0.74	0.52
Total uncertainty	4.74	4.73	4.32	3.58	2.90	2.46

Table A.19: γ-jet uncertainties for anti-k_t $R = 1.0$ trimmed jets for $45 < p_T^{\gamma} < 260$ GeV $1.80 < |\eta| < 2.10$ after bin merging and smoothing

	Uncertainty [%]				
p_T^{γ} [GeV]	260-310	310-400	400-500	500-600	600-800
Average p_T^{γ} [GeV]	280.66	343.71	430.27	524.59	683.59
Average p_T^{jet} [GeV]	267.53	325.24	407.56	506.20	652.16
1.0 - Data/MC	0.72	0.66	0.68	1.19	1.83
m^{jet}/p_T^{jet}	1.54	1.37	1.13	0.94	0.91
Generator	1.05	0.93	0.92	0.94	0.94
Photon Energy Scale	0.64	0.64	0.62	0.61	0.60
Cut on leading anti-k_t $R = 0.4$ jet outside large R jet	0.39	0.43	0.44	0.45	0.45
Cut on $\Delta\phi(\text{photon} - \text{jet})$	0.02	0.02	0.02	0.02	0.04
Photon Purity	0.09	0.05	0.02	0.01	0.00
JER	0.02	0.01	0.01	0.02	0.03
Definition of inside/outside large R jet	0.15	0.21	0.29	0.32	0.32
Cut on $p_T^{\text{subleading jet}}/p_T^{\gamma}$	0.08	0.07	0.06	0.03	0.03
k-term	0.08	0.06	0.05	0.04	0.04
Statistics	0.58	0.71	0.91	1.29	1.84
Total uncertainty	2.22	2.08	2.02	2.36	3.02

Table A.20: γ-jet uncertainties for anti-k_t $R = 1.0$ trimmed jets for $260 < p_T^{\gamma} < 800$ GeV $1.80 < |\eta| < 2.10$ after bin merging and smoothing

Appendix B

Additional Information for the γ-jet JES Uncertainty of Variable R Jets

B.1 The Uncertainties for VR Jets Derived using γ-jet Events after Bin Merging and Smoothing

	Uncertainty [%]						
p_T^{γ} [GeV]	25-45	45-65	65-85	85-110	110-160	160-210	210-260
Average p_T^{γ} [GeV]	31.3291	52.2119	73.1259	98.6675	139.235	181.234	231.285
Average p_T^{jet} [GeV]	29.7932	49.649	70.2465	95.6257	134.155	173.095	217.253
1.0 - Data/MC	0.81	0.83	0.84	0.45	0.31	0.40	0.52
Generator	0.46	0.46	0.46	0.50	0.56	0.47	0.37
Photon Energy Scale	0.53	1.14	1.33	1.24	0.80	0.65	0.63
Cut on the leading anti-k_t $R = 0.4$ jet outside VR jet	0.39	0.39	0.39	0.38	0.33	0.34	0.39
Cut on $\Delta\phi(\text{photon} - \text{jet})$	0.15	0.21	0.88	0.35	0.13	0.04	0.03
Photon Purity	6.19	1.19	0.88	0.59	0.25	0.12	0.04
JER	0.19	0.19	0.16	0.08	0.03	0.02	0.01
Definition of inside/outside VR jet	0.21	0.34	0.56	0.35	0.27	0.22	0.17
k-term	1.05	1.05	1.05	0.93	0.50	0.31	0.24
Statistics	2.15	1.27	1.22	0.71	0.31	0.20	0.21
Total uncertainty	6.75	2.58	2.71	2.03	1.29	1.07	1.04

Table B.1: γ-jet uncertainties for small VR jets for $25 < p_T^{\gamma} < 260$ GeV $0.00 < |\eta| < 0.80$ after bin merging and smoothing

	Uncertainty [%]					
p_T^{γ} [GeV]	260-310	310-400	400-500	500-600	600-800	800-1000
Average p_T^{γ} [GeV]	281.48	345.47	439.89	539.52	665.29	907.44
Average p_T^{jet} [GeV]	260.35	314.04	395.69	486.94	603.42	803.55
1.0 - Data/MC	0.59	0.54	0.43	0.55	0.98	2.22
Generator	0.30	0.24	0.22	0.22	0.22	0.22
Photon Energy Scale	0.62	0.61	0.61	0.60	0.58	0.57
Cut on leading anti-k_t $R = 0.4$ jet outside VR jet	0.40	0.37	0.33	0.32	0.32	0.32
Cut on $\Delta\phi(\mathrm{photon} - \mathrm{jet})$	0.02	0.04	0.18	0.32	0.39	0.50
Photon Purity	0.02	0.01	0.01	0.01	0.01	0.00
JER	0.01	0.01	0.01	0.01	0.01	0.01
Definition of inside/outside VR jet	0.14	0.11	0.09	0.10	0.11	0.12
k-term	0.20	0.18	0.17	0.17	0.17	0.17
Statistics	0.24	0.29	0.44	0.81	1.85	4.45
Total uncertainty	1.05	1.00	0.99	1.28	2.25	5.05

Table B.2: γ-jet uncertainties for small VR jets for $260 < p_T^{\gamma} < 1000$ GeV $0.00 < |\eta| < 0.80$ after bin merging and smoothing

	Uncertainty [%]						
p_T^{γ} [GeV]	25-45	45-65	65-85	85-110	110-160	160-210	210-260
Average p_T^{γ} [GeV]	31.10	52.10	73.15	98.52	139.17	181.18	231.47
Average p_T^{jet} [GeV]	29.71	48.45	68.65	94.01	131.79	169.98	213.33
1.0 - Data/MC	0.41	1.50	0.76	0.70	1.53	2.09	2.68
Generator	0.94	0.94	0.93	0.79	0.43	0.48	0.53
Photon Energy Scale	0.54	1.13	1.33	1.24	0.80	0.65	0.63
Cut on the leading anti-k_t $R = 0.4$ jet outside VR jet	0.51	0.51	0.51	0.47	0.35	0.35	0.40
Cut on $\Delta\phi(\mathrm{photon} - \mathrm{jet})$	0.15	0.21	0.88	0.34	0.13	0.04	0.03
Photon Purity	6.41	1.07	0.97	0.82	0.25	0.11	0.04
JER	0.19	0.19	0.16	0.08	0.03	0.02	0.01
Definition of inside/outside VR jet	0.21	0.34	0.57	0.34	0.27	0.22	0.17
k-term	1.05	1.05	1.05	0.93	0.50	0.31	0.24
Statistics	2.85	1.54	1.50	0.94	0.48	0.33	0.33
Total uncertainty	7.21	3.08	2.98	2.36	1.98	2.33	2.87

Table B.3: γ-jet uncertainties for small VR jets for $25 < p_T^{\gamma} < 260$ GeV $0.80 < |\eta| < 1.20$ after bin merging and smoothing

	Uncertainty [%]				
p_T^γ [GeV]	260-310	310-400	400-500	500-600	600-800
Average p_T^γ [GeV]	281.98	345.48	437.69	534.55	674.00
Average p_T^{jet} [GeV]	254.66	306.57	382.04	478.81	597.89
1.0 - Data/MC	2.96	2.94	2.74	2.85	3.61
Generator	0.50	0.46	0.44	0.44	0.44
Photon Energy Scale	0.62	0.61	0.61	0.60	0.58
Cut on leading anti-k_t $R = 0.4$ jet outside VR jet	0.41	0.39	0.36	0.35	0.35
Cut on $\Delta\phi(\text{photon} - \text{jet})$	0.02	0.04	0.17	0.33	0.38
Photon Purity	0.02	0.01	0.01	0.01	0.00
JER	0.01	0.01	0.01	0.01	0.01
Definition of inside/outside VR jet	0.14	0.11	0.09	0.09	0.11
k-term	0.20	0.18	0.16	0.15	0.15
Statistics	0.38	0.47	0.69	1.00	1.21
Total uncertainty	3.13	3.11	2.96	3.15	3.91

Table B.4: γ-jet uncertainties for small VR jets for $260 < p_T^\gamma < 800$ GeV $0.80 < |\eta| < 1.20$ after bin merging and smoothing

	Uncertainty [%]						
p_T^γ [GeV]	25-45	45-65	65-85	85-110	110-160	160-210	210-260
Average p_T^γ [GeV]	31.74	52.09	72.88	98.53	139.29	181.12	231.28
Average p_T^{jet} [GeV]	26.73	48.55	69.65	93.21	132.44	171.05	214.78
1.0 - Data/MC	0.32	1.62	1.71	2.89	1.76	1.39	1.48
Generator	1.01	1.01	1.02	1.07	1.18	0.92	0.65
Photon Energy Scale	0.51	1.15	1.33	1.25	0.80	0.65	0.63
Cut on the leading anti-k_t $R = 0.4$ jet outside VR jet	0.52	0.52	0.52	0.48	0.34	0.34	0.39
Cut on $\Delta\phi(\text{photon} - \text{jet})$	0.15	0.20	0.87	0.37	0.13	0.04	0.03
Photon Purity	6.44	1.04	0.95	0.73	0.30	0.12	0.03
JER	0.19	0.19	0.16	0.08	0.03	0.02	0.01
Definition of inside/outside VR jet	0.21	0.33	0.56	0.36	0.27	0.22	0.17
k-term	1.05	1.05	1.05	0.94	0.49	0.31	0.24
Statistics	2.94	1.47	1.53	1.16	0.67	0.47	0.49
Total uncertainty	7.27	3.13	3.38	3.79	2.47	1.92	1.87

Table B.5: γ-jet uncertainties for small VR jets for $25 < p_T^\gamma < 260$ GeV $1.20 < |\eta| < 1.50$ after bin merging and smoothing

	Uncertainty [%]				
p_T^γ [GeV]	260-310	310-400	400-500	500-600	600-800
Average p_T^γ [GeV]	281.23	344.75	439.39	543.72	659.04
Average p_T^{jet} [GeV]	256.31	306.87	391.00	470.51	590.74
1.0 - Data/MC	1.56	1.59	1.73	2.29	3.47
Generator	0.55	0.53	0.52	0.52	0.52
Photon Energy Scale	0.62	0.61	0.61	0.60	0.58
Cut on leading anti-k_t $R = 0.4$ jet outside VR jet	0.41	0.39	0.36	0.35	0.35
Cut on $\Delta\phi(\text{photon} - \text{jet})$	0.02	0.04	0.19	0.32	0.37
Photon Purity	0.02	0.02	0.01	0.00	0.00
JER	0.01	0.01	0.01	0.01	0.01
Definition of inside/outside VR jet	0.14	0.11	0.09	0.09	0.10
k-term	0.20	0.18	0.16	0.15	0.15
Statistics	0.57	0.71	0.97	1.13	1.25
Total uncertainty	1.92	1.97	2.19	2.72	3.81

Table B.6: γ-jet uncertainties for small VR jets for $260 < p_T^\gamma < 800$ GeV $1.20 < |\eta| < 1.50$ after bin merging and smoothing

	Uncertainty [%]						
p_T^γ [GeV]	25-45	45-65	65-85	85-110	110-160	160-210	210-260
Average p_T^γ [GeV]	30.81	52.64	73.23	98.98	138.98	181.27	230.63
Average p_T^{jet} [GeV]	26.11	47.67	68.18	93.10	130.11	168.21	211.54
1.0 - Data/MC	0.35	1.59	1.13	1.66	1.71	1.82	1.98
Generator	1.56	1.56	1.56	1.49	1.28	1.14	0.91
Photon Energy Scale	0.50	1.15	1.33	1.24	0.81	0.65	0.63
Cut on the leading anti-k_t $R = 0.4$ jet outside VR jet	1.16	1.15	1.13	0.90	0.30	0.15	0.14
Cut on $\Delta\phi(\text{photon} - \text{jet})$	0.15	0.20	0.89	0.35	0.13	0.04	0.03
Photon Purity	6.45	1.06	0.95	0.67	0.31	0.18	0.08
JER	0.19	0.19	0.16	0.08	0.03	0.02	0.01
Definition of inside/outside VR jet	0.21	0.33	0.57	0.35	0.27	0.22	0.17
k-term	1.05	1.05	1.05	0.93	0.50	0.31	0.24
Statistics	2.96	1.49	1.62	1.27	0.74	0.54	0.59
Total uncertainty	7.46	3.50	3.54	3.24	2.51	2.35	2.37

Table B.7: γ-jet uncertainties for small VR jets for $25 < p_T^\gamma < 260$ GeV $1.50 < |\eta| < 1.80$ after bin merging and smoothing

	Uncertainty [%]				
p_T^{γ} [GeV]	260-310	310-400	400-500	500-600	600-800
Average p_T^{γ} [GeV]	281.19	344.94	437.41	542.53	645.87
Average p_T^{jet} [GeV]	250.88	299.96	382.93	442.98	539.08
1.0 - Data/MC	2.11	2.21	2.42	2.78	3.52
Generator	0.78	0.70	0.69	0.69	0.69
Photon Energy Scale	0.62	0.61	0.61	0.60	0.59
Cut on leading anti-k_t $R = 0.4$ jet outside VR jet	0.14	0.14	0.14	0.14	0.14
Cut on $\Delta\phi(\text{photon} - \text{jet})$	0.02	0.04	0.21	0.30	0.37
Photon Purity	0.04	0.02	0.01	0.01	0.01
JER	0.01	0.01	0.01	0.01	0.01
Definition of inside/outside VR jet	0.14	0.11	0.09	0.09	0.10
k-term	0.20	0.18	0.16	0.16	0.15
Statistics	0.68	0.79	1.11	1.34	1.57
Total uncertainty	2.45	2.54	2.83	3.24	3.99

Table B.8: γ-jet uncertainties for small VR jets for $260 < p_T^{\gamma} < 800$ GeV $1.50 < |\eta| < 1.80$ after bin merging and smoothing

	Uncertainty [%]						
p_T^{γ} [GeV]	25-45	45-65	65-85	85-110	110-160	160-210	210-260
Average p_T^{γ} [GeV]	30.85	52.44	73.04	98.61	139.03	181.16	230.49
Average p_T^{jet} [GeV]	25.71	47.14	69.90	94.05	131.80	170.68	211.94
1.0 - Data/MC	2.75	1.42	1.29	1.27	1.29	0.83	0.91
Generator	2.09	2.09	2.08	1.89	1.36	1.34	1.25
Photon Energy Scale	0.50	1.14	1.34	1.24	0.80	0.65	0.63
Cut on the leading anti-k_t $R = 0.4$ jet outside VR jet	0.53	0.53	0.66	0.76	0.31	0.17	0.16
Cut on $\Delta\phi(\text{photon} - \text{jet})$	0.15	0.18	0.89	0.36	0.13	0.04	0.03
Photon Purity	7.36	2.44	1.12	0.84	0.32	0.17	0.09
JER	0.19	0.19	0.15	0.08	0.03	0.02	0.01
Definition of inside/outside VR jet	0.21	0.31	0.58	0.36	0.27	0.22	0.17
k-term	1.05	1.05	1.05	0.93	0.50	0.31	0.24
Statistics	4.47	2.82	2.77	1.75	0.85	0.63	0.73
Total uncertainty	9.37	4.81	4.41	3.50	2.33	1.87	1.85

Table B.9: γ-jet uncertainties for small VR jets for $25 < p_T^{\gamma} < 260$ GeV $1.80 < |\eta| < 2.10$ after bin merging and smoothing

	Uncertainty [%]				
p_T^{γ} [GeV]	260-310	310-400	400-500	500-600	600-800
Average p_T^{γ} [GeV]	280.36	343.60	431.26	522.74	697.81
Average p_T^{jet} [GeV]	254.91	301.41	372.63	452.57	643.12
1.0 - Data/MC	1.37	2.04	3.42	5.60	9.54
Generator	1.16	1.12	1.10	1.07	1.08
Photon Energy Scale	0.62	0.61	0.61	0.60	0.55
Cut on leading anti-k_t $R = 0.4$ jet outside VR jet	0.16	0.16	0.16	0.16	0.16
Cut on $\Delta\phi(\mathrm{photon} - \mathrm{jet})$	0.02	0.04	0.16	0.29	0.38
Photon Purity	0.04	0.02	0.05	0.07	0.00
JER	0.01	0.01	0.01	0.01	0.01
Definition of inside/outside VR jet	0.14	0.11	0.09	0.09	0.11
k-term	0.20	0.18	0.16	0.16	0.15
Statistics	0.97	1.44	2.92	5.84	11.26
Total uncertainty	2.15	2.82	4.68	8.20	14.81

Table B.10: γ-jet uncertainties for small VR jets for $260 < p_T^{\gamma} < 800$ GeV $1.80 < |\eta| < 2.10$ after bin merging and smoothing

	Uncertainty [%]						
p_T^{γ} [GeV]	25-45	45-65	65-85	85-110	110-160	160-210	210-260
Average p_T^{γ} [GeV]	31.41	52.08	72.55	98.30	138.84	180.23	230.77
Average p_T^{jet} [GeV]	27.01	43.59	66.61	94.95	132.10	170.68	213.59
1.0 - Data/MC	2.68	1.50	1.39	1.38	1.10	1.06	1.33
Generator	0.76	0.76	0.76	0.76	0.87	1.19	1.35
Photon Energy Scale	0.54	1.09	1.35	1.23	0.81	0.66	0.63
Cut on the leading anti-k_t $R = 0.4$ jet outside VR jet	0.52	0.52	0.61	0.76	0.31	0.17	0.16
Cut on $\Delta\phi(\mathrm{photon} - \mathrm{jet})$	0.15	0.17	0.96	0.32	0.13	0.05	0.03
Photon Purity	7.33	2.50	1.11	0.50	0.39	0.19	0.12
JER	0.19	0.19	0.17	0.08	0.03	0.02	0.01
Definition of inside/outside VR jet	0.21	0.29	0.65	0.34	0.27	0.23	0.18
k-term	1.05	1.05	1.05	0.92	0.50	0.32	0.25
Statistics	4.36	2.93	3.05	1.89	0.95	0.71	0.93
Total uncertainty	9.07	4.51	4.21	3.08	2.03	1.92	2.24

Table B.11: γ-jet uncertainties for small VR jets for $25 < p_T^{\gamma} < 260$ GeV $2.10 < |\eta| < 2.80$ after bin merging and smoothing

	Uncertainty [%]				
p_T^{γ} [GeV]	260-310	310-400	400-500	500-600	600-800
Average p_T^{γ} [GeV]	280.24	341.37	426.74	0.00	621.82
Average p_T^{jet} [GeV]	252.07	299.88	326.57	0.00	529.06
1.0 - Data/MC	1.60	1.77	1.82	3.63	3.99
Generator	1.20	0.91	0.79	0.76	0.59
Photon Energy Scale	0.62	0.62	0.62	0.13	0.60
Cut on leading anti-k_t $R = 0.4$ jet outside VR jet	0.16	0.16	0.16	0.52	0.16
Cut on $\Delta\phi(\text{photon} - \text{jet})$	0.03	0.06	0.08	0.15	0.34
Photon Purity	0.10	0.07	0.06	7.79	0.01
JER	0.01	0.01	0.01	0.19	0.01
Definition of inside/outside VR jet	0.15	0.12	0.11	0.21	0.08
k-term	0.22	0.19	0.18	1.05	0.16
Statistics	1.25	1.53	1.62	5.59	4.21
Total uncertainty	2.46	2.60	2.65	10.30	5.88

Table B.12: γ-jet uncertainties for small VR jets for $260 < p_T^{\gamma} < 800$ GeV $2.10 < |\eta| < 2.80$ after bin merging and smoothing

	Uncertainty [%]					
p_T^{γ} [GeV]	45-65	65-85	85-110	110-160	160-210	210-260
Average p_T^{γ} [GeV]	52.519	73.257	98.5723	139.181	181.206	231.246
Average p_T^{jet} [GeV]	57.7671	80.1426	106.085	145.884	187.31	236.306
1.0 - Data/MC	1.52	0.67	0.41	0.64	0.69	0.65
m^{jet}/p_T^{jet}	0.58	0.58	0.58	0.52	0.43	0.38
Generator	0.64	0.63	0.56	0.31	0.21	0.14
Photon Energy Scale	0.69	0.81	0.89	0.69	0.61	0.62
Cut on the leading anti-k_t $R = 0.4$ jet outside VR jet	0.77	0.77	0.70	0.53	0.47	0.41
Cut on $\Delta\phi(\text{photon} - \text{jet})$	0.46	0.43	0.29	0.12	0.04	0.03
Photon Purity	1.13	0.73	0.57	0.26	0.13	0.05
JER	0.02	0.06	0.13	0.09	0.05	0.02
Definition of inside/outside VR jet	0.18	0.18	0.16	0.11	0.10	0.14
Cut on $p_T^{\text{subleading jet}}/p_T^{\gamma}$	0.50	0.45	0.19	0.14	0.14	0.12
k-term	0.25	0.25	0.22	0.16	0.16	0.14
Statistics	1.42	1.28	0.75	0.32	0.20	0.19
Total uncertainty	2.83	2.25	1.79	1.34	1.19	1.11

Table B.13: γ-jet uncertainties for large VR jets for $45 < p_T^{\gamma} < 260$ GeV $0.00 < |\eta| < 0.80$ after bin merging and smoothing

	Uncertainty [%]					
p_T^γ [GeV]	260-310	310-400	400-500	500-600	600-800	800-1000
Average p_T^γ [GeV]	281.46	345.85	440.25	539.28	665.14	903.42
Average p_T^{jet} [GeV]	286.05	347.38	438.84	537.55	656.47	886.99
1.0 - Data/MC	0.63	0.61	0.57	0.59	0.88	1.79
m^{jet}/p_T^{jet}	0.38	0.37	0.37	0.37	0.37	0.37
Generator	0.10	0.07	0.06	0.05	0.05	0.05
Photon Energy Scale	0.62	0.61	0.59	0.57	0.55	0.50
Cut on leading anti-k_t $R = 0.4$ jet outside VR jet	0.35	0.31	0.33	0.34	0.30	0.26
Cut on $\Delta\phi(\text{photon} - \text{jet})$	0.03	0.03	0.04	0.04	0.04	0.12
Photon Purity	0.01	0.01	0.01	0.01	0.00	0.00
JER	0.00	0.00	0.00	0.00	0.00	0.00
Definition of inside/outside VR jet	0.22	0.30	0.30	0.26	0.24	0.23
Cut on $p_T^{\text{subleading jet}}/p_T^\gamma$	0.12	0.17	0.22	0.25	0.26	0.26
k-term	0.10	0.06	0.02	0.01	0.01	0.01
Statistics	0.20	0.22	0.28	0.39	0.57	0.99
Total uncertainty	1.08	1.07	1.07	1.10	1.32	2.19

Table B.14: γ-jet uncertainties for large VR jets for $260 < p_T^\gamma < 1000$ GeV $0.00 < |\eta| < 0.80$ after bin merging and smoothing

	Uncertainty [%]					
p_T^γ [GeV]	45-65	65-85	85-110	110-160	160-210	210-260
Average p_T^γ [GeV]	52.70	73.22	98.51	139.06	181.24	231.59
Average p_T^{jet} [GeV]	54.14	76.15	102.73	141.58	182.09	230.14
1.0 - Data/MC	2.65	3.18	2.13	2.02	2.05	2.21
m^{jet}/p_T^{jet}	0.10	0.10	0.10	0.18	0.29	0.35
Generator	0.61	0.61	0.60	0.55	0.51	0.53
Photon Energy Scale	0.69	0.80	0.89	0.69	0.61	0.62
Cut on the leading anti-k_t $R = 0.4$ jet outside VR jet	0.77	0.73	0.67	0.52	0.47	0.41
Cut on $\Delta\phi(\text{photon} - \text{jet})$	0.46	0.44	0.29	0.12	0.04	0.03
Photon Purity	1.08	0.79	0.65	0.25	0.12	0.05
JER	0.02	0.06	0.13	0.09	0.05	0.02
Definition of inside/outside VR jet	0.18	0.18	0.16	0.11	0.10	0.14
Cut on $p_T^{\text{subleading jet}}/p_T^\gamma$	0.50	0.46	0.18	0.14	0.14	0.14
k-term	0.25	0.25	0.22	0.16	0.16	0.14
Statistics	1.47	1.34	0.85	0.42	0.29	0.29
Total uncertainty	3.51	3.82	2.75	2.35	2.30	2.44

Table B.15: γ-jet uncertainties for large VR jets for $45 < p_T^\gamma < 260$ GeV $0.80 < |\eta| < 1.20$ after bin merging and smoothing

	Uncertainty [%]				
p_T^γ [GeV]	260-310	310-400	400-500	500-600	600-800
Average p_T^γ [GeV]	281.90	345.29	436.99	536.50	665.16
Average p_T^{jet} [GeV]	278.12	338.71	426.34	524.75	642.14
1.0 - Data/MC	2.35	2.33	2.24	2.38	2.68
m^{jet}/p_T^{jet}	0.35	0.35	0.35	0.35	0.35
Generator	0.49	0.34	0.19	0.16	0.16
Photon Energy Scale	0.62	0.61	0.59	0.58	0.56
Cut on leading anti-k_t $R = 0.4$ jet outside VR jet	0.35	0.31	0.34	0.36	0.34
Cut on $\Delta\phi(\text{photon} - \text{jet})$	0.03	0.03	0.04	0.03	0.03
Photon Purity	0.02	0.01	0.01	0.01	0.01
JER	0.00	0.00	0.00	0.00	0.00
Definition of inside/outside VR jet	0.22	0.30	0.30	0.26	0.25
Cut on $p_T^{\text{subleading jet}}/p_T^\gamma$	0.14	0.15	0.16	0.16	0.16
k-term	0.10	0.06	0.02	0.01	0.01
Statistics	0.32	0.41	0.64	0.86	0.97
Total uncertainty	2.56	2.54	2.49	2.67	2.97

Table B.16: γ-jet uncertainties for large VR jets for $260 < p_T^\gamma < 800$ GeV $0.80 < |\eta| < 1.20$ after bin merging and smoothing

	Uncertainty [%]					
p_T^γ [GeV]	45-65	65-85	85-110	110-160	160-210	210-260
Average p_T^γ [GeV]	52.24	73.09	98.33	139.00	180.81	231.22
Average p_T^{jet} [GeV]	49.87	71.43	98.96	139.79	180.12	228.24
1.0 - Data/MC	2.66	3.75	3.32	2.21	2.26	2.48
m^{jet}/p_T^{jet}	2.05	2.05	2.04	1.82	1.41	1.08
Generator	0.22	0.23	0.29	0.48	0.41	0.25
Photon Energy Scale	0.68	0.80	0.91	0.68	0.61	0.62
Cut on the leading anti-k_t $R = 0.4$ jet outside VR jet	0.78	0.73	0.68	0.52	0.47	0.41
Cut on $\Delta\phi(\text{photon} - \text{jet})$	0.46	0.44	0.29	0.12	0.04	0.03
Photon Purity	1.09	0.80	0.76	0.29	0.14	0.05
JER	0.01	0.05	0.14	0.09	0.05	0.02
Definition of inside/outside VR jet	0.18	0.18	0.16	0.11	0.10	0.14
Cut on $p_T^{\text{subleading jet}}/p_T^\gamma$	0.50	0.47	0.17	0.14	0.14	0.14
k-term	0.25	0.25	0.22	0.15	0.16	0.14
Statistics	1.54	1.44	1.02	0.57	0.40	0.40
Total uncertainty	4.06	4.77	4.28	3.11	2.85	2.86

Table B.17: γ-jet uncertainties for large VR jets for $45 < p_T^\gamma < 260$ GeV $1.20 < |\eta| < 1.50$ after bin merging and smoothing

	Uncertainty [%]				
p_T^{γ} [GeV]	260-310	310-400	400-500	500-600	600-800
Average p_T^{γ} [GeV]	281.62	344.98	437.88	539.60	663.41
Average p_T^{jet} [GeV]	276.59	336.99	429.41	525.07	649.13
1.0 - Data/MC	2.45	2.19	1.88	2.01	2.26
m^{jet}/p_T^{jet}	0.97	0.90	0.81	0.76	0.75
Generator	0.21	0.26	0.32	0.34	0.34
Photon Energy Scale	0.62	0.61	0.59	0.58	0.56
Cut on leading anti-k_t $R = 0.4$ jet outside VR jet	0.35	0.31	0.34	0.36	0.34
Cut on $\Delta\phi(\text{photon} - \text{jet})$	0.03	0.03	0.04	0.03	0.03
Photon Purity	0.03	0.02	0.01	0.00	0.00
JER	0.00	0.00	0.00	0.00	0.00
Definition of inside/outside VR jet	0.22	0.30	0.30	0.26	0.25
Cut on $p_T^{\text{subleading jet}}/p_T^{\gamma}$	0.14	0.15	0.16	0.16	0.16
k-term	0.10	0.06	0.02	0.01	0.01
Statistics	0.45	0.54	0.86	1.23	1.57
Total uncertainty	2.79	2.56	2.37	2.61	2.96

Table B.18: γ-jet uncertainties for large VR jets for $260 < p_T^{\gamma} < 800$ GeV $1.20 < |\eta| < 1.50$ after bin merging and smoothing

	Uncertainty [%]					
p_T^{γ} [GeV]	45-65	65-85	85-110	110-160	160-210	210-260
Average p_T^{γ} [GeV]	52.67	72.97	98.38	138.95	181.23	230.85
Average p_T^{jet} [GeV]	47.77	67.53	95.18	135.84	177.51	225.01
1.0 - Data/MC	5.58	2.84	3.79	2.15	1.99	2.30
m^{jet}/p_T^{jet}	2.04	2.04	2.03	1.72	1.20	0.98
Generator	0.34	0.36	0.48	0.79	0.75	0.60
Photon Energy Scale	0.68	0.79	0.92	0.68	0.61	0.62
Cut on the leading anti-k_t $R = 0.4$ jet outside VR jet	0.96	0.97	1.16	1.45	0.77	0.39
Cut on $\Delta\phi(\text{photon} - \text{jet})$	0.46	0.44	0.28	0.12	0.04	0.03
Photon Purity	1.14	0.90	0.60	0.31	0.16	0.06
JER	0.01	0.05	0.14	0.09	0.05	0.02
Definition of inside/outside VR jet	0.18	0.18	0.16	0.11	0.10	0.14
Cut on $p_T^{\text{subleading jet}}/p_T^{\gamma}$	0.50	0.48	0.17	0.14	0.14	0.14
k-term	0.25	0.25	0.23	0.15	0.17	0.15
Statistics	6.38	3.86	1.97	0.78	0.47	0.48
Total uncertainty	8.91	5.49	5.04	3.39	2.69	2.73

Table B.19: γ-jet uncertainties for large VR jets for $45 < p_T^{\gamma} < 260$ GeV $1.50 < |\eta| < 1.80$ after bin merging and smoothing

	Uncertainty [%]				
p_T^γ [GeV]	260-310	310-400	400-500	500-600	600-800
Average p_T^γ [GeV]	281.29	344.84	437.19	540.20	641.43
Average p_T^{jet} [GeV]	272.81	332.60	427.12	519.94	596.28
1.0 - Data/MC	2.44	2.03	1.23	1.41	1.77
m^{jet}/p_T^{jet}	0.90	0.72	0.33	0.17	0.14
Generator	0.52	0.48	0.47	0.47	0.47
Photon Energy Scale	0.62	0.61	0.59	0.57	0.57
Cut on leading anti-k_t $R = 0.4$ jet outside VR jet	0.32	0.30	0.27	0.26	0.26
Cut on $\Delta\phi(\text{photon} - \text{jet})$	0.03	0.03	0.03	0.03	0.03
Photon Purity	0.02	0.01	0.02	0.02	0.01
JER	0.00	0.00	0.00	0.00	0.00
Definition of inside/outside VR jet	0.22	0.30	0.30	0.26	0.25
Cut on $p_T^{\text{subleading jet}}/p_T^\gamma$	0.14	0.15	0.16	0.16	0.16
k-term	0.10	0.06	0.02	0.01	0.01
Statistics	0.55	0.68	1.03	1.35	1.54
Total uncertainty	2.81	2.43	1.86	2.13	2.50

Table B.20: γ-jet uncertainties for large VR jets for $260 < p_T^\gamma < 800$ GeV $1.50 < |\eta| < 1.80$ after bin merging and smoothing

	Uncertainty [%]					
p_T^γ [GeV]	45-65	65-85	85-110	110-160	160-210	210-260
Average p_T^γ [GeV]	53.02	72.57	98.30	138.93	181.04	229.68
Average p_T^{jet} [GeV]	47.61	67.20	92.05	133.35	176.90	224.22
1.0 - Data/MC	5.52	1.87	0.80	1.11	1.10	1.02
m^{jet}/p_T^{jet}	1.94	1.94	1.94	2.06	1.75	0.89
Generator	0.24	1.03	2.81	2.25	1.51	1.19
Photon Energy Scale	0.68	0.80	0.92	0.68	0.61	0.62
Cut on the leading anti-k_t $R = 0.4$ jet outside VR jet	0.96	0.97	1.14	1.49	0.75	0.39
Cut on $\Delta\phi(\text{photon} - \text{jet})$	0.46	0.44	0.29	0.12	0.04	0.03
Photon Purity	1.14	0.91	0.84	0.32	0.15	0.06
JER	0.02	0.05	0.14	0.08	0.05	0.02
Definition of inside/outside VR jet	0.18	0.18	0.17	0.11	0.10	0.14
Cut on $p_T^{\text{subleading jet}}/p_T^\gamma$	0.50	0.47	0.18	0.14	0.14	0.14
k-term	0.25	0.25	0.23	0.15	0.17	0.15
Statistics	6.38	3.74	1.96	0.96	0.61	0.59
Total uncertainty	8.84	5.03	4.39	3.79	2.81	2.05

Table B.21: γ-jet uncertainties for large VR jets for $45 < p_T^\gamma < 260$ GeV $1.80 < |\eta| < 2.10$ after bin merging and smoothing

	Uncertainty [%]				
p_T^γ [GeV]	260-310	310-400	400-500	500-600	600-800
Average p_T^γ [GeV]	280.33	343.35	429.71	528.86	683.59
Average p_T^{jet} [GeV]	274.16	334.62	417.13	522.64	656.52
1.0 - Data/MC	0.87	0.67	0.60	1.27	2.47
m^{jet}/p_T^{jet}	0.44	0.33	0.31	0.31	0.31
Generator	1.03	0.87	0.74	0.71	0.70
Photon Energy Scale	0.62	0.61	0.60	0.58	0.56
Cut on leading anti-k_t $R = 0.4$ jet outside VR jet	0.32	0.30	0.28	0.26	0.26
Cut on $\Delta\phi(\text{photon} - \text{jet})$	0.03	0.03	0.04	0.03	0.03
Photon Purity	0.02	0.01	0.01	0.02	0.00
JER	0.00	0.00	0.00	0.00	0.00
Definition of inside/outside VR jet	0.22	0.30	0.31	0.26	0.24
Cut on $p_T^{\text{subleading jet}}/p_T^\gamma$	0.14	0.15	0.16	0.16	0.16
k-term	0.10	0.06	0.03	0.01	0.01
Statistics	0.72	0.99	1.39	1.64	1.88
Total uncertainty	1.76	1.69	1.87	2.32	3.27

Table B.22: γ-jet uncertainties for large VR jets for $260 < p_T^\gamma < 800$ GeV $1.80 < |\eta| < 2.10$ after bin merging and smoothing

Bibliography

[1] **ATLAS** Collaboration, "Jet energy measurement and its systematic uncertainty in proton–proton collisions at $\sqrt{s} = 7$ TeV with the ATLAS detector", `arXiv:1406.0076 [hep-ex]`.

[2] **ATLAS** Collaboration, T. Carli, G. Choudalakis, D. Gingrich, C. Issever, L. Kogan, J. Kvita, M. Relich, T. Spreitzer, A. Taffard, A. Tanasijczuk, M. Vetterli, and F. Vives, "Backup Note For Measurement of the Jet Energy with the ATLAS Detector Using photon+jet events in proton-proton collisions at $\sqrt{s} = 7$ TeV", tech. rep., CERN, Geneva, Jul, 2012. `https://svnweb.cern.ch/trac/atlasperf/browser/CombPerf/JetETMiss/JESPaper2011Data/gammajet/Supporting_documentation.pdf`.

[3] A. Dattagupta, J. Horton, L. Kogan, S. Lammers, G. Lefebvre, B. Malaescu, A. Olariu, P. Starovoitov, and M. Vetterli, "Jet energy scale and resolution determination using gamma/Z+jet events in the ATLAS data at $\sqrt{s} = 8$ TeV", Tech. Rep. ATL-COM-PHYS-2014-791, CERN, Geneva, Sep, 2014. ATLAS Internal note.

[4] **ATLAS** Collaboration, A. Dattagupta, J. Horton, L. Kogan, S. Lammers, G. Lefebvre, B. Malaescu, A. Olariu, P. Starovoitov, and M. Vetterli, "Backup Note For the Jet Energy Scale and Resolution Determination using gamma/Z+jet events in the ATLAS data at $\sqrt{s} = 8$ TeV", tech. rep., CERN, Geneva, Sep, 2014. `https://svnweb.cern.ch/trac/atlasperf/browser/CombPerf/JetETMiss/VJetBalance2012CONF/BackUp`.

[5] K. Behr, C. Issever, L. A. Kogan, and J. Zhong, "The Performance and Calibration of Jets with Small Variable R", Tech. Rep. ATL-COM-PHYS-2014-1152, CERN, Geneva, Sep, 2014. ATLAS Internal note.

[6] L. A. Kogan, K. Behr, C. Issever, and J. Zhong, "The Performance and Calibration of Large Variable R Jets at the ATLAS Detector", Tech. Rep. ATL-COM-PHYS-2014-1152, CERN, Geneva, Sep, 2014. ATLAS Internal note.

[7] D. E. Morrissey, T. Plehn, and T. M. Tait, "Physics searches at the LHC", *Phys.Rept.* **515** (2012) 1–113, `arXiv:0912.3259 [hep-ph]`.

[8] **ATLAS** Collaboration, "The ATLAS Experiment at the CERN Large Hadron Collider", *J. Instrum.* **3** (2008) S08003. 437 p. Also published by CERN Geneva in 2010.

[9] L. R. Evans and P. Bryant, “LHC Machine”, *J. Instrum.* **3** (2008) S08001. 164 p. This report is an abridged version of the LHC Design Report (CERN-2004-003).

[10] “Observation of a new particle in the search for the standard model higgs boson with the atlas detector at the lhc”, *Physics Letters* **B 716** no. 1, (2012) 1 – 29.

[11] “Observation of a new boson at a mass of 125 gev with the cms experiment at the lhc”, *Physics Letters* **B 716** no. 1, (2012) 30 – 61.

[12] G. S. Guralnik, C. R. Hagen, and T. W. B. Kibble, “Global conservation laws and massless particles”, *Phys. Rev. Lett.* **13** (Nov, 1964) 585–587. `http://link.aps.org/doi/10.1103/PhysRevLett.13.585`.

[13] F. Englert and R. Brout, “Broken symmetry and the mass of gauge vector mesons”, *Phys. Rev. Lett.* **13** (Aug, 1964) 321–323. `http://link.aps.org/doi/10.1103/PhysRevLett.13.321`.

[14] P. Higgs, “Broken symmetries, massless particles and gauge fields”, *Physics Letters* **12** no. 2, (1964) 132 – 133. `http://www.sciencedirect.com/science/article/pii/0031916364911369`.

[15] **ATLAS** Collaboration, “Combined measurements of the mass and signal strength of the Higgs-like boson with the ATLAS detector using up to 25 fb^{-1} of proton-proton collision data”, Tech. Rep. ATLAS-CONF-2013-014, CERN, Geneva, Mar, 2013.

[16] **ATLAS** Collaboration, “Study of the spin of the new boson with up to 25 fb^{-1} of ATLAS data”, Tech. Rep. ATLAS-CONF-2013-040, CERN, Geneva, Apr, 2013.

[17] **ATLAS** Collaboration, “Updated coupling measurements of the Higgs boson with the ATLAS detector using up to 25 fb^{-1} of proton-proton collision data”, Tech. Rep. ATLAS-CONF-2014-009, CERN, Geneva, Mar, 2014.

[18] **CMS** Collaboration, “Combination of standard model Higgs boson searches and measurements of the properties of the new boson with a mass near 125 GeV”, Tech. Rep. CMS-PAS-HIG-13-005, CERN, Geneva, 2013.

[19] **CMS** Collaboration, “Measurement of the properties of a higgs boson in the four-lepton final state”, *Phys. Rev. D* **89** (May, 2014) 092007. `http://link.aps.org/doi/10.1103/PhysRevD.89.092007`.

[20] A. Altheimer, A. Arce, L. Asquith, J. Backus Mayes, E. Bergeaas Kuutmann, *et al.*, “Boosted objects and jet substructure at the LHC. Report of BOOST2012, held at IFIC Valencia, 23rd-27th of July 2012”, *Eur.Phys.J.* **C74** (2014) 2792, `arXiv:1311.2708 [hep-ex]`.

[21] S. S. A. Livermore and C. Issever, *A search for massive top quark resonances with the ATLAS detector at the Large Hadron Collider*. PhD thesis, Oxford U., Oxford, Jan, 2013. Presented 01 Mar 2013.

[22] “Standard model of elementary particles”, May, 2014. `http://en.wikipedia.org/wiki/File:Standard_Model_of_Elementary_Particles.svg`.

[23] F. Halzen and A. D. Martin, *Quarks and leptons : an introductory course in modern particle physics*. Wiley, 1984.

[24] **Particle Data Group** Collaboration, K. Olive *et al.*, “Review of Particle Physics”, *Chin.Phys.* **C38** (2014) 090001.

[25] R. K. Ellis, W. J. Stirling, and W. B. R., *QCD and collider physics*. Cambridge University Press, 1996.

[26] T. Sjostrand, “Monte Carlo Generators”, `arXiv:hep-ph/0611247 [hep-ph]`.

[27] J. M. Campbell, J. Huston, and W. Stirling, “Hard Interactions of Quarks and Gluons: A Primer for LHC Physics”, *Rept.Prog.Phys.* **70** (2007) 89, `arXiv:hep-ph/0611148 [hep-ph]`. doi 10.1088/0034-4885/70/1/R02.

[28] T. Sjostrand, S. Mrenna, and P. Z. Skands, “A Brief Introduction to PYTHIA 8.1”, *Comput.Phys.Commun.* **178** (2008) 852–867, `arXiv:0710.3820 [hep-ph]`.

[29] T. Sjostrand, S. Mrenna, and P. Z. Skands, “PYTHIA 6.4 Physics and Manual”, *JHEP* **0605** (2006) 026, `arXiv:hep-ph/0603175 [hep-ph]`.

[30] G. Corcella, I. Knowles, G. Marchesini, S. Moretti, K. Odagiri, *et al.*, “HERWIG 6.5 release note”, `arXiv:hep-ph/0210213 [hep-ph]`.

[31] M. Bahr, S. Gieseke, M. Gigg, D. Grellscheid, K. Hamilton, *et al.*, “Herwig++ Physics and Manual”, *Eur.Phys.J.* **C58** (2008) 639–707, `arXiv:0803.0883 [hep-ph]`.

[32] V. Gribov and L. Lipatov, “Deep inelastic e p scattering in perturbation theory”, *Sov.J.Nucl.Phys.* **15** (1972) 438–450.

[33] Y. L. Dokshitzer, “Calculation of the Structure Functions for Deep Inelastic Scattering and e+ e- Annihilation by Perturbation Theory in Quantum Chromodynamics.”, *Sov.Phys.JETP* **46** (1977) 641–653.

[34] G. Altarelli and G. Parisi, “Asymptotic Freedom in Parton Language”, *Nucl.Phys.* **B126** (1977) 298.

[35] B. Andersson, G. Gustafson, G. Ingelman, and T. Sjostrand, “Parton Fragmentation and String Dynamics”, *Phys.Rept.* **97** (1983) 31–145.

[36] B. Webber, “A QCD Model for Jet Fragmentation Including Soft Gluon Interference”, *Nucl.Phys.* **B238** (1984) 492.

[37] E. . Berger, “Research directions for the decade. Proceedings, 1990 Summer Study on High-Energy Physics, Snowmass, USA, June 25 - July 13, 1990”,. `http://lss.fnal.gov/archive/1990/conf/Conf-90-249-E.pdf`. Singapore, Singapore: World Scientific (1992) 808 p.

[38] G. P. Salam, “Towards Jetography”, *Eur.Phys.J.* **C67** (2010) 637–686, `arXiv:0906.1833 [hep-ph]`.

[39] G. P. Salam and G. Soyez, “A Practical Seedless Infrared-Safe Cone jet algorithm”, *JHEP* **0705** (2007) 086, `arXiv:0704.0292 [hep-ph]`.

[40] **ATLAS** Collaboration, “Performance of Jet Algorithms in the ATLAS Detector”, Tech. Rep. ATL-PHYS-INT-2010-129, CERN, Geneva, Dec, 2010.

[41] M. Cacciari, G. P. Salam, and G. Soyez, “The anti- k t jet clustering algorithm”, *JHEP* **2008** no. 04, (2008) 063. `http://stacks.iop.org/1126-6708/2008/i=04/a=063`.

[42] D. Krohn, J. Thaler, and L.-T. Wang, “Jets with Variable R”, *JHEP* **0906** (2009) 059, `arXiv:0903.0392 [hep-ph]`.

[43] **ATLAS** Collaboration, “Jet energy measurement with the ATLAS detector in proton-proton collisions at $\sqrt{s} = 7$ TeV”, *Eur.Phys.J.* **C73** (2013) 2304, `arXiv:1112.6426 [hep-ex]`.

[44] **CMS** Collaboration, “Determination of Jet Energy Calibration and Transverse Momentum Resolution in CMS”, *JINST* **6** (2011) P11002, `arXiv:1107.4277 [physics.ins-det]`.

[45] C. T. Hill, “Topcolor assisted technicolor”, *Phys.Lett.* **B345** (1995) 483–489, `arXiv:hep-ph/9411426 [hep-ph]`.

[46] **ATLAS** Collaboration, “Performance of jet substructure techniques for large-r jets in proton-proton collisions at $\sqrt{s} = 7$ tev using the atlas detector”, *JHEP* **2013** no. 9, (2013) 1–83. `http://dx.doi.org/10.1007/JHEP09%282013%29076`.

[47] **CMS** Collaboration, “Boosted Top Jet Tagging at CMS”, Tech. Rep. CMS-PAS-JME-13-007, CERN, Geneva, 2014.

[48] **CMS** Collaboration, “Identifying Hadronically Decaying Vector Bosons Merged into a Single Jet”, Tech. Rep. CMS-PAS-JME-13-006, CERN, Geneva, 2013.

[49] P. Nason, “A New method for combining NLO QCD with shower Monte Carlo algorithms”, *JHEP* **0411** (2004) 040, `arXiv:hep-ph/0409146 [hep-ph]`.

[50] S. Frixione, P. Nason, and C. Oleari, “Matching NLO QCD computations with Parton Shower simulations: the POWHEG method”, *JHEP* **0711** (2007) 070, `arXiv:0709.2092 [hep-ph]`.

[51] S. Alioli, K. Hamilton, P. Nason, C. Oleari, and E. Re, “Jet pair production in POWHEG”, *JHEP* **1104** (2011) 081, `arXiv:1012.3380 [hep-ph]`.

[52] J. Thaler and K. Van Tilburg, “Identifying Boosted Objects with N-subjettiness”, *JHEP* **1103** (2011) 015, `arXiv:1011.2268 [hep-ph]`.

[53] M. Cacciari, G. P. Salam, and G. Soyez, “FastJet User Manual”, *Eur.Phys.J.* **C72** (2012) 1896, `arXiv:1111.6097 [hep-ph]`.

[54] **ATLAS** Collaboration, “Performance of boosted top quark identification in 2012 ATLAS data”, Tech. Rep. ATLAS-CONF-2013-084, CERN, Geneva, Aug, 2013.

[55] **ATLAS** Collaboration, “Search for $t\bar{t}$ resonances in the lepton plus jets final state with ATLAS using 4.7 fb^{-1} of *pp* collisions at $\sqrt{s} = 7$ TeV”, *Phys.Rev.* **D88** no. 1, (2013) 012004, `arXiv:1305.2756 [hep-ex]`.

[56] **ATLAS** Collaboration, “A search for $t\bar{t}$ resonances in the lepton plus jets final state with ATLAS using 14 fb^{1} of pp collisions at $\sqrt{s} = 8$ TeV”, Tech. Rep. ATLAS-CONF-2013-052, CERN, Geneva, May, 2013. Not published in the proceedings.

[57] A. Altheimer, T. Andeen, K. Behr, E. Bergeaas Kuutmann, J. Blanco, G. Brooijmans, C. Buttar, S. Calvet, S. Crepe-Renaudin, T. Cornelissen, B. Decheneux, P.-A. Delsart, D. Duda, F. Fassi, J. Ferrando, D. Ferreira De Lima, S. Fleischmann, M. Franchini, A. Gershon, T. Heck, M. A. Hyaya, C. Issever, W. Ji, K. Johns, D. Kar, V. Kaushik, L. Kogan, T. Kuhl, P. Maettig, L. Masetti, C. Oropeza Barrera, C. Pollard, V. Sanchez Martinez, M. Stanescu Bellu, E. Thompson, L. Valery, J. Veatch, M. Vos, C. Wasicki, J. Zhong, and H. Zhu, “A search for $\mathbf{t\bar{t}}$ resonances in the lepton plus jets final state using 15 $\text{fb}^{\mathbf{-1}}$ of pp collisions at $\sqrt{\mathbf{s}} = \mathbf{8}$ TeV”, Tech. Rep. ATL-COM-PHYS-2013-090, CERN, Geneva, Jan, 2013. ATLAS Internal note.

[58] A. Altheimer, K. Behr, E. Bergeaas Kuutmann, G. Brooijmans, C. Buttar, S. Calvet, J. Caudron, S. Crepe-Renaudin, T. Cornelissen, B. Dechenaux, P.-A. Delsart, D. Duda, F. Fassi, J. Ferrando, D. Ferreira De Lima, S. Fleischmann, A. Gershon, N. Gutierrez-Ortiz, S. Groh, T. Heck, C. Issever, K. Johns, D. Kar, L. Kogan, T. Kuhl, X. Lei, C. Leroy, P. Maettig, L. Masetti, R. Nayyar, C. Oropeza Barrera, C. Pollard, V. Sanchez Martinez, D. Shoaleh-Saadi, M. Stanescu-Bellu, E. Thompson, L. Valery, J. Veatch, M. Vos, C. Wasicki, and J. Zhong, “A search for $\mathbf{t\bar{t}}$ resonances in the lepton plus jets final state using 20 fb^{-1} of pp collisions at $\sqrt{\mathbf{s}} = \mathbf{8}$ TeV”, Tech. Rep. ATL-COM-PHYS-2014-003, CERN, Geneva, Jan, 2014. ATLAS Internal note.

[59] **ATLAS** Collaboration, “Light-quark and gluon jet discrimination in pp collisions at $\sqrt{s} = 7$ TeV with the ATLAS detector”, `arXiv:1405.6583 [hep-ex]`.

[60] “Lhc commissioning with beam”, 2014. `http://lhc-commissioning.web.cern.ch/lhc-commissioning/`.

[61] J. Haffner, “The CERN accelerator complex. Complexe des accélérateurs du CERN”,. General Photo, Copyright © CERN.

[62] **ATLAS** Collaboration, “Luminosity public plots”, 2014. `https://twiki.cern.ch/twiki/bin/view/AtlasPublic/LuminosityPublicResults`.

[63] J. Pequenao, “Computer generated image of the whole ATLAS detector”, Mar, 2008.

[64] **ATLAS** Collaboration, “Lar public plots”, 2014. `https://twiki.cern.ch/twiki/bin/view/AtlasPublic/LArCaloPublicResultsDetStatus`.

[65] **ATLAS** Collaboration, "TileCal plots for approval : 7TeV collision events",. `https://twiki.cern.ch/twiki/bin/view/AtlasPublic/TileCaloPublicResults`.

[66] **ATLAS** Collaboration, W. Lampl, S. Laplace, D. Lelas, P. Loch, H. Ma, S. Menke, S. Rajagopalan, D. Rousseau, S. Snyder, and G. Unal, "Calorimeter Clustering Algorithms: Description and Performance", ATL-LARG-PUB-2008-002. ATL-COM-LARG-2008-003.

[67] S. Menke, "Pile-up in Jets in ATLAS",. `https://cds.cern.ch/record/1598801`. Shown at Boost 2013 Conference.

[68] **ATLAS** Collaboration, "Expected Performance of the ATLAS Experiment - Detector, Trigger and Physics", `arXiv:0901.0512 [hep-ex]`.

[69] **ATLAS** Collaboration, "Expected photon performance in the atlas experiment", ATL-PHYS-PUB-2011-007. `https://cdsweb.cern.ch/record/1345329`.

[70] **ATLAS** Collaboration, "Measurements of the photon identification efficiency with the ATLAS detector using 4.9 fb1 of pp collision data collected in 2011", Tech. Rep. ATLAS-CONF-2012-123, CERN, Geneva, Aug, 2012.

[71] **ATLAS** Collaboration, F. Monticelli, J. M. Lorenz, A. Tricoli, and T. Kohno, "Performance of the Electron and Photon Trigger in p-p Collisions at $sqrts = 7$ TeV with the ATLAS Detector at the LHC in 2011", Tech. Rep. ATL-DAQ-INT-2012-001, CERN, Geneva, May, 2012. Internal note.

[72] M. Stoebe, S. Chekanov, J. Cantero, B. Vachon, M. Stockton, C. Glasman, J. Terron, and O. Rifki, "Measurement of the inclusive isolated prompt photon cross section in pp collisions at $\sqrt{s} = 8$ TeV with the ATLAS detector using 20.3 fb^{-1} ", Tech. Rep. ATL-COM-PHYS-2014-744, CERN, Geneva, Jun, 2014. ATLAS Internal supporting note for the 2012 inclusive cross section measurement.

[73] **ATLAS** Collaboration, "The ATLAS Data Quality Defect Database System", *Eur.Phys.J.* **C72** (2012) 1960, `arXiv:1110.6119 [physics.ins-det]`.

[74] **GEANT4** Collaboration, S. Agostinelli *et al.*, "GEANT4: A Simulation toolkit", *Nucl.Instrum.Meth.* **A506** (2003) 250–303.

[75] R. Corke and T. Sjostrand, "Interleaved Parton Showers and Tuning Prospects", *JHEP* **1103** (2011) 032, `arXiv:1011.1759 [hep-ph]`.

[76] A. Martin, W. Stirling, R. Thorne, and G. Watt, "Parton distributions for the LHC", *Eur.Phys.J.* **C63** (2009) 189–285, `arXiv:0901.0002 [hep-ph]`.

[77] **ATLAS** Collaboration, "ATLAS tunes of PYTHIA 6 and Pythia 8 for MC11", Tech. Rep. ATL-PHYS-PUB-2011-009, CERN, Geneva, Jul, 2011.

[78] **ATLAS** Collaboration, "Summary of ATLAS Pythia 8 tunes", Tech. Rep. ATL-PHYS-PUB-2012-003, CERN, Geneva, Aug, 2012.

[79] J. Pumplin, D. Stump, J. Huston, H. Lai, P. M. Nadolsky, *et al.*, "New generation of parton distributions with uncertainties from global QCD analysis", *JHEP* **0207** (2002) 012, `arXiv:hep-ph/0201195 [hep-ph]`.

[80] H.-L. Lai, M. Guzzi, J. Huston, Z. Li, P. M. Nadolsky, *et al.*, "New parton distributions for collider physics", *Phys.Rev.* **D82** (2010) 074024, `arXiv:1007.2241 [hep-ph]`.

[81] **ATLAS** Collaboration, "Electron and photon reconstruction and identification in ATLAS: expected performance at high energy and results at 900 GeV", Tech. Rep. ATLAS-CONF-2010-005, CERN, Geneva, Jun, 2010.

[82] **ATLAS** Collaboration, "Measurement of the inclusive isolated prompt photon cross section in *pp* collisions at $\sqrt{s} = 7$ TeV with the ATLAS detector", *Phys.Rev.* **D83** (2011) 052005, `arXiv:1012.4389 [hep-ex]`.

[83] **ATLAS** Collaboration, "Measurement of isolated-photon pair production in *pp* collisions at $\sqrt{s} = 7$ TeV with the ATLAS detector", *JHEP* **1301** (2013) 086, `arXiv:1211.1913 [hep-ex]`.

[84] Q. Buat, J. Leveque, N. Lorenzo Martinez, and Polci, "Definition of the photon cleaning procedure for 2011 data", Tech. Rep. ATL-COM-PHYS-2012-134, CERN, Geneva, Feb, 2012. ATLAS Internal note.

[85] M. Hance, D. Olivito, and H. Williams, "Performance Studies for e/gamma Calorimeter Isolation", Tech. Rep. ATL-COM-PHYS-2011-1186, CERN, Geneva, Sep, 2011. ATLAS Internal note.

[86] S. Laplace and J. de Vivie, "Calorimeter isolation and pile-up", Tech. Rep. ATL-COM-PHYS-2012-467, CERN, Geneva, May, 2012. ATLAS Internal note.

[87] **ATLAS** Collaboration, "Electron reconstruction and identification efficiency measurements with the ATLAS detector using the 2011 LHC proton-proton collision data", *Eur. Phys. J. C* no. arXiv:1404.2240. CERN-PH-EP-2014-040, (Apr, 2014) 74. 38 p.

[88] **ATLAS** Collaboration, "Measurement of the muon reconstruction performance of the ATLAS detector using 2011 and 2012 LHC proton-proton collision data", `arXiv:1407.3935 [hep-ex]`.

[89] **ATLAS** Collaboration, "Commissioning of the ATLAS high-performance b-tagging algorithms in the 7 TeV collision data", Tech. Rep. ATLAS-CONF-2011-102, CERN, Geneva, Jul, 2011.

[90] **ATLAS** Collaboration, "Calibration of the performance of *b*-tagging for *c* and light-flavour jets in the 2012 ATLAS data", Tech. Rep. ATLAS-CONF-2014-046, CERN, Geneva, Jul, 2014.

[91] M. Agustoni, M. Aharrouche, A. Ahmad, N. Besson, M. Boonekamp, L. Carminati, J. de Vivie, H. De La Torre, J. Del Peso, J. Farley, V. Gallo, S. Glazov, C. Handel, S. Haug, M. Karnevskiy, I. Koletsou, N. Lorenzo Martinez, N. Makovec, L. Mandelli, Y. Nakahama, R. Turra, and G. Unal, "Electromagnetic energy scale in-situ calibration and performance: Supporting document for the egamma performance paper", Tech. Rep. ATL-COM-PHYS-2011-263, CERN, Geneva, Mar, 2011. ATLAS Internal note.

[92] J.-B. Blanchard, J.-B. de Vivie, and P. Mastrandrea, "In situ scales and smearings from Z and J/Ψ events", Tech. Rep. ATL-COM-PHYS-2013-1653, CERN, Geneva, Dec, 2013. ATLAS Internal note.

[93] **ATLAS** Collaboration, "Electron performance measurements with the ATLAS detector using the 2010 LHC proton-proton collision data", *Eur.Phys.J.* **C72** (2012) 1909, `arXiv:1110.3174 [hep-ex]`.

[94] **ATLAS** Collaboration, "Testbeam studies of production modules of the ATLAS tile calorimeter", *Nucl.Instrum.Meth.* **A606** (2009) 362–394.

[95] **ATLAS** Collaboration, "Readiness of the ATLAS Tile Calorimeter for LHC collisions", *Eur.Phys.J.* **C70** (2010) 1193–1236, `arXiv:1007.5423 [physics.ins-det]`.

[96] **ATLAS** Collaboration, "Local Hadronic Calibration", Tech. Rep. ATL-LARG-PUB-2009-001-2. ATL-COM-LARG-2008-006. ATL-LARG-PUB-2009-001, CERN, Geneva, Jun, 2008.

[97] **ATLAS** Collaboration, "Jet energy resolution in proton-proton collisions at $\sqrt{s} = 7$ TeV recorded in 2010 with the ATLAS detector", *Eur.Phys.J.* **C73** (2013) 2306, `arXiv:1210.6210 [hep-ex]`.

[98] **ATLAS** Collaboration, "Pile-up subtraction and suppression for jets in ATLAS", Tech. Rep. ATLAS-CONF-2013-083, CERN, Geneva, Aug, 2013.

[99] M. Cacciari and G. P. Salam, "Pileup subtraction using jet areas", *Phys.Lett.* **B659** (2008) 119–126, `arXiv:0707.1378 [hep-ph]`.

[100] M. Cacciari, G. P. Salam, and G. Soyez, "The Catchment Area of Jets", *JHEP* **0804** (2008) 005, `arXiv:0802.1188 [hep-ph]`.

[101] **ATLAS** Collaboration, "Jet mass and substructure of inclusive jets in $\sqrt{s} = 7$ TeV *pp* collisions with the ATLAS experiment", *JHEP* **1205** (2012) 128, `arXiv:1203.4606 [hep-ex]`.

[102] R. Alon, L. Asquith, S. Baker, E. Bergeaas Kuutmann, B. Chapleau, S. Chekanov, A. R. Davison, E. Duchovni, T. Farooque, J. Ferrando, L. S. Gomez Fajardo, M. Karagoz, S. Livermore, A. Lewis, D. W. Miller, E. Oliver, J. Proudfoot, C. Sandoval, A. Schwartzman, P. Sinervo, M. Villaplana, and M. Vos, "Backup Note for Measurement of Jet Mass and Substructure in QCD with the ATLAS

Experiment", Tech. Rep. ATL-COM-PHYS-2011-401, CERN, Geneva, Apr, 2011. ATLAS Internal note.

[103] A. R. Davison and I. Ochoa, "Validating the ATLAS Large R-parameter Jet Mass Scale and Resolution with Hadronically Decaying Boosted W Bosons Using the 2012 Dataset.", Tech. Rep. ATL-COM-PHYS-2013-865, CERN, Geneva, Jun, 2013. ATLAS Internal note.

[104] **ATLAS** Collaboration, "Jet etmiss public results", May, 2014. `https://twiki.cern.ch/twiki/bin/view/AtlasPublic/JetEtmissPublicResults`.

[105] **ATLAS** Collaboration, "Probing the measurement of jet energies with the ATLAS detector using photon+jet events in proton-proton collisions at $\sqrt{s} = 7$ TeV", Tech. Rep. ATLAS-CONF-2012-063, CERN, Geneva, Jul, 2012.

[106] **ATLAS** Collaboration, "Lar event veto for release 17", 2014. `https://twiki.cern.ch/twiki/bin/view/AtlasComputing/LArEventVetoRel17`.

[107] **ATLAS** Collaboration, "In situ jet pseudorapidity intercalibration of the ATLAS detector using dijet events in sqrts=7 TeV proton-proton 2011 data", Tech. Rep. ATLAS-CONF-2012-124, CERN, Geneva, Aug, 2012.

[108] **ATLAS** Collaboration, "Data preparation checklist for physics analysis", 2014. `https://twiki.cern.ch/twiki/bin/viewauth/Atlas/DataPreparationCheckListForPhysicsAnalysis`.

[109] M. Relich and A. Taffard, *Searches for Heavy Neutrinos and Supersymmetry in Dilepton Events at the ATLAS Experiment.* PhD thesis, Irvine, CA, USA, UC Irvine, 2013. Presented 02 Dec 2013.

[110] "How to clean jets 2012", 2014. `https://twiki.cern.ch/twiki/bin/viewauth/AtlasProtected/HowToCleanJets2012`.

[111] **ATLAS** Collaboration, "Jet substructure recommendations", 2014. `https://twiki.cern.ch/twiki/bin/view/AtlasProtected/JetSubstructureRecommendations`.

[112] **ATLAS** Collaboration, "Systtool svn repositary", May, 2014. `https://svnweb.cern.ch/cern/wsvn/atlas-gulefebv/SystTool/tags/SystTool-00-01-02`.

[113] J. Zhong. Personal communication.

[114] M. Baak, G. Besjes, D. Cote, A. Koutsman, J. Lorenz, *et al.*, "HistFitter software framework for statistical data analysis", `arXiv:1410.1280 [hep-ex]`.

[115] **ATLAS** Collaboration, "Pileup effects on jet substructure at high μ", 2014. `https://twiki.cern.ch/twiki/bin/view/AtlasPublic/JetEtmissApproved2013HighMuSubstructure`.